DIODE-PUMPED Tm³⁺-DOPED SESQUIOXIDE LASERS FOR ULTRASHORT PULSE APPLICATIONS IN THE 2μm REGION
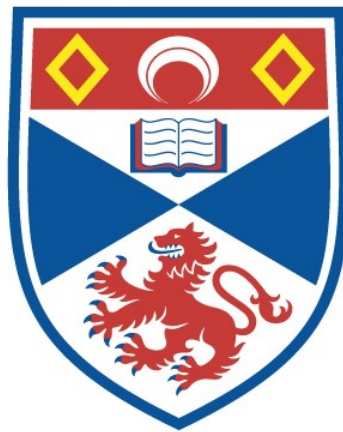
Neil Kenneth Stevenson

A Thesis Submitted for the Degree of EngD
at the
University of St Andrews

2020

Diode-pumped Tm^{3+}-doped sesquioxide lasers for ultrashort pulse applications in the 2μm region

Neil Kenneth Stevenson

University of
St Andrews

This thesis is submitted in partial fulfilment for the degree of
Doctorate of Engineering (EngD)
at the University of St Andrews

November 2019

Academic supervisor:

     Professor Christian Thomas Alcuin Brown, University of St Andrews

Industrial supervisor:

     Doctor Alexander Alexandrovich Lagatsky, Fraunhofer UK

Declarations

Candidate's declaration:

I, Neil Kenneth Stevenson, do hereby certify that this thesis, submitted for the degree of EngD, which is approximately 62,000 words in length, has been written by me, and that it is the record of work carried out by me, or principally by myself in collaboration with others as acknowledged, and that it has not been submitted in any previous application for any degree.

I was admitted as a research student at the University of St Andrews in September 2015.

I received funding from an organisation or institution and have acknowledged the funder(s) in the full text of my thesis.

Date ..17/02/2020....   signature of candidate ....

Supervisor's declaration:

I hereby certify that the candidate has fulfilled the conditions of the Resolution and Regulations appropriate for the degree of EngD in the University of St Andrews and that the candidate is qualified to submit this thesis in application for that degree.

Date .17/02/2020....   signature of supervisor ....

Permission for publication:

In submitting this thesis to the University of St Andrews we understand that we are giving permission for it to be made available for use in accordance with the regulations of the University Library for the time being in force, subject to any copyright vested in the work not being affected thereby. We also understand, unless exempt by an award of an embargo as requested below, that the title and the abstract will be published, and that a copy of the work may be made and supplied to any bona fide library or research worker, that this thesis will be electronically accessible for personal or research use and

that the library has the right to migrate this thesis into new electronic forms as required to ensure continued access to the thesis.

I, Neil Kenneth Stevenson, confirm that my thesis does not contain any third-party material that requires copyright clearance.

The following is an agreed request by candidate and supervisor regarding the publication of this thesis:

PRINTED COPY

No embargo on print copy

ELECTRONIC COPY

No embargo on electronic copy

Date ..17/02/2020.....   signature of candidate ....

Date ..17/02/2020.....   signature of supervisor ....

Underpinning Research Data or Digital Outputs

Candidate's declaration:

I, Neil Kenneth Stevenson, understand that by declaring that I have original research data or digital outputs, I should make every effort in meeting the University's and research funders' requirements on the deposit and sharing of research data or research digital outputs.

Date ..17/02/2020.....   signature of candidate ....

Permission for publication of underpinning research data or digital outputs:

We understand that for any original research data or digital outputs which are deposited, we are giving permission for them to be made available for use in accordance with the requirements of the University and research funders, for the time being in force.

We also understand that the title and the description will be published, and that the underpinning research data or digital outputs will be electronically accessible for use in accordance with the license specified at the point of deposit, unless exempt by award of an embargo as requested below.

The following is an agreed request by candidate and supervisor regarding the publication of underpinning research data or digital outputs:

No embargo on underpinning research data or digital outputs.

Date ..17/02/2020.....   signature of candidate ....

Date ..17/02/2020.....   signature of supervisor ....

Abstract

This thesis presents the development of Tm^{3+}-doped sesquioxide laser sources in the 2–2.1 μm spectral region. The primary focus of this development has been aimed towards high power diode-pumped mode-locked laser sources capable of femtosecond pulse generation. In addition to this, the early development of a compact and low threshold ultrafast laser inscribed waveguide laser has also been realised.

Continuous wave characterisation of bulk solid-state crystalline $Tm:LuScO_3$ and ceramic $Tm:Lu_2O_3$ lasers has been completed using ~795 nm multimode single emitter laser diode pump sources. Average output powers of 660 mW and 901 mW, and emission wavelengths of 2.1 μm and 2.06 μm were achieved from the $Tm:LuScO_3$ and $Tm:Lu_2O_3$ lasers, respectively. In addition, both lasers demonstrated smooth and continuous tuning ranges spanning more than 160 nm in the ~2–2.1 μm spectral region.

In the mode-locked regime, pulse durations as short as 170 fs were recorded at an average output power of 113 mW and an emission wavelength of 2094 nm from a diode-pumped mode-locked $Tm:LuScO_3$ laser through the use of an ion-implanted InGaAsSb quantum-well-based semiconductor saturable absorber mirror. A diode-pumped $Tm:Lu_2O_3$ laser, utilising the same semiconductor saturable absorber mirror, was able to generate pulses as short as 278 fs at an average output power of 555 mW and a wavelength of 2081 nm through the use of a steeply diving optic axis birefringent filter. This same filter was also used to demonstrate broadly tunable femtosecond pulses in both laser configurations. Subsequent amplification of the ultrashort pulse laser sources realised maximum amplified average output powers of 540 mW and 855 mW, respectively.

The results presented in this thesis demonstrate the potential for diode-pumped Tm^{3+}-doped sesquioxide laser sources to be developed into an enabler technology for the advancement of a number of photonics applications and techniques in the mid-infrared region.

Acknowledgements

It is difficult to put into words how grateful I am to those who have supported me throughout the last few years; be that in an academic/professional manner or on a much more personal basis. I have met, learnt from, and enjoyed the company of a great many people during my time as an EngD student and while naming them all may represent a herculean task, I will endeavour to do so in some form or manner.

First and foremost, I would like to thank my supervisors, the research institutions they each represent and the Centre of Doctoral Training in Applied Photonics. Without them, the research contained within this thesis would not have been possible. The guidance and encouragement provided by Professor Tom Brown and Doctor Alex Lagatsky has been greatly appreciated. In addition, I would like to thank all those at the Fraunhofer Centre of Applied Photonics who made the EngD a truly enjoyable experience (the "teambuilding" social outings are of particular note) and thank those within the CDT and St Andrews for helping me wade through the administrative red tape.

It would also be prudent to acknowledge those collaborators who contributed to some of the success achieved during this thesis. As such, thanks are extended to the following individuals: Daniel Morris and Professor Daniel Esser for establishing the collaborative amplifier work undertaken at Heriot-Watt University and for welcoming me and my laser into their lab, James Morris for lending his expertise to inscribe and characterise the waveguides in $Tm:Lu_2O_3$ and for his help during laser performance characterisation, and Professor Alan Kemp for his discussions pertaining to steeply diving optic axis birefringent filters and for providing the base script used in modelling the performance of said filters.

I would next like to thank my family and friends for the many ways they have supported me, consoled me, and allowed me to vent and relax during the last four years. Be it via a home cooked meal, free alcohol, a weekend break out of the city to play with the dog(s), a trip up the hills or to a beach, adventures in Eastwind, or an unexpectedly heavy session that ran into the early hours of the morning – this would not have been possible without you.

To my parents, thank you for your unwavering support throughout my life. Though your advice and wise words may have fallen on deaf ears at times, some did sink in and has undoubtedly allowed me to get where I am today.

Finally, I would like to thank my fiancé Rachel. Like a lighthouse during stormy seas she has guided me from the rocks on numerous occasions and provided a safe harbour in the form of a welcoming smile. Having someone that can understand, without explanation, that sometimes you just need to pig out after a hard day in the lab has proved invaluable. Without her, I would never have started on this adventure. This thesis is devoted to her.

Research data underpinning this thesis are available at https://doi.org/10.17630/289e627f-5177-4b34-8c62-976384401ae0

"There is an art or rather a knack to flying. The knack lies in learning how to throw yourself at the ground and miss. Pick a nice day and try it.

The first part is easy. All it requires is simply the ability to throw yourself forward with all your weight, and the willingness not to mind that it's going to hurt."

The Hitchhiker's Guide to the Galaxy

Contents

List of publications

Journal publications

1. J. Morris, N. K. Stevenson, H. T. Bookey, A. K. Kar, C. T. A. Brown, J.-M. Hopkins, M. D. Dawson, and A. A. Lagatsky, "1.9 μm waveguide laser fabricated by ultrafast laser inscription in Tm:Lu2O3 ceramic," Opt. Express 25, 14910-14917 (2017).

2. N. K. Stevenson, C. T. A. Brown, J.-M. Hopkins, M. D. Dawson, C. Kränkel, and A. A. Lagatsky, "Diode-pumped femtosecond Tm 3+-doped LuScO3 laser near 2.1 μm," Opt. Lett. 43, 1287-1290 (2018).

3. N. K. Stevenson, C. T. A. Brown, J.-M. Hopkins, M. D. Dawson, and A. A. Lagatsky, "Broadly tunable femtosecond pulses around 2.06 μm from a diode-pumped Tm^{3+}-doped solid-state laser source," Opt. Express 27, 11103–11111 (2019).

Conference submissions

1. N. K. Stevenson, J. Morris, H. Bookey, A. K. Kar, C. T. A. Brown, J.-M. Hopkins, M. D. Dawson, and A. A. Lagatsky, "Waveguide Tm:Lu2O3 ceramic laser fabricated by ultrafast laser inscription," in *2017 Conference on Lasers and Electro-Optics Europe & European Quantum Electronics Conference (CLEO/Europe-EQEC)* (IEEE, 2017), p. CJ-10.3.

2. N. K. Stevenson, C. T. A. Brown, J. -M. Hopkins, M. D. Dawson, and A. A. Lagatsky, "Broadly tunable diode-pumped femtosecond Tm:LuScO3 laser," in *8th EPS-QEOD Europhoton Conference* (Europhysics Conference Abstracts, 2018), p. ThA2.6.D.

3. D. Morris, M. Reilly, N. K. Stevenson, A. A. Lagatsky, and M. J. D. Esser, "Power-scalable ultrafast Ho:YAG slab amplifier at 2094 nm," in *Solid State Lasers XXVIII: Technology and Devices* (SPIE, 2019), p. 108960T.

4. N. K. Stevenson, C. T. A. Brown, J. M. Hopkins, M. D. Dawson, and A. A. Lagatsky, "Diode-pumped Tm3+-doped sesquioxide ultrashort pulse seed oscillators for Ho-amplifiers," in *2019 Conference on Lasers and Electro-Optics Europe & European Quantum Electronics Conference (CLEO/Europe-EQEC)* (IEEE, 2019), p. CA-P.32.

5. N. K. Stevenson, C. T. A. Brown, and A. A. Lagatsky, "Femtosecond Tm:Lu2O3 ceramic MOPA at 2080 nm," in *Laser Congress 2019 (ASSL, LAC, LS&C)* (Optical Society of America, 2019), p. ATu5A.4.

List of figures

List of tables

Abbreviations

AR	–	anti-reflection
(SD-)BRF	–	(steeply diving optic axis) birefringent filter
CW	–	continuous wave
DFG	–	difference frequency generation
FROG	–	frequency-resolved optical gating
FSR	–	free spectral range
FWHM	–	full-width at half-maximum
GDD	–	group delay dispersion
GTI	–	Gires-Tournois interferometer
HR	–	high reflectivity
IR	–	infrared
KLM	–	Kerr lens mode-locking
KTP	–	potassium titanyl phosphate
LNB	–	lithium niobate
(Q)ML	–	(Q-switched) mode-locked
MOPA	–	master oscillator power amplifier
OC	–	output coupler
OPO	–	optical parametric oscillation
QCL	–	quantum cascade laser
ROC	–	radius of curvature
RF	–	radio frequency
SCG	–	supercontinuum generation
SESAM	–	semiconductor saturable absorption mirror
SPIDER	–	spectral phase interferometry for direct electric-field reconstruction

SPM   –   self-phase modulation

TBP   –   time-bandwidth product

ULI   –   ultrafast laser inscription

(X)UV   –   (extreme) ultraviolet

1   Introduction

"The laser is a solution seeking a problem" – this is how Theodore Maiman referred to his development of the first laser in 1960 [1,2]. Since then the laser has become a household recognised technology and a staple device of the 21st century, aiding in the advancement of techniques and technologies in many fields, including medical research and healthcare, environmental sensing and spectroscopy, manufacturing and industrial processing, and telecommunications. This thesis will discuss a much more specialised and advanced form of laser source than the flashlamp pumped ruby laser constructed by Maiman nearly 60 years ago, presenting the development of diode-pumped solid-state ultrashort pulse lasers in the 2–2.1 μm spectral region based on Tm^{3+}-doped sesquioxide gain media.

1.1   Laser applications in the mid-infrared spectral region

The mid-IR spectral region of approximately 2–20 μm offers many beneficial features for applications and techniques currently undertaken in the visible or, more commonly, the near-IR. The most prevalent of these features is what is referred to as the "molecular fingerprint region" and can be exploited in various forms of optical spectroscopy. Within this spectral region a large number of molecules experience strong vibrational transitions, including molecules important in the study of pollution and climate change such as carbon dioxide, sulphur dioxide, nitrogen dioxide, and methane (Fig. 1) [3]. This same region is also occupied by the molecular resonances of many common explosives [3,4] and drugs [5], allowing for non-intrusive study and stand-off threat detection of such molecules. Detection of these absorption features in the mid-IR band is also aided by two relatively transparent windows in the Earth's atmosphere, around 3.5–5 μm and 8–13 μm, which means that the trace gas detection of environmental pollutants and toxins can be performed using relatively straight forward techniques such as direct absorption spectroscopy [6]. The medical sciences have also found use of optical spectroscopy in the mid-IR in diagnosis procedures. Breath samples can be analysed to detect molecular species associated with diseases, providing important information without the need for invasive and complex blood sample testing [7]. Furthermore, the use of spectroscopy could be implemented to detect and identify

various molecular markers existing in breath samples to diagnose different lung diseases, cancers, and diabetes [8].
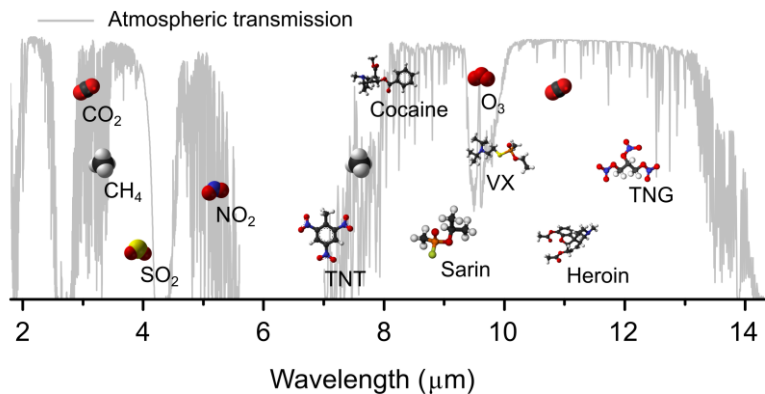
Fig. 1. Resonances of selected molecular species in the mid-IR spectral region [9]. Atmospheric transmission data is shown by the grey line [10].

Medical research has also utilised laser technology in a more direct approach with the development of laser scalpels. While visible and near-IR laser sources based on Nd:YAG and ruby gain media are more widely known for cosmetic procedures in hair and tattoo removal [11,12], a move to the mid-IR opens up the use of laser tools to be used in surgery as precise cutting implements. In general, the cells present in every type of soft tissue consist of water (~65%) and protein strands (~35%). CW laser sources that target the absorption peaks of water and proteins around 2–3 μm and 6–8 μm, respectively, have been used in the past to demonstrate less invasive, high precision laser surgery [13], with a significant reduction in blood loss and dissection time over conventionally used mechanical devices [14]. By targeting the absorption peaks of the water and proteins present in cells in the IR region, effective tissue ablation can be achieved whilst reducing the risk of photochemically damaging the nucleobases found in DNA. This is a considerable drawback of short wavelength ultraviolet (UV) excimer laser sources used in laser refractive surgery, where the tissue molecules that experience high absorption in the UV spectral region are proteins, DNA, and melanin [13].

In the field of manufacturing and industrial processing, the CO_2 laser, emitting between 9 and 10 μm, still dominates sheet metal cutting despite growing competition from other laser sources such as high power fibre lasers and disk lasers [15]. This domination is not so much due to any significant advantage from the emission wavelength but is more thanks to the generations of development that have gone into the gas laser source and the understanding of their performance that has been gained as a result. The advantages provided by high power fibre lasers and disk lasers in energy efficiency, footprint size,

and beam delivery flexibility have made the cutting market more competitive in recent years. However, the lack of understanding surrounding cutting and beam-material interactions have meant that CO_2 lasers still outperform when cutting thick metallic materials [15]. The industrial processing of transparent and brittle materials such as glass are becoming more relevant as the use of intricate touchscreens on smartphones and tablets continues to expand. Specialised near-IR laser sources offer a benefit over CO_2 lasers in that the lower absorption coefficient of near-IR radiation allows for a volumetric absorption and cuts without chips. This is compared with the surface absorption interaction found with CO_2 lasers due to a higher absorption coefficient [15,16].

2 μm laser sources provide a particularly unique advantage when it comes to the additive free, clear-to-clear welding of plastics. The absorption spectra of many common plastics (*e.g.*, PMMA, PET, and polycarbonate) show that the 2 μm wavelength sits between two significant absorption peaks around 1700 nm and 2200 nm. This places 2 μm laser radiation in a "goldilocks" region in-between very little absorption found in the visible region and very strong absorption where UV lasers around 355 nm and CO_2 lasers at 10 μm are used. The moderate absorption experienced in plastics around 2 μm means the light can penetrate through the sample whilst being attenuated and heating up the local region. This is in contrast to the surface heating found with UV and CO_2 lasers and the limited modifications found when using visible laser sources [17,18]. Welding of plastics without the need for additional chemical additives is particularly relevant to the medical industry as it simplifies biocompatibility testing [19]. The use of 2 μm laser radiation has also been studied for the fabrication of laser induced periodical surface structuring of semiconductor materials. This universal phenomena can be used as a method of surface texturing on almost any material and has been shown to produce diffraction grating like structures on steel and superhydrophobic surfaces on silicon wafers [20]. The phenomena can also be exploited as a time and cost effective method of surface texturing of photovoltaic cells, providing a significant increase in the light harvesting efficiency of the semiconductor substrate [21].

The generation of extreme UV (XUV) and soft X-ray radiation has driven development in many areas of science. High resolution X-ray microscopy means it is possible to image buried nanostructures [22] and begin to probe primary atomic element resonances [23]. Structural information of complex protein molecules can also be retrieved, modelled, and investigated through exposure to these ultrashort wavelengths [24–26]. Moreover, with the generation of XUV and X-ray radiation

comes the possibility to produce pulses with durations in the order of tens to hundreds of attoseconds. These pulses can then be used in the study of electron dynamics [27–29], investigating processes that take place within electron shells. The sources used to generate these extremely short wavelengths (~2–100 nm) in the first place, however, tend to be purpose built national synchrotron or free electron laser facilities providing limited access to researchers. Laser frequency conversion based on nonlinear crystals is a proven method of extending the wavelength range of laser sources and accessing spectral regions from the UV to the mid-IR, but even this approach is prevented from generating sources below ~200 nm by strong absorption in the crystals for wavelengths in the deep-UV.

An alternative method of accessing the XUV and soft X-ray spectral regions is that of high harmonic generation (HHG) [30–32]. This highly nonlinear process is driven by ultrashort pulse lasers with incredibly high peak intensities focused onto gas targets. Intensities in the range of $\sim 10^{13}$–10^{14} W/cm^2 are needed to achieve the necessary up conversion required to drive the laser frequency to its higher harmonics. HHG makes it possible to generate XUV and X-ray wavelengths on a table-top scale, moving away from the requirement of very large and expensive facilities and allowing individual research groups access to their own sources for small-scale experiments and investigations. The current driving laser source behind HHG is the femtosecond Ti:sapphire laser. Through chirped pulse amplification [33], sub-15 fs pulse systems with petawatt peak powers at few Hz repetition frequency are commercially available. Moving away from the near-IR though, HHG from the mid-IR spectral region offers potential to generate ultrahigh harmonics and much wider spanning emission, realising transform-limited pulse durations of 0.035 fs [34], and theoretically allowing for the generation of pulses as short as 0.0025 fs [35]. And while the use of multiple frequency conversion and amplification stages allow fundamental Ti:sapphire sources to reach into the mid-IR, high power mode-locked sources emitting around and beyond 2 μm would be well placed to satisfy to requirements of a driving source for XUV and X-ray emission.

In recent years the area of optical telecoms has also had a growing interest to move towards the 2 μm region. Whilst the current optical telecommunications network, the underpinning technology that facilitates the Internet of Things lifestyle enjoyed by the majority of the developed world, is dominated by the 1550 nm telecom band utilising the high performance of Er^{3+}-doped fibre amplifiers and low transmission loss in silica fibres, there is a call to open up a new 2 μm telecom band as an alternative or additional avenue of research with the aim of increasing the transmission bandwidth of the

existing telecommunications network [36]. New technologies and techniques have allowed the current demand in bandwidth to be met with the existing telecom bands, but the capacity of current fibre technology is quickly approaching the nonlinear Shannon limit (a limit imposed on the maximum amount of information that can be transported for each wavelength division multiplex channel) [37]. If the growth in demand continues without a major change in technology then a "capacity crunch" is anticipated in the coming years [38]. This new 2 μm telecom band would be able to make use of developments in hollow-core photonic bandgap fibres [39,40] and wideband Tm^{3+}-doped fibre amplifiers [41,42], as well as occupying a so-called "sweet spot" between 1.8 and 2.1 μm for the emerging field of silicon photonics where the development of silicon-photonics-based devices has begun [43]. However, questions still remain about the development of suitable compact semiconductor 2 μm sources that are able to operate in the demanding environment of high temperature telecom racks. InP can be extended to 2 μm by induced compressive strain but suffers from a limited operating temperature range restricting it use to the very edge of server racks. GaSb-based devices are more promising for high temperature operation but face challenges in fabrication [36]. Research in this area is ongoing but sources capable of driving this push into a new telecom band need to be found before the window can be opened.

1.2   State-of-the-art laser source development in the mid-IR

The previous section has detailed a few examples of novel applications and benefits to existing techniques that can be achieved by moving to the mid-IR spectral region. The laser sources required to take advantage of such benefits, *i.e.* those that emit at and beyond 2 μm, do exist and are available to researchers. However, these sources are generally bulky, expensive, and limited in power when operating in the ultrashort pulse regime. This ultimately restricts their applications. In order to become a true enabler technology, mid-IR laser sources need to become more widely available to a larger portion of the research community. This means making them more compact, robust, and affordable.

The mid-IR spectral region can be accessed directly using laser sources that naturally emit in the mid-IR, *e.g.*, quantum cascade lasers (QCL), Tm^{3+}- and Ho^{3+}-doped amorphous and crystalline materials, Cr^{2+}- and Fe^{2+}-doped chalcogenides or CO_2 lasers, or via stages of nonlinear frequency conversion techniques and amplification from a near-IR laser source [44]. Some examples of these approaches are shown in Fig. 2. Whilst reliable and commercially available near-IR lasers sources are well established,

using them as a fundamental source to access the mid-IR through frequency conversion ultimately results in a complex and expensive laboratory configuration. However, this approach of reaching the mid-IR has been taken by numerous commercial manufacturers (Chromacity Ltd, Toptica Photonics AG, and Menlo Systems GmbH, to name a select few) and has been used in the demonstration of remote stand-off and open-path detection and identification of hydrocarbon gases [45,46], and chemical aerosols and solids in free space [47] and on surfaces [48]. For example, in [45], Kara *et al.* employed a commercial ultrashort pulse optical parametric oscillator (OPO) based on a MgO-doped periodically poled lithium niobate (LNB) nonlinear crystal pumped by a passively mode-locked Yb:fibre laser. The source could be tuned from 2.8–3.9 μm and, by selecting a particular grating position, provided instantaneous coverage of the strongest absorption bands in methane and ethane from 3.1–3.5 μm. It should be noted that whilst this source was used in more of a quasi-CW spectroscopy approach, the development of mid-IR broadband sources is closely related to the development of mid-IR mode-locked lasers as they can act as the preliminary source of high peak power pulses for further frequency up-conversion to the mid-IR spectral region.

The second order nonlinear spectral shifting processes of OPO and difference frequency generation (DFG) require the use of highly nonlinear optical materials to work effectively. Nonlinear oxide crystals such as LNB or potassium titanyl phosphate (KTP) are commonly used. However, the transparency of these crystals is a main limiting factor in how far a spectrum can be moved into the mid-IR spectral region. Multi-phonon absorption limits the output to wavelengths of ≤5 μm. Advances in nonlinear crystal development has meant that crystals with transparencies extending beyond 10 μm are now available [49]. These nonlinear crystals have been used to generate usable laser emission at wavelengths reaching far into the molecular fingerprint region. For example, OPOs constructed from the nonlinear crystals $CdSiP_2$ and orientation patterned GaP have been reported to have demonstrated long wavelength tuning ranges of ~6.5–7.2 μm [50] and 5.5–13 μm [51], respectively, when pumped by 1 μm femtosecond pulse laser sources. Similarly, a 2 μm pumped ultrafast OPO constructed from orientation patterned GaAs has demonstrated a tuning range spanning from 2.6 μm to 6.1 μm [52].
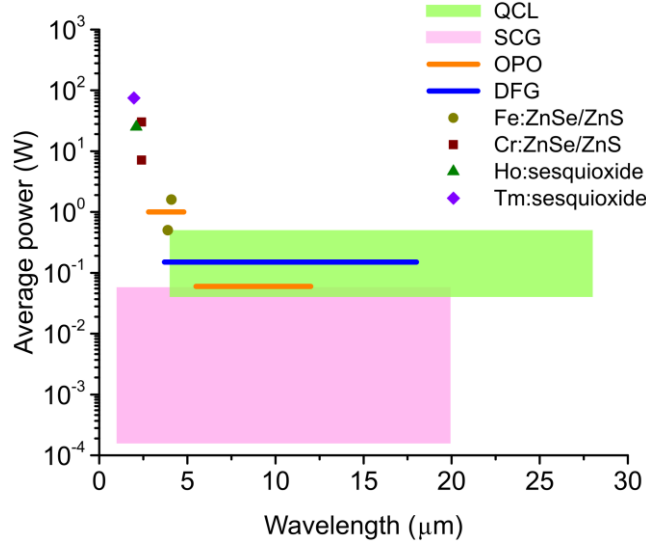
Fig. 2. Quantum cascade lasers (QCL) offer direct access to the mid-IR region. These laser sources can be designed to operate at desired set wavelengths or with single-mode tuning ranges over approximately 150 nm [53–56]. Select transition and lanthanide doped laser sources, *e.g.,* Fe, Cr, Ho, and Tm, are able to naturally emit at the shorter end of the mid-IR spectral region and bring with them impressive average output powers. These present themselves as useful seed sources for further spectral broadening deeper into the mid-IR [57–60]. Supercontinuum generation (SCG) sources provide instantaneous access to wide regions of the mid-IR from an initial near-IR or mid-IR pump source using highly nonlinear fibres and waveguides [61–67]. Optical parametric oscillators (OPO) can be tuned over wide ranges in the mid-IR spectral region and are predominantly only limited by the transparency of the nonlinear crystals used in the oscillator. Additionally, this method can utilised using both CW or pulsed sources [51,68]. Difference frequency generation (DFG) offers a relatively more robust approach to frequency conversion compared with OPOs. However, direct pumping at longer wavelengths has proved unattractive due to a lack of laser sources with sufficiently high average power or high pulse energy sources with megahertz repetition frequencies [69].

In addition to providing high peak powers for efficient frequency conversion, mode-locked ultrashort pulse laser sources can also act as an important tool in the generation of frequency combs. Since their first emergence in the 1990s, these frequency combs have profoundly transformed the precision of measurements of frequency and time. While combs have had an impact in the visible and near-IR regions, with use in developing ultraprecise optical atomic clocks [70–72] and precision spectroscopy [72,73], the mid-IR region is still under development [74]. Simply put, a frequency comb is an optical spectrum consisting of evenly spaced peaks or "teeth". Given that the frequencies of the teeth are known, the spacing between them is so exact that unknown frequencies can be measured using them, in a way creating an optical

ruler. Traditionally, frequency combs are generated using ultrashort pulse mode-locked lasers with pulse durations in the range of tens of femtoseconds to a few picoseconds. An alternative approach in the generation of frequency combs is to use a tunable single frequency CW source and a whispering gallery mode micro-resonator to produce what are referred to as Kerr combs [44,75,76]. By this process the pump laser forms part of the comb and the additional teeth are generated through cascade degenerate and non-degenerate four wave mixing. Whilst these micro-resonators offer a compact method for generating frequency combs, it was mode-locked laser systems that acted as the tool that allowed John Hall and Theodor Hänsch, joint winners of a half of the 2005 Nobel Prize in Physics, to make their developments in laser based precision spectroscopy.

The pulses of ultrashort pulse lasers contain many frequencies as a result of the mode-locking process (quite what this entails will be discussed in the Chapter 2) which establishes a fixed phase relationship between different oscillating modes. A periodic train of these pulses produces a frequency spectrum consisting of discreet lines with a constant spacing equal to the pulse repetition frequency, f_{rep}, thus giving you a frequency comb [44]. The span of the comb is determined by the laser gain bandwidth achievable from the gain medium, in that a shorter pulse duration will produce a frequency comb with a larger bandwidth. The frequency comb can then be shifted to different spectral regions through the use of techniques such as DFG, OPO, as used by Kara *et al.*, or supercontinuum generation (SCG). A particularly attractive form of DFG, known as intrapulse difference frequency generation, provides a way to generate inherently stabilised pulses with a carrier envelope offset frequency fixed at zero [44]. Through this approach the difference frequencies are generated between the teeth of a single comb, *i.e.* the frequency components originate from the same pulse. Moreover, this technique offers additional advantages in simplicity and compactness, and has been shown to deliver sources capable of reaching into the deep mid-IR >10 μm from fundamental near-IR [77] and 2 μm [69,78] laser sources.

Beyond acting as compact laser sources for direct access to the mid-IR, QCLs have been shown to generate frequency combs through various techniques. In single frequency operation they can be used to pump microresonators and generate Kerr combs around the central emission frequency, demonstrating combs around 4.5 μm from commercially available laser sources [79,80]. Direct modulation of the injection current and hence the gain can be used in an active mode-locked regime to produce picosecond ultrashort pulses and combs from the laser sources [81,82]. Passive mode-locking of QCLs has also recently been demonstrated [83], with reported pulse durations of 750 fs at a central emission wavelength of 3.6 μm. The most success, however, has been found

in specially engineered multi-mode broad-gain QCLs which have been shown to emit phase-locked continuous wave frequency combs via four wave mixing within the QCL [84–86]. These sources have been used to demonstrate broadband dual-comb spectroscopy in the mid-IR spectral region [87,88]. Low output powers on the order of a few miliwatts restrict their use in real-world applications though, meaning that, while QCLs provide a means to produce compact and efficient frequency comb generators, their use has been mainly limited to tunable CW spectroscopy.

Solid-state gain media, like Ti:sapphire or Cr:ZnSe, do not suffer from such limitations and can achieve ultrashort femtosecond pulses with average powers in excess of 100 mW directly from the oscillator. Clearly, nonlinear frequency conversion processes can be applied to near-IR mode-locked sources to extend them into the mid-IR spectral region. However, this brings with it extra complications and cost. It would be beneficial to have a mode-locked source that already emits in the mid-IR. Thus reducing the quantum defect and implied inefficiencies whilst also potentially reducing the systems overall footprint. For example, a Ti:sapphire mode-locked laser, the workhorse of ultrashort pulses in the near-IR, would require a frequency conversion stage in order to access the mid-IR. Compare this to a Cr:ZnSe mode-locked source, which naturally emits around 2.4 μm and therefore already has access to the mid-IR without any frequency conversion, and the benefit in overall compactness and cost is clear.

It is worth noting that near-IR fibre sources do offer a more compact fundamental laser source, but are restricted to low average output powers, <100 mW, due to tight mode confinement leading to detrimental nonlinearities. This means that an amplification stage with careful management of dispersion is required before any frequency conversion can take place, raising the overall system cost. While the fibre configuration has evolved to delve further into the mid-IR directly, the approach suffers from limited performance characteristics when mode-locked [89–95]. Ultrashort pulse Tm:fibre lasers emitting around 1.9–2 μm have been widely demonstrated and are now commercially available from companies such as AdValue Photonics and InnoLas Photonics GmbH. Ho:fibre, and Tm,Ho-codoped fibre lasers have also been demonstrated and are able to emit at slightly longer wavelengths further into the mid-IR, around 2–2.1 μm, making them more suited for frequency conversion techniques utilizing nonlinear crystals such as $ZnGeP_2$ [96] and orientation-patterned GaAs [52] or SCG in highly nonlinear fibres [97]. However, these sources, much like the Tm:fibre lasers, generally exhibit relatively long pulse durations on the order of hundreds of femtoseconds to a few picoseconds. Shorter pulses can be achieved through compression after the oscillator but this adds additional complexity and cost. In the case of [92], the short pulse

duration of 190 fs is accompanied by an average power of only 1 mW (20 pJ pulse energy, 50 MHz repetition frequency). Whilst this low an output power is atypical of ~2 μm fibre lasers, output powers ranging from approximately 5–150 mW mean that, much like their near-IR relatives, these laser sources require additional amplification stages to increase the average output power to "useful" levels.

The Cr^{2+}-doped gain media Cr:ZnSe and Cr:ZnS have been the focus of significant development since the first demonstration and investigation of laser action and performance in 1996 [98] and 1997 [99]. More recently, the broad gain spectrum of the Cr^{2+}-doped chalcogenide laser sources have been exploited to demonstrate femtosecond pulse mode-locked operation around 2.4 μm [100]. Using a variety of mode-locking techniques, pulse durations as long as 11 ps and as short as 47 fs have been reported for Cr:ZnSe, with average output powers ranging from 40–400 mW. Whilst the demonstration of 47 fs long pulses have been the shortest reported from a Cr:ZnSe laser to date [101], the authors acknowledge that a Cr:ZnS laser has achieved shorter. Indeed, pulse durations of <29 fs with average output powers of 440 mW have been reported from a mode-locked Cr:ZnS laser [102]. The Cr:ZnS laser crystal is similar to Cr:ZnSe in terms of spectroscopic properties but has some important advantages, including a shift of approximately 100 nm to shorter wavelengths of both the absorption and emission bands. This means that the system can be more effectively pumped by widely commercially available Er:fibre lasers and that the laser emission bandwidth exists further into the atmospheric transmission window between 1.9 μm and 2.5 μm, making for a more stable ultrashort pulse operation [103]. Ultrashort pulse Cr:ZnS laser sources have gone on to be developed into pump sources for specially designed "double-nanospike" chalcogenide waveguides for mid-IR SCG [104], demonstrating a supercontinuum spanning from ~1.2 μm to ~3.6 μm from only 0.2 nJ pump pulse energy [105].

Fe^{2+}-doped chalcogenide laser sources also offer a direct route to the mid-IR spectral region by exhibiting a natural emission wavelength of ~4.1 μm. The impact of Fe:ZnS/ZnSe has not been as profound as the likes of Cr, however, due to thermal quenching of the emission lifetime limiting room temperature operation [106,107]. A vast drop off in the emission lifetime around 150 K has meant that all published CW characterisation of the laser sources have been performed at cryogenic temperatures. A limited number of available pump laser sources around 3–3.5 μm, matching the peak absorption wavelength of the laser gain media, further compounded the challenges faced by the laser sources. The growing performance and availability of Cr:ZnSe ($\lambda \approx$ 2.7 μm) and Er:YAG ($\lambda \approx$ 2.9 μm) lasers has helped in this regard. Recent developments

of the Fe^{2+}-doped chalcogenide laser sources have realised low threshold laser action in an inscribed cladding waveguide [108], a 750 nm tuning range [109], and room temperature nanosecond pulse operation [110], but mode-locked ultrashort generation appears to still remain elusive. Amplification of femtosecond pulses in the 4 μm spectral region using Fe:ZnSe has been demonstrated, however [111,112].

Alongside Cr:ZnSe and Cr:ZnS, other popular solid-state laser sources in the mid-IR spectral region include those built around Ho^{3+}-doped, Tm^{3+}-doped, and Tm, Ho-codoped gain media [113]. These will be discussed in more detail in the next chapter. For now it is easier to repeat that the main advantage these rare earth doped sources offer, particularly Tm^{3+}-doped and Tm, Ho-codoped, is their ability to emit around the 2 μm spectral region under direct diode pumping. Widely available, high power AlGaAs laser diodes emitting around 800 nm offer a significant reduction in cost and physical size compared with Er:fibre and Tm:fibre pump sources commonly used by Cr:ZnS, and Cr:ZnSe and Ho^{3+}-doped lasers, respectively. For example, a commercial Tm:fibre laser offers a £/W factor of 1300 (10 W, Bktel Photonics) while a high power laser diode offers considerably more power for the price with a £/W factor of only 44 (10 W, Sheaumann Laser, Inc). Clearly this is not the only factor to consider; quantum defect and pump beam quality will also contribute to the efficiency of the pumping process. However, such high power laser diode pump sources, available in a small form factor and at a fraction of the price of fibre laser sources, offer an attractive alternative. Indeed, the first diode-pumped Kerr-lens mode-locked Cr:ZnSe laser has recently been reported [114]. Whilst the performance is impressive though, >500 mW average power and pulse durations as short as 45 fs, the high power InP laser diodes used are not yet as widely available as AlGaAs diodes.

The development of mode-locked diode-pumped Tm^{3+}-doped lasers would not just be limited to mid-IR spectroscopy and the generation of frequency combs. Ultrashort pulse, high average power 2 μm laser sources bring benefits to laser scalpel surgery by reducing the damage to surrounding tissue, forming smaller scars than those formed after the use of conventional surgical lasers or scalpels [115]. Reducing the overall cost of these systems by replacing complex and expensive frequency conversion modules and bulky pump modules with cheaper, more compact and robust diode-pumped systems naturally emitting in the required wavelength region, opens the technology up to the wider field allowing more to benefit from it. Compact and efficient ultrafast 2 μm lasers can also be used as seed sources for developing high-energy amplifier systems operating in the mid-IR 3–12 μm spectral region [116]. This would benefit many

applications in the areas of pulse laser deposition [117] and strong field physics [118], as well as the development of table top x-ray coherent sources [35].

Whilst there are clearly many routes to access and generate ultrashort pulses in the mid-IR spectral region around 2 μm, from well-established now commercially available approaches to those still early in development, the work presented in this thesis will show that the advancement of directly diode-pumped Tm^{3+}-doped laser sources represents a clear route to the creation of compact and affordable mid-IR mode-locked laser sources.

1.3   Synopsis

The structure of the thesis is such that it can be separated into roughly two halves. The first half will cover the essential theoretical grounding, starting with Chapter 2 which contains the main bulk of the required theoretical understanding and begins by covering the more general fundamentals of the laser process as well as those that are important in Tm lasers. Following this section, the breadth of pump sources available to Tm^{3+}-doped gain media will be compared and contrasted, after which a detailed analysis of the properties and mechanisms of mode-locked lasers will be undertaken. This analysis will cover different approaches to developing ultrashort pulse mode-locked sources, how these sources are optimised, and how the sources are fully characterised. The chapter will conclude by discussing techniques for power amplification of ultrashort pulse laser sources through the master oscillator power amplifier (MOPA) approach. Once justification of the work and a good foundation of knowledge has been established, including a more detailed introduction to the Tm^{3+}-doped sesquioxide laser gain media of interest, the second half of the thesis will present the original experimental work undertaken and the gathered results.

Chapter 3 contains the initial demonstration and characterisation of diode-pumped $Tm:LuScO_3$ and $Tm:Lu_2O_3$ lasers in the continuous wave (CW) regime; this includes work that lead to the first published report of a diode-pumped $Tm:LuScO_3$ laser. Chapter 4 follows up on this with the evaluation of the diode-pumped Tm^{3+}-doped laser sources in the mode-locked regime, including work that represents the first published demonstration of a diode-pumped ultrashort pulse $Tm:LuScO_3$ laser source and the first published use of an enhanced birefringent filter (BRF) for the tuning of mode-locked femtosecond pulses in the 2–2.1 μm spectral region. Chapter 5 then goes on to discuss efforts made in the amplification of the developed ultrashort pulse seed lasers, with the previously characterised $Tm:LuScO_3$ laser being used to seed a Ho:YAG slab amplifier

in a collaborative experiment with Heriot-Watt University and the Tm:Lu$_2$O$_3$ laser used to seed an in-house developed in-band pumped Tm:Lu$_2$O$_3$ amplifier. The last experimental chapter digresses somewhat from the main focus of the thesis and looks at the development of compact waveguide lasers in Tm^{3+}-doped sesquioxides instead of the traditional bulk solid-state gain geometry. The work detailed in the chapter represents the first published demonstration of an ultrafast laser inscribed (ULI) waveguide laser in Tm:Lu$_2$O$_3$. Finally, Chapter 7 concludes the thesis by highlighting the main achievements of the work undertaken as part of this doctorate and provides some closing remarks on future developments in the area of diode-pumped solid-state ultrashort pulse lasers in the 2 μm spectral region.

2 Practical background theory

To fully understand the processes discussed in the later experimental chapters, some theoretical background knowledge must be established. Many well-known authors have spent a great deal of time over the years creating fantastic tomes of information and repeating what they have written would not do these works justice. Instead the reader should consult the likes of Lasers by Siegman [119], Principles of Laser by Svelto [120], or Ultrashort Laser Pulse Phenomena by Diels and Rudolph [121] if a more detailed description of certain aspects is required.

Within this chapter the fundamentals of the laser process will firstly be discussed before taking a more specific look at the processes that take place in the Tm and Ho laser ions of interest used during this work. Following this, an evaluation of the available laser sources that can be used to pump said doped gain media will be undertaken, paying particular attention to compact pump sources in the form of laser diodes. A detailed look at the mechanics of mode-locked lasers will then discuss the various important components of ultrashort pulse laser sources, including dispersion management and different mode-locking techniques. The chapter will then conclude by examining some select approaches to increasing the average power of ultrashort pulse lasers through the master oscillator power amplifier configuration.

2.1 Ion-doped solid-state laser fundamentals

A laser, in the most simplest explanation, is generated by the process of amplification of light. Therein lies the source of the acronym that preceded the now generally used noun: Light Amplification by Stimulated Emission of Radiation. To understand the process in more detail though, requires a more thorough explanation into the "stimulated emission". In the most basic of terms, let us consider a simple two level laser ion system wherein the ion is in the ground state, E_0. If a photon of sufficient energy encounters this ion, its energy is absorbed and the ion is excited to a higher energy level, E_1. The required energy of the incoming photon would have to be equal to the difference between these two energy levels, *i.e.* $E_{ph} = h \cdot v = E_1 - E_0$. The excited ion would then remain in this upper state for a duration defined by the upper state lifetime, after which it would decay back to the ground state and the extra energy would be lost as a new photon through spontaneous emission. However, if a second photon were to

interact with the excited ion while it existed in the upper state, it would cause the ion to drop to ground state and emit another photon identical in frequency, direction, phase, and polarisation to itself through the process of stimulated emission. In effect, amplifying the initial signal that interacted with the excited ion. In reality, amplification cannot be achieved in a two level system due to not being able to realise a state known as inversion, whereby the population of the excited state, N_1, is greater than the population of the ground, N_0. In a two level system, the maximum population of the upper level is $N_1 = N_0$, because absorption and emission compensate each other. To achieve a state of inversion the system must have at least three levels.

2.1.1   Four and quasi-three level systems

Four level lasers exhibit an energy level system similar to the idealised system shown in Fig. 3 left. In this regime we can assume that there is only one pump level, E_3, and that the decays to the upper laser level, E_2, and the ground level, E_0, happen rapidly. These fast decays lead to negligible population of E_3 and E_1, and mean that a state of inversion can be easily achieved by any population in the upper laser level. By placing the inverted laser medium between two resonator mirrors, the process of stimulated emission is triggered by spontaneously emitted photons that are travelling back and forth between the mirrors. The laser field quickly builds within the resonator as stimulated emitted photons stimulate more photons in a cascade effect. If one of the mirrors is partially reflective then the field can be coupled out, resulting in the well-recognised beam.
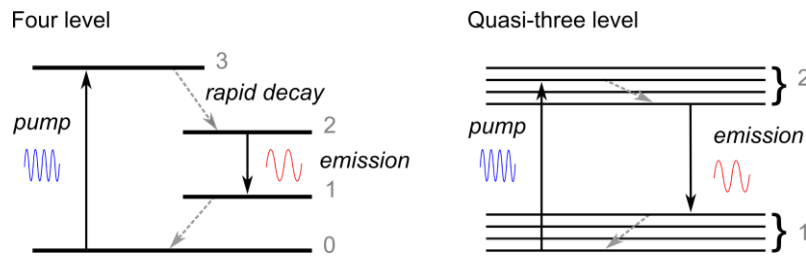
Fig. 3. Schematic diagrams of the four (left) and quasi-three level (right) systems.

Another important laser level scheme is that known as quasi-three level. In this scheme the upper and lower laser levels are formed by two Stark manifolds. The pump level may form a part of the same Stark manifold as the upper lasing level, as in the case of Fig. 3 right, or may exist at a higher energy level. Excitation in the former of these cases is referred to as in-band pumping. We are also able to assume fast decays from the

pump level to the upper laser level and from the lower lasing sub-level to the ground state sub-level, similar to the four level system. Therefore, in most common cases, the excitation terminates in an upper sub-level of the upper manifold. Inversion takes place between the lowest level of the upper manifold and the highest level of the lower manifold. However, in the case of the quasi-three level system the ground level and the lower laser level cannot be considered as decoupled as they are in the four level system. This means that the population of lower laser level is dependant on temperature and that a non-negligable thermal population is present in the lower laser level. The process of reabsorption of the laser emission must then also be taken into account in any analysis performed. Likewise, in the case of a highly inverted medium, re-emission of the pump wavelength should not be ignored.

It is the quasi-three level system that the lasers constructed and characterised in this work can be described with. There are also other energy transfer mechanisms that must be introduced before a clear picture of the processes in the Tm^{3+} and Ho^{3+} laser ions can be discussed.

2.1.2   Energy transfer processes

In addition to excitation of the upper laser level via absorption of pump photons, there are other energy transfer mechanisms that contribute to populating (and depopulating) the upper laser level and can lead to increased (decreased) efficiency. These nonradiative processes take place between separate but closely spaced laser ions, generally requiring the use of high doping concentrations within the laser gain medium. The processes detailed below will each consider an initially excited donor ion and a ground state or partially excited acceptor ion.

Energy migration

Through the process of energy migration, the entire excitation energy of the donor ion is transferred to an acceptor ion. The acceptor ion may be identical to the donor, as seen in Fig. 4 left, or be a different laser ion but feature similar energy levels, as is the case when the phenomenon occurs in codoped systems with a sensitizer ion. Excitation energy may be passed between consecutive ions allowing the energy to be transferred through the crystal with each new donor ion undergoing nonradiative de-excitation. This can lead to a reduced laser efficiency if the energy is transported to a region of crystal defects where non-radiative decay occurs.

Upconversion

Strictly speaking the process of upconversion should be separated into two distinct varieties; energy transfer upconversion and excited state absorption upconversion. The former of these two processes occurs when both the donor and acceptor ion are in an excited state and energy is transferred from the donor to the acceptor. This interionic process raises the energy level of the acceptor ion while de-exciting the donor ion, as seen in the centre diagram of Fig. 4. Excited state absorption upconversion, on the other hand, can be explained as the series of sequential absorption of pump photons exciting the ion beyond the normal pump level. The process of upconversion is normally seen as a form of parasitic loss. However, it can be constructively applied in upconversion lasers [122–124]. Depending on the energy level scheme, elevated excitation can be achieved via a single pump laser or through multiple wavelengths targeting specific transitions.
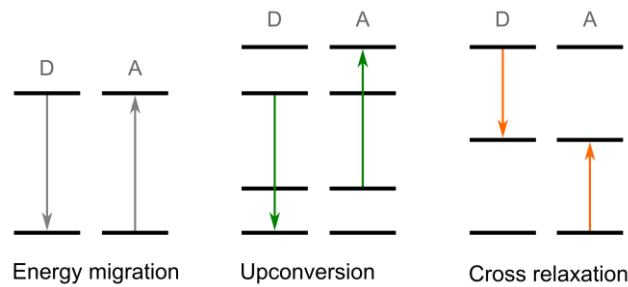
Fig. 4. Examples of the nonradiative interionic energy transfer processes energy migration (left), upconversion (centre), and cross relaxation (right), with labelled donor ion (D) and accepter ions (A).

Cross relaxation

Energy transferred through cross relaxation leads to both the donor and acceptor ion ending up in some non-ground state intermediate level. An example of the process leading to the donor and acceptor ion having the same populated energy level can be seen in Fig. 4. The transfer takes place between two nearby ions similar to the process of energy transfer upconversion. The differences being: the final state of the acceptor ion is on a lower energy level than the initial state of the donor, and the acceptor ion does not have to be in an excited state to begin with. The importance of this process in Tm^{3+}-doped lasers will become clear in the following section.

2.1.3 Thulium and holmium laser ions

With the intention of creating an ultrashort pulse source capable of being diode-pumped and emitting in the ~2–2.1 μm spectral region, the spectroscopic properties of Tm^{3+}-doped gain media present a very promising avenue of investigation. This section will present a generalised look at the Tm^{3+} laser ion, including a brief history of its use in laser sources. In order to provide a wider appreciation of the various configuration of lanthanide dopants able to emit in the mid-IR, a brief overview of the Ho^{3+} laser ion and Tm, Ho-codoped systems will also be discussed.

Thulium

The development of Tm^{3+}-doped gain media can be traced back to 1962 and 1963 in work by Johnson *et al.* with the demonstration of $Tm:CaWO_4$ and $Tm:SrF_2$ laser sources under liquid nitrogen cooling at 77 K [125]. It was not until the 1970s that room temperature demonstrations of a Tm^{3+}-doped lasers were reported [126]. While these sources were flashlamp pumped, using Cr^{3+} as a sensitizer ion, the inception and development of the Ti:sapphire laser in the 1980s [127] meant a pump source capable of directly exciting the Tm^{3+} laser ion around 800 nm could be utilised. More recently, the advent of high power AlGaAs laser diodes, originally developed for pumping Nd^{3+}-doped laser materials, can now be used to pump Tm^{3+}-doped gain media more efficiently.

Populating the $^3F_4$ upper laser level with 800 nm laser radiation is aided by the process of cross relaxation with a nearby ground state Tm^{3+} ion (Fig. 5). The relaxation from the $^3H_4$ manifold to the upper laser level causes a nearby ion to be excited from the ground state to the same level, resulting in the referred to "two-for-one" pump scheme. This process increases the theoretical power efficiency to 80%; well beyond the quantum defect imposed by the difference between the energy of the pump and laser emission photons. The origin of blue upconversion light can also be easily explained when considering pumping around 800 nm. Fig. 5 shows that emissions from the $^1G_4$ manifold are responsible for the emission of blue light around 480 nm. Excitation from the $^3H_5$ level is caused by excited state absorption populates the $^1G_4$ level. Thankfully, due to a nonradiative decay to the $^3F_4$ level, the lifetime of the $^3H_5$ manifold is very short, reducing the impact of upconversion on the performance of the laser. Furthermore, the route to the $^3H_5$ level is only possible through $^3H_4$ which is depopulated through cross relaxation decay [128].
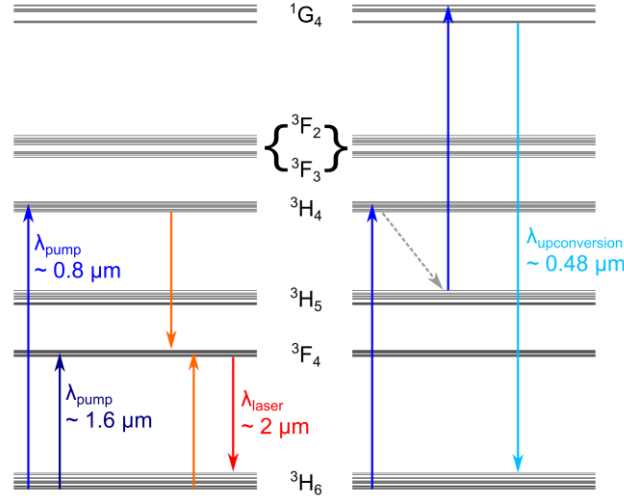
Fig. 5. (Left) Energy level scheme of Tm^{3+} ions showing pumping mechanisms at 0.8 μm for laser diodes and 1.6 μm for in-band pumping. Cross relaxation for the "two-for-one" pump scheme is shown in orange. (Right) Excited state absorption up conversion scheme showing how the $^1G_4$ manifold is populated by 0.8 μm pump photons. The dashed grey line indicates a nonradiative decay transition.

Direct population of the upper laser level is also possible through in-band pumping around 1.6 μm. Whilst this reduces the quantum defect, the process of cross relaxation is no longer possible resulting in a similar theoretical efficiency limit to pumping around 800 nm. The origin of blue upconversion emission when in-band pumping becomes more complicated to explain as it requires the use of multiple metastable states to reach the $^1G_4$ manifold. This process has not been shown on Fig. 5 but can be explained. Excited population in the upper laser level experiences excited state upconversion, exciting the ion to the $^3H_4$ level where it nonradiatively decays to the $^3H_5$ level. From this level further upconversion takes place via the $^3F_2$, $^3F_2$ manifold, like in the previous case with 800 nm pumping.

Interestingly, thulium holds a fairly unique position in the group of lanthanide rare earth laser ions. The lanthanides are characterised by fully filled 5s, 5p, and 6s electron subshell orbitals and commonly exhibit a +3 oxidation state, losing two 6s electrons and one 4f electron. For example, Tm [Xe]$6s^2 4f^{13}$ becomes Tm^{3+} [Xe]$4f^{12}$ while Nd [Xe]$6s^2 4f^4$ becomes Nd^{3+} [Xe]$4f^2$. Generally, when doped into a host the 4f orbital of the laser ion is shielded from the surrounding crystal field by the electrons within the fully filled 5s and 5p electron subshells. This leads to the influence of the crystal field on the 4f laser transitions being strongly reduced. In contrast, the Ti^{3+} laser ion [Ar]3d has no shield electrons around the 3d laser transitions resulting in the crystal field of sapphire producing the well-known broad energy levels and wide tuning range under laser conditions. In the case of the Tm^{3+} laser ion, and indeed the Yb^{3+} laser ion, lanthanide

contraction results in the 5s and 5p electrons being drawn closer to the nucleus, leaving the 4f orbital with reduced shielding from the crystal field. This phenomenon is caused by the increasing atomic number exerting a stronger attraction on the filled electron shells as one goes along the lanthanide series from lanthanum (57) to lutetium (71). The effect on the Tm^{3+} and Yb^{3+} laser ions, atomic numbers 69 and 70, respectively, is so great that the linewidth of the 4f laser transitions is approximately an order of magnitude higher than that experienced by other rare earth ions [129]. Reduced shielding from the crystal field also means that the effects of different host crystals on the spectroscopic properties of the laser crystal are more pronounced leading to broadening and spectral shifting of the luminescence bands. This can be seen when examining the natural emission wavelength from the $^3F_4 - {}^3H_6$ transition for different dopant host media. For example, Tm:YAG generally emits around 2.01 μm, Tm:YLF around 1.9 μm, and Tm:LuAG around 2.02 μm [130].

Importantly for this work, the broad transitions from the Tm^{3+} laser ion can be exploited in the generation of ultrashort pulse mode-locked lasers. In the last few years numerous publications have reported on the generation of sub-100 fs pulses from Tm^{3+}-doped gain media using various mode-locking techniques. $Tm:MgWO_4$ has been reported to have generated pulses as short as 86 fs at an average output power of 39 mW using a graphene saturable absorber as the mode-lock initiator [131]. Slightly shorter pulses of 78 fs have been generated from a Tm:CLNGG laser at an average output power of 54 mW using a single walled carbon nanotube based saturable absorber [132]. However, the shortest pulses from a Tm^{3+}-doped laser to date, indeed the shortest pulses from a mode-locked 2 μm solid-state laser, have been demonstrated using a $Tm:(Lu_{2/3}Sc_{1/3})_2O_3$ laser [133]. The mixed sesquioxide ceramic laser was able to generate pulses as short as 63 fs after extracavity compression (74 fs directly from the oscillator) using a semiconductor saturable absorber mirror (SESAM) to initiate mode-locking. The authors attribute the performance to the flat and smooth gain spectra of the Tm^{3+}-doped mixed sesquioxide ceramic which will be discussed in more detail in the Chapter 3. It is worth noting that all of these performances were recorded using Ti:sapphire pump sources.

Holmium

Like thulium, the development of Ho^{3+}-doped laser gain medium began in the 1960s [125], but it was not until the 1970s that the operating temperature was raised from liquid nitrogen levels to operate at room temperature, albeit in a pulsed

regime [134]. In contrast to Tm^{3+}, Ho^{3+} does not possess strong absorption bands in the near-IR region, thus in-band pumping around 1.9 μm is used to facilitate the $^5I_7 - ^5I_8$ laser transition around 2.1 μm. Whilst pumping around 1.9 μm does mean a very high theoretical quantum efficiency, it does present a problem when looking for efficient pump sources. Bulk diode-pumped Tm^{3+}-doped solid-state and Tm:fibre lasers are widely used as pump sources for Ho^{3+}-doped gain media, but it would seem that there has been very little progress made in the development of directly diode-pumped Ho^{3+}-doped lasers in recent years. Despite the growing commercial availability of 1.9 μm laser diodes, there only appear to be a handful of reported demonstrations in the last ten years [135–137]. Furthermore, due to a reduced lanthanide contraction effect, the 4f orbital of the Ho^{3+} ion is more shielded than the equivalent orbital found in Tm^{3+} and Yb^{3+} ions. This means that the laser transition has a narrower linewidth and that Ho^{3+}-doped gain media generally demonstrate much longer pulse durations than those examples given above.

Tm, Ho-codoping

An alternative means of utilising the long emission wavelength of holmium but with the benefit of widely available 800 nm laser diodes is to look towards Tm, Ho-codoped gain media. Excitation of the laser action process in the codoped system is made possible by methods and pumping processes already discussed previously in this section. Absorption of 800 nm pump light by the Tm^{3+} ion leads to a populated $^3F_4$ level via cross relaxation in the normal manner. However, rapid energy migration that would normally only take place between Tm^{3+} ions now includes nearby ground state Ho^{3+} ions, populating the $^5I_7$ upper laser level of the Ho^{3+} ions [138,139].

The development of mode-locked Tm, Ho-codoped gain media has seen numerous demonstrations of ultrashort pulse laser sources in the 2–2.1 μm spectral region. Pulse durations ranging from 67 fs (79 fs before extra-cavity compression) to 7.8 ps have been reported using various host crystals and saturable absorbers [140–147]. Despite these impressive results, Tm, Ho-codoped lasers are somewhat dogged by increased losses due to upconversion. The presence of upconversion is greater in these double-doped materials than it is in single-doped thulium materials. In Tm, Ho-codoped gain materials, upconversion is the result of two processes. The first of which can be explained as excited state upconversion and involves the absorption of a 800 nm pump photon, promoting excitation from the $^5I_7$ Ho^{3+} upper laser level to the $^5S_2/^5F_4$ level leading to visible upconversion fluorescence. However, the majority of the

upconversion is the result of interionic energy transfer upconversion, whereby a Tm^{3+} ion in the $^3F_4$ level transitions to the ground state, exciting a Ho^{3+} ion from the $^5I_7$ level to the $^5I_5$ level. From this level, fluorescence can occur at ~900 nm [138].

2.2   High power laser diode pump sources

The main driving technology behind the work presented in this thesis is that of the semiconductor laser diode. These compact and cheap devices have had a profound impact on the modern world of photonics and represent the main source of laser radiation in consumer products. As well as finding direct applications in the areas of spectroscopy, telecommunications, and defence, they have had widespread use as laser pump sources. The most widely used pump sources for Tm^{3+}-doped gain media tend to be high beam quality laser sources such as Ti:sapphire lasers or, the less commonly used, Raman fibre lasers. These lasers tend to be bulky and, as shown in Fig. 6, are hugely expensive in comparison to laser diodes. This is particularly prominent with commercial Ti:sapphire lasers, whereby a system can cost greater than 400x more than an equivalent powered laser diode. While there are indeed trade-offs made in regards to beam quality when considering laser diodes, the benefit in cost and efficiency the use of these compact sources can make to a system should not be understated.

This does not mean that there is no longer a place for Ti:sapphire pump sources. A near-diffraction-limited and tunable laser source would be very useful when characterising new and early development gain media; tuning the pump wavelength to match absorption peaks whilst ensuring the best possible overlap within the pump volume. For reasons that shall be discussed further at a later stage, these high beam quality sources are also particularly useful when trying to demonstrate the best possible performance from an ultrashort pulse mode-locked laser. When it comes to continued development of laser sources though, particularly with end user cost and compactness in mind, high power laser diodes become an attractive option.

The underlying principles of laser diode operation will not be discussed here as they are beyond the scope of this thesis. For further information to reader is encouraged to consult the likes of Svelto [148] or Neamen [149].
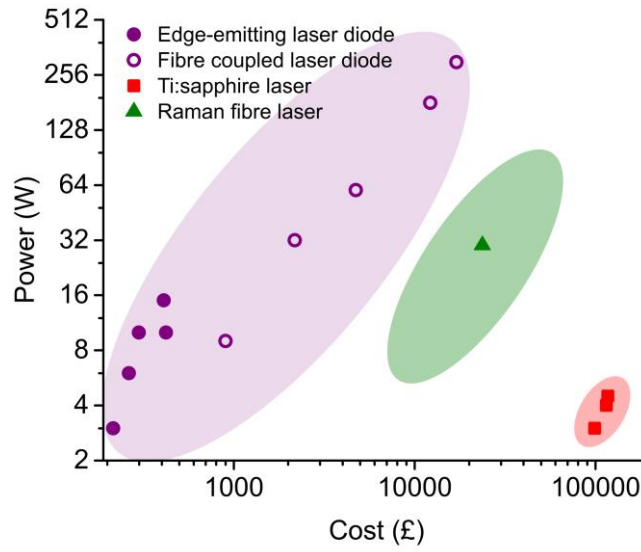
Fig. 6. A price/power comparison of the various laser pump sources open to Tm^{3+}-doped gain media. Laser diodes and Ti:sapphire lasers would be suited for pumping around 800 nm, while Raman fibre sources emitting around 1.6 μm would be used for in-band pumping. Cost figures for the laser diode and Ti:sapphire sources were gathered from Sheaumann Laser, Inc and Coherent, Inc, respectively. The price for the Raman fibre laser source shown is that of a previously acquired system from IPG Photonics Corporation. This was extrapolated to cover the various other power options available.

2.2.1 Single emitters

Double heterojunction structures tend to form practical single emitter laser diodes in one of two formats; narrow stripe laser diodes or broad area laser diodes. While these may come under different names, the main differences between the two types of devices is the width of the semiconductor gain chip and the resultant effect this difference has on the performance and characteristics of the diodes. Both stripe variants do share a common structure, however. Here we will consider only buried heterojunction index-guided lasers as they are favoured by manufactures more than the likes of gain-guided lasers.

In addition to the guiding achieved through the use of the double heterojunction structure, the use of additional semiconductor material at the sides of the active region means that the beam can be further confined to the gain region. Fig. 7(a) shows a detailed schematic of such a structure where the emission in the active GaAs region (red oval) is confined by a difference in refractive index in both the vertical direction, due the heterojunction structure, and in the horizontal direction by surrounding doped AlGaAs material. Due to the thickness of the active GaAs region, single transverse mode

operation is achieved in the vertical direction. Providing the width of the strip is small enough (typically only a few micrometres) then a single transverse mode is also possible in the horizontal direction, resulting in a high beam quality from the laser diode. Whilst providing near-diffraction-limited laser beams, these narrow stripe laser diodes are usually only able to offer powers <1 W. Broad area laser diodes, on the other hand, can offer output powers in excess of 15 W. This high power comes at the expense of beam quality, however. To facilitate such high power output without damaging the laser diode, the stripe width is increased. Widths in the range of 100–400 μm are common for output powers of between 3 W and 15 W, resulting in a significantly reduced beam quality in the horizontal direction.
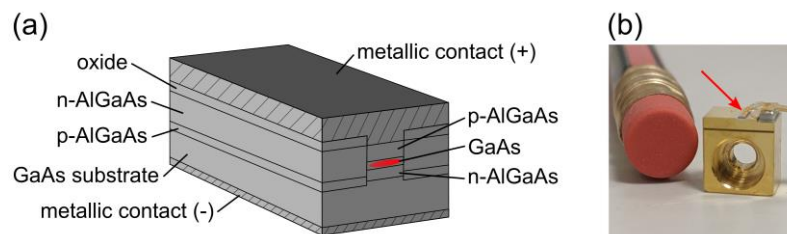
Fig. 7. (a) Detailed schematic of a buried heterojunction index-guided semiconductor laser diode [148]. C-mount type single emitted laser diode similar to those used during this thesis. The red arrow points to the laser diode. A pencil eraser has been included to provide a sense of scale.

Due to the vertical width of the gain region being smaller than the horizontal width, the divergence in the vertical direction will be larger than that in the horizontal direction. Typical divergence values for broad area laser diodes are ~30° for the vertical direction and <10° for the horizontal direction. This leads to the axes being referred to as the fast axis and slow axis, respectively. The different divergence between the fast and slow axes means the horizontal elliptical beam quickly rotates 90° ending up vertically orientated. Effective fast axis collimation can be provided by the placement of an aspheric lens close to the output facet of the laser diode. Collimation of the slow axis is usually provided by a cylindrical lens placed after the asphere. Some form of beam reshaping is then performed through more lenses to achieve the beam size required. In the case of broad area laser diodes, the large difference in beam quality between the fast and slow axes (M^2 values for the fast and slow axes of ~1 and >10, respectively, are typical) means that a very elliptical collimated beam is required if a single focusing lens is to be used to produce a circular waist.

Fig. 7(b) shows a C-mount type single emitter laser diode similar to those used most frequently during this thesis. The semiconductor laser diode itself is indicated by the red

arrow. The purpose of the mount here is to provide easily accessible electrical contacts for the laser diode and to act as a heatsink. Thermoelectrically cooling the mount through the use of a Peltier device is an effective way of controlling the laser diode temperature; preventing damage due to overheating and stabilising the emission wavelength. Similar laser diodes were found to have temperature tuning parameters of ~0.27 nm/°C, meaning that fine tuning the emission wavelength to better match absorption peaks or to offset the wavelength drift found when increasing the pump current could be done by increasing or decreasing the set point temperature of the mount.

2.2.2 Multi-emitter modules

Even higher powers than those achieved through broad area single emitter laser diodes can be achieved with multi-emitter modules. These tend to take the form of laser diode bars, where each bar contains multiple individual emitters. The emitters may be evenly spaced broad area emitters or grouped subarrays of narrow stripe emitters. For example, a commercially available 80 W CW laser diode bar is made up from 19 individual emitters with widths of 150 μm, separated by 500 μm. Multi-emitter modules can be found commercially available as laser diode bars, or they can form the active laser diode source in other modules.

Fibre-coupled laser diodes

Whilst low power high beam quality laser diodes can be fibre-coupled into single-mode fibre packages, these were not used as part of this thesis. Instead here we will only concern ourselves with high power multi-mode multiple emitter fibre-coupled laser diode sources.

Fibre coupling of high power multi-emitter modules has the advantage that it makes the output easier to utilise. Collimation of the beam can be achieved with one lens at the end facet of the fibre as, assuming power is evenly distributed over the modes of the fibre, the beam quality becomes roughly defined by the numerical aperture and core size of the fibre. From this approximation, M^2 values can range from around 30 to over 150. Furthermore, the separation of laser beam generation and delivery means that thermal management of the laser diode source can be positioned away from the main laser oscillator. In the event of a pump source failure, fibre-coupled modules also allow for an easier replacement compared with a single emitter and the required collimation optics.

One significant drawback of fibre-coupled modules is that there is often no control over the polarisation of the emission as the fibre used is not polarisation maintaining. This restricts the use of Brewster cut gain elements with fibre-coupled laser diodes.

Stacked arrays

Despite these diode laser sources not being directly used in this thesis, their capability to output considerably high powers (>0.9 kW) from compact form factors (approximately 50 mm × 20 mm × 50 mm) should not be ignored. These arrays are built up from multiple laser bars, stacked vertically. As a result, slow axis beam quality from these laser sources is very poor and phase plates are usually required to impart some useful profile onto the beam and provide fast and slow axis collimation. Furthermore, due to the very high powers involved, effective heat management is a must and manufacturers will often mount the arrays in packages built for active thermoelectric or passive water-cooling. Low beam quality combined with high power means these laser sources are better suited to pumping large slab lasers or amplifiers rather than setups requiring effective pump/laser mode overlap.

2.3   Mode-locked lasers

The process of generating ultrashort pulses, with durations in the range of a few picoseconds to hundreds of femtoseconds, is clearly of high importance to this thesis. Ultrashort pulses, generated by laser sources using the mode-locking techniques discussed in this section, can act as a high intensity driving laser sources for many of the applications presented in Chapter 1. Beyond the generation of these pulses, however, still remains the stabilisation and characterisation of said pulses. These aspects become as equally important when trying to analyse the performance of, and realise, a stable mode-locked laser source. In this section, we will discuss a number of prominent mode-locking techniques, in addition to how to overcome instabilities, manage important mode-locking parameters, and how to characterise the performance of ultrashort pulse laser sources.

2.3.1   Mode-locking techniques

The process of mode-locking can be explained as a means of establishing a phase relationship between the many longitudinal modes that exist within a standing wave

laser cavity. In a CW laser, this relationship does not exist and the modes propagate with generic phases resulting in an averaged continuous emission. With the fixed phase relationship, the modes within the cavity will constructively interfere with one another resulting in a periodic waveform with a period that is equal to the roundtrip time of the cavity. The emission from the laser is now pulsed, with the pulse containing a concentrated version of the all the radiation within the cavity. As was eluded to before, a gain material with a large gain bandwidth will be able to support more modes, providing the components within the cavity and various other factors are also capable of supporting them, resulting in a pulse with a shorter duration as described by $\tau_p \Delta \nu =$ TBP, where TBP is a pulse shape dependant constant known as the time-bandwidth product, τ_p is the pulse duration, and $\Delta \nu$ is the gain bandwidth relating to the number of longitudinal modes. This is not the entire picture, however. The employed mode-locking technique plays an important role in the pulse forming process (Fig. 8).
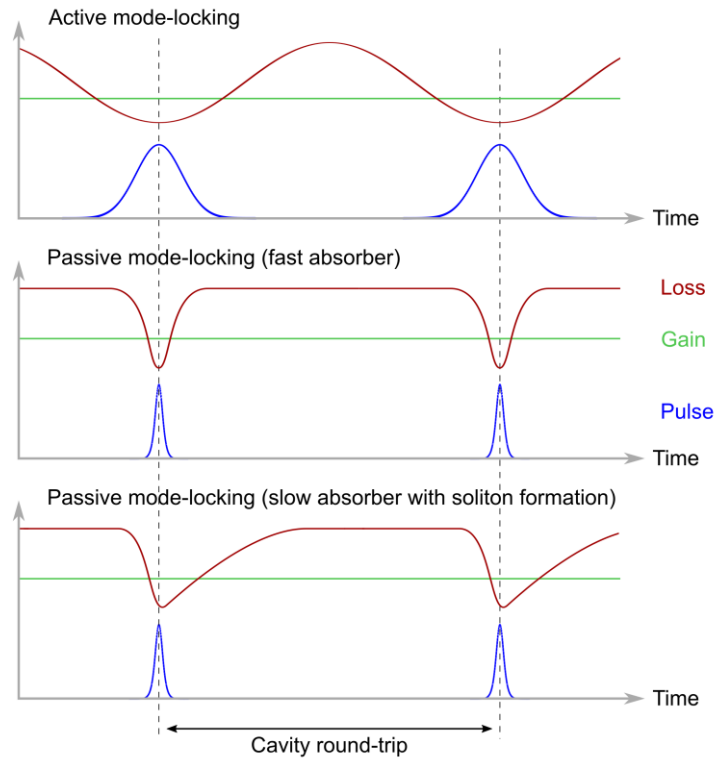
Fig. 8. Time dynamics of gain and pulse formation with select forms of mode-locking techniques for solid-state lasers.

It is important to acknowledge that two distinct types of mode-locking exist: active and passive. With active mode-locking, short pulses are generated by some external driving source. This could be achieved with a loss or phase modulator, *e.g.*, an acousto-optic modulator, within the resonator. In this case, the modulator is able to synchronise the

loss at a period equal to the resonator round-trip time and, with appropriate timing of the loss modulation, leads to the generation of ultrashort pulses [150,151]. As active mode-locking is, generally speaking, unable to attain sub-picosecond performance due to the limitations of the modulator and was not undertaken during this thesis, no more shall be said on the subject. In passive mode-locking, some form of saturable absorber, which possesses an intensity dependent loss, within the cavity is required to initiate the mode-locking process. These absorbers generally fall into one of two categories, those with a slow recovery time and those with a fast recovery time, and can come in a number of forms. As we will also see, the saturable absorber may not be the only factor at play during the passive mode-locking process.

Kerr lens mode-locking

When first discovered, the effects behind Kerr lens mode-locking were not well understood [152]. The generation of femtosecond mode-locked pulses without an obvious saturable absorber within the cavity led to it initially being referred to as "magic mode-locking" [153]. The interest this produced within the laser community thankfully meant that a great deal of effort went into understanding the phenomenon and it was soon explained that the Kerr lens approach to mode-locking exploits self-focusing from the nonlinear, intensity dependant refractive index of a bulk material within the cavity [154]. This is usually the gain material, but secondary undoped plates of the likes of sapphire or ZnSe, for example, within the cavity can also act as the Kerr medium. The overall effective refractive index of the material can be given as $n = n_0 + n_2 I$, where n_0 is the usual linear refractive index, I is the intensity of the incident beam, and n_2 is the nonlinear refractive index. Initially the system will start in a CW operation but will change to a pulse operation in order to reduce optical losses, in the case of hard aperture Kerr lens mode-locking (KLM), or to improve overlap of the laser and pump modes leading to higher gain, as is the case for soft aperture KLM. An illustration of the hard aperture approach can be seen in Fig. 9. This transition to pulsed operation does not begin on its own, however. Depending on how critical the cavity design is [155] and the strength of the Kerr lensing effect [153], an injection of noise into the system is required to start the transition. This can be achieved by vibrating one of the laser cavity mirrors, usually with a piezo actuator, or by introducing some minor fluctuations to the pump source. Alternatively, an additional saturable absorber, typically a slow one, can be placed within the cavity to begin the pulse forming process and build the high intensities required to cause sufficient self-focusing. This KLM-assisted approach can be used to

achieve self-starting mode-locking [156,157]. However, KLM on its own is generally referred to as non-self-starting.
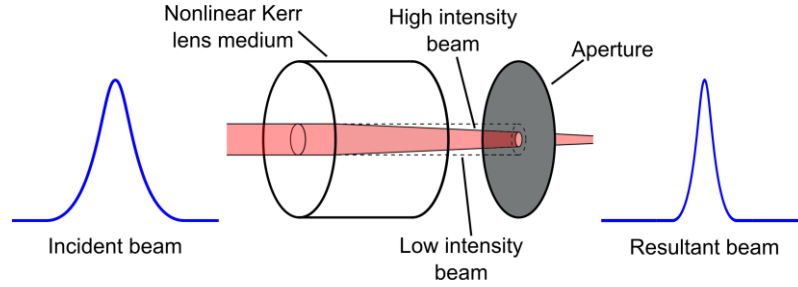
Fig. 9. Simplified illustration of hard aperture Kerr lens mode-locking.

The Kerr lens, in either its hard or soft aperture variant, can be described as a nearly ideal, albeit artificial, fast absorber. That is to say that the recovery time of the absorber is much shorter than the pulse duration and that the loss modulation closely follows the optical power building within the cavity. Furthermore, pulse forming is primarily determined by the absorber, with effects such as cavity dispersion and self-phase modulation (SPM) providing some additional pulse forming.

Semiconductor saturable absorber mirror

The first intracavity SESAM device, referred to at the time as an antiresonant semiconductor Fabry-Pérot saturable absorber, was used to mode-lock a Nd:YLF solid-state laser and generate ultrashort laser pulses with a duration of 3.3 ps [158]. Since then, SESAMs have evolved to cover a wide range of wavelengths, can be utilised in both bulk solid-state and fibre lasers, and are commercially available. These SESAMs can come in a number of different structures [159], but all have some common features. These include a substrate upon which a Bragg mirror that provides high reflectivity for a target wavelength range is grown, and some form of quantum well or quantum dot saturable absorber layer. Whether or not a second Bragg mirror or AR coating is added on top of this absorber layer depends on the type of SESAM. The SESAM used during this thesis featured no such additional Bragg structure or coating and relied on the Fresnel reflection (~30%) from the semiconductor material surrounding the quantum-well-based saturable absorber layers to act as the top reflector. An illustration of a structure similar to that used can be seen in Fig. 10 [146].
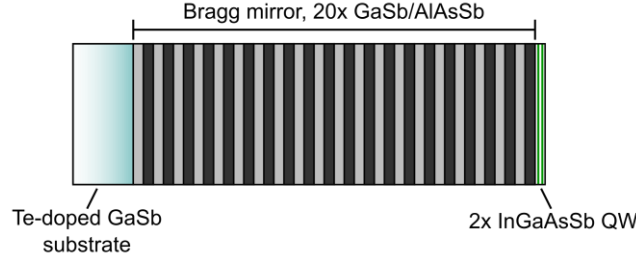
Fig. 10. Schematic illustration of an InGaAsSb quantum-wall-based SESAM, similar to that used during this thesis [146]. The quantum well (QW) absorber layers are separated and surrounded by layers of AlGaAsSb. The entire structure is approximately 0.5 mm thick.

The quantum well layers operate as saturable absorbers by incident photons exciting electrons from the valence band to the upper conduction band resulting in a high loss. There are only a limited number of unoccupied states in the upper band though, and when these states are filled no more absorption can occur. In this condition the absorber is said to be saturated, leading to a balance in the absorption and emission such that it exhibits low loss allowing the pulse to form. The intensity at which this saturation takes place is given by

$$ I_{sat} = \frac{h\nu}{\sigma_A T_A} \, , \tag{2.1} $$

where σ_A and T_A are the absorption cross section and recovery time of the absorber, respectively. This recovery time is the length of time it takes for the electrons and newly created holes to recombine and dictates how long it takes for the SESAM to return to a state of high loss. It is also referred to as the recombination or relaxation time. Another important term that will later come up is the saturation fluence, F_{sat}. This can be defined as

$$ F_{sat} = \frac{h\nu}{\sigma_A} \tag{2.2} $$

and is the energy per unit area applied to the SESAM required to cause significant absorption saturation (Fig. 11). By changing the cavity mode waist at the SESAM one can control the SESAM fluence for a given intracavity pulse energy. Other important SESAM parameters include the modulation depth (ΔR) and the non-saturable loss (ΔR_{ns}). Respectively, these refer to the devices nonlinear change in reflectivity and the loss of the fully saturated SESAM. The modulation depth is generally only a few percent while non-saturable losses should be as small as possible.

Traditionally, a compromise between quality and relaxation time has to be made when growing SESAM devices. High growth temperatures around 700 °C produce devices with good optical quality but slow relaxation times. Low temperatures around 400 °C results in devices containing defects, meaning that while they demonstrated worse quality they have faster relaxation times. However, a technique to provide high optical quality devices with fast relaxation times can be found in ion-implantation. It has been shown that ion-implantation can decrease the relaxation time and be used to tailor the properties of SESAM devices to better suit specific requirements. Implantation of N^+, As^+, Ni^+, or O^+ ions, for example, at dosages ranging from 10^{10}–10^{12} cm^{-2} introduce recombination centres in the form of defects whilst retaining saturation fluences well below the damage threshold of the device. Reductions in the relaxation time from hundreds to tens of picoseconds with only a slight negative effect on the devices reflectivity and insertion loss have been reported [160,161], making these ion-implanted devices better suited to mode-locking ultrashort pulse lasers [144].
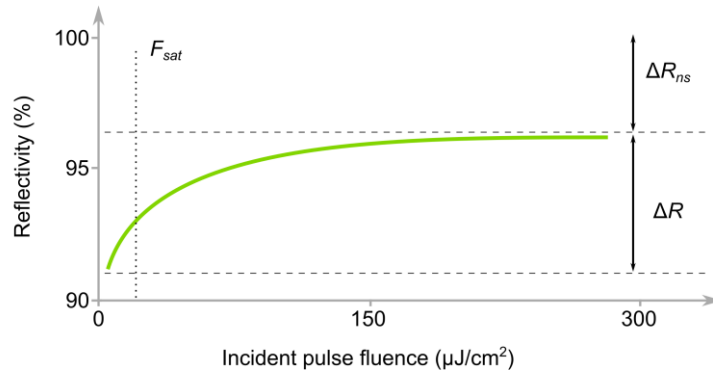
Fig. 11. Nonlinear reflectivity of a typical SESAM device as a function of the incident pulse fluence. F_{sat}, saturation fluence; ΔR_{ns}, non-saturable loss; ΔR, modulation depth [150,153].

While quantum-well-based SESAMs, like the one used in this thesis, are well established when compared to their quantum dot equivalent, it must be acknowledged that the quantum dot systems can offer some advantages. Namely, in demonstrating large inhomogeneous broadening due to a variation of dot sizes and exhibiting ultrafast recovery times in the low picosecond regime (~0.7–0.8 ps), they offer the potential to support the generation of much shorter pulses than their quantum-well-based counterparts [162–164]. Even then, the recovery of the saturable absorber time is too long for it to be considered as fast absorber. Instead it falls into the category of a slow absorber.

On their own, slow absorbers cannot support passive mode-locking of sub-picosecond pulses due to their long recovery times. The effects of dynamic gain saturation in combination with a slow absorber can strongly support the formation of pulses much shorter than the recovery time of the absorber by creating a gain window in which the pulse forms. However, this type of pulse formation is mostly found in dye lasers and is not present in solid-state lasers. As has been said previously, KLM-assisted mode-locking utilises the long pulses initially formed by the SESAM to generate the intensities necessary for self-focusing. Clearly, though, in a cavity with a weak Kerr medium, no KLM can take place. Therefore, some other pulse forming process must take place in order for slow absorbers to be used in generating femtosecond pulse mode-locked lasers. This can be explained as the interplay of SPM and dispersion found in soliton mode-locking [165].

Soliton mode-locking

The pulse shaping found in soliton mode-locking is purely due to the balance of group delay dispersion (GDD) and SPM caused by the Kerr effect imparting a nonlinear phase delay on the pulse, with some additional loss mechanism required to start and stabilise the process. In our case, this loss is found in the form of a SESAM. Due to the reduced importance of the SESAM in the pulse forming process, however, pulses with durations much shorter than the recovery time of the saturable absorber can be obtained.

It has been shown that the soliton solution to Haus' master equation is only stable for negative dispersion and positive SPM [150,166]. By this, the soliton propagates without distortion due to the effects of SPM exactly cancelling those caused by dispersion. Strictly speaking, due to the placement of the dispersive elements and nonlinear Kerr medium within a bulk solid-state cavity, quasi-soliton mode-locking rather than true soliton mode-locking is obtained. For the sake of ease though, this quasi-soliton mode-locking will be referred to as soliton mode-locking for the remainder of this thesis. The pulse duration for this stable soliton pulse can be obtained using

$$\tau_p = 1.7627 \frac{2|D|}{\delta E_p}, \tag{2.3}$$

where D is the total round-trip GDD within the cavity, E_p is the pulse energy, and δ is the SPM coefficient as defined by

$$\delta = \left(\frac{2\pi}{\lambda}\right)\left(\frac{2L}{A_{eff}}\right)n_2 \,, \tag{2.4}$$

where L is the length of the gain element and A_{eff} is the effective laser mode area in the gain element, and n_2 is the nonlinear refractive index of the laser gain medium.

From (2.3) it can be seen that the pulse duration scales linearly with the total absolute value of dispersion and has an inverse relationship with the pulse energy. That is to say that one would expect the pulse duration to increase when increasing the negative dispersion within the cavity, and that one would expect the pulse duration to decrease with increasing intracavity pulse energy. As the soliton propagates around the cavity it loses energy. This lost energy, referred to as the continuum, is initially contained within a low-intensity background pulse which is stretched in time due to the effects of dispersion not being counteracted by the negligible SPM it experiences. Providing that the continuum loss is larger than the soliton loss then a stable soliton pulse can be supported for all values of dispersion. Therefore, for very small absolute values of dispersion, the minimum pulse duration is found when the losses experienced by the soliton and the continuum become equal. The additional loss from the slow saturable absorber used to start the mode-locking process can also be used to prevent the continuum from reaching lasing threshold and destabilising the soliton.

The minimum achievable pulse duration is also restricted by the pulse breaking up into two, or more, pulses [167,168]. The reason for the break up is due to over saturation of the saturable absorber such that it can no longer stabilise the propagating pulse. Beyond this point, multiple propagating pulses with lower energy per pulse will be preferred. The addition of further negative dispersion into the cavity can be used to increase the break up threshold at the expense of increased pulse duration. Alternatively, the intracavity waist at the saturable absorbed can be increased. This transition to multi-pulsing is commonly signalled by a narrowing of the recorded optical spectrum and an increase in pulse duration. The appearance of secondary peaks on an intensity autocorrelation trace is also common, providing the monitored delay span is sufficiently large.

Supressing *Q*-switching instabilities

The addition of saturable absorber elements into solid-state lasers for the purpose of passive mode-locking, also bring with them a tendency to introduce *Q*-switching instabilities which, if left unchecked, can drive the laser to operate in the *Q*-switched

mode-locking (QML) regime (Fig. 12) [169]. In this regime, the laser output pulse train is modulated under a *Q*-switched envelope whose frequency is typically in the kilohertz regime and determined by the upper-state lifetime of the laser gain material. Depending on the strength of this modulation, the variation in pulse energy may only be small. However, for a very strong modulation, like that shown in Fig. 12, the pulse energies between the pulse packets can be extremely small with the pulses contained within the packet having a much greater pulse energy. This modulation is clearly in contrast to stable CW mode-locking where the emission features no modulation and has a constant pulse energy. For applications which require a constant pulse energy, these *Q*-switching instabilities are unwanted. Indeed, the onset of QML in the seed sources of high energy laser amplifiers can cause significant damage to optics. As such it is important to understand how to supress these *Q*-switching instabilities and attain stable CW mode-locked laser sources.
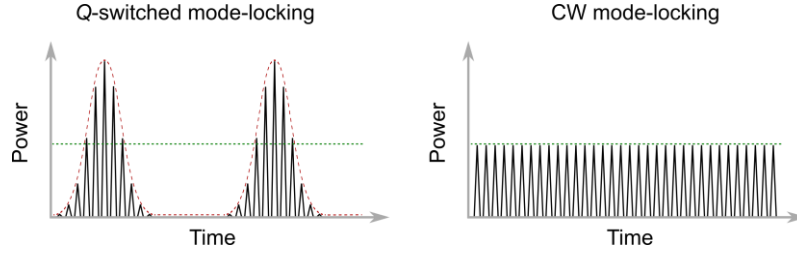
Fig. 12. Comparison between the output of mode-locked lasers operating in the *Q*-switched mode-locking regime and the CW mode-locking regime. The average output power (green) is the same in both cases.

Hönninger *et al.* have defined a QML parameter that represents the minimum intracavity pulse energy required to obtain stable CW mode-locking [170]. In its simplest form, the stability condition for a stable mode-locked laser with a SESAM can be written as

$$E_{p,in}^{\,2} > E_{sat,L} E_{sat,A} \Delta R \,, \tag{2.5}$$

where $E_{p,in}$ is the intracavity pulse energy and the square root of the term on the right is the critical intracavity pulse energy, $E_{p,c}$. $E_{sat,L}$ and $E_{sat,A}$ are the saturation energies of the laser gain medium and the absorber, respectively, and ΔR is the modulation depth of the SESAM. This equation says that for $E_{p,in} > E_{p,c}$ stable CW mode-locking could be obtainable. However, in the case of soliton mode-locking some modifications must be made to (2.5) for it to be accurate. With the inclusion of terms to represent the interplay of SPM and dispersion as well as gain filtering, (2.5) is recast as

$$E_{sat,L}gK^2E_{p,in}{}^3 + E_{p,in}{}^2 > E_{sat,L}E_{sat,A}\Delta R , \qquad (2.6)$$

where

$$K \equiv \frac{4\pi n_2 L_K}{|D|A_{eff}\lambda\Delta\nu_g}\frac{0.315}{1.76} . \qquad (2.7)$$

Here, L_K is the length of the Kerr medium (usually the gain medium) per round trip, D is the total amount of round-trip dispersion, λ is the central emission wavelength of the pulse, A_{eff} is the effective laser mode area inside the gain medium, and $\Delta\nu_g$ is the gain bandwidth.

Analysis of (2.6) and (2.7) shows potential routes to supress Q-switching instabilities and prevent QML. Although it should be highlighted that some of these are easier to control than others. For example, a reduction in the modulation depth of the SESAM would reduce the critical intracavity pulse energy but leads to weaker self-starting. Furthermore, changing this parameter whilst maintaining lasing is generally not possible, although some examples of actively changing SESAM parameters via pump-induced heating [171] or applied voltage [172] have been reported. Reducing the beam waist at the SESAM can easily be performed during lasing, however, and would also have the effect of reducing the critical intracavity pulse energy by reducing $E_{sat,A}$. Indeed, refinement of the SESAM waist size along with the optimisation of A_{eff}, with the aim of increasing the K factor without negatively effecting the pump and laser mode overlap, is how Q-switching instabilities were supressed during this thesis.

2.3.2   Dispersion management

In the previous section we discussed the important part dispersion played in the process of soliton mode-locking. To briefly summarise, net negative dispersion is required for stable soliton mode-locking and varying the amount of dispersion within the cavity can have effects on the achievable pulse duration and the point at which pulse break up occurs. To this end, it would be useful to briefly touch on the number of different ways dispersion within an ultrashort pulse mode-locked cavity can be controlled (Fig. 13). Some of these approaches present a method to fine tune the introduced dispersion and operate over a wide bandwidth, whilst others provide a set amount of dispersion over a narrower operating range but have the benefit of doing so in a compact and robust manner.

Material induced dispersion

When a pulse travels through a medium, it experiences a phase shift dependent on the frequency of the light (ω) and the refractive index (n) and length of the medium (L):

$$\phi(\omega) = \frac{\omega L}{c} n(\omega) = \frac{2\pi L}{\lambda} n(\lambda). \tag{2.8}$$

A linearly varying phase shift brings an absolute delay without changing the temporal profile of the pulse. However, higher order phase shifts, such as those experienced by ultrashort pulses, can cause the pulse shape to change and are therefore relevant. The phase shift can be expressed in a Taylor series to highlight the terms important for the propagation of the pulse:

$$\phi(\omega) = \phi_0 + \frac{\partial \phi}{\partial \omega}(\omega - \omega_0) + \frac{1}{2}\frac{\partial^2 \phi}{\partial \omega^2}(\omega - \omega_0)^2 + \frac{1}{6}\frac{\partial^3 \phi}{\partial \omega^3}(\omega - \omega_0)^3 + \ldots \tag{2.9}$$

The first term is the aforementioned linear phase shift which brings an absolute time delay, the second term describes the group delay, *i.e.*, the delay of the peak of the pulse envelope, and the third and fourth terms describe the GDD and third order dispersion (TOD), respectively [150]. It is only these third and fourth terms that broaden the pulse, where GDD introduces a linear chirp and TOD brings a quadratic chirp. The shorter the pulse duration the more terms of the expansion are significant, such that TOD only becomes a concern for extremely short pulses typically ≪30 fs long. As a result we need only concern ourselves with the second order dispersion, GDD.
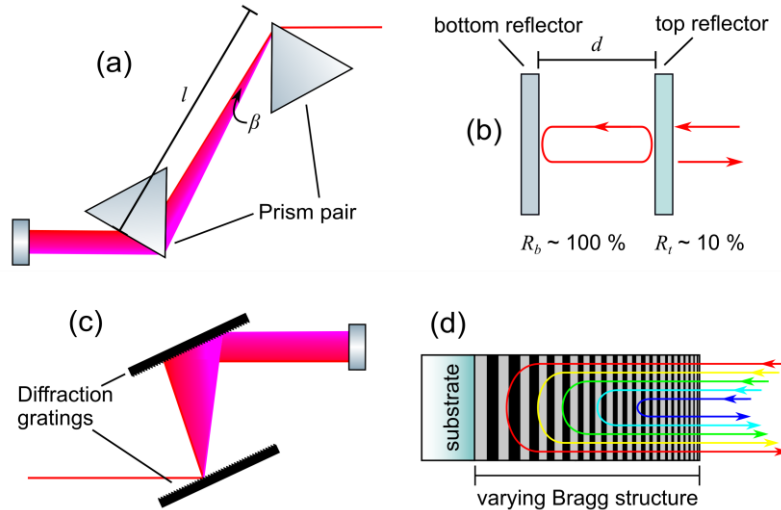
Fig. 13. Examples of methods of dispersion compensation that can be applied in mode-locked solid-state lasers. (a) prism pair and (b) Gires-Tournois interferometer, (c) grating pair, (d) chirped mirror.

Depending on the sign of the GDD, the introduced dispersion either acts to spread the leading edge or the trailing edge of the pulse. In the case of positive dispersion, for instance, the components of the pulse with higher frequencies are delayed compared to those with lower frequencies, *i.e.*, red is faster than blue, leading to a positive chirp or up-chirp. The opposite is true for negative dispersion. The amount of GDD introduced from a bulk material can be calculated from

$$D = \frac{\lambda^3 z}{2\pi c^2} \frac{d^2 n}{d\lambda^2},$$ (2.10)

where z is the propagation length through the material and n is the refractive index of said material. This differential is normally applied to the respective Sellmeier equation for the material in question. The gain material within a solid-state laser cavity is a good example of a source of bulk dispersion that must be considered when estimating the total GDD within the laser cavity. Depending on the material used and the wavelength range of interest, this dispersion may either be positive (1mm of Al_2O_3 at 800 nm: ~ 58 fs^2) or negative (1mm of YAG at 2 μm : ~ -61 fs^2). The broadening effect this has on the pulse can then be calculated providing one knows the pulse duration of the incoming pulse, $\tau_{p,0}$ [173]. For an initially unchirped Gaussian pulse, the pulse duration becomes

$$\tau_p = \tau_{p,0} \sqrt{1 + \left(\frac{(4\ln 2)D}{\tau_{p,0}^2} \right)^2}.$$ (2.11)

The amount of broadening one can expect is well visualised in Fig. 14 where for given values of dispersion it is clear to see that shorter pulses experience much stronger broadening compared with longer pulse durations.

Prism pairs

A method of providing fine and adjustable control of the GDD within the cavity is that of a double-pass prism pair [Fig. 13(a)]. By exploiting a combination of angular and material dispersion the amount of dispersion can be controlled through the separation of the prisms, l, or through the insertion depth of the second prism, h. Commonly used in Ti:sapphire systems, this combination allows the increase in separation distance to provide more negative dispersion in a coarse tuning manner, while the insertion depth of the second prism can be used to fine tune by providing positive dispersion without altering the ray directions. Unfortunately, this combination of negative and positive dispersion is not achievable around 2 μm as the material dispersion from the prism

(usually made from fused silica) is negative. Instead the prism insertion depth must be used to finely introduce more or less negative dispersion.
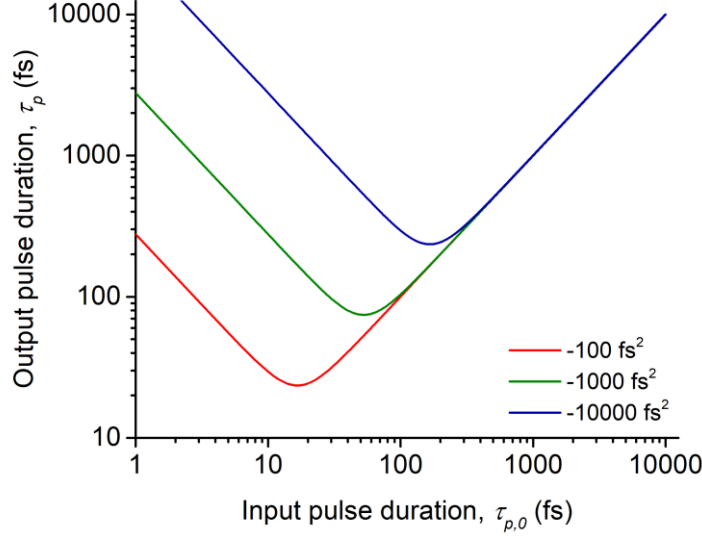
Fig. 14. Theoretical pulse broadening for an initially unchirped Gaussian pulse.

The amount of GDD introduced by the prism pair can be calculated via

$$D = \frac{\lambda^3}{2\pi c^2} \frac{d^2 P}{d\lambda^2}, \tag{2.12}$$

where

$$\frac{d^2 P}{d\lambda^2} \approx 4 \left[\frac{\partial^2 n}{\partial \lambda^2} + \left(2n - \frac{1}{n^3} \right) \left(\frac{\partial n}{\partial \lambda} \right)^2 \right] l \sin \beta - 8 \left(\frac{\partial n}{\partial \lambda} \right)^2 l \cos \beta \tag{2.13}$$

and relates to the optical path length, and

$$\beta = \sin^{-1} \left(\frac{h}{l} \frac{\cos \theta_2}{\cos \frac{\pi - 2\theta_B}{2}} \right). \tag{2.14}$$

The angle θ_B is Brewster's angle (~55° at 2 μm) and therefore assumes the prisms have been placed into the cavity to experience minimum loss. The angle θ_2 relating to the beam spread angle, β, can be calculated from

$$\theta_2 = \sin^{-1} \left[n \sin \left(\pi - 2\theta_B - \sin^{-1} \frac{\sin \theta_B}{n} \right) \right]. \tag{2.15}$$

From these equations it is possible to determine what prism separation would be required to realise a desired amount of dispersion. Fig. 15 shows the calculated GDD from an Infrasil prism pair for different insertion depths and prism separation lengths. This type of calculation is important when considering cavity designs due to the bulky nature of the double-pass prism pair.
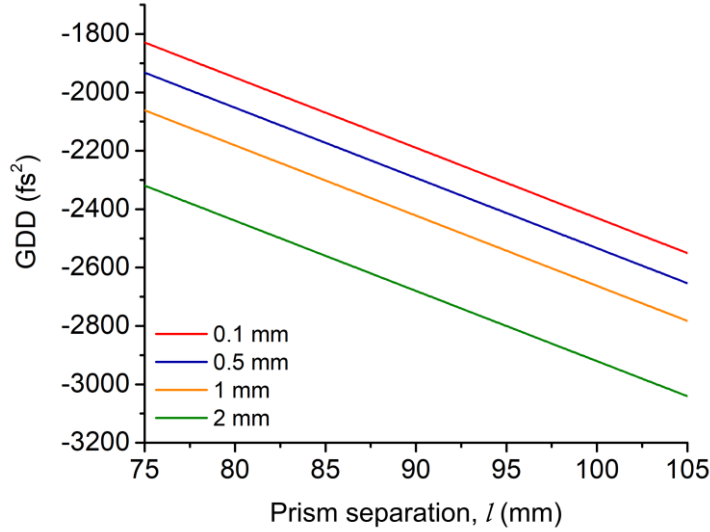
Fig. 15. Group delay dispersion provided by a double-pass Infrasil prism pair at 2 μm for different prism insertion depths as a function of prism separation.

Gires-Tournois interferometer

A more compact means of introducing negative GDD is found with the Gires-Tournois interferometer (GTI) [174]. The operating principle of a GTI is similar to that of a Fabry-Pérot interferometer except that it is operated in reflection and can therefore additionally fulfil the role of a flat cavity mirror [Fig. 13(b)]. If we first consider an air-spaced etalon with two reflective surfaces, the top being partially reflective and the bottom mirror being highly reflective over the wavelength range of operation, the reflected power is equal for all wavelengths but experiences a frequency-dependent phase change due to the resonance of the etalon [150]. The dispersion experienced is proportional to the spacing of the etalon, d, and can be determined via

$$D = \frac{-2t_{RT}^2 \left(1 - R_t\right)\sqrt{R_t} \sin\left(\frac{2\pi c}{\lambda} t_{RT}\right)}{\left[1 + R_t - 2\sqrt{R_t} \cos\left(\frac{2\pi c}{\lambda} t_{RT}\right)\right]^2} , \tag{2.16}$$

where t_{RT} is the round-trip time of the etalon defined as $t_{RT} = 2n{\cdot}d/c$ with n being the refractive index of the material within the etalon. By varying the gap between the reflective surfaces, tunable GDD can be achieved.

The main drawback of the GTI in regards to dispersion compensation is the limited bandwidth they provide. This bandwidth can be increased with a smaller etalon spacing, however, this is done at the expense of the amount of negative dispersion. This can be seen in Fig. 16 where the increase in spacing provides considerably more negative dispersion but with a reduced bandwidth. As such, a GTI better suited to shorter pulses with larger bandwidths would require multiple passes to achieve the same dispersion that would be achievable from a GTI designed to accommodate the narrower bandwidth of longer pulses.
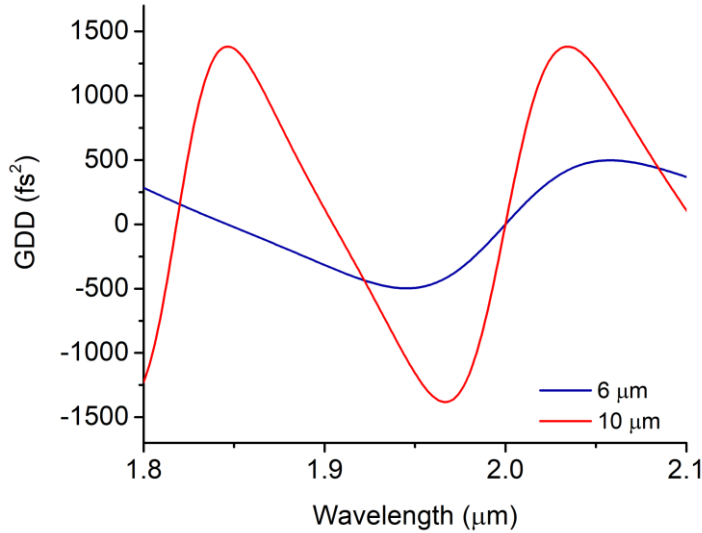
Fig. 16. Comparison of GDD from air-spaced GTIs with R_t = 2% and separations of 6 μm and 10 μm.

It is also possible to manufacture these GTI structures with monolithic designs based on thin film dielectric media. These then take the form of specially modified Bragg mirrors with precisely adjusted spacer layers added in the uppermost section to act as the GTI. Whilst not having the immediately accessible method of tuning the available dispersion open to them like with the air-spaced design, these dielectric GTI type mirrors offer a much more robust means of introducing negative dispersion into the laser cavity. Furthermore, it has been shown that the addition of multiple GTI structures in the top layer can provide a near constant negative dispersion over a broad bandwidth [175]. Indeed, the GTI type mirrors used for dispersion compensation in this work had an

operating bandwidth spanning more than 2–2.1 μm whilst maintaining >99.9% reflectivity.

2.3.3   Characterisation of ultrashort pulse lasers

The complete characterisation of ultrashort pulse lasers requires the analysis of multiple aspects of the laser emission. Whilst some of these aspects require no more than would be required to characterise a "simple" CW laser source, *e.g.*, average power and optical spectrum, the more complicated nature of ultrashort pulse mode-locked lasers mean that other aspects need specialised equipment and techniques. Furthermore, whereas peak powers for lasers with relatively long pulse durations (on the order of a few nanoseconds) can be directly measured providing one has a fast enough photodiode to monitor the optical power against time, the very short pulse durations involved with mode-locked lasers means this is not possible. Instead, the peak power, P_{peak}, is inferred from the pulse energy, E_p, and pulse duration, τ_p, where $P_{peak} \approx E_p/\tau_p$. The equation, in this form, assumes a square pulse profile. A conversion factor based on the temporal profile of the pulse must be applied to get a more accurate value of the peak power. For soliton pulses with a sech^2 profile, the correction factor is approximately equal to 0.88, while for Gaussian shaped pulses the correction factor is approximately 0.94.

Pulse energy is another value that had to be determined through calculation during this thesis. Pyroelectric based energy sensors do exist and are commercially available, but these sensors generally only operate for repetition frequencies in the kilohertz regime and for minimum pulse energies on the order of a few microjoules. As such they are unsuitable for measuring the range of pulse energies (1–10 nJ) and repetition frequencies (~100 MHz) encountered during the experimental work detailed in the following chapters. Instead, pulse energy can be easily calculated via $E_p = P_{avg}/f_{rep}$, where P_{avg} is the average output power and f_{rep} is the repetition frequency.

Pulse duration

While nanosecond pulse durations, like those produced from *Q*-switched laser sources, can be measured using photodiodes with fast rise and fall times, these photodiodes are still too slow to record the temporal profile of pulses with durations in the pico- and femtosecond regime. For these ultrashort pulse durations, specialised equipment and techniques are required to gather data pertaining to the duration of the pulses. The most common approach, in simple terms, is to use the pulse to measure

itself through the use of an autocorrelator. Using autocorrelation means that slow photodiodes can be used to indirectly record events that happen much faster than the photodiode would normally be able to measure. Even this approach comes in a number of different variations, though. Each having their own benefits and drawbacks.

The method used to determine the pulse duration in this thesis was that of non-collinear autocorrelation, also known as intensity autocorrelation (APE pulseCheck). As shown in Fig. 17(a), this approach involves splitting the input beam into two arms and then recombining them in some nonlinear medium. One arm is variably delayed with respect to the other and both arms are then overlapped in the nonlinear medium, usually a second order nonlinear crystal. Movement of the arm under computer control using a motorised stage allows for easy synchronisation of the movement and resultant time delay, providing an output with a fast refresh rate. In the case of the nonlinear crystal, a second harmonic signal is generated whose intensity is proportional to the product of the intensities of the two input pulses. As such, the maximum signal is obtained when the two pulses temporally overlap within the crystal and a recording of pulse energy against delay time yields the intensity autocorrelation curve.

Due to only one signal being recorded, the final curve is devoid of any interference fringes and can be referred to as background-free. This approach also enables a high dynamic range to be achieved, meaning that weak satellites in the wings of the pulse can be detected; this is useful when trying to view multiple pulsing behaviour after pulse break up has occurred. Manual adjustable control of a secondary delay arm and the focusing lens can also be used to ensure the pulses are combining effectively within the crystal and providing a high intensity response. The main drawback of intensity autocorrelators is their inability to provide information about chirp.
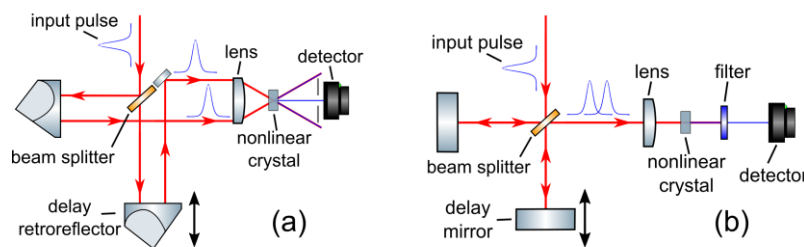
Fig. 17. Simple schematics showing the different operating principles of intensity (a) and interferometric autocorrelators (b).

As the name would suggest, the process behind the interferometric autocorrelator approach involves interfering the pulse with itself in a Michelson interferometer and producing superimposed copies of the pulse that propagate collinearly into the

nonlinear crystal [Fig. 17(b)]. As with the intensity autocorrelator, a rapidly translating delay line is used to interfere the pulse with itself. As a result of the second harmonic created by the interaction of the two beams coherently combining with the second harmonics created by each individual beam, interference occurs due to the addition of several beams and creates interference fringes with respect to time. Owing to the fringes this approach cannot be described as background-free. However, with the fringes, it is possible to gain additional information about any imparted chirp on the pulse. Care must be taken though, not to confuse a short pulse duration with a pulse that is chirped.

Having acquired an intensity autocorrelation curve, the full-width at half-maximum (FWHM) autocorrelation pulse duration is given by τ_{au} and can be used to determine the FWHM pulse duration τ_p. However, information about the pulse shape must be known before the correct pulse duration can be calculated. Depending on the mode-locking regime the laser is operating in, it is easy to assume what kind of pulse shape is present. For active mode-locking one would expect a Gaussian profile, while for soliton mode-locking one would expect a $sech^2$ profile. That being said, it is best practise to fit the respective profile to the autocorrelation data to justify the use of the appropriate conversion factor from Table 1. By this, the pulse duration from a passively mode-locked laser displaying a $sech^2$ pulse profile can be calculated as $\tau_p \approx 0.6482\tau_{au}$.

Table 1. Conversion factors for Gaussian and soliton $sech^2$ pulse shapes. τ_p, FWHM pulse duration; TBP, time-bandwidth product; τ_{au}, FWHM intensity autocorrelation pulse duration [176].

Pulse shape	τ_p/τ	TBP	τ_p/τ_{au}
Gaussian: $I(t) \propto \exp\left(\frac{t^2}{\tau^2}\right)$	$2\sqrt{\ln 2}$	0.4413	0.7071
$sech^2$: $I(t) \propto sech^2\left(\frac{t}{\tau}\right)$	1.7627	0.3148	0.6482

Whilst these techniques provide a means to infer pulse durations in a relatively straight forward way, in certain situations both the interferometric and intensity autocorrelation techniques can seriously misrepresent the temporal profile of the pulse. Non-random pulse trains with random components can be presented as smooth clean pulses absent of any variation in pulse duration or intensity. As such it is important to monitor the spectral profile of the pulses in addition to the temporal profile. Information from the

optical spectrum is also required to calculate the TBP of the pulses and determine how close they are to being transform-limited; an indicator of any chirp.

Other example of techniques that provide a more complete pulse characterisation and allow for accurate measurement of sub-10 fs pulse durations would be the frequency-resolved optical gating (FROG) [177,178] method and spectral phase interferometry for direct electric-field reconstruction (SPIDER) [179]. Though neither of these approaches were used during this thesis, their ability to provide additional information about the spectral phase and any uncompensated chirp is important when examining ultrashort pulses with durations in the sub-10 fs regime.

The FROG method, specifically the SHG-FROG method, is similar in construction to that of an intensity autocorrelator as shown in Fig. 17(a), except that the detector is replaced with a spectrometer. Numerous recorded spectra for different delay times are required to be passed through a complex computer algorithm before information about the pulse can be displayed in the form of a FROG trace. Analysis of this trace can then provide values for the pulse duration and residual chirp. Due to the need to gather multiple spectra, this information cannot be displayed in real time, however. The SPIDER method, on the other hand, is able to provide information in real time due to it not requiring a computer algorithm to analyse collected spectra. Whilst this can be considered an advantage over the FROG method, the FROG algorithm is able to provide consistency checks as part of its operation. Furthermore, SPIDER requires a more complicated optical setup, with components required to split the incoming pulse after which one pulse is then temporally stretched and chirped using a glass block, for example, while the other is replicated with each replicated pulse then being temporally separated. The separated pulses are then mixed with the stretched pulse in a nonlinear medium with the generated signal recorded using a spectrometer. Following multiple comparatively rapid transforms, phase information can be acquired from the recorded interferogram. Gallmann *et al*. have previously summarised and compared the two techniques; highlighting their advantages and disadvantages [180].

Optical spectrum

Precise measurement of the central emission wavelength and bandwidth of the optical pulse is required to gain an accurate value of the TBP. As long as the optical spectrometer in use has a high enough resolution within the spectral range of interest, typically <1 nm, and has been calibrated appropriately, then there is no real restriction on the type of optical spectrometer that can be used. Once the optical spectrum has

been recorded the central emission wavelength (λ) and FWHM optical bandwidth ($\Delta\lambda$) can be extracted and used, along with the pulse duration, to determine the TBP via

$$\tau_p \frac{\Delta\lambda \cdot c}{\lambda^2} = \text{TBP} \,. \qquad (2.17)$$

Considering the optical spectrum can provide valuable information about the stability of the mode-locked laser, an optical spectrometer with a refresh rate of greater than a few hertz is advised so that the effect of changes in alignment or pump power can be monitored in real time. For example, an optical spectrum exhibiting Kelly sidebands [181] is indicative of performance reaching the minimum achievable pulse duration. The sidebands can also be used as a tool to retrieve information about dispersion within the cavity. Kelly sidebands are not often seen with bulk mode-locked lasers and are more commonly found in fibre lasers due to the increased nonlinearity and dispersion present.

A fast refresh rate, rotating grating spectrometer with a wavelength range of 1.5–6.3 μm and a resolution of ~0.6 nm (APE waveScan) was used to record the optical spectra of the mode-locked lasers presented later in this thesis.

Pulse repetition frequency

The repetition frequency of pulsed lasers can either be calculated from $f_{rep} \approx c/(2 \cdot L)$, where L is the cavity length, or measured for a more precise value. The high repetition frequency of mode-locked lasers, generally around 100 MHz for bulk free space lasers, means that high bandwidth photodiodes are required to properly record the pulse repetition frequency. Specialised photodiodes are available from a number of suppliers and offer bandwidths of multiple gigahertz. Such high speed photodetectors also offer high rise and fall times on the order of ~30–100 ps, although these are still not fast enough to resolve the pulse profile of ultrashort pulses. A biased fibre-coupled extended InGaAs photodiode, with a maximum bandwidth of 10 GHz, was used exclusively when recording pulse repetition frequencies during the experimental work described later in this thesis.

The information gathered from the fast photodiode can be used to determine more than just the repetition frequency of the mode-locked laser source. When viewed in the radio frequency (RF) domain, the extinction ratio of the fundamental signal above the background carrier signal along with the consistency of the extinction ratio over the harmonics can be used as an indicator of the stability of the mode-locked laser.

Amplitude modulations when viewed in the time domain or secondary peaks around the fundamental signal in the RF domain are also indicators of *Q*-switching instabilities like those discussed in the previous section.

2.4   The master oscillator power amplifier configuration

In order to achieve the pulse energies required for many of the applications discussed in the introductory chapter, the amplification of a fundamental source tends to be necessary. To that end, we will here discuss the approach of the master oscillator power amplifier (MOPA). Included in this will be an analysis of various amplifier designs and a review of their performances pertaining to the amplification of ultrashort pulses in the 2 μm spectral region.

The basic principle of a MOPA does not vary from system to system. As the name suggests it is made up of two components; a master laser and a power amplifier. The master laser, or seed, defines important parameters of the system such as pulse duration and beam quality, while the power amplifier increases the average/peak power by passing the pulse through a medium with stored energy. The decoupling is particularly useful when it would be too difficult to construct one cavity to fulfil all the desired objectives or when a seed laser already exists and only an increase in output power is required. It does, however, bring complexity in terms of set up and some impact on pulse duration can be expected due to gain narrowing and the effects of travelling through dispersive materials. The spatial effects of gain narrowing can lead to a progressive decrease in beam diameter and can risk optical damage.

2.4.1   Amplifier designs

Complex systems with numerous optical components can be avoided with clever design of the amplifier. Some select examples of different designs used in the past will be introduced in this section.

Chirped pulse amplification

While not being an outright amplifier in its own right, chirped pulse amplification is an important process in many pulsed amplifier setups. The significance of its importance is illustrated by half of the 2018 Nobel Prize in Physics being awarded to Donna Strickland and Gerard Mourou for development of the method [33]. Without it,

pulse energies within the amplifier can become high enough that related high intensity nonlinear effects, such as self-focusing or multi-photon-ionisation, can distort the pulse or in some cases cause significant damage to optical components [182]. The process involves chirping and temporally stretching a pulse through the use of a strongly dispersive element, *e.g.,* a grating pair, with a positive GDD thus increasing the pulse duration and reducing the peak power to manageable levels, before passing it through the amplifier. After amplification, the pulse is compressed using another dispersive element, this time with negative GDD, to compensate the initial stretching and restore the shape of the pulse. The final result, is a pulse with considerable energy that has not experienced any drastically detrimental nonlinear effects or damaged the amplifier on its way through. In reality, the post amplifier compressor stage can still experience nonlinear distortions in systems with very high peak powers and associated intensities. Petawatt class lasers, like the Vulcan laser at STFC Central Laser Facility in the UK and the numerous laser sources of the pan-European Extreme Light Infrastructure, get around this problem by using large beam diameters on the order of 0.1–1 m.

Multipass amplifier

As the name suggests, a multipass amplifier allows for multiple passes of a pulse through a gain medium by using, what can be, quite a convoluted beam line. An example of one of these many optic designs can be seen in Fig. 18(a). The complicated beamline allows the design to achieve a higher number of passes than a simple double-pass amplifier based on polarisation rotation [Fig. 18(b)]. As a result of the folded beamline, every pulse generated by the seed laser can be injected into the amplifier meaning the repetition frequency remains unchanged. Care must be taken to avoid temporal overlap of pulses at the gain medium, however. While this can lead to gain depletion, it can easily be avoided if the optical length of the amplifier beamline is less than the round trip length of the seed cavity. In this case the injected pulse will complete its number of passes and leave the amplifier before another enters.

The number of reported mulitpass amplifiers in the mid-IR is fairly limited when compared to the amount of work that has been done using regenerative amplifiers. An example of one of these systems can be found in [183]. Here, Coluccelli *et al.* employed Ho:YLF as the gain medium to amplify a small region of the spectrum produced from a Er:fibre frequency comb. Using a 20 W Tm:fibre pump source double passed through the gain element, the authors report that the amplifier was able to achieve greater than 30 dB gain, $\sim10^3$, from 2048–2068 nm with a peak of 41 dB, $\sim10^4$, at 2053 nm. The

amplified comb carried 1.6 W of average power at a repetition frequency of 100 MHz and a pulse duration of 508 fs. This average power and repetition frequency corresponds to a pulse energy of approximately 16 nJ.
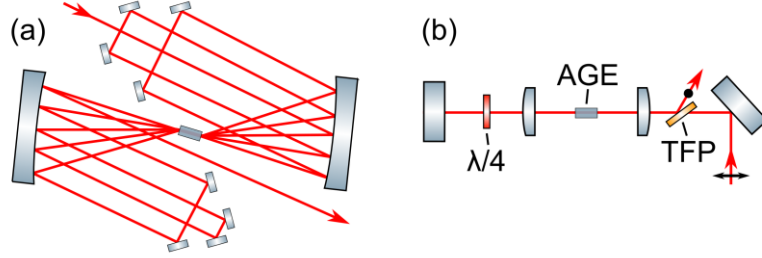
Fig. 18. (a) An example of a many optic multipass (five passes) amplifier design, similar to that used by Coluccelli *et al*. (b) A compact double-pass amplifier design using polarisation rotation and a thin film polariser (TFP) to separate the input and output beams.

Another example of a Ho:YLF multipass amplifier has been demonstrated by Hinkelmann *et al.* [184]. Here they report that their six pass, dual end pumped (Tm:fibre laser, ~18 W) Ho:YLF amplifier achieved a gain of 42 dB, corresponding to a pulse energy output of 145 μJ, at a repetition frequency of 10 kHz with pulse durations of 8.3 ps. At the highest repetition frequency of 500 kHz, the authors report a output pulse energy of 11.2 μJ with pulse durations of 5.5 ps. An ultrashort pulse Ho:fibre laser was used as a seed source for these investigations. Whilst the repetition frequencies reported in this work were not as high as those in [183], they are still multiple orders of magnitudes greater than those demonstrated from the regenerative amplifiers presented in the following section. Conversely, the pulse energies achieved from the multipass amplifiers are much lower, illustrating the trade off in amplifier gain and repetition frequency that must be considered when thinking about which amplifier design better suits the task at hand.

In addition to Ho^{3+}-doped gain materials, Fe^{2+} and Cr^{2+}-doped ZnSe has been used in multipass amplifiers in recent years [112,185]. Despite demonstrating millijoule output pulse energy and femtosecond pulse durations, low repetition frequencies, 0.1 kHz and 1 kHz for the Fe:ZnSe and Cr:ZnSe systems, respectively, and complex seed sources represent significant challenges for future development.

Regenerative amplifier

The regenerative amplifier can be thought of as a special kind of multipass amplifier, in that it achieves multiple passes through the amplifier gain element by trapping the pulse inside a resonator. The design has the advantage that it permits any number of passes through the gain medium. This means that an input of only a few nanojoules can be amplified to several millijoules [186]. To achieve this requires some key optical components. These include a Pockels cell, Faraday rotator, and thin film polarisers. A simple schematic showing the layout of a generalised regenerative amplifier can be seen in Fig. 19. When considering a regenerative amplifier it is also worth considering the final repetition frequency required from the laser source. To facilitate many number of passes through the gain medium, only a small number of pulses from the seed are allowed to pass into the regenerative amplifier. This reduces the effective repetition frequency of the laser source. As such, the regenerative amplifier can be thought of as a pulse energy (peak power) amplifier rather than an average power amplifier like the folded beamline multipass amplifier approach.
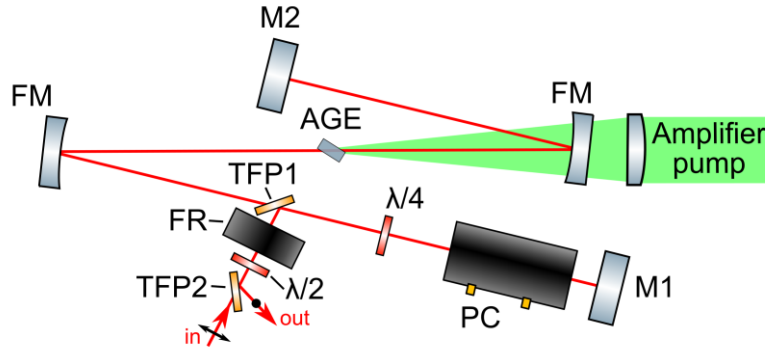
Fig. 19. Simple diagram of a regenerative amplifier. TFP1 and TFP2, thin film polarisers; PC, Pockels cell; FR, Faraday rotator; AGE, amplifier gain element; FM, fold mirror; $\lambda/2$ and $\lambda/4$, half-wave and quarter-wave plate, respectively.

The stages of amplification in a regenerative amplifier can be broken down into three stages: the pump phase, the amplification phase, and the cavity dump phase. In this first stage the Pockels cell has zero voltage applied to it and the gain medium builds up stored energy as it is pumped. Lasing is prevented by a combination of the Brewster's angle cut amplifier gain element and the quarter-wave plate and the rear mirror inducing a 90° rotation of the horizontally emitted radiation. If an injected pulse is polarised in the horizontal direction, it will pass through TFP2 and experience a 90° rotation in polarisation thanks to the half-wave plate and the Faraday rotator (45° from each component). Now vertically polarised, the pulse will reflect off TFP1 into the main resonator. After coming back through the quarter-wave plate it will be horizontally

polarised and will pass through TFP1 onwards through the resonator. On completing one round trip the pulse then encounters the quarter-wave plate and mirror again, rotating the polarisation back to the vertical. Now when encountering TFP1 it is reflected out of the resonator and passes through the Faraday rotator and the half-wave plate. The polarisation rotation due to the Faraday rotator is negated by the half-wave plate, so the pulse remains vertically polarised and on encountering TFP2 is reflected towards the output.

In the amplification phase, and in order to contain a pulse within the resonator, a voltage is applied to the Pockels cell such that it imparts a quarter-wave retardation. The voltage is applied as soon as the pulse leaves the cell heading towards the gain medium. As a result of the extra quarter-wave retardation, the pulse no longer undergoes a polarisation rotation and remains in the cavity when encountering TFP1. It is clear that timing of this switch on is important in ensuring that the cell has time to activate before the pulse returns. Switching the Pockels cell also causes any additional pulses arriving from the oscillator to be ejected after reflecting off M1 and hitting TFP1.

After sufficient time has passed that the pulse has built up enough energy, the cavity dump phase is triggered. The Pockels cell is switched to a half-wave retardation voltage, or zero voltage, such that when the pulse now passes through the quarter-wave plate and mirror combination the polarisation of the pulse changes from the horizontal to the vertical direction. As before in the pump phase, the pulse is now reflected out of the cavity at TFP1, through the half-wave plate and Faraday rotator and out the output after reflecting off TFP2.

Table 2. Performance summary for selected regenerative amplifiers around the 2 μm spectral region. Unless otherwise specified, pump power shown here is incident power.
a, absorbed.

Gain medium	Ref.	Pump power, W	Input pulse energy, nJ	Output pulse energy, mJ	No. roundtrips	Gain	f_{rep}, kHz	λ, nm
Ho:YLF	[187]	48	~0.15	1.1	24	7×10^6	10	2050
Ho:YLF	[188]	9.2	4	4	36	1×10^6	0.1	2052
Ho:YLF	[189]	50	1	9.7	24	10×10^6	1	2050
Ho:YAG	[187]	~36	0.7	0.5	33	7×10^5	10	2090
Ho:YAG	[190]	~4.6[a]	25	~0.71	10	3×10^4	1	~2090
Tm:YAP	[191]	~11[a]	25	~0.71	34	3×10^4	1	~1940

While the regenerative amplifier can allow for the build-up of high energy pulses, it can suffer from a number of issues. These include the need for careful management of dispersion compensation due to chromatic dispersion that is introduced by the Pockels cell, additional smaller pulses circulating within the resonator as a result of misalignment, voltage drift in the Pockels cell allowing small fractions of other injected pulses to experience amplification or background noise from a second trapped pulse within the resonator. Despite these drawbacks, regenerative amplifiers have been used in part to demonstrate ultrashort pulses with energies in the millijoule regime around 2 μm using Ho^{3+}-doped and Tm^{3+}-doped gain media. A summary table of this performance can be seen in Table 2.

3 Tm^{3+}-doped sesquioxide laser gain media

The family of Tm^{3+}-doped sesquioxide laser gain materials have characteristics that make them particularly noteworthy when considering sources for diode-pumped ultrashort pulse generation in the 2 μm spectral region. As has been discussed in the previous chapter, Tm^{3+}-doped gain materials offer a route to the 1.9–2 μm spectral region via direct diode pumping. While most of these laser sources emit around 1.9 μm, in the middle of a strong atmospheric absorption band, the Tm^{3+}-doped sesquioxides exhibit broad and relatively smooth gain reaching far beyond 2 μm. This makes stable ultrashort pulse generation possible without the need for cavity purging.

The term "sesquioxide" refers to the molecular composition of the host crystal where oxygen is present in the ratio of three atoms to two of another element. For example, sapphire (Al$_2$O$_3$) could be described as a sesquioxide. Here we will only concern ourselves with the cubic C-type structure sesquioxides Lu$_2$O$_3$, and LuScO$_3$. From here on, when we speak of the sesquioxides we are referring to these two host crystals. It should be acknowledged that a bulk of the early research into the Tm^{3+}-doped sesquioxide laser gain materials was performed by Koopmann *et al.* between 2010 and 2013 [129], under the supervision of Günter Huber. The base information pertaining to the properties of the Tm^{3+}-doped sesquioxides discussed in this section is based on the knowledge they gathered.

This chapter will act as an introduction to the Tm^{3+}-doped sesquioxides used in this thesis. A brief summary of the various laser gain element growth methods will be undertaken before focusing on those that produced the high optical quality elements used in this work. After this, an examination of the properties of the gain media will highlight the benefits and, in some cases, the limitations of the Tm^{3+}-doped sesquioxides. Finally, the first of the experimental sections of this thesis will detail the continuous wave laser characterisation of the Tm:LuScO$_3$ and Tm:Lu$_2$O$_3$ laser sources.

3.1 Fabrication methods

Well established crystal growth methods, such as the Czochralski technique [192,193], have proven themselves capable of growing high quality single

crystal materials. Indeed, the Czochralski process has become a driving factor in the semiconductor industry; growing silicon boules weighing around 300 kg and 300 mm in diameter in a highly repeatable and reliable manner [194]. The technique works by dipping a seed crystal tipped rod into the surface of a crucible filled with molten raw material. The melt crystallises at the seed due to the lower temperature of the rod and the growing crystal is then pulled up out of the melt. Controlling the pulling and rotation speed, along with the melt temperature, allows for control of the crystal boule diameter. This proven technique has faced complications when applied to the growth of sesquioxides though. It has been reported that problems associated to a low thermal conductivity at the high melt temperatures meant that only short crystals on the order of a few millimetres could be pulled from the melt before contact between the seed and the melt was lost.

Another approach to crystal growth that has faced better success when growing the sesquioxides is the Nacken-Kyropoulos technique [195,196]. Like the Czochralski process, the Nacken-Kryropoulos technique features a seed and melt. In this process, however, the seed is dipped into the melt and cooled such that the crystal grows into the melt. Because this technique circumvents the problems faced when pulling the crystal from the melt as in the Czochralski method, it has been used to produce sesquioxide crystals. However, there is limited control over the growth parameters when compared with the Czochralski method, and contact between the growing crystal and the walls of the crucible leads to stress inside the crystal. As a result, the crystals grown through this process have, in the past, only been suitable for spectroscopic evaluation or low power level laser experiments.

Thankfully, alternative methods to fabricate high quality sesquioxide laser gain elements suitable for high power applications have been introduced. The heat-exchanger method and the processes involved in making laser ceramic gain media, discussed in the following sections, were each respectively used to fabricate the high optical quality crystalline $Tm:LuScO_3$ and ceramic $Tm:Lu_2O_3$ gain elements used in this thesis.

3.1.1   Heat-exchanger method

Originally referred to as the gradient furnace technique, the heat-exchanger method was developed for the growth of sapphire in 1970 by Schmidt *et al*. [197]. The growth process shown in Fig. 20(a)–(c) can be described as follows. In (a), a seed crystal is placed in the bottom of the crucible where its temperature can be controlled via an

external gas flow and the rest of the crucible is filled with high purity (>99.999%) raw material. The crucible is heated using an induction coil and the raw material melts (b). The seed is cooled such that only its tips melts. Increasing the cooling of the seed causes the crystal to grow from the bottom of the crucible into the melt, as depicted in (c). By carefully managing the heating of the crucible, the crystal is prevented from making contact with the crucible walls until very late in the crystal growth process. As a result, low-stress crystals can be grown. Greater detail of the growth process used to grow sesquioxide crystals using the heat-exchanger method can be found in [129] and [198].
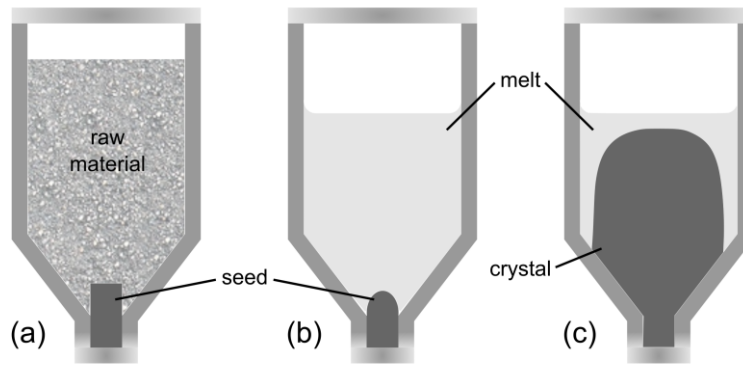
Fig. 20. The crystal growth process of the heat-exchanger method is depicted through (a)–(c) [129].

Another complication that must be faced when fabricating sesquioxide crystals is one caused by their high melting points and the restrictions this places on the materials that can be used to make crucibles. Considering the melting temperatures for the sesquioxides is >2400 °C, the number of possible materials is limited. As the use of a crucible and molten raw material is key for the techniques discussed above, a suitable material must be chosen with care. Based on their melting/sublimation temperatures, suitable materials could include osmium, tantalum, rhenium, tungsten, and carbon. Due to high reactivity with oxygen present in the melt and the high toxicity of osmium, this list is quickly whittled down so that only rhenium remains. However, despite remaining chemically stable towards the melt, rhenium does react with oxygen. Therefore, stringent control over the atmospheric conditions during the growth must be maintained. Even then, inclusions formed of rhenium particles can still occasionally be found in the crystals. Rhenium inclusions within the laser gain element can lead to increased losses due to scattering or destruction of the element if the rhenium particles are vaporised under high power operation. The likelihood of these inclusions occurring can be reduced through annealing of the crucible or by performing several "cleaning" crystal growths. Whilst post growth annealing of the crystals can be used to remove

oxygen deficiencies, it has been found to result in cracking and a significant increase in stress in the volume surrounding any rhenium particles due to expansion of rhenium gas as it is heated [129]. In regards to laser gain media, these cracks and stress centres lead to increased absorption and scattering losses, as well as depolarisation losses in certain cavity configurations.

3.1.2 Laser ceramics

A method of sesquioxide laser gain element fabrication that does not require the use of high temperatures and expensive rhenium crucibles is that of creating laser ceramics [199,200]. Unlike the single crystals produced by the Czochralski, Nacken-Kyropoulos, and heat-exchanger methods, laser ceramics are made up of microcrystallites and can be described as polycrystalline. These regions of different microcrystallites are often referred to as grains and can dictate the transparency of the ceramic. Scattering from grain boundaries, from inclusions or pores, and from surface roughness, for example, can lead to high losses. By reducing the grain size and the number of defects, the quality of the ceramic can be made high enough that laser elements can be produced. Indeed, YAG ceramics have received particular attention over the years and now demonstrate laser performance comparable to single crystal when doped with rare earth ions such Nd^{3+}, Tm^{3+}, or Yb^{3+} [201–203]. Considering the Tm^{3+}-doped sesquioxides, $Tm:Lu_2O_3$ and $Tm:LuScO_3$ ceramics have been fabricated in the past showing very similar physical and spectroscopic characteristics compared with their single crystal counterparts [204,205].

The process of making polycrystalline ceramic laser gain elements is summarised in Fig. 21. It involves the cold, high pressure pressing of a powder filled mould of a desired shape followed by sintering under vacuum for a number of hours to form the ceramic sample and then final processing and polishing. Due to the mould roughly defining the final size and shape of the element, ceramics can be fabricated in a more varied number of configurations than those grown as single crystals. This can include gradient doped elements or elements with undoped cladding or caps, in addition to fibre or waveguide like structures [200].

Laser gain elements featuring cubic crystal structures, such as YAG and the sesquioxides, are commonly made as ceramics. It was thought that their cubic structure meant they were the only materials that could be produced as polycrystalline ceramics. However, very recent work has shown that when the grain size is sufficiently small (compared to the wavelength of incident light) Mie scattering, that would normally

occur at the gain boundaries between refractive indices of different crystal orientations, is suppressed [206]. This could permit laser gain materials that would normally be grown solely through single crystalline growth methods to benefit from the laser ceramic fabrication process.
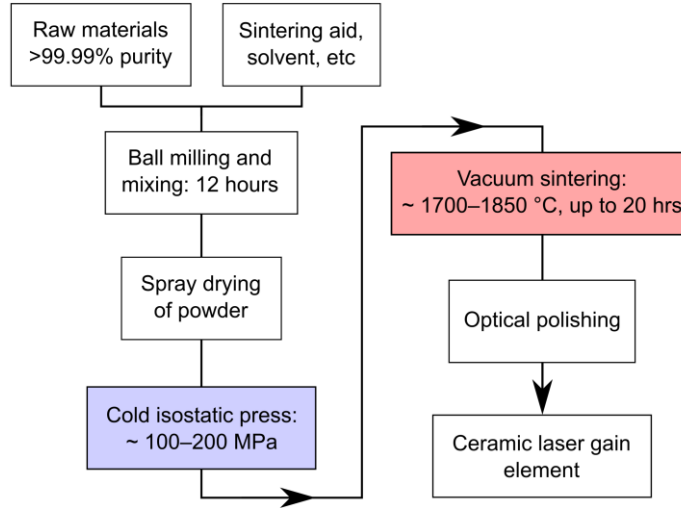
Fig. 21. Simplified flowchart of the processes involved in making laser ceramics [199,200].

3.2 Thermo-mechanical and optical properties

Due to the cubic crystalline structure of the sesquioxides, they can be described as isotropic. This means that they exhibit properties that do not depend on their crystal orientation. In laser gain materials, properties such as emission and absorption cross section can depend very strongly on the orientation of the crystal. Ti:sapphire, alexandrite, and Tm:YLF are some examples of laser gain media that have such a dependence and are required to be cut in specific orientations and use pump sources that emit with a certain polarisation to achieve the best performance. The Tm^{3+}-doped sesquioxides do not exhibit such a dependence and can therefore benefit from the advanced production methods of polycrystalline ceramic gain elements and high power unpolarised fibre-coupled laser diode pump sources. It also means that the emission and absorption cross sections of $Tm:Lu_2O_3$ and $Tm:LuScO_3$, shown in Fig. 22(a) and Fig. 22(b), respectively, do not depend on crystal orientation.

Broad features in the absorption spectra of $Tm:Lu_2O_3$ and $Tm:LuScO_3$ around 795 nm are well suited for diode pumping. With the absorption peaks for $Tm:Lu_2O_3$ and $Tm:LuScO_3$ existing around 796 nm and 793 nm, respectively, the emission from high

power AlGaAs laser diodes can be temperature tuned to match the respective peaks or to accommodate for any emission wavelength drift with increasing current. Considering typical high power broad area laser diodes have an emission bandwidth of a few nanometers, the broad absorption features mean that a slight shift in pump wavelength can be accommodated for and that a large percentage of the pump light is absorbed. As will be seen later in this chapter, high doping concentrations (>0.5 at.%) of the gain elements used in this work lead to absorptions upwards of 60%. High doping concentrations are also required to achieve the cross relaxation pump scheme that permits efficiencies beyond that imposed by the quantum defect.
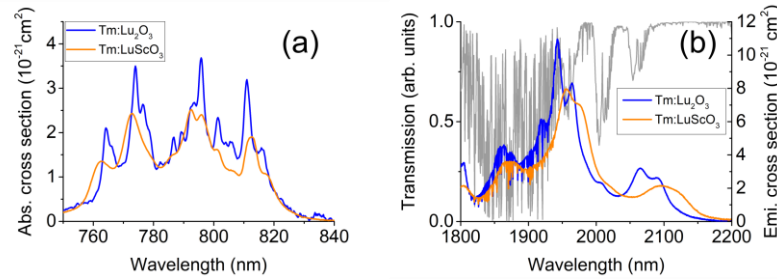
Fig. 22. Absorption and emission cross sections for the Tm^{3+}-doped sesquioxides are shown in (a) and (b), respectively [129]. Atmospheric transmission is shown by the grey line [10].

In the past, these high doping concentrations have been shown to have a detrimental effect on the thermal conductivity of the laser gain element. This effect is made worse by large differences in the masses between the dopant ion and the lattice cation [207]. In [60], Koopmann *et al.* compared the thermal conductivity of $Tm:Lu_2O_3$ with another widely used Tm^{3+}-doped laser gain material, Tm:YAG, and showed that Tm:YAG experienced a strong decrease in thermal conductivity with increasing doping concentration. However, this was not the case for $Tm:Lu_2O_3$, which experienced a decrease of only 12.8 W/m·K to 11.3 W/m·K for an increase of doping concentration from 0 at.% to 5 at.%. For a roughly equivalent increase in doping concentration, the thermal conductivity of Tm:YAG was found to decrease from 10 W/m·K to 6 W/m·K (Fig. 23). By comparing the masses of the lattice cations, Y (m_Y = 88.9 u) and Lu (m_{Lu} = 175 u), with the Tm dopant (m_{Tm} = 169 u), the difference in change of thermal conductivity can be explained to be the result of the small and large differences between the masses of Tm and Lu, and Tm and Y, respectively.
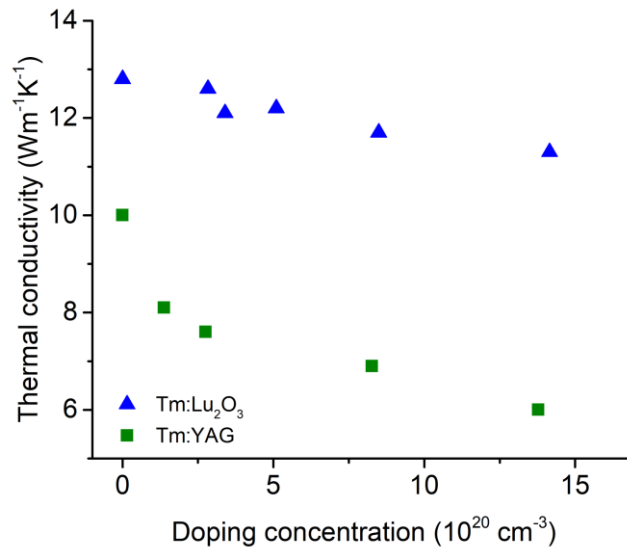
Fig. 23. Change in thermal conductivity of Tm:YAG and Tm:Lu$_2$O$_3$ with respect to increasing Tm^{3+} doping concentration [129]. Doping concentration is given in units of 10^{20} cm^{-3} due to different cation density of the hosts.

Tm:LuScO$_3$ has also been reported to not suffer a drastic decrease in thermal conductivity as a result of increased doping [129]. However, the large difference in the masses of the Lu and Sc (m$_{Sc}$ = 45 u) components within the disordered lattice results in LuScO$_3$ having a relatively low thermal conductivity of 3.6 W/m·K [208]. This is a drawback of the mixed sesquioxide host material, which otherwise features very useful enhancements over the unmixed hosts. These enhancements include broader and smoother emission and absorption features, benefiting diode pumping and ultrashort pulse generation. This smoothing can be seen well in Fig. 22(a) and Fig. 22(b). An additional beneficial feature that all the Tm^{3+}-doped sesquioxides have over other Tm^{3+}-doped gain media can also be seen in Fig. 22(b). This is the presence of gain well beyond 2 μm; avoiding the atmospheric absorption band around 1.9 μm, and greatly aiding the realisation of stable mode-locked operation. However, due to the quasi-three level operation of Tm, this gain is dependent on the applied inversion levels required to reach threshold. For very low inversion levels, the maximum gain for Tm:Lu$_2$O$_3$ and Tm:LuScO$_3$ can be found around 2095 nm and 2104 nm, respectively [60,129,205]. If the inversion is increased slightly, the gain peak for Tm:Lu$_2$O$_3$ can be seen to move to ~2.07 μm whilst the maximum gain for Tm:LuScO$_3$ remains around 2.1 μm. Further increase of the inversion level will see the maximum gain for Tm:LuScO$_3$ drop below 2.1 μm, with the peak found around 1.98 μm (Fig. 24). Under these high inversion levels, the gain peak for Tm:Lu$_2$O$_3$ exists around 1.94 μm. The impact this effect has on

laser operation is that in cavities featuring high parasitic losses or those with high output coupling, the wavelength will shift to shorter wavelengths that feature more gain. As will be seen later on, this can have a negative impact on the tuning capability of the laser source.
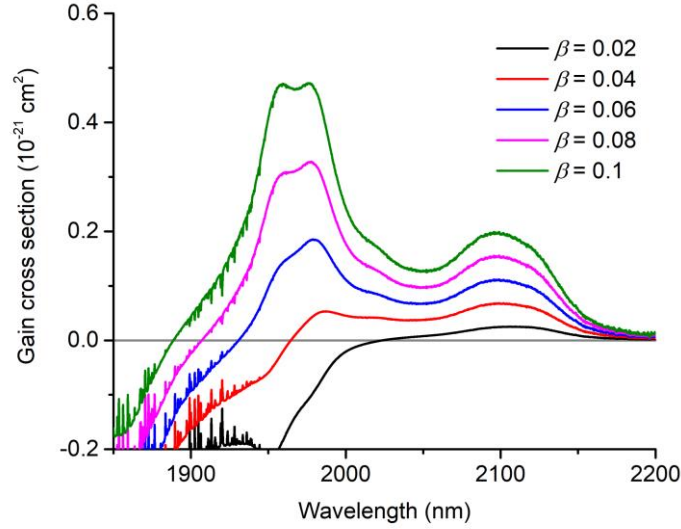
Fig. 24. Gain cross section of Tm:LuScO$_3$ previously calculated from the effective absorption cross section and calculated emission cross section for different inversion levels, β [129].

In regards to the transmission of the host crystal, the sesquioxides are well placed for operating in the mid-IR spectral region with a wide transparency range spanning ~0.2–8 µm [209]. The refractive index of the host crystals throughout this range can be calculated using the respective Sellmeier equation [210]. For Tm:Lu$_2$O$_3$, the equation is

$$n(\lambda) = \left(3.62004 + \frac{0.0412526}{\lambda^2 - 0.0239454} - 0.0086344\lambda^2 \right)^{\frac{1}{2}} \tag{3.1}$$

where λ has the unit of µm. To the best of the authors knowledge, no Sellmeier equation has been reported for LuScO$_3$. For the purpose of this work, considering that the mixed sesquioxide host of the Tm:LuScO$_3$ crystals used had a 1:1 mixing ratio, it has been assumed that the refractive index of LuScO$_3$ can be estimated as an average between that of Lu$_2$O$_3$ and Sc$_2$O$_3$, where the refractive index of Sc$_2$O$_3$ can be calculated using

$$n(\lambda) = \left(3.83252 + \frac{0.0492688}{\lambda^2 - 0.0237987} - 0.014094\lambda^2 \right)^{\frac{1}{2}}. \tag{3.2}$$

Using (3.1) and an average of (3.1) and (3.2), the refractive index of Lu_2O_3 and $LuScO_3$ for $\lambda = 2$ μm have been calculated as 1.9 and 1.92, respectively. Whilst not used in this work, it is worth noting that other temperature dependent Sellmeier equations have been reported for Lu_2O_3 and Sc_2O_3 for temperatures up to 250 °C [211].

3.3   Continuous wave characterisation

Initial characterisation of the Tm^{3+}-doped gain media used in this work began by investigating the performance in the continuous wave (CW) regime. This approach allows for the optimisation of cavity architecture, crystal parameters, and pump configurations before the additional complexity of mode-locking the source is added. In addition, tuning characteristics can be investigated to provide a better picture of the gain available when moving to the mode-locked regime.

This type of characterisation, albeit in a straightforward two mirror linear cavity configuration approach, has been completed for $Tm:LuScO_3$ and $Tm:Lu_2O_3$ in the past in other reported works [60,129,205,212,213]. Under pumping from a Ti:sapphire pump source tuned to 796 nm, a 7.7 mm long 1 at.% Tm^{3+}-doped $LuScO_3$ crystal was able to generate a maximum output power of 705 mW for an absorbed pump power of 1.36 W at several wavelengths between 2090 nm and 2115 nm simultaneously. The corresponding slope efficiency of 55% is considerably greater than the Stokes efficiency of around 38% and is only achievable due to the "two-for-one" cross relaxation process. Wavelength tuning of the source using a quartz BRF realised continuous and smooth tuning from 1960 nm to 2115 nm. Similar characterisation of $Tm:Lu_2O_3$ saw a 15 mm long 1 at.% Tm^{3+}-doped Lu_2O_3 crystal rod pumped by a laser diode tuned to emit at 796 nm with a maximum available power of 110 W. From this setup, a maximum output power of 75 W and a maximum slope efficiency of 42% with respect to incident pump power were achieved at wavelengths around 2065 nm. Inserting a BRF allowed the source to be continuously tuned 1922 nm to 2134 nm whilst achieving an output power of more than 1 W. Such characterisation of $Tm:LuScO_3$ and $Tm:Lu_2O_3$ gives a jumping off point for what could be achievable when considering a new laser source.

In the following section, the CW characterisation of diode-pumped $Tm:LuScO_3$ and $Tm:Lu_2O_3$ laser sources will be discussed. Characterisation of the laser diode pump sources used in the CW and later in the mode-locked regime will also be introduced and discussed in detail.

3.3.1   Tm:LuScO₃

The CW performance of the Tm:LuScO₃ laser was characterised using a four-mirror *z*-fold cavity design, as shown in Fig. 25. A multimode single emitter C-mount laser diode (LD) with emitting area of 90 μm × 1 μm ($x × y$ axes) operating at 793 nm with a maximum specified output power of 4 W was used as a pump source. The laser diode was housed in a thermoelectrically cooled mount and maintained at a temperature of 24 °C using indium foil to provide good heat flow between the diode and the mount. This temperature was chosen to best match the ~793 nm absorption peak of Tm:LuScO₃ by monitoring the emission wavelength and noting the change caused by temperature and pump current. The pump beam was first collimated in the fast axis by a 3.1 mm focal length aspheric lens (L1) before passing through a pair of cylindrical lenses (L2 and L3; focal lengths of -7.7 mm and 200 mm, respectively) for beam expansion and collimation in the slow axis. The collimated beam was then focused using a 100 mm achromatic doublet lens (L4) to a pump waist radii of 43 μm × 23 μm at the position of the crystal (Fig. 26). This was measured using a commercial CCD camera beam profiler. The beam quality parameter, M^2, of the pump beam was calculated to be 17 and 1.2 for the *x* and *y* axes, respectively. The pump beam steering dielectric mirror (SM) was used to minimise the overall setup footprint. All optics used in the beam reshaping and collimation setup were anti-reflection (AR) coated, or coated for high-reflectivity (HR) in the case of the steering mirror, for the pump wavelength to minimise loses.

The four-mirror laser cavity consisted of a plane-wedged HR mirror (M3), two curved mirrors with a radius of curvature (ROC) of 75 mm (M1 and M2), and a plane-wedged output coupler (OC), and operated in stability region I. Operating in stability region I, as defined by the cavity stability diagram, resulted in collimated beams in the two arms of the cavity. The long cavity arm had a length of approximately 0.95 m, while the short cavity arm had an approximate length of 0.25 m. A plane-plane, 4 mm long, 3 mm × 3 mm in aperture, AR coated, 4 at.% Tm³⁺-doped LuScO₃ (LC), grown at the University of Hamburg, was placed at the waist of the cavity between M1 and M2. The crystal was mounted onto a heatsink, which was maintained at 20 °C using a thermoelectric cooler device. Indium foil was again used to ensure a good thermal contact. The laser cavity waist within the laser crystal was calculated to have a radii of 24 μm × 21 μm. The cavity was designed using a combination of LaserCanvas and LASCAD laser cavity design software. These software were also used to design all subsequent cavities and beamlines mentioned in the remainder of the thesis. Apart from the output couplers, all cavity mirrors were designed to be HR coated (>99.9%)

between 1836 nm and 2176 nm, and AR coated for around 800 nm. The output couplers used had transmissions of 1%, 2%, 4%, and 5% between 1900 nm and 2100 nm.
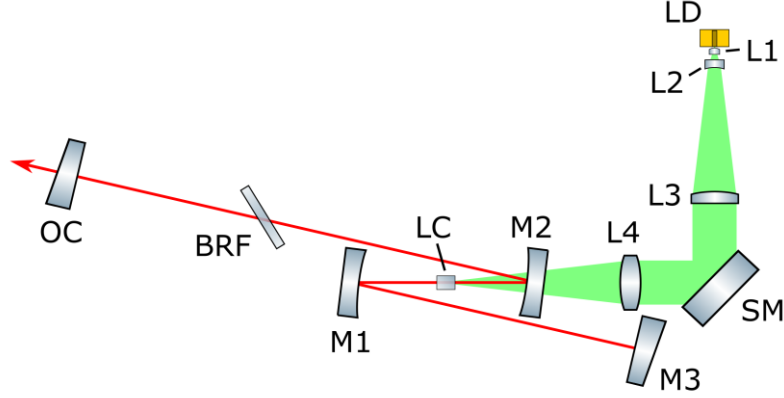
Fig. 25. Diagram of the cavity configuration used in characterising the CW laser performance of Tm:LuScO$_3$ and later Tm:Lu$_2$O$_3$. The BRF was only present during characterisation of the tuning capabilities of the laser sources. For reference, the x-axis is in the plane of the page, while the y-axis would be perpendicular to this.
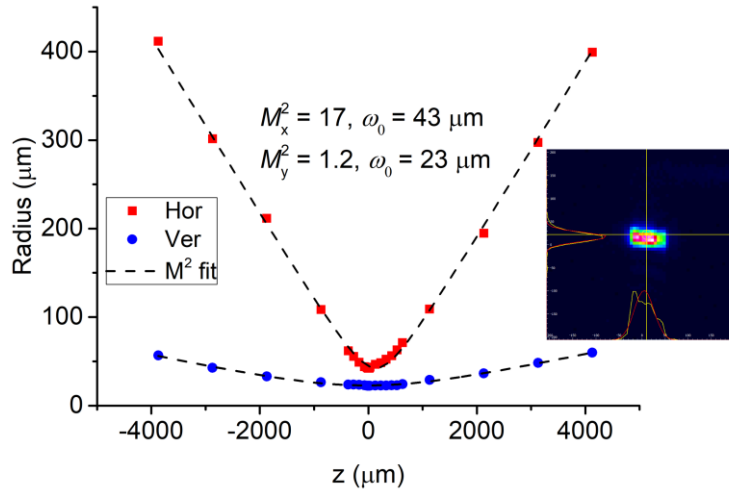
Fig. 26. Beam divergence plot of the 90 μm × 1 μm strip, 4 W pump laser diode measured after the pump reshaping and focusing optics. Insert is an image of the laser diode pump waist as viewed on the CCD beam profiler.

By increasing the applied current to the laser diode, the lasing threshold and maximum output powers for the Tm:LuScO$_3$ laser over the range of output couplers could be recorded. The maximum CW output power of 660 mW was achieved using the 2% output coupler with a corresponding slope efficiency of 33% (with respect to absorbed

pump power) [Fig. 27(a)] at a central emission wavelength of 2103 nm [Fig. 27(b)]. An emission wavelength around 2100 nm is indicative of low loss operation for Tm:LuScO$_3$. A laser threshold of 192 mW of absorbed pump power was measured. Absorbed pump power could be calculated by measuring the unabsorbed pump light transmitted through M1 and knowing the incident power on the crystal for any given drive current of the laser diode, taking into account the pump loss on the off axis curved mirror. It was found that the gain element absorbed about 67% of the pump radiation. It should be noted that further increase in the output coupling resulted in a laser efficiency drop. Such behaviour has been observed in the past in a Tm, Ho co-doped laser and is believed to be due to the presence of increased upconversion losses originating from the upper laser level $^3F_4$ of Tm^{3+} [214]. Performance of the other output couplers is summarised in Table 3.
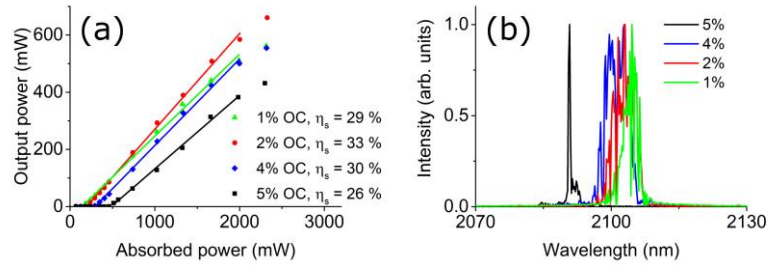
Fig. 27. (a) CW power characteristics for the diode-pumped Tm:LuScO$_3$ laser. (b) Emission spectra for the associated output couplers (OC).

In order to confirm this increased presence of upconversion with higher output coupling, an attempt was made to collect and measure the visible fluorescence whilst lasing under different output coupling conditions. Despite the very clear blue coloured emission from the pumped region of the crystal, the only signals detected were around 705–750 nm. This emission would correspond to a decay from the $^3F_3$ or $^3H_4$ levels rather than an emission around 475 nm one would expect from the $^1G_4$ level. A positive relationship between higher output coupling and slightly increased emission intensity around 700 nm is reported by Lagatsky *et al*. However, the small difference in signal intensity recorded in the measurements of Tm:LuScO$_3$ (0.512 for 1% and 0.554 for 5%) combined with the lack of signal around 475 nm offered little in the way of a definite conclusion to these measurements. Additionally, the presence of inversion dependant losses, *e.g.*, upconversion, prevents the reliable use of round-trip cavity loss analysis methods such as Findlay-Clay [215,216]. Even by excluding the 5% output coupler from the analysis, due to the noticeable shift in wavelength being indicative of additional loss mechanisms such as ground-state absorption, it is difficult to separate the

increase in threshold due to increased upconversion losses or increased output coupling. Futhermore, as a result of the decrease in slope efficiency with increasing output coupling, the method of Caird analysis [217] cannot be used to determine losses either.

Tunability of the laser was investigated by inserting a 1.6 mm quartz BRF at Brewster's angle into the long arm of the cavity [218,219]. Using the 2% output coupler, a tuning range of 1973–2141 nm was recorded under roughly 2 W of incident pump power (1.3 W of absorbed pump power). This smooth and continuous tuning, as seen in Fig. 28, is comparable to that reported by Koopmann *et al.* in [212], albeit with a different profile. The recorded tuning range is believed to be predominantly limited by the available gain around 2100 nm at the given inversion level, with the potential to be additionally impacted by increasing mirror transmission at wavelengths away from 1900–2100 nm. The difference in profile is presumed to simply be due to different mirrors coatings being used in the experiments.

Table 3. CW performance summary of the Tm:LuScO$_3$ laser. The 2% output coupler provided the best performance in terms of maximum power and slope efficiency.

OC (%)	$P_{th,abs}$ (mW)	P_{max} (mW)	η_s (%)	λ (nm)
1	141	562	29	2105
2	192	660	33	2103
4	294	554	30	2101
5	487	431	26	2091
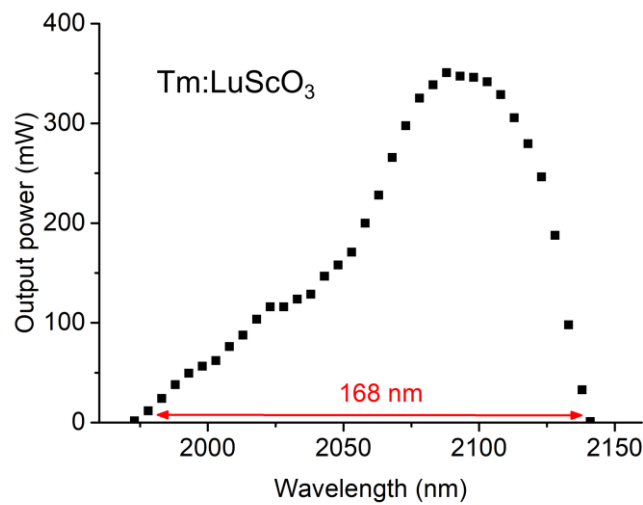
Fig. 28. Tuning curve achieved from the Tm:LuScO$_3$ laser using the 2% output coupler with the 1.6 mm thick BRF.

Conclusions

The performance presented here represents, to the best of the authors knowledge, the first demonstration of a diode-pumped Tm:LuScO$_3$ laser operating beyond 2 μm and gave great promise going forward in attempting to mode-lock the source. It can be seen that the maximum output power realised was predominantly limited by the absorbed pump power. This could be increased by using higher power pump diodes or by increasing the length of the gain medium. Increasing the length of the gain medium in the case of high power laser diode pumping, however, does not realise an overall improved mode overlap due to the large difference in beam quality between the laser and pump. Meaning that whilst it may increase the absorbed pump power, an equal increase in laser performance would not be anticipated. The option of using higher power pump diodes was also not pursued due to concerns over damaging the gain elements; such damage had already been experienced using the 4 W laser diodes. With the power and tuning range achieved when using the 2% output coupler it was fully anticipated that femtosecond pulses at an appreciable output power could be achieved. The results of mode-locked experiments are discussed in the next chapter.

3.3.2 Tm:Lu$_2$O$_3$

The increased thermal conductivity of Tm:Lu$_2$O$_3$ allowed for the use of higher power pump diodes when investigating the CW performance of the laser gain medium without risking damage to the gain element. In addition to this, the greater emission cross section available when using Tm:Lu$_2$O$_3$, combined with the increased pump power, promised a route to reach higher average powers than those achieved from the Tm:LuScO$_3$ laser. Experiments began by adapting the cavity depicted in Fig. 25 to include a 3mm long, 3 mm × 3 mm in aperture AR coated 3.5% at. Tm^{3+}-doped Lu$_2$O$_3$ ceramic gain element purchased from Konoshima Chemical Co., Ltd. With the intention of going mode-locked at a later date, the cavity was aligned to operate in stability region II producing a calculated laser cavity waist within the gain element of 25 μm × 23 μm. The optical pump set up was modified to focus the 200 μm × 1 μm strip 6 W laser diode to a waist of 85 μm × 28 μm (Fig. 29). Lenses L1, L2, L3, and L4 in Fig. 25 would now correspond to a 2.75 mm aspheric lens, a -12.7 mm cylindrical lens, a 200 mm cylindrical lens, and a 100 mm achromatic doublet lens, respectively. This new high power laser diode was calculated to have an M^2 parameter of 23 and 1.6 in the x and y directions, respectively, and was maintained at a temperature of 33 °C. In a similar manner to that used for the previous laser diode, this temperature was chosen in

order for the laser diode emission wavelength to best match the absorption peak of Tm:Lu$_2$O$_3$ (~796 nm) over its operating power range. The pump beam waist was positioned at the location of the cavity mode waist and the pump optics were chosen to provide the best overlap. All other optics within the cavity remained the same, while output couplers of 1%, 2%, 3%, 4%, and 5% were used to investigate the laser performance.
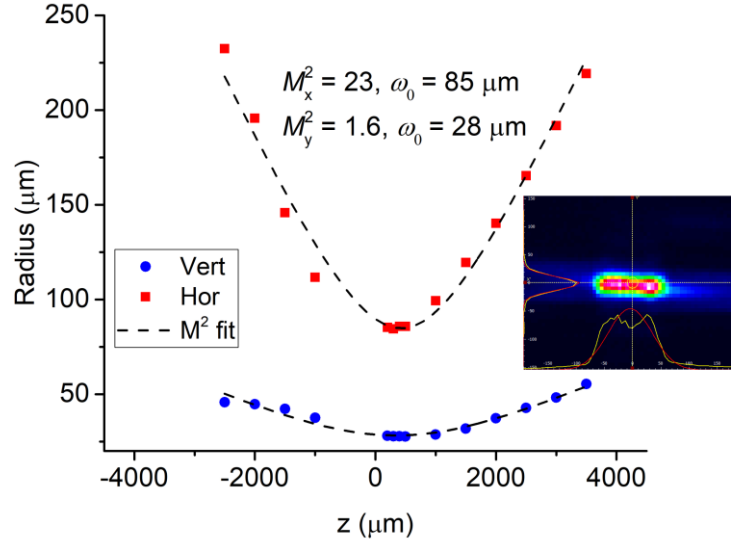
Fig. 29. Beam divergence plot of the 200 μm × 1 μm strip, 6 W pump laser diode measured after the pump reshaping and focusing optics. Insert is an image of the laser diode pump waist as viewed on the CCD beam profiler.

Of the output couplers tested it was found that the 2% provided the highest output power of 618 mW at a wavelength of 2064 nm, with a corresponding slope efficiency of 31% [Fig. 30(a)]. Thresholds in the range of 185–341 mW of absorbed pump power were measured over the series of output couplers; increasing with the transmission of the output coupling mirrors. Absorbed pump power was determined in the same way as had been done previously with approximately 50% of the pump light being absorbed by the gain element. Slope efficiencies over the range of output couplers used were found to drop after increasing the output coupling beyond 2%. It is believed that the cause of this is related to increased upconversion losses in a similar manner to that experienced in the Tm:LuScO$_3$ laser. Emission wavelengths were found to remain around 2065 nm for all output couplers, except in the case of the 5% output coupler when the laser also partially emitted around 1966 nm [Fig. 30(b)]. This additional emission line is thought to be caused by the higher output coupling increasing the inversion level and providing more gain around the 1960 nm peak found with Tm:Lu$_2$O$_3$. The performance of the

laser when using the other output couplers is summarised in Table 4. Determining intracavity losses is again complicated by the presence of additional loss mechanisms restricting the use of Findlay-Clay and Caird analyses.
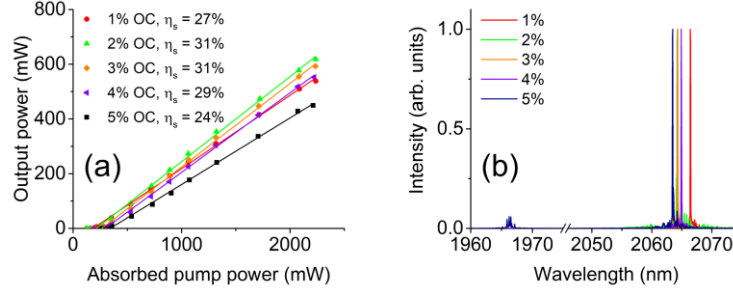
Fig. 30. (a) CW power characteristics for the diode-pumped Tm:Lu_2O_3 laser using ROC 75 mm cavity mirrors and 100 mm pump lens. (b) Emission spectra for the associated output couplers (OC). Only the 5% output coupler demonstrated dual wavelength lasing.

Table 4. CW performance summary of the Tm:Lu_2O_3 laser using ROC 75 mm cavity mirrors and 100 mm pump lens.

OC (%)	$P_{th,abs}$ (mW)	P_{max} (mW)	η_s (%)	λ (nm)
1	185	538	27	2066
2	223	618	31	2064
3	264	593	31	2064
4	296	552	29	2065
5	341	449	24	1966/2063

Despite the higher available pump power and greater emission cross section, average output powers were not found to surpass those achieved with the Tm:$LuScO_3$ laser. The poorer beam quality of the pump laser diode leading to worse pump/laser mode overlap is presumed to be the cause of this lower efficiency performance. Nevertheless, endeavours were made to mode-lock the source and demonstrate femtosecond pulse operation. This is discussed in more detail in Chapter 4. After recording limited mode-locked performance, work returned to the CW regime in the hope of improving the performance of the laser. This work was primarily focused on improving the pump and laser mode overlap within the gain element by optimising the optical configuration in the hope of realising a more stable and reliable Tm:Lu_2O_3 laser source. To this end, larger ROC mirrors were placed into the cavity along with a longer focal length pump

lens. These had the effect of creating a less divergent pump beam and mode waist, and improving cavity stability.

M1 and M2 in Fig. 25 were replaced with 150 mm ROC mirrors, resulting in new calculated laser mode waist radii of 53 μm × 51 μm. To maintain cavity stability, the lengths of the long and short arms of the cavity were changed to approximately 0.9 m and 0.29 m, respectively. The pump lens, L4, was replaced with a 200 mm achromatic doublet lens which focused the pump beam to a measured waist size of 146 μm × 40 μm. In this new configuration output powers as high as 901 mW were recorded for an absorbed pump power of approximately 2.7 W when using the 2% output coupler. This performance corresponded to a slope efficiency of 40% and was recorded at a central emission wavelength of 2065 nm. Power plots and emission spectrum data gathered for the 1%, 2%, and 3% output couplers used can be seen in Fig. 31(a) and Fig. 31(b), respectively. In addition, the performance is detailed in Table 5.
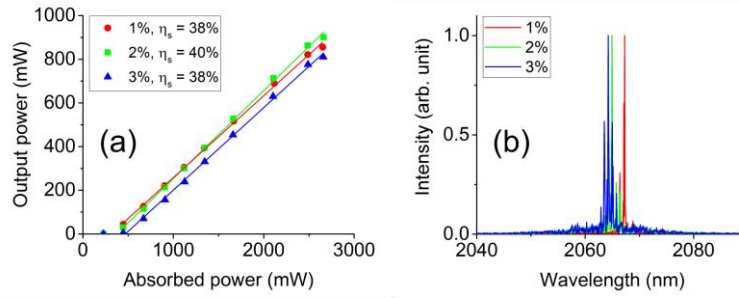
Fig. 31. (a) CW power characteristics for the diode-pumped $Tm:Lu_2O_3$ laser using ROC 150 mm cavity mirrors and 200 mm pump lens. (b) Emission spectra for the associated output couplers (OC). Emission wavelengths are largely similar to those recorded in the previous cavity configuration.

Table 5. CW performance summary for the $Tm:Lu_2O_3$ laser using larger 150 mm ROC cavity mirrors and a longer 200 mm pump lens. A significant improvement in performance in comparison with the previous $Tm:Lu_2O_3$ laser cavity configuration can be seen.

OC (%)	$P_{th,abs}$ (mW)	P_{max} (mW)	η_s (%)	λ (nm)
1	313	855	38	2067
2	372	901	40	2065
3	469	810	38	2064

Investigations into the spectral tuning range of the laser source were undertaken using the 1% output coupler and the same 1.6 mm quartz BRF used previously. Under

approximately 2.7 W of incident pump power (1.3 W of absorbed pump power), a tuning range of 1941–2126 nm was recorded (Fig. 32). Whilst this tuning range is slightly larger than that recorded when using Tm:LuScO$_3$ it can be seen that it has a more structured profile. Features at 2011 nm, 2066 nm, and ~2090 nm can be clearly seen. These peaks can be associated with similar peaks seen on the emission cross section plot found in Fig. 22 and gain profiles published in previously reported works [60,129]. In a similar way to the tuning range recorded with the Tm:LuScO$_3$ laser, it is believed that the range presented here is primarily limited by the available gain around 2050 nm at the given inversion level, with the cavity mirror coatings further reducing the available gain at wavelengths less than 1900 nm and greater than 2100 nm.
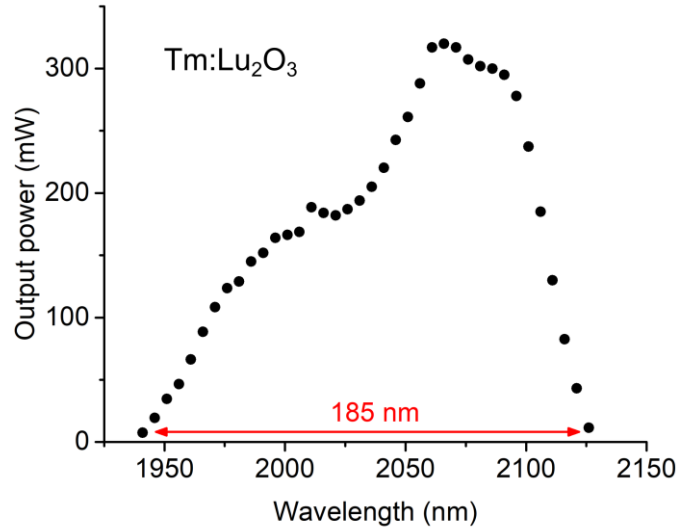
Fig. 32. Recorded tuning curve from the Tm:Lu$_2$O$_3$ laser when using the larger 150 mm ROC cavity mirrors and a longer 200 mm pump lens. This performance was achieved using the 1.6 mm thick BRF and the 1% output coupler.

Conclusions

In terms of slope efficiency and maximum output power, the performance recorded in this new optical configuration outclassed not only that previously demonstrated by the Tm:LuScO$_3$ laser but also the earlier iteration of the Tm:Lu$_2$O$_3$ laser. Whilst the tuning curve is slightly less smooth, the available gain demonstrated over the tuning range is more than capable of generating ultrashort pulse durations. Furthermore, when one compares the slopes on the power plot in Fig. 31(a) with those in Fig. 27(a) it can

be seen that at higher pump power there is little to no sign of thermal rollover from the Tm:Lu$_2$O$_3$ laser. This lack of thermal impact can also be seen in the previous iteration of the Tm:Lu$_2$O$_3$ laser and can be attributed to the significantly higher thermal conductivity of the Lu$_2$O$_3$ host in comparison to LuScO$_3$. Indeed, the performance presented here suggested that, once mode-locked, a femtosecond source capable of significantly high average powers, suitable for further amplification, could be developed.

4 Femtosecond pulse generation

Many of the applications introduced in Chapter 1 require high peak power/pulse energy sources to be fully utilised. Sources capable of generating pulse durations in the femtosecond regime provide a clear route to generate these high peak powers/pulse energies. Whilst mode-locked Ti:sapphire laser systems dominate in the near-IR region, significant challenges remain in the mid-IR. Emitting around 2.4 µm and exhibiting a very broad tunability, Cr:ZnSe is a strong contender and has even been referred to as "Ti:sapphire of the mid-IR" [220]. Numerous reported demonstrations of the capabilities of the gain media have shown the generation of sub-100 fs pulses with average powers >1 W in the mid-IR. However, Cr:ZnSe requires pumping at around 1.8 µm meaning that bulky Tm:fibre or Er:fibre sources tend to be used [100]. This requirement restricts the overall compactness of the source as well as increasing the total cost to the end user. In the previous chapter, the properties and CW performance of the Tm^{3+}-doped sesquioxides, $Tm:LuScO_3$ and $Tm:Lu_2O_3$, were discussed and presented. These laser gain materials provide a means to generate ultrashort pulses in the 2 µm region and offer a significant advantage over Cr:ZnSe in that they have a plethora of available pump sources to choose from, ranging from high beam quality and high cost Ti:sapphire and Raman shifted Er:fibre sources, to low beam quality and low cost high power laser diodes around 800 nm.

Clearly, with the aim of making these systems more practical and less costly, laser diode pumping should be employed. However, the development of diode-pumped ultrashort pulse Tm^{3+}-doped lasers is not a straight forward process. Poor pump beam quality can lead to lower efficiencies, high thermal loads, *Q*-switching instabilities, and weaker SPM thus requiring precise cavity and saturable absorber engineering for stable mode-locking. Indeed, the number of diode-pumped mode-locked Tm^{3+}-doped lasers reported to date is rather limited, with only a few demonstrations of sub-picosecond operation (Fig. 33).

Here, the performance and characterisation of diode-pumped soliton mode-locked $Tm:LuScO_3$ and $Tm:Lu_2O_3$ lasers shall be discussed. In addition, tunable ultrashort pulse operation around 2.06 µm utilising a specially designed steeply diving birefringent filter (SD-BRF) are presented and analysed. The characteristics and design process of the SD-BRF are also discussed.
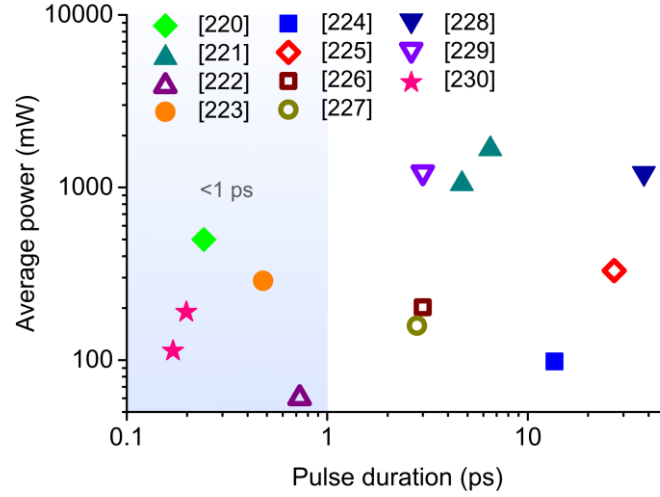
Fig. 33. State-of-the-art performance summary of diode-pumped mode-locked Tm^{3+}-doped solid-state lasers in the ~2–2.1 μm spectral region [221–231].

4.1 Tm:LuScO$_3$

As has been shown in Section 3.3.1, the Tm^{3+}-doped sesquioxide Tm:LuScO$_3$ has a very broad a smooth tuning curve, demonstrating its wide gain region spanning from 1.95 μm to beyond 2.1 μm. This has been exploited in the past to demonstrate some of the shortest pulses currently achieved in the 2 μm region. Indeed, a crystalline Tm:LuScO$_3$ laser has demonstrated a 105 fs pulse duration [232], and, more recently, pulses as short as 74 fs were generated with an output power of 34 mW from a Tm:LuScO$_3$ mixed-ceramic laser [133]. It should be highlighted that both of these results were achieved using high beam quality Ti:sapphire lasers as pump sources. By instead using commercially available laser diode pump sources it was intended that pulse durations on the same order as those already demonstrated for the gain material could be achieved but at higher output powers and in an overall more compact and efficient setup.

Mode-locked performance of the Tm:LuScO$_3$ laser was characterised using a *z*-fold cavity design similar to that used for the previous CW characterisation in Chapter 3 (Fig. 34). To initiate mode-locking and stabilise the soliton, the high reflectivity mirror in the short arm of the cavity was replaced with an ion-implanted InGaAsSb quantum-well-based structure. Similar devices, have previously been characterised by a low-signal reflection of approximately 99.5–98% over the range of 1950–2100 nm with estimated modulation depth and nonsaturable loss parameters of 0.3–1% and 0.2–0.9%,

respectively, over the same range [143,144,232,233]. The cavity was also aligned so that it operated in stability region II, thus producing a second intracavity beam waist with an average radius of 110 μm on the SESAM without the need for any additional cavity optics. The SESAM element was mounted on a brass heatsink maintained at a temperature of 20°C using a thermoelectric cooler. Two GTI type HR mirrors (>99.9% between 1915 nm and 2140 nm) with ~ -480 fs^2 GDD per reflection at 2095 nm were inserted into the long arm of the cavity (GTM1 and GTM2) maintaining the same mode waist within the laser crystal (LC). It is estimated that the 4 mm long gain crystal also added an additional dispersion of around -300 fs^2. The pump source and optics remained unchanged from the initial CW characterisation setup, ensuring an optimised pump/laser mode overlap within the gain element.
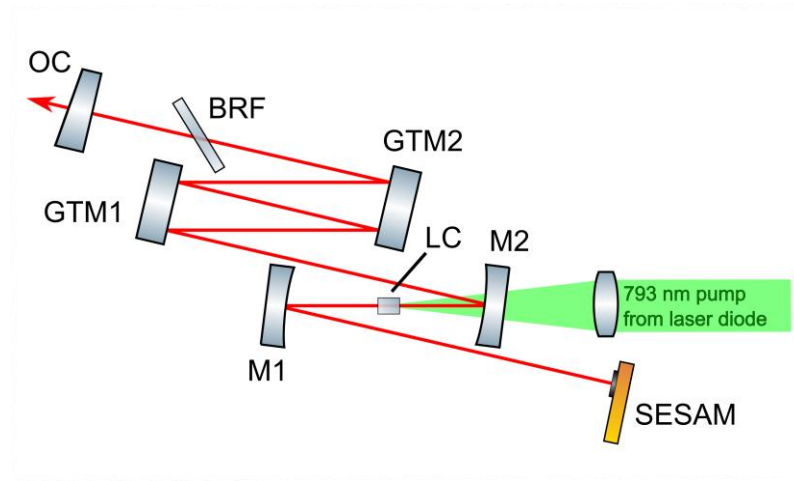
Fig. 34. Experimental setup for mode-locked characterisation of the Tm:LuScO₃ laser. The number of reflections at each GTI mirror was changed from one to two during characterisation of the lasers performance. The birefringent filter (BRF) was used in later mode-locked tuning experiments.

Initial investigations into mode-locked performance were undertaken with a 2% output coupler (OC) and one reflection at each of the GTI mirrors resulting in a total round-trip GDD of approximately -2220 fs^2. By gradually increasing the pump power, the self-starting transition between CW and mode-locked operation was observed at an average output power of 65 mW [Fig. 35(a)]. Single pulse operation was maintained up to a maximum average output power of 123 mW, beyond which multiple pulse mode-locking was observed. Near-transform-limited pulses with a duration of 163 fs (assuming a sech^2 intensity autocorrelation profile) were recorded at an average output power of 123 mW [Fig. 35(b)]. The corresponding optical spectrum at 2093 nm, seen in Fig. 35(c), had a FWHM bandwidth of 28.4 nm giving a TBP of 0.32. The spike on the optical spectrum seen near the peak of the pulse envelope is indicative of being very

near to the pulse break up point, suggesting this recorded performance is at the limit of that achievable from the cavity configuration whilst maintaining single pulse operation.
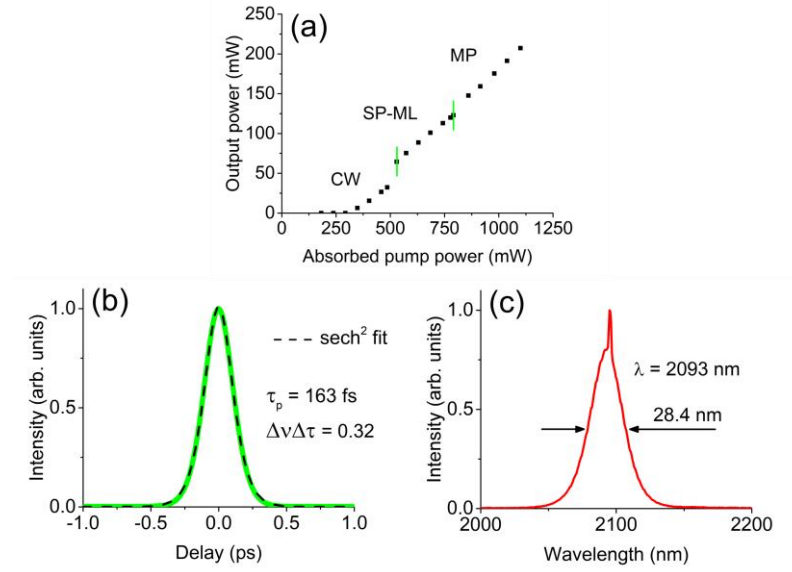
Fig. 35. (a) Power characteristics of the mode-locked Tm:LuScO$_3$ laser with the 2% output coupler and one reflection at each GTI mirror. CW, continuous wave; SP-ML, single-pulse mode-locked operation; MP, multi-pulse mode-locked operation. The autocorrelation trace with sech^2 fit (b) and optical spectrum (c) for pulses recorded at the maximum single-pulse output power of 123 mW.

Replacing the 2% output coupler with a 4% one realised higher average output powers and longer pulse durations in the single pulse regime. The transition from CW to mode-locked operation was recorded to be at an average output power of 111 mW, while the transition from the single pulse to multiple pulse regime was observed at an average output power of 281 mW. Single pulse durations as short as 195 fs were recorded at an average output power of 230 mW, with a corresponding optical bandwidth of 23.8 nm at a central wavelength of 2095 nm. Examining the radio frequency (RF) spectrum of the laser showed a fundamental beat note at 119.7 MHz with an extinction ratio of 68 dB above the carrier. However, on closer inspection of the RF spectrum, evidence of Q-switching instabilities were prevalent. This was true for both cavity configurations and could not be overcome.

Increasing the number of reflections off the GTI mirrors to four added an additional -1920 fs^2 GDD, bringing the total round-trip dispersion to approximately -4140 fs^2. This was done to increase the pulse break up point in the hope of realising Q-switching instability free mode-locked operation by increasing the maximum fluence on the SESAM. As adding additional dispersion would be expected to increase the pulse duration, lower output coupling mirrors of 1% and 2% were chosen to retain the

intracavity pulse energy and somewhat offset the increase in pulse duration caused by the increased round-trip dispersion.

With the 1% output coupler in use, self-starting *Q*-switched mode-locked operation was observed to begin at an average output power of 49 mW, while the transition to CW single-pulse mode-locked operation was observed at an average output power of 78 mW [Fig. 36(a)]. The intracavity laser field fluence on the SESAM at the mode-locking threshold was estimated to be 113 μJ/cm^2. The laser cavity beam waist inside the gain medium was estimated to be 27 μm × 14 μm at such optimised conditions. Increasing the pump power further saw that single pulse operation was attainable up to a maximum average output power of 113 mW. Increasing the pump power further still caused the laser to jump into the multiple pulse mode-locking regime. Pulse durations as short as 170 fs were recorded at an average output power of 113 mW [Fig. 36(c)], with single pulse operation confirmed by examining a 50 ps span autocorrelation trace seen in Fig. 36(d). The corresponding optical spectrum centred at 2093 nm, had a bandwidth of 27.2 nm [Fig. 36(b)], thus indicating a TBP of 0.32. Stable mode-locked operation was confirmed by the RF spectrum [Fig. 36(e)], which shows the fundamental beat note at 115.23 MHz with an extinction ratio of 71 dB above the carrier. A 1 GHz span, seen in Fig. 36(f), showed no *Q*-switching instabilities and a near constant extinction ratio over the harmonic beat notes.

Switching to the 2% output coupler resulted in a maximum average output power of 190 mW [Fig. 37(a)] during single-pulse mode-locked operation, limited only by the available pump power. In this case, self-starting *Q*-switched mode-locking was observed first at 127 mW of average output power followed by a transition to single-pulse mode-locked operation at 171 mW, which was maintained up to a maximum generated power of 190 mW. The threshold for mode-locking was estimated to be at an intracavity fluence on the SESAM of 145 μJ/cm^2. At the maximum output power, pulses as short as 198 fs were produced [Fig. 37(c)], while the corresponding optical spectrum was found to centre at 2094 nm with a bandwidth of 23.5 nm [Fig. 37(b)] giving a TBP of 0.32. The RF spectrum recorded with a span of 200 kHz and a resolution bandwidth of 200 Hz shows the fundamental beat note at 115.26 MHz with an extinction ratio of 71 dB above the carrier [Fig. 37(e)]. In addition and in keeping with that found with the 1% OC, a 50 ps autocorrelation trace and a 1 GHz span RF spectrum, as seen in Fig. 37(d) and Fig. 37(f), respectively, confirmed single-pulse *Q*-switching instability free operation.
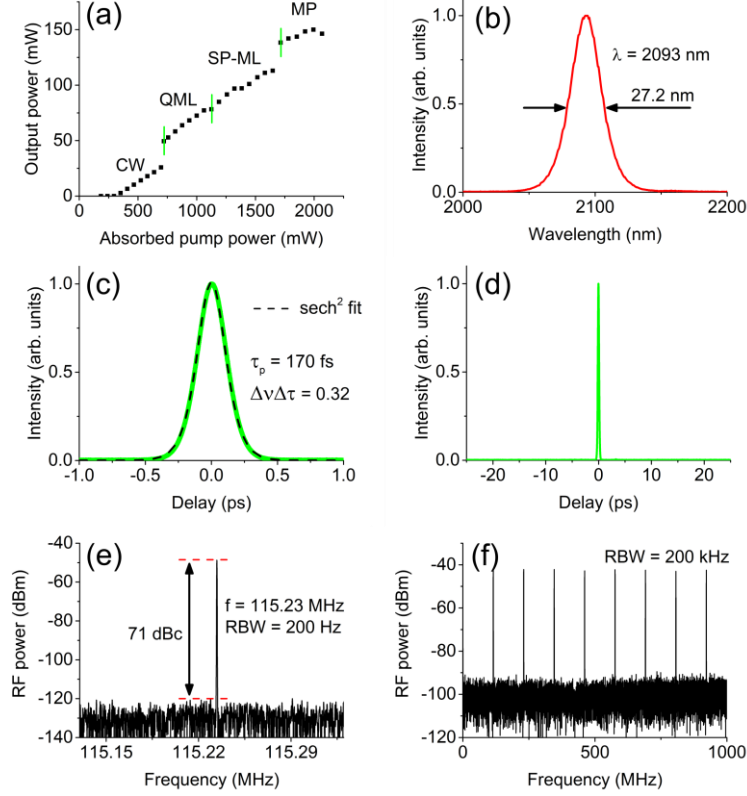
Fig. 36. (a) Power characteristics for mode-locked operation with the 1% output coupler and two reflection at each GTI mirror. QML, *Q*-switched mode-locked operation. Optical spectrum (b), autocorrelation traces over 2 ps (c) and 50 ps (d) spans, and 200 kHz (e) and 1 GHz (f) RF spectra for pulses recorded at the single-pulse maximum output power of 113 mW.

The output beam quality of the laser was determined by performing an M^2 measurement using a scanning slit beam profiler in combination with a 75 mm plano-convex lens. The results of the measurements showed a slightly astigmatic focus and M^2 values of 1.2 and 1.1 in the horizontal and vertical directions, respectively (Fig. 38).

Having shown stable single-pulse mode-locked operation it is useful to examine the variation of pulse duration with output power (intracavity pulse energy) in order to confirm true soliton mode-locking. Considering the performance recorded when using the 1% OC, it was found that the pulse durations decreased inversely proportional to the intracavity pulse energy (E_p) as soliton mode-locking theory predicts [150]. Pulse durations decreased from 246 fs at the mode-locking threshold to 170 fs at the edge of single-pulse operation. Two distinct regions exist between the pulses recorded under *Q*-switched mode-locked operation and those recorded when CW mode-locking was achieved. This offset is thought to be due to comparably slightly higher output powers recorded when in the *Q*-switched mode-locked regime. Only pulses recorded in the CW mode-locked regime have been included in Fig. 39.
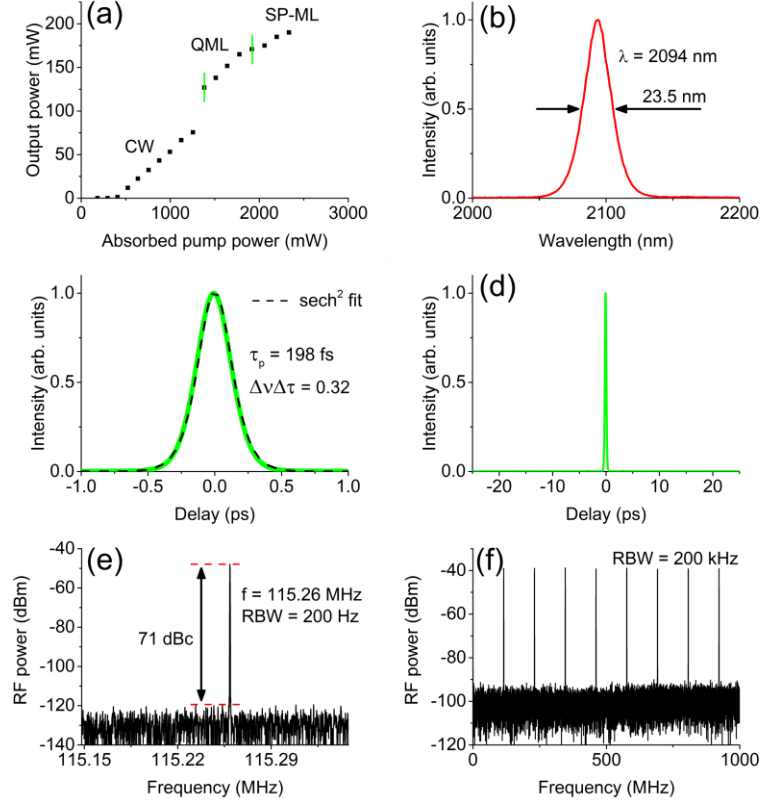
Fig. 37. (a) Power characteristics for mode-locked operation with the 2% output coupler and two reflection at each GTI mirror. QML, *Q*-switched mode-locked operation. Optical spectrum (b), autocorrelation traces over 2 ps (c) and 50 ps (d) spans, and 200 kHz (e) and 1 GHz (f) RF spectra for pulses recorded at the single-pulse maximum output power of 190 mW.
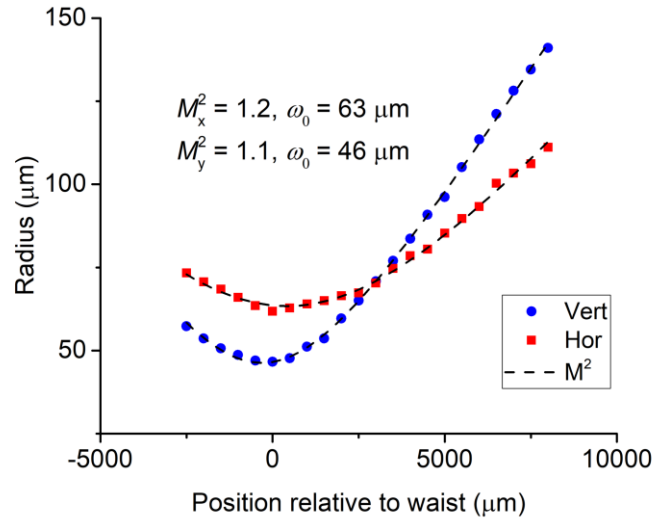
Fig. 38. Beam divergence of the diode-pumped Tm:LuScO₃ ultrashort pulse laser. The *x*-axis has been given as distance relative to the waist to ease viewing, in reality the waists were separated by ~8 mm.

Assuming a totally round-trip cavity dispersion of -4140 fs^2, the SPM coefficient, δ, was calculated to be 8.8×10^{-7} W^{-1} by fitting a curve of $1/E_p$ to the data, as per (2.3). Using (2.4), an estimate of the nonlinear refractive index, n_2, was calculated to be 4.4×10^{-16} cm^2/W. As there is no known reported value for the nonlinear refractive index of Tm:LuScO$_3$ it is hard to gauge the accuracy of this calculated value. However, when comparing it to the nonlinear refractive index of Tm:Lu$_2$O$_3$ ceramic, which has been reported in the past as 3.3×10^{-16} cm^2/W at 2070 nm [234], one can say that the value calculated for Tm:LuScO$_3$ is at least comparable to that of Tm:Lu$_2$O$_3$.

In addition to examining the pulse duration change with output power (intracavity pulse energy), one can also look at the dependence of pulse duration on GDD. Comparing the minimum pulse durations achieved using the 2% output coupler for approximately -2220 fs^2 and -4140 fs^2 GDD, it can be seen that the pulse duration achieved with the lower absolute value of dispersion is 35 fs shorter than that achieved with the higher absolute value. Whilst this could be an effect of the increased output power recorded with the lower negative GDD it is also in agreement with soliton mode-locking theory that states that the pulse duration scales linearly with the negative GDD inside the laser cavity (*i.e.* $\tau_p \propto |D|$) [150]. By introducing more dispersion one would expect the pulse duration to increase further. However, this avenue of investigation was not pursued.
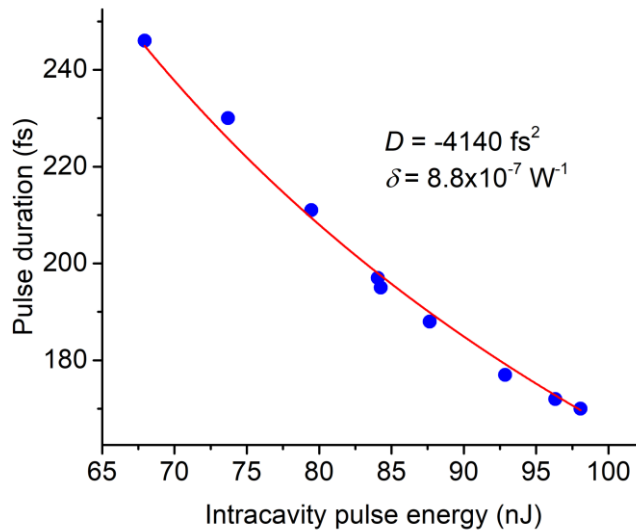
Fig. 39. Change in pulse duration with intracavity pulse energy (average output power) for the mode-locked Tm:LuScO$_3$ laser using the 1% output coupler. The red curve is a fit to $1/E_p$. δ is the SPM coefficient and D is the estimated total round-trip cavity dispersion.

4.1.1 Conclusions

While it was not possible to truly confirm the linear relationship between pulse duration and GDD, the confirmation of soliton behaviour from the variation of pulse duration with intracavity pulse energy is clear. In the performance recorded, the maximum average output power for single pulse operation was limited by the pulse break up threshold and by the maximum absorbed pump power. Increasing the total round-trip cavity dispersion realised higher average output powers, at the expense of pulse duration, but the only routes to increasing the maximum absorbed pump power would be the use of higher power pump diodes or by increasing the length of the laser crystal. The reasons one would not necessarily choose to use higher pump diodes or increase the length of the gain medium have been discussed in Section 3.3.1.

Utilising high beam quality Ti:sapphire pump sources, Tm:LuScO$_3$ lasers have been shown to be capable of generating pulses shorter than those presented here [133,235]. Improved mode overlap and stronger SPM are made possible by the near-diffraction-limited pump source. It is possible that such performance could also be achieved through the use of single mode laser diodes; this avenue of investigation was not pursued during this thesis, however. Shorter pulses still could also be realised through the use of lower output coupling, *e.g.*, 0.5%, thus increasing the intracavity pulse energy. This would have a large impact on the maximum average output power and was therefore not pursued.

These results represent, to the best of the authors knowledge, the first reported successful demonstration of mode-locked ultrashort pulses from a diode-pumped Tm:LuScO$_3$ source, and at the time of writing were the shortest reported pulse durations from a solid-state diode-pumped Tm^{3+}-doped source in the ~2–2.1 μm region.

4.2 Tm:Lu$_2$O$_3$

Whilst Tm:Lu$_2$O$_3$ may not have such a broad or smooth gain spectrum around 2–2.1 μm, it benefits from a much higher thermal conductivity and a higher emission cross section. As has already been seen, this ultimately means that while it may not be able to naturally emit at 2.1 μm like Tm:LuScO$_3$, it can utilise much more powerful laser diode pump sources to generate higher average output powers. In addition, the gain spectrum in the 2 μm region is still broad enough to support sub-200 fs pulse generation. Demonstrations of mode-locked sources utilising the Tm:Lu$_2$O$_3$ gain medium have

achieved pulses as short as 175 fs using a Ti:sapphire pump source [236] and sub-250 fs pulses at a maximum output power of 500 mW under laser diode pumping [221].

Initial experiments to develop a mode-locked Tm:Lu$_2$O$_3$ source began by adapting the *z*-fold four mirror (75 mm ROC) CW source introduced in the Section 4.1. Inserting a pair of GTI mirrors in the long arm of the cavity and making multiple bounces off each mirror resulted in a six-mirror *z*-fold design very similar to that shown in Fig. 34. The total round-trip dispersion was calculated to be -3852 fs^2 at 2065 nm; this was made up of approximately -3760 fs^2 from the GTI mirrors and -92 fs^2 from the 3 mm Tm:Lu$_2$O$_3$ ceramic laser gain element.

This Tm:Lu$_2$O$_3$ source was not able to generate reliable and stable soliton mode-locking, however. Whilst mode-locked operation was obtained, the pulse duration was not found to depend on the output power (intracavity pulse energy), indeed little variation in pulse duration was found with increasing output power. Pulse durations were found to remain around 600 fs from an output power of 143 mW, at the mode-locking threshold, up to a maximum power of 285 mW. The apparent absence of soliton mode-locking is thought to be primarily due to poor cavity waist positioning in the gain element resulting in very weak SPM. It was hoped that the use of larger ROC cavity mirrors (replacing the 75 mm with 150 mm) and longer focal length pump lens (200 mm instead of 100 mm) would allow for a more optimal pump/laser mode overlap to occur within the length of the gain element. While this did improve CW performance, as shown in the previous chapter, it did not result in the intended improvement in mode-locked operation. Repeated attempts to move to a cavity alignment which would position the waist within the gain element were met with very poor performance. Adjusting the alignment to return the power saw the waist once again shifted from within the gain element. With the longer focal length mirrors and pump lens, and in this offset waist alignment, an improvement in the maximum output power was achieved, generating pulses as short as 485 fs at 401 mW. However, the stability of the source in this configuration was extremely limited meaning it needed to be repeatedly manipulated to maintain mode-locked operation.

To continue forward with Tm:Lu$_2$O$_3$ mode-locked experiments a more stable source was required. This was found in a previously demonstrated, in-house developed diode-pumped Tm:Lu$_2$O$_3$ laser [221]. The source used an AR coated 5 mm long, 2 mm $\times$ 3 mm in aperture 1.5 at.% Tm^{3+}-doped Lu$_2$O$_3$ ceramic gain element (GE) and was pumped by a fibre-coupled (100 μm core diameter) laser diode source producing a maximum power of 40 W at 795 nm and characterised by a measured beam quality

factor, M^2, of 25. Pump light from the fibre facet was collimated with a 45 mm AR coated spherical lens (L1) and focused to a waist with radii of 100 μm × 99 μm using a 75 mm achromatic doublet lens (L2). A six-mirror *z*-fold cavity was built around the gain element (Fig. 40) with HR coated 300 mm ROC fold mirrors (M1 and M2), a 2% output coupler (OC), two additional plane HR mirrors (M3 and M4), and a SESAM. Of the mirrors used, one curved mirror, M2, and one plane mirror, M3, were also coated to act as GTI type mirrors, each introducing approximately -470 fs^2 of GDD per pass. With the addition of a further -155 fs^2 from the gain element, the total round trip dispersion equalled -2035 fs^2. The curved mirrors provided a calculated laser cavity waist radii inside the gain element of 96 × 98 μm, while a second intracavity waist of 167 μm × 171 μm was produced on the ion-implanted InGaAsSb quantum-well-based SESAM. The SESAM and gain element were maintained at temperatures of 20 °C and 22 °C, respectively, using thermoelectric coolers.
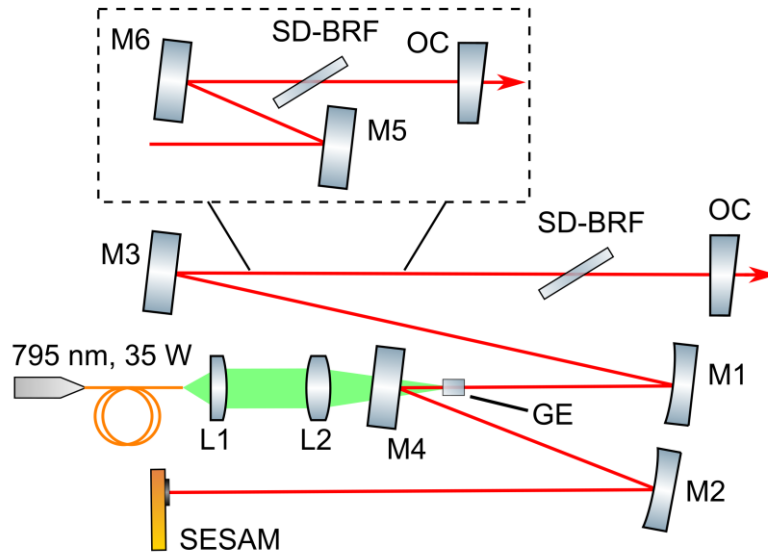
Fig. 40. Experimental setup for the diode-pumped mode-locked characterisation of Tm:Lu$_2$O$_3$ based on [221]. The optics in the dashed box were used when additional GDD was added to the cavity. The steeply diving birefringent filter (SD-BRF) was used later in mode-locked tuning experiments.

Self-starting mode-locked operation was initially realised at an output power of 227 mW under an incident pump power of 6.2 W. At this point the intracavity fluence on the SESAM was estimated to be 154 μJ/cm^2. By gradually increasing the pump power from this point, single pulse generation was maintained up to an output power of 423 mW. Increasing the pump power further triggered a transition to the multi-pulse

regime. Pulse durations as short as 299 fs were recorded at the maximum power for single pulse mode-locked operation. A corresponding optical bandwidth of 17.6 nm at a central wavelength of 2068 nm giving a TBP of 0.37. A fast photodiode was used to measure a pulse repetition frequency of 82.3 MHz. However, examining the RF spectrum showed *Q*-switching instabilities throughout the mode-locking region which could not be supressed.

Inserting a 2.7 mm thick, quartz SD-BRF (discussed in more detail in the Section 4.3) into the long arm of the cavity realised stable, *Q*-switching instability free mode-locked performance. The cause of this is thought to be due to the introduction of some additional SPM occurring within the filter and the addition of -718 fs^2 round trip dispersion from the quartz material. With the SD-BRF in the cavity and orientated to operate in the 1st order, the mode-locking threshold was found at an output power of 226 mW for an incident pump power of 7.1 W. The GE was measured to absorb approximately 40% of the incident pump light. However, the cavity configuration and quickly diverging pump beam meant it was impossible to accurately measure the transmitted pump power and reliably determine the value of absorbed pump power. As such, pump powers here are defined as incident pump power. Single pulse operation was maintained up to a maximum output power of 555 mW [Fig. 41(a)] with the laser emission tuned using the filter to 2081 nm [Fig. 41(b)]. At the maximum single pulse output power, a minimum pulse duration of 278 fs [Fig. 41(c)] was measured with a corresponding optical bandwidth of 17.1 nm, indicating near-transform-limited pulse durations with a TBP of 0.33. Confirmation of single pulse operation can be seen in the 50 ps span autocorrelation trace found in Fig. 41(d), while stable mode-locked operation was confirmed by the RF spectrum which shows a fundamental beat note at 82.25 MHz with an extinction ratio of 68 dBc [Fig. 41(e)]. This stability is further backed up with a 1 GHz span [Fig. 41(f)] showing no *Q*-switching instabilities and very little decay over the harmonic beat notes.
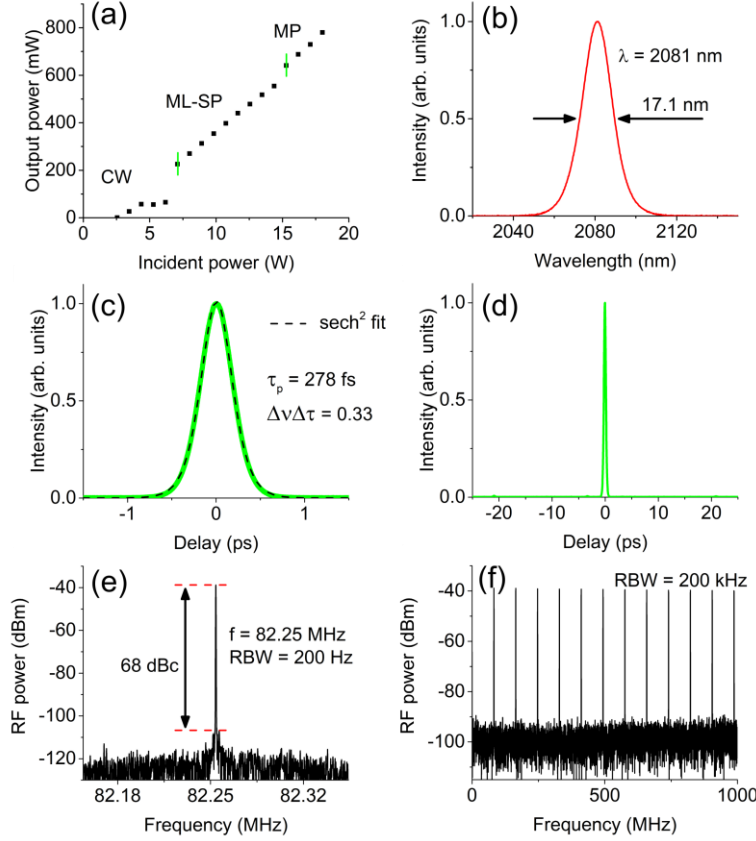
Fig. 41. (a) Power characteristics for mode-locked operation of the Tm:Lu$_2$O$_3$ laser in the six mirror configuration tuned to ~2080 nm. Optical spectrum (b), autocorrelation traces over 3 ps (c) and 50 ps (d) spans, and 200 kHz (e) and 1 GHz (f) RF spectra for pulses recorded at the single-pulse maximum output power of 555 mW.

Examining the variation of pulse duration with intracavity pulse energy (Fig. 42) shows an excellent fit with the $1/E_p$ relationship. The estimated total round-trip GDD of -2753 fs^2 is made up of four GTI mirror passes, the 5 mm long Tm:Lu$_2$O$_3$ gain element, and the 2.7 mm thick quartz SD-BRF. In this instance, all GDD values have been determined at 2080 nm except for the GTI mirrors where there is little variation in the value of introduced dispersion between 2065 nm and 2080 nm. The calculated SPM parameter of 1.05×10^{-7} W^{-1} is clearly much less than that found in the mode-locked experiments when using Tm:LuScO$_3$ and is primarily due to the larger waist inside the gain element. In the same manner as before, the nonlinear refractive index, n_2, for Tm:Lu$_2$O$_3$ around 2080 nm was calculated to be 10.3×10^{-16} cm^2/W. This value is slightly larger than that calculated in [234] and could be due to an inaccurate estimate of round-trip GDD present in the cavity. However, the required value of dispersion necessary to match the reported value of n_2 is unrealistically low at approximately -890 fs^2 given a calculated SPM parameter of 0.34×10^{-7} W^{-1}.
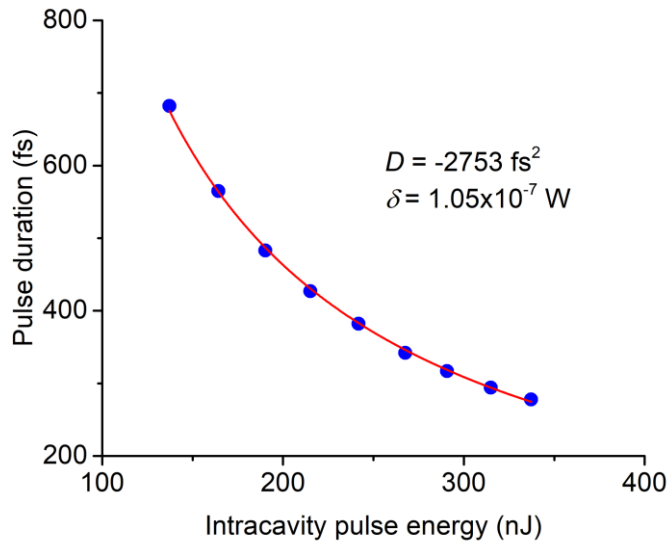
Fig. 42. Change in pulse duration with intracavity pulse energy (average output power) for the mode-locked Tm:Lu$_2$O$_3$. The red curve is a fit to $1/E_p$. δ is the SPM coefficient and D is the estimated total round-trip cavity dispersion.

When the source was tuned to operate around 2065 nm, it was found that pulse break up occurred at a much lower output power compared to that found when the source was tuned to around 2080 nm. At a central wavelength of 2064 nm the maximum single pulse output power was recorded as 198 mW, with corresponding pulse durations and optical bandwidth of 706 fs and 7.3 nm, respectively. This early transition into multi-pulse operation is believed to be the result of the marginally higher gain available around 2064 nm compared with that at 2080 nm for the given inversion level. In order to achieve higher output powers, more dispersion was introduced into the cavity with the placement of an additional GTI mirror (M5) in combination with another HR mirror (M6) into the long arm of the cavity. In this eight mirror configuration, slightly improved performance was realised with a maximum single pulse output power of 307 mW being achieved for an incident pump power of 16.2 W when operating in the 2nd order of the SD-BRF [Fig. 43(a)]. A minimum pulse duration of 730 fs was recorded at this output power, corresponding to an optical bandwidth of 6.8 nm at a central wavelength of 2065 nm. The optical spectrum and autocorrelation trace for the pulse can be found in Fig. 43(b) and Fig. 43(c), respectively. The increase in pulse duration found here can be attributed to the increase in GDD inside the laser cavity. Increasing the pump power beyond 16.2 W saw the laser fall out of mode-locked operation with stable mode-locking only being achieved again by lowering the pump power. Stable *Q*-switching instability free mode-locking was maintained from the mode-locking

threshold, at an output power of 244 mW, to the maximum output power as confirmed by examining the RF spectrum over a 1 GHz span with the fundamental beat note found at 82.27 MHz [Fig. 43(e) and Fig. 43(f)].
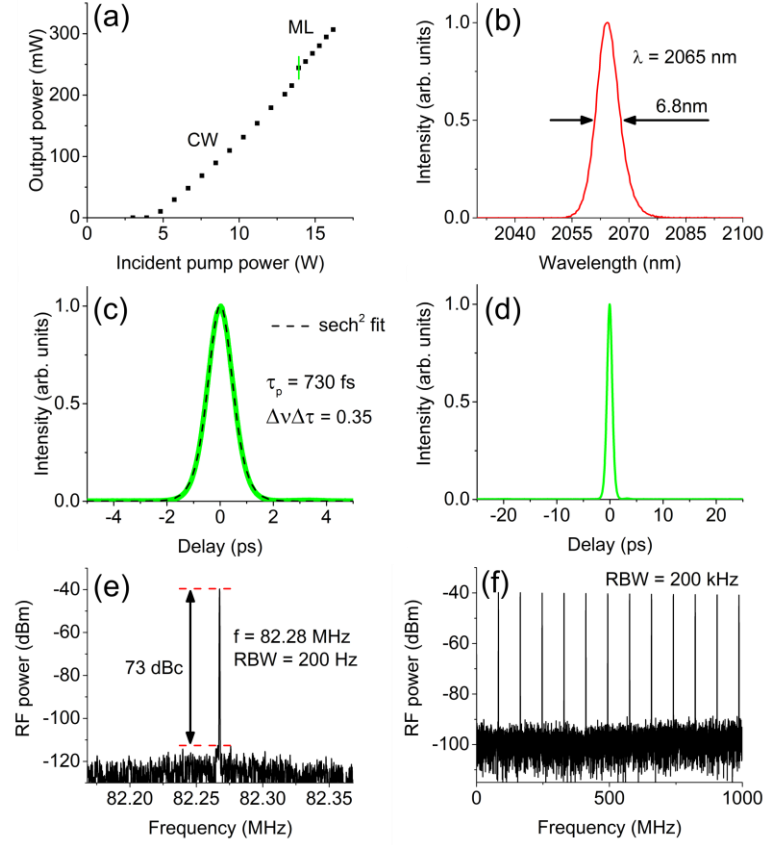
Fig. 43. (a) Power characteristics for mode-locked operation of the Tm:Lu$_2$O$_3$ laser in the eight mirror configuration tuned to 2065 nm. Optical spectrum (b), autocorrelation traces over 3 ps (c) and 50 ps (d) spans, and 200 kHz (e) and 1 GHz (f) RF spectra for pulses recorded at the single-pulse maximum output power of 307 mW.

4.2.1   Conclusions

Comparing the performances from the Tm:Lu$_2$O$_3$ mode-locked source when tuned to 2080 nm and 2064 nm, it is clear that the performance found at 2080 nm far exceeds that recorded at 2064 nm. The limitations in performance when tuned to 2064 nm are not fully understood as time did not allow for a complete study of the source's behaviour in this region. However, it is thought that the SD-BRF is fundamental in the pursuit of enhancing the performance of the source around 2060 nm as without the filter output powers of >400 mW and pulse durations of <300 fs were recorded, albeit with *Q*-switching instabilities. Further optimisation of cavity parameters (*e.g.*, output

coupling, dispersion, and SESAM waist size) and study of the laser could realise a stable, high output power, ultrashort pulse source around 2060 nm.

4.3   Tunable mode-locked pulses

As was shown previously, without any additional wavelength filtering a laser will emit around the highest gain peak of the chosen laser gain material at the specific inversion level. For the mode-locked Tm:LuScO$_3$ and Tm:Lu$_2$O$_3$ lasers presented earlier, these emission wavelengths were around 2094 nm and 2066 nm, respectively. However, it is possible to tune this emission wavelength to target an explicit application. For example, tuning around 800 nm from Ti:sapphire sources can be done to facilitate the use of different fluorophores in two-photon excitation microscopy, while in the 2–2.1 µm region this tuning would be better suited to, for example, targeting the gain peaks of high energy amplifier systems or for tuning into the anomalous dispersion regime of highly nonlinear fibres for enhanced efficiency SCG.

Wavelength tuning in ultrashort pulse lasers is predominantly achieved in one of two ways; a slit and prism pair combination or a BRF (Fig. 44). The slit and prism pair approach provides a fine level of control over not only the emission wavelength but also the optical pulse bandwidth and the level of GDD introduced into the cavity. By moving a slit of set width through the expanded beam, the emission wavelength can be tuned. Decreasing or increasing the slit width can control the optical bandwidth of the oscillating pulse which has the ultimate effect of increasing or decreasing the pulse duration. Finally the GDD can be tailored to give the best performance at this chosen wavelength and pulse duration by changing the separation distance or insertion depths of the prisms. While this approach seems ideal in its level of control and apparent ease of use, for any commercial system the slit and prism pair approach does present a challenge in robustness. That is not to say that it is impossible as the approach has been commercialised for tunable ultrashort pulse laser (*e.g.*, Coherent Mira), although these systems could not be described as compact. Furthermore, even in its more compact variation, two prisms and a mirror, the prism pair still introduces an extra four surfaces into the cavity. Each of these surfaces introduces a small percentage of loss and makes initial alignment more complicated.
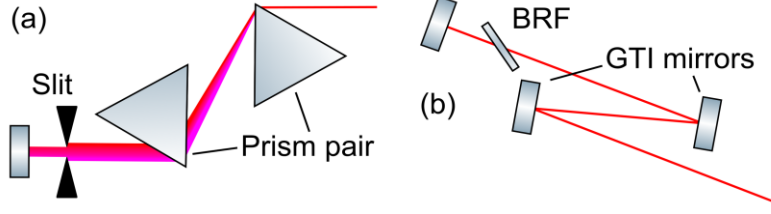
Fig. 44. Two techniques for dispersion compensation and spectral tuning in mode-locked laser sources; slit and prism pair (a), and BRF and GTI mirrors (b).

The alternate approach to tuning by using a BRF offers the possibility of a much more compact and robust setup. On its own it introduces just two extra surfaces into the cavity resulting in greatly reduced losses when compared with the prism pair. Clearly, the BRF on its own does not introduce any controllable dispersion compensation, as such the addition of highly reflective and robust dispersion compensation mirrors such as dielectric coated GTI mirrors would be required. However, the tolerances on these mirrors for low loss operation are much more accommodating compared with the prism pair meaning that alignment is faced without any significant complications.

With the aim of developing compact and robust sources the combination of a BRF and GTI mirrors is much more attractive than that of the slit and prism pair. It should be stated though, that a traditional BRF is not well suited for the tuning of ultrashort pulse lasers due to their, generally, narrow transmission bandwidths. Larger bandwidths are achievable by making the filter thinner, but one quickly approaches thicknesses that make such a solution impractical. A variation of the BRF better suited to CW tuning of broadband sources and mode-locked sources is that of the SD-BRF. The effect of cutting the birefringent material such that the optic axis dives into the filters surface, instead of running parallel to it as in a traditional on-surface BRF, provides a larger transmission bandwidth for a given plate thickness compared with a conventional BRF.

In this section the performance of conventional and modified BRFs in tuning mode-locked Tm:LuScO$_3$ and Tm:Lu$_2$O$_3$ lasers shall be presented. Modelled theoretical analysis of the BRFs are shown, in addition to a detailed introduction to the SD-BRF, in order to more clearly show the differences in the performance of the different types of filter.

4.3.1 Picosecond pulses from an on-surface birefringent filter

In the design of traditional, on-surface, BRFs the birefringent material is cut so that the optic axis runs parallel to the surface of the plate ($\theta = 90°$ in Fig. 45). Tuning of the

laser emission wavelength can be achieved by rotating the plate around the surface normal, changing the angle of rotation (α). Assuming the plate is inserted in the cavity at Brewster's angle ($\beta_e \approx 57°$ for quartz at 2.1 µm [237]), then the wavelength-dependent polarisation changes due to the material's birefringence induce Fresnel reflection losses at the plates surface for the s-polarised component of the beam. This causes a wavelength dependent transmission loss as the plate is rotated [219]. The thickness of the plate (t) defines the free spectral range (FSR) and the transmission bandwidth; as the plate thickness increases, the FSR and transmission bandwidth decrease. It is possible to model the FSR and transmission bandwidths by finding and analysing the eigenvalues of the Jones matrix for a full round trip of the filter [238–240], where the single pass is given by

$$
M_{BRF} = \begin{pmatrix} 1 & 0 \\ 0 & q \end{pmatrix} \begin{pmatrix} \sin\alpha_{eq} & \cos\alpha_{eq} \\ -\cos\alpha_{eq} & \sin\alpha_{eq} \end{pmatrix} \begin{pmatrix} 1 & 0 \\ 0 & e^{i\Theta} \end{pmatrix}
$$
$$
\times \begin{pmatrix} \sin\alpha_{eq} & -\cos\alpha_{eq} \\ \cos\alpha_{eq} & \sin\alpha_{eq} \end{pmatrix} \begin{pmatrix} 1 & 0 \\ 0 & q \end{pmatrix} . \tag{4.1}
$$
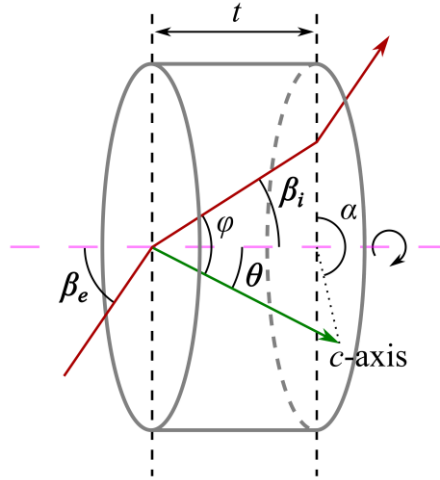
Fig. 45. Schematic illustration of a SD-BRF with light beam (red line) incident at Brewster's angle [240]. The optic axis (*c*-axis) is identified by the green line, while the pink dashed line indicates the surface normal. β_i, the internal Brewster's angle; θ, optic axis angle with respect to surface normal.

The first and last matrices here describe the transmission of the light entering and exiting the Brewster angled filter surfaces, where the parameter q is the Fresnel coefficient for the high loss polarisation, given as

$$q = \frac{2n}{(n^2+1)} . \tag{4.2}$$

The second and fourth terms are the rotation matrices that take the rotation angle of the filter to realign the axes of the calculation. To this end, the parameter α_{eq} becomes important as it describes the equivalent angle of rotation, taking the propagation of the beam through the plate into account. Whilst this does not have a significant effect in the case of the on-surface BRF, whereby the angle between the propagating beam and the optic axis (φ) remains the same, it does have an impact in the case of $\theta \neq 90°$ as shall be seen in the next section. α_{eq} is given by

$$\cos \alpha_{eq} = (\cos \beta_i \cos \theta \cos \alpha - \sin \beta_i \sin \theta) / \sin \varphi . \tag{4.3}$$

Finally, the third term in (4.1) examines the phase difference between the ordinary and extraordinary components of the beam as it passes through the birefringent plate. The phase change is given by

$$\Theta = f_b \frac{2\pi}{\lambda} \frac{\delta t}{\cos \beta_i} , \tag{4.4}$$

where δ is the difference in refractive index of the extraordinary and ordinary components of the beam, $i.e.$ $\delta = n_e - n_o$, and f_b is given by

$$\begin{aligned} f_b &= \cos^2 \theta \sin^2 \alpha \\ &+ \left(\cos \beta_i \cos \theta \cos \alpha - \sin \beta_i \sin \theta \right)^2 . \end{aligned} \tag{4.5}$$

As the gain material has no birefringence and is inserted into the cavity at right angle to the incident beam, it can be ignored when considering the Jones matrix for the full round trip of the cavity. And since we are envisioning a standing wave cavity, the full round trip Jones matrix for the cavity is then simply

$$M_{cavity} = M_{BRF} \times M_{BRF} . \tag{4.6}$$

Initial tunable mode-locked performance was demonstrated using the previously discussed diode-pumped Tm:LuScO$_3$ laser in Section 4.2. A 1.6 mm quartz BRF was inserted at Brewster's angle into the long arm of the cavity as shown in Fig. 34. With the cavity aligned to operate with four reflections off the GTI mirrors, the total round

trip GDD for the cavity, including an additional -438 fs^2 from the BRF (-137 fs^2/mm at 2095 nm [241,242]), was estimated to be -4578 fs^2. Crystal and SESAM waist sizes were unchanged from those used previously.

With a 1% output coupler and at 1.7 W of incident pump power (1.1 W of absorbed power) tunable picosecond pulses were recorded in the range of 2074–2104 nm [Fig. 46(a)] with a maximum output power of 55.4 mW around 2090 nm. For wavelengths shorter than 2088 nm, QML behaviour was observed, while stable mode-locked operation was observed for wavelengths longer than 2088 nm and up to 2104 nm. The autocorrelation trace and optical spectrum for the laser tuned to 2094 nm can be found in Fig. 46(b) and Fig. 46(c), respectively, indicating the generation of slightly chirped 2.06 ps pulses. It is believed that, due to the strong spectral filtering of the BRF, the laser operated in the non-soliton mode-locking regime, and, at such conditions, the pulse duration was mainly dictated by the relaxation dynamic of the SESAM.
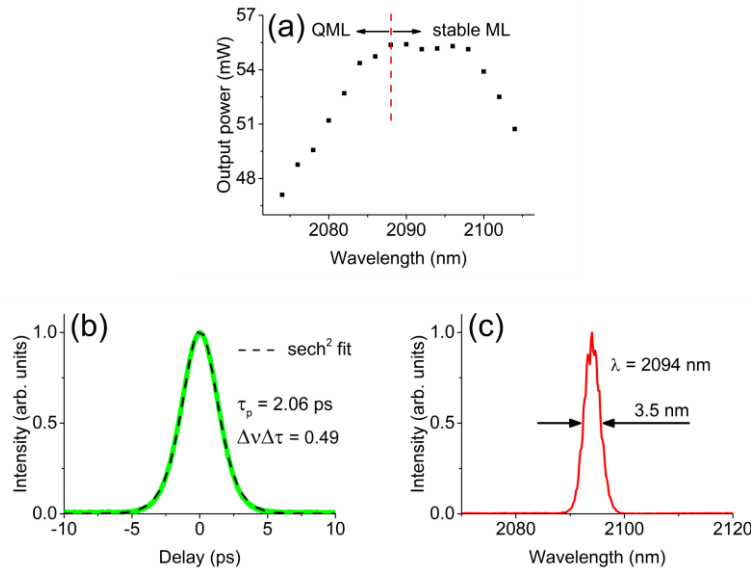
Fig. 46. (a) Tunability of the Tm:LuScO$_3$ laser during mode-locked operation. An autocorrelation trace and optical spectrum for the laser tuned to 2094 nm are shown in (b) and (c), respectively.

Modelling of this performance using the approach described above was undertaken to investigate the potential factors limiting the observed pulse durations, in addition to investigating what performance could be expected from a thinner filter with a larger transmission bandwidth. A MathCad script, originally written for modelling the tuning of a Cr:LiSaF laser around 850 nm [239], was adapted for this work to model the 1.6 mm thick BRF used and a much thinner 0.25 mm BRF at a wavelength of 2094 nm. In

both cases $\theta = 90°$, as is the case for an on-surface filter. The modelled transmission bandwidths for each BRF can be seen in Fig. 47.

Both filters offer a similar transmission contrast and it is clear to see that the 0.25 mm thick BRF has the largest transmission bandwidth, as one would expect [Fig. 47(a)]. As only a small percentage of introduced loss by the BRF is required to force the laser to operate at the intended wavelength and bandwidth, 1% or less, it is more practical to consider the 99% transmission bandwidths as was done by Stormont *et al*. As such, the 99% bandwidths for the 1.6 mm and 0.25 mm thick BRFs were calculated to be 4.6 nm and 28 nm, respectively [Fig. 47(b)]. The narrow bandwidth calculated for the 1.6 mm BRF gives some perspective as to just how strong the spectral filtering taking place when using said filter to tune the emission wavelength in the mode-locked source is.
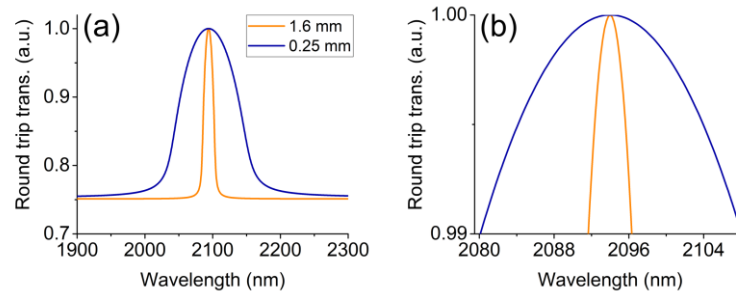
Fig. 47. (a) Modelled transmission curves of on-surface quartz BRFs of different thickness. (b) shows a zoomed in view detailing the 99% transmission.

Conclusions

Whilst it is difficult to say with certainty whether the pulse duration demonstrated is limited by the available optical bandwidth or some other mode-locking parameter, there is still some interplay between the filtering of the BRF and the recorded pulse durations. Due to this, one would expect much shorter pulses from the thinner 0.25 mm BRF as it would be able to support much larger optical bandwidths. Indeed, the largest optical bandwidth recorded from the mode-locked $Tm:LuScO_3$ source when operating without the BRF was 27.2 nm; this equated to a pulse duration of 170 fs (Fig. 36). This performance would suggest that sub-200 fs pulses could be achieved from a 0.25 mm BRF and that, due to the smooth gain profile of $Tm:LuScO_3$ around 2090 nm, a similar tuning range to that of the 1.6 mm filter may be realised. However, in reality the handling and mounting of such a thin plate calls into question the practicality of such a filter. As a result the performance of the thin on-surface BRF was not pursued further.

4.3.2 Broadly tunable femtosecond pulses using an enhanced birefringent filter

Despite not being well known by the wider laser community, the SD-BRF offers a number of potential advantages over its on-surface sibling discussed in Section 4.3.1. A single carefully designed filter could generate a larger FSR and transmission bandwidth for a given thickness compared with an on-surface BRF. In addition to this they also allow for a faster tuning rate, as well as providing a means to vary the optical transmission bandwidth through multiple separate orders of operation with different transmission bandwidths at a particular wavelength for different angles α. When such SD-BRFs are applied to broadband mode-locked lasers, it can be seen that the ability is gained not only to set the emission wavelength but also coarsely control the optical bandwidth and thus, potentially the pulse duration. These filters have been theoretically analysed and experimentally demonstrated in the past, with the primary focus of these reports involving the tuning of femtosecond NaCl colour centre [238] and Cr:LiSaF lasers [239,243], and the CW tuning of ultrabroad laser gain materials such as Ce:LiCAF, Ti:sapphire, Cr:ZnSe, and Fe:ZnSe [240]. There had been no reported demonstration of this enhanced filter in the tuning of ultrashort pulses in the mid-IR, however. With no fundamental limitation on the use of a SD-BRF for the tuning of a Tm^{3+}-doped sesquioxide laser, said filter could provide an excellent substitute for the on-surface BRF when trying to achieve broadly tunable femtosecond pulses.

In much a similar way to the modelling of the on-surface BRF, a SD-BRF was modelled to find optimal design parameters to provide the best balance between transmission bandwidth and transmission contrast for a target wavelength of 2090 nm. Past theoretical analysis of the SD-BRFs have aimed to provide parameters for broadband tunability. For instance, in [240] Demirbas proposed that the optic axis angle θ of 25° ± 2° is optimum for quartz, while Naganuma *et al.* state that, due to the minimal change in refractive index from 0.5 μm to 2 μm, a near 24° angle is suited for any required wavelength within the range. The optimal thickness of the plate, in terms of best achievable transmission contrast, increases in integer values defined by the optical path length and difference in phase of the ordinary and extraordinary components of the beam, such that

$$t = \lambda N \frac{\cos(\beta_i)}{\delta f_b} \,, \tag{4.7}$$

where N is referred to as the filter rank and is a positive integer value. Examining the effect that varying the optic axis angle and filter rank had on the performance of the filter lead to an optic axis angle of 24° and a thickness of 2.7 mm being chosen.

Fig. 48(a) shows the transmission curves for the first four orders of the SD-BRF. It can be seen that the 1st order, shown in red at a centre wavelength of 2090 nm for a rotation angle α of 28.2°, has the largest bandwidth, followed by the 2nd in green, the 3rd in blue, and the 4th shown in orange. All four orders provided a similar transmission contrast. The 99% bandwidths, as shown in Fig. 48(b), were calculated to be 28 nm, 14 nm, 9 nm, and 7 nm for the 1st–4th orders, respectively. Fig. 48(c) shows tuning spectra using the 1st order of operation. Tuning from 2028 nm to 2123 nm from only 1° of rotation can be achieved, giving a predicted tuning rate of 95 nm/° for this case.
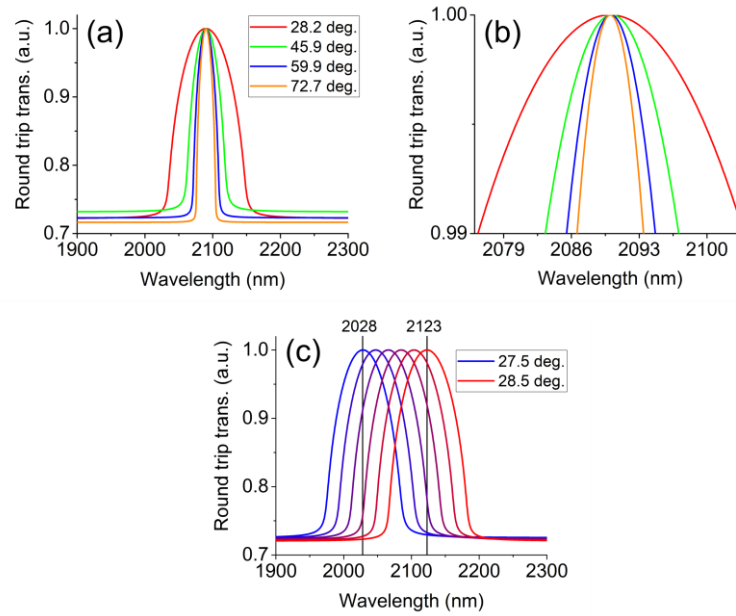
Fig. 48. (a) Modelled transmission curves for the first four orders of the SD-BRF at different angles α. A zoomed in view detailing the 99% transmission bandwidth is shown in (b). (c) Changes in transmission wavelength for the first order over 1° of rotation.

Tm:LuScO₃

Initial characterisation of the SD-BRF was performed in the CW regime with a diode-pumped six-mirror z-fold Tm:LuScO$_3$ laser similar to that discussed in previous chapters. In anticipation of moving into the mode-locked regime the cavity was set to operate in stability region II, however slight changes to the cavity alignment due to the replacement of the pump laser diode meant that the second waist on the HR at the short

end of the cavity now had a radius of 130 μm. In addition, the cavity waist inside the laser crystal had radii of 26 μm x 24 μm. The replacement laser diode was characterised and found to have a beam quality factor of 18 and 1.3 in the x and y directions, respectively. Using the same pump optics as those used previously, the pump waist radii were measured to be 54 μm x 22 μm.

With the SD-BRF inserted into the cavity at Brewster's angle and under 1.8 W of incident pump power at 793 nm (1.2 W absorbed power), output wavelength tuning extending from 1986 nm to 2140 nm was obtained (Fig. 49) using a 1% OC. From these data, it can be seen that all four SD-BRF orders have a very similar profile indicating that the orders were capable of supporting the same tuning range and that the BRF was operating as designed. It is believed that the tuning range here, as previously, is limited only by the available gain of Tm:LuScO$_3$ around 2.06 μm at the given pump power level.

Moving to the mode-locked regime involved firstly removing the SD-BRF and replacing the short arm end HR mirror with the same ion-implanted InGaAsSb quantum-well-based SESAM used previously. Once the SESAM was aligned, self-starting single pulse stable mode-locked operation was achieved. A minimum pulse duration of 173 fs (assuming a sech^2 intensity autocorrelation profile) was measured with an average output power of 128 mW. The pulse had a centre wavelength of 2093 nm and an optical bandwidth of 26.8 nm at FWHM.
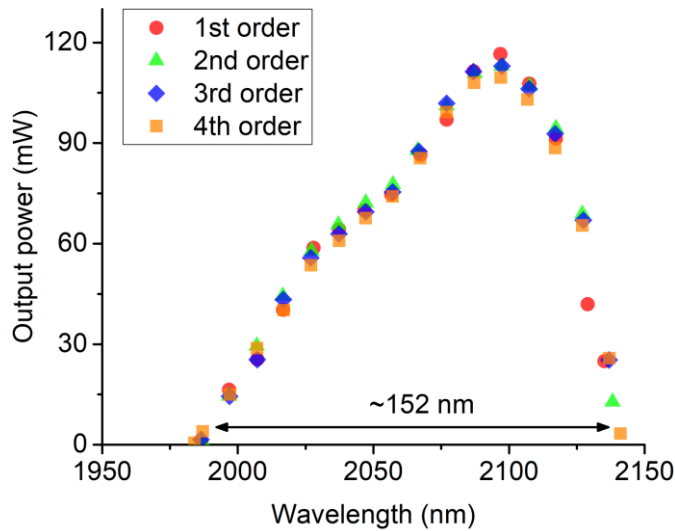
Fig. 49. CW tuning of the Tm:LuScO$_3$ laser over the first four orders of the SD-BRF.

The SD-BRF was reintroduced into the long arm of the cavity and rotated so as to operate in the 1st order. Under 2.6 W of incident pump power (1.8 W absorbed power) broadly tunable mode-locked operation was recorded. Pulse durations varying from 240 fs to 538 fs were generated over a tuning range of 2019–2110 nm [Fig. 50(a)]. It is believed that the variation of the pulse duration across the tunability range is predominantly due to the inversely proportional relationship between the pulse duration and the intracavity energy, and thus the average output power, found in the soliton mode-locking regime. Additionally, further increasing of the pulse duration in the 2030–2080 nm range could also be associated with the smaller modulation depth of the SESAM in that region compared to the 2.1 μm region. The shortest pulse duration of 240 fs was produced at an output power of 93 mW. Fig. 50(b) and Fig. 50(c) show the optical spectrum and intensity autocorrelation trace for a pulse recorded at 2090 nm, respectively. A pulse duration of 245 fs with a corresponding optical bandwidth of 19.6 nm was recorded, giving a TBP of 0.33 and indicating near-transform-limited pulse operation. In addition, monitoring of the autocorrelation traces over a 50 ps span showed no signs of multipulsing while clean RF spectra confirmed Q-switching instability free operation at a pulse repetition frequency of 114.3 MHz. This was found at all points throughout the tuning range. Mode-locked operation was self-starting, with stable and consistent performance maintained for a number of hours.

Rotating the BRF to operate in the 2nd order gave similar results to the 1st order in terms of tuning range and variation of pulse duration and output power with the wavelength. However, comparably longer pulse durations (349–685 fs) were recorded over the 2025–2114 nm tuning range with average output powers of between 36 mW and 63 mW [Fig. 50(d)]. The optical spectrum and autocorrelation trace for a pulse at 2095 nm shown in Fig. 50(e) and Fig. 50(f), respectively, provide a good point of comparison between the pulse durations and optical spectrum. This increase in pulse duration is presumed to be the result of lower output power (intracavity pulse energy). The narrower transmission bandwidth provided by the 2nd order of the SD-BRF could be an additional factor which limited optical bandwidth and duration of the generated pulses. As with the 1st order, the mode-locking stability was confirmed by examining widespan autocorrelation traces and RF spectra.
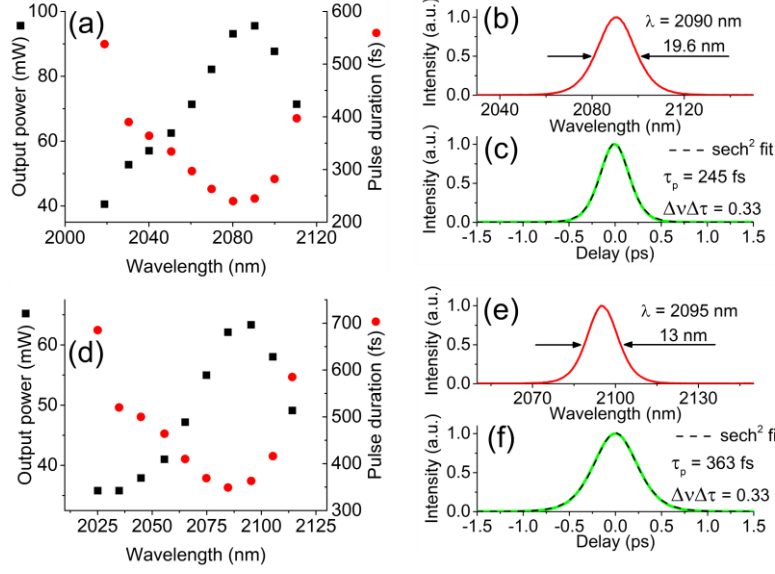
Fig. 50. (a) Tm:LuScO$_3$ mode-locked laser tuning characteristics for the 1st order of operation of the SD-BRF with the 1% output coupler. (b) and (c) show the optical spectrum and autocorrelation trace for a pulse recorded at 2090 nm, respectively. (d), (e), and (f) show the performance recorded when operating in the 2nd order of the SD-BRF using the 1% output coupler.

Increasing the output coupling to 2% resulted in higher average output powers but with a narrower tuning range and longer pulse durations. Operating in the 1st order, a tuning range of 2070–2102 nm was recorded, with the output power and pulse durations varying from 78 mW to 119 mW and 435 fs to 670 fs, respectively [Fig. 51(a)]. It can be seen that the pulse durations and output power followed a similar profile to that seen with the 1% OC, with the maximum output power and minimum pulse duration found around 2090 nm. Fig. 51(b) and Fig. 51(c) show the optical spectrum and intensity autocorrelation traces for a pulse recorded at 2090 nm, respectively. A pulse duration of 435 fs with an associated optical bandwidth of 11 nm were measured, giving a TBP of 0.33. Moving to the 2nd order with the 2% output coupler gave a similar tuning range of 2072–2108 nm, with output powers varying between 74 mW and 103 mW and near-transform-limited pulses ranging from a maximum pulse of 811 fs to a minimum pulse duration of 563 fs [Fig. 51(d)]. The optical spectrum and autocorrelation trace for pulses recorded near 2090 nm, shown in Fig. 51(e) and Fig. 51(f), respectively, show narrowing of the optical bandwidth and increase in the pulse duration when compared with the 1st order performance. This could again be the result of the optical filtering effect of the SD-BRF or it could be due to the lower observed output power like was seen when using the 1% OC. As with the 1% OC, clean RF spectra and widespan

autocorrelation traces confirmed stable single pulse mode-locked operation throughout the tuning range at a pulse repetition frequency of 114.3 MHz.

Only picosecond pulse durations were realised when operating in the 3rd order of the SD-BRF and using the 1% OC. A narrower tuning range than that recorded from the 1st and 2nd order was observed with relatively unstable operation. No mode-locked operation was achieved when operating in the 4th order of the SD-BRF. These results can be associated with the relatively narrow optical bandwidths of the SD-BRF at higher orders that could be preventing pulse spectral broadening and stable soliton mode-locking.
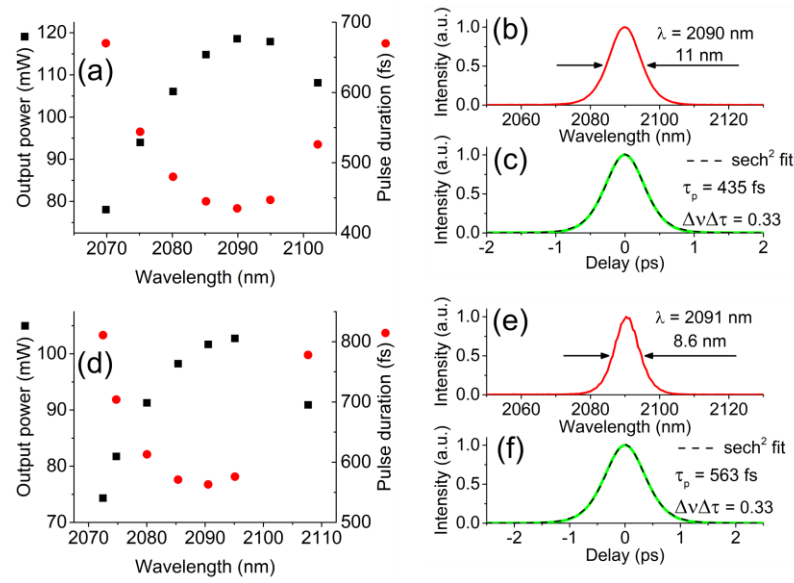
Fig. 51. (a) Mode-locked tuning characteristics using the 2% output coupler and operating in the 1st order of the SD-BRF. The optical spectrum and autocorrelation trace for a pulse recorded at 2090 nm are shown in (b) and (c), respectively. (d), (e), and (f) show the performance recorded when operating in the 2nd order of the SD-BRF using the 2% output coupler.

Tm:Lu$_2$O$_3$

As when studying the tunability of the Tm:LuScO$_3$ laser, tuning of the Tm:Lu$_2$O$_3$ laser using the SD-BRF was initially undertaken in the CW regime. The high power Tm:Lu$_2$O$_3$ laser cavity, shown in Fig. 40 in its six mirror configuration, was modified to operate in the CW regime by replacing the SESAM with a HR mirror. No other changes were made to the cavity configuration. With a 2% output coupler in use and under 16.2 W of incident pump power a maximum tuning range of 1903–2119 nm was recorded with the SD-BRF orientated to operate in the 4th order (Fig. 52). Unlike the

performance recorded when tuning the Tm:LuScO$_3$ laser, seen in Fig. 49, the tuning range for the Tm:Lu$_2$O$_3$ laser was found to strongly depend on which order of the filter was being used. The 4th order demonstrated continuous tuning over roughly 216 nm, while the 3rd order had a slightly shorter tuning range of 1915–2119 nm. Both orders closely followed the profile and range recorded when using a 1.6 mm on-surface BRF (not shown in Fig. 52). The 2nd and 1st orders had much shorter tuning ranges, with the 1st order unable to maintain continuous tuning. Continuous tuning from 1942 nm to 2117 nm was recorded when operating in the 2nd order, while non-continuous tuning from 1943 nm to 2095 nm was recorded for the 1st order.
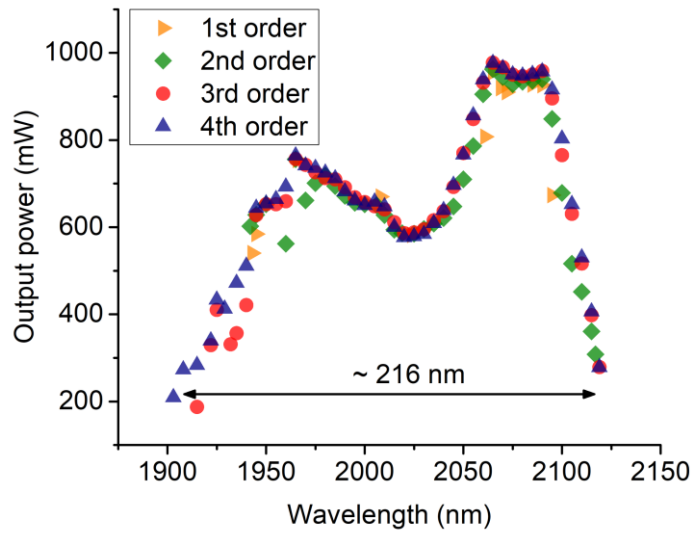
Fig. 52. CW tuning of the Tm:Lu$_2$O$_3$ laser over the first four orders of the SD-BRF. Continuous tuning was observed over the full range for the 3rd and 4th orders, while a reduced range was recorded for the 2nd order. Non-continuous tuning was observed when operating in the 1st order of the filter.

Closer inspection of the recorded emission lines shows small clusters or individual points around 1945 nm, 1966 nm, 2008 nm, and between 2061 nm and 2095 nm. These regions almost perfectly match peak like features found on the high inversion level gain and emission cross section plots for Tm:Lu$_2$O$_3$ [60]. This suggests that the transmission bandwidth of the 1st order is so wide that these main peaks define the laser emission wavelength until the filter is tuned far away from them. So far that a neighbour peak then immediately becomes dominant thus making the emission wavelength appear to jump despite a smooth continuous rotation of the filter. Higher orders, like the 3rd and 4th, have much narrower transmission bandwidths in comparison so are able to suppress these gain peaks and provide continuous tuning.

To confirm this working theory the jumps in emission were additionally investigated by inserting the SD-BRF into the previously developed Tm:Lu$_2$O$_3$ diode-pumped laser discussed in Chapter 3. With this source, smooth and continuous tuning between approximately 1950–2105 nm was found for all four orders. As the pump and cavity mode overlap in this earlier Tm:Lu$_2$O$_3$ laser is much better, it is safe to assume that the inversion level is lower. This has the effect of smoothing out the gain and reducing the prominence of the peaks around 1943/1963 nm and 2066/2090 nm, thus allowing for continuous tuning when operating in the 1st order of the SD-BRF. The inversion level in the high power Tm:Lu$_2$O$_3$ laser is thought to have been much higher than in the early Tm:Lu$_2$O$_3$ source, suggesting that the gain peaks are more likely to hamper continuous tuning.

Ultimately the inability to achieve broad and smooth CW tuning from the SD-BRF raised questions as to how successful any tuning during mode-locked operation would be. Indeed, with the SESAM placed back in the cavity and the filter orientated to operate in the 2nd order, tunable mode-locked pulses were only realised in a narrow band immediately around 2099 nm. Rotating to the 1st order found a better tuning range of 2060–2090 nm. However, this range was found to depend on the applied pump power. Fig. 53 shows the recorded tuning ranges for pump powers of 6.2 W, 8 W, 9.8 W, and 11.6 W. Continuous tuning ranges of 2069–2093 nm, 2071–2093 nm, and 2073–2091 nm were recorded for pump powers of 8W, 9.8 W, and 11.6 W, respectively.
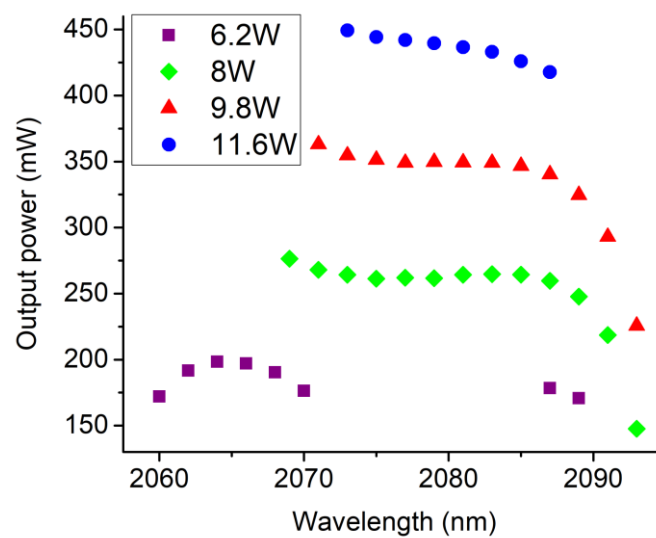
Fig. 53. Mode-locked tuning ranges of the Tm:Lu$_2$O$_3$ laser operating in the 1st order of the SD-BRF for different applied pump powers.

For higher pump powers, wavelengths less than 2070 nm saw multi-pulsing behaviour, while at lower pump powers only CW emission was recorded between 2070 nm and 2085 nm. When trying to tune beyond 2090 nm only CW emission around 1940 nm was observed. This behaviour can again be explained be examining the gain profile of $Tm:Lu_2O_3$. At lower inversion levels the peaks around 2066 nm and 2090 nm are at similar levels. As the inversion level is increased, the gain peak around 2066 nm increases at a higher rate than the peak around 2090 nm. This higher gain around 2066 nm is enough to increase the pulse energy beyond the multi-pulsing threshold. Conversely, at lower pump powers there is not enough gain and intracavity power to allow for stable mode-locked operation. The CW emission around 1940 nm when trying to tune beyond 2090 nm is due to the filters inability to fully suppress the considerable gain at the emission peak.

Stable, *Q*-switching instability free mode-locked operation was confirmed throughout the tuning ranges by monitoring the RF spectra. Clean 1 GHz span spectra were recorded for all pump powers and fundamental beat notes of 82.25 MHz were found in all instances. Exemplar optical spectra and autocorrelation traces over the four different pump powers can be seen in Fig. 54. The optical spectrum and autocorrelation trace for a pulse tuned to 2066 nm under 6.2 W of pump power can be found in Fig. 54(a) and Fig. 54(b), respectively. At this wavelength and pump power, the FWHM optical bandwidth of the pulse was measured to be 7.4 nm whilst the corresponding pulse duration was calculated to be 679 fs (assuming a $sech^2$ intensity autocorrelation profile). Similar profiles for the optical spectra and autocorrelation traces for pump powers of 8 W, 9.8 W, and 11.6 W can be found in Fig. 54(c) and Fig. 54(d), Fig. 54(e) and Fig. 54(f), and Fig. 54(g) and Fig. 54(h), respectively. At these pump powers the pulses shown centre on 2081 nm. The minimum pulse duration of 315 fs was found under 11.6 W of pump power at a centre wavelength of 2073 nm. The corresponding optical bandwidth of 16.2 nm, indicates a TBP of 0.36. Due to the relatively flat power profile found when tuning between approximately 2070 nm and 2085 nm at higher pump powers, there is little in the way of variation in pulse duration. Indeed at 8 W pump power pulse durations were found to only vary between 489 fs and 598 fs over the spectral tuning range of 2071–2085 nm. Beyond 2085 nm the pulse duration increases rapidly as the output power (intracavity pulse energy) decreases. Similar performance is found when examining the pulse durations recorded for 9.8 W and 11 W, with the pulse durations varying from 377 fs to 456 fs and from 315 fs to 368 fs for each respective pump power.
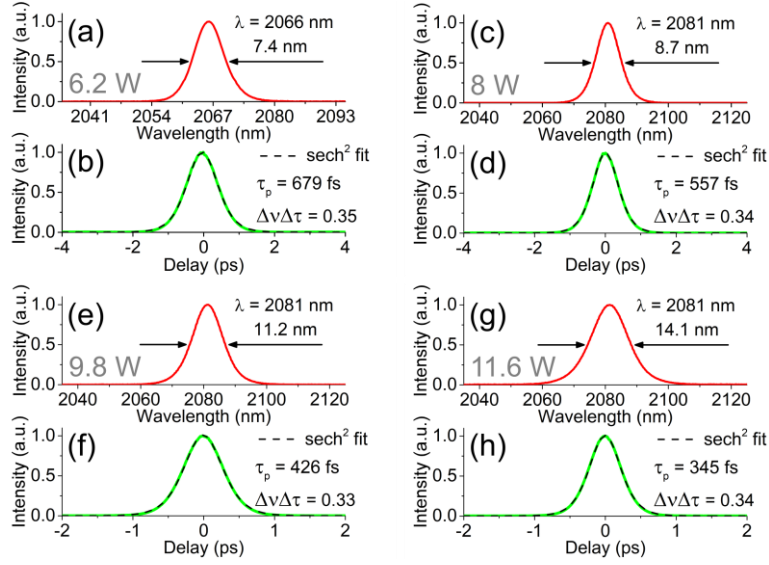
Fig. 54. Exemplar optical spectra and autocorrelation traces recorded when spectrally tuning the mode-locked Tm:Lu$_2$O$_3$ source at pump powers of 6.2 W, (a) and (b); 8 W, (c) and (d); 9.8 W, (e) and (f); and 11.6 W, (g) and (h).

No mode-locked operation was found when operating in the 3rd and 4th orders of the SD-BRF. It is believed that this shortcoming can be explained using the same approach as discussed in the previous section; that the narrow optical bandwidths supported by the higher orders could be preventing pulse spectral broadening and stable soliton mode-locking. Despite the limited tunability recorded when operating in the 2nd order in this cavity configuration, slightly improved tunability around 2065 nm was found with the introduction of an additional GTI mirror and HR mirror. In this eight mirror configuration stable single pulse, *Q*-switching instability free, mode-locked tuning from 2062–2067 nm was recorded for 16.2 W of incident pump power. Over this tuning range, output powers and pulse durations were recorded to vary from 278 mW to 245 mW, and 840 fs to 937 fs, respectively. Whilst this performance, in regards to pulse duration and output power, was poorer than that found in the six mirror configuration around 2080 nm, it would be well suited to seed Ho:YLF amplifiers around 2060 nm where the narrow gain bands of Ho^{3+}-doped laser gain materials are better suited to longer pulse durations. The performance found around 2080 nm when using the six mirror cavity configuration, whilst superior to the eight mirror performance, is unfortunately positioned such that it would unsuitable to seed existing Ho^{3+}-doped amplifiers. At 2080 nm though the source would clearly be suited to seed an amplifier based on Tm:Lu$_2$O$_3$. An amplifier based on the same laser gain medium as the seed means that the broad and relatively smooth gain peak present with Tm:Lu$_2$O$_3$ around 2050–2100 nm that allowed for the generation of such short pulses in the first place

would easily accommodate the full pulse packet for further amplification. This would be the objective for an upcoming investigation into ultrashort pulse amplification discussed in Chapter 5.

Conclusions

When considering the performance recorded for Tm:LuScO$_3$, it can be seen that the SD-BRF can be used as a means to not only set the emission wavelength but also coarsely control the pulse duration of mode-locked pulses. Indeed, pulse durations of 245 fs, 363 fs, and 1 ps have been experimentally demonstrated around 2090–2095 nm for the 1st, 2nd, and 3rd orders, respectively. It was quite clear that the pulse durations increase and the corresponding optical bandwidths decrease with the higher orders. However, it is difficult to separate the SD-BRF narrowing effect from the effects of lower intracavity pulse energy when explaining the reduced bandwidth recorded with higher orders of the filter. It is believed that stable operation could be realised with higher orders but that the laser cavity parameters such as beam waists and dispersion would have to be additionally tailored for such mode-locking regimes.

Based on the demonstrated performance, it can be concluded that the mode-locked Tm:LuScO$_3$ laser could be used as a seed source for existing Ho^{3+}-doped amplifiers in the 2050–2090 nm range. In particular, the >100 mW average power output level and ~570 fs pulses ($\Delta\lambda \approx 8.5$ nm) achieved with the 2% output coupler and the 2nd order of the BRF would be particularly suitable for the narrow gain bands of Ho:YAG at 2090 nm. Additionally, when using the 1% output coupler, the gain peaks of Ho:YLF around 2050/2060 nm can be reached as well with an average mode-locked power of >50 mW.

In regards to the characterisation of the SD-BRF using Tm:Lu$_2$O$_3$, the picture is not so clear. Once again the SD-BRF has shown that such a filter can be used to tune mode-locked pulses over a broad range in the 2 μm region whilst maintaining sub-picosecond pulse durations. The performance achieved with the Tm:Lu$_2$O$_3$ laser when compared with that achieved with Tm:LuScO$_3$ highlights the importance of choosing an appropriate gain material when trying to implement this technique, however. For Tm:LuScO$_3$, as the inversion level increases there is very little change in the profile of the gain peak around 2100 nm. This allows the wide transmission bandwidth of the low order of the SD-BRF to continuously tune without hindrance. In contrast, and as previously discussed, the separate peaks in the Tm:Lu$_2$O$_3$ gain profile at ~2065 nm and ~2090 nm become more pronounced as the inversion level increases. It is believed that

this is the main limiting factor when explaining the reduced mode-locked tuning range. Much broader mode-locked tuning has been demonstrated in the past from $Tm:Lu_2O_3$ by using a slit and prism [234]. This would suggest that the use of the SD-BRF as a compact and robust means to spectrally tune mode-locked laser sources should be addressed on a case by case basis, considering the sources gain profile and the range of wavelength tuning required.

5   Ultrashort pulse amplification

The direct generation of ultrashort pulses in the 2 μm region with the power levels required to be practically useful in applications such as materials processing, stand-off long distance spectroscopy, or SCG is often not possible. Instead, MOPA systems, as discussed in Section 2.4, are employed to boost the power of a seed with predefined spectral and temporal properties to the desired levels. Current solid-state laser amplifiers used to attain the required powers tend to utilize Ho^{3+}-doped gain media such as Ho:YAG and Ho:YLF. Whilst the performance of these gain media have been widely reported in the past, they are not well suited for the amplification of ultrashort pulses in the hundreds of femtoseconds to few picoseconds pulse duration regime. The narrow gain bands around 2090 nm (Ho:YAG) and 2050/2060 nm (Ho:YLF) are better suited for the amplification of pulse durations in the pico- and nanosecond regime. In order to fully amplify the broad spectrum of ultrashort pulses, the amplifier gain medium should have equally broad gain in the wavelength region of interest. An approach that circumvents any mismatch in seed and amplifier gain is to utilize the same laser gain medium for both the seed oscillator and the amplifier. With excellent thermo-mechanical properties and broadband gain in the 2050–2090 nm range, the Tm^{3+}-doped sesquioxide $Tm:Lu_2O_3$ is well suited in this regard.

This chapter will cover two separate investigations into the amplification of femtosecond pulse trains from diode-pumped Tm^{3+}-doped sesquioxide seed sources. Firstly, a collaborative proof-of-concept experiment undertaken at Heriot-Watt University which used the diode-pumped mode-locked $Tm:LuScO_3$ laser discussed in Chapter 4 as a seed source for a Ho:YAG slab amplifier. Secondly, the in-house evaluation of $Tm:Lu_2O_3$ as an amplifier gain medium for amplifying the power of the femtosecond pulse $Tm:Lu_2O_3$ seed source is covered.

5.1   Ho:YAG narrow bandwidth amplifier

The purpose of this collaborative experiment between Heriot-Watt University and Fraunhofer CAP was to evaluate the early performance of a newly created Ho:YAG slab amplifier and to investigate the feasibility of using a diode-pumped mode-locked Tm^{3+}-doped sesquioxide laser as a seed source in lieu of a commercially available ultrashort pulse 2 μm fibre laser. This work was performed at Heriot-Watt University.

5.1.1 Slab amplifier setup

A 55 mm long, 10 mm × 1.5 mm in aperture 0.75 at.% Ho^{3+}-doped YAG slab crystal, mounted between two mains-water-cooled copper blocks, formed the amplifier gain element (AGE) within the amplifier setup as depicted by that contained with the dashed box in Fig. 55. This slab was pumped by a diode-pumped Tm:YLF slab laser, developed by the group at Heriot-Watt, capable of emitting a maximum of 340 W at a centre wavelength of 1908 nm, matching the main absorption band of Ho:YAG [244]. Pump light was focused to waist radii of 2.7 mm and 0.1 mm in the x and y directions, respectively, using two AR coated lenses of focal length 228 mm (L5) and 114 mm (L6), while a silver mirror (M6) provided beam steering control. The positions of the focusing lenses and amplifier gain element were optimised by constructing a cavity around the Ho:YAG slab and optimising the CW laser performance. As this optimisation of the pump optic setup was undertaken prior to the commencement of the collaborative work it will not be discussed.
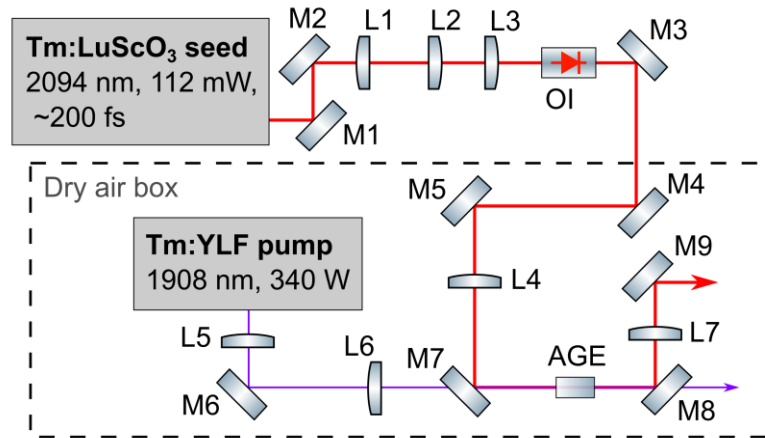
Fig. 55. Ultrashort pulse Tm:LuScO₃ seed and Ho:YAG amplifier setup used at Heriot-Watt University. The Tm:YLF slab pump laser and Ho:YAG amplifier were contained within a windowed housing (dashed line) purged with dry air.

Two dielectric mirrors, HR coated for 1760–2250 nm at a 45° angle of incidence (M4 and M5), were used to direct and steer the seed beam towards the amplifier gain element. The lens L4 was used to focus the seed beam to a waist radius closely matching that of the pump in the vertical direction. During the amplifier experiments this lens was changed between a 200 mm spherical lens, a 200 mm cylindrical lens, and a spherical doublet pair with an equivalent focal length of ~136 mm. Simulations performed by the Heriot-Watt group found that a hypothetical cylindrical lens of focal length 136 mm would provide a reasonably good overlap with the 0.1 mm pump beam

radius in the vertical direction. A spherical lens of equivalent focal length was calculated to provide a waist of approximately 0.1 mm in both the x and y directions.

After the focusing lens, the seed and pump beams were combined using a dichroic mirror (M7; HR 2100 nm and AR 1900 nm at 45°) and directed towards the Ho:YAG slab. A second dichroic (M8) then separated the two beams, directing the now amplified seed through a collimation lens (L7) and off another 45° HR coated mirror (M9) sending the beam towards the diagnostic equipment. Everything within the dashed box shown in Fig. 55 was placed inside a dry air box. This was done to maintain the performance of the Tm:YLF pump laser.

5.1.2   Tm:LuScO$_3$ seed source

The ultrashort pulse seed source provided by Fraunhofer CAP used in these collaborative experiments was to be based on the diode-pumped tunable mode-locked Tm:LuScO$_3$ source discussed in Section 4.3.2. Capable of average output powers of ~120 mW and pulse durations of ~400 fs when tuned to 2090 nm, the source would be well suited to seed the Ho:YAG amplifier and to investigate the amplification of such ultrashort pulses. The addition of the SD-BRF would not only allow for targeting of the Ho:YAG gain peaks, whilst allowing for pulses with longer durations/narrower optical bandwidths, but would also define a polarisation for the seed source; this drastically reduces the loss that would be experienced by the normally randomly polarised seed beam on encountering an optical isolator. As the isolator is a key component required to maintain performance of the seed oscillator and protect it from any amplified signal that is reflected back along the beam path, it would be ill advised to go without it.

In the process of rebuilding the laser source using more robust optical mounts for transportation, the failure of a pump laser diode and subsequent cracking of the laser crystal set back the planned delivery date of the source considerably. Unfortunately, this meant that in order to get the source installed at Heriot-Watt in as timely a manner as possible the implementation of the filter was not successfully completed. Issues faced when trying to achieve reliable mode-locking with the BRF in place could not be resolved. Ultimately this left the source more comparable to that discussed in Section 4.1; devoid of the SD-BRF, randomly polarised and producing around 113 mW average output power, with pulse durations of approximately 200 fs at a central wavelength of 2093 nm and a repetition frequency of 115 MHz. Whilst this would still be suitable for a proof-of-concept investigation, it did not represent the ideal seed source first envisaged.

5.1.3 Amplified pulses near 2093 nm

With the Tm:LuScO$_3$ ultrashort pulse seed source delivered and installed, reshaping and steering of the beam from the laser was required for it to match the pump waist within the slab amplifier. Two 45° HR coated dielectric mirrors (M1 and M2) placed directly after the output of the laser provided steering of the beam and directed it towards the reshaping optics. A telescope made up from a 150 mm focal length spherical lens (L1) and two cylindrical lenses, f_x = 100 mm (L2) and f_y = 200 mm (L3) reshaped and collimated the slightly astigmatic beam. After passing through the AR coated optical isolator (OI), a 45° HR coated dielectric mirror (M3) directed the beam through an AR coated window into the dry air box containing the amplifier. Mainly due to losses of the randomly polarised light on the optical isolator, the incident seed power on the amplifier gain medium was measured to be 57 mW.

Experiments began by passing the seed beam through the Ho:YAG slab with no lens in place to focus the seed. No measurable amplification was detected. Next, a 200 mm spherical lens was placed in the position of L4 and amplification of the signal was measured after 63 W of incident pump power was applied. A maximum amplified power (P$_{out}$ − P$_{seed}$) of 220 mW was measured for a pump power of 218 W. The spherical lens was then swapped for a cylindrical lens of equal focal length orientated to focus in the vertical direction. In this configuration a lower amplified power of 89 mW was recorded for the same applied pump power. Finally, a spherical doublet pair (f = 228 mm and f = 341 mm) with an equivalent focal length of approximately 136 mm was used to focus the seed beam. The position of the lens was optimised for maximum amplified signal and an amplified power of 430 mW was measured for an applied pump power of 218 W. Increasing the pump power further to the maximum of 280 W saw a maximum amplified power of 480 mW. In terms of the total output power from the amplifier, this equated to 540 mW and a gain of approximately 10 (Fig. 56).

Optical spectra of the amplified pulses were recorded at pump powers of 0 W, 44 W, and 125 W. Examining these spectra in Fig. 57, one can compare them to the incident seed pulse shown in Fig. 57(a). With no applied pump power the optical spectra was found to have significant dips in the profile at wavelengths near 2090 nm and 2097 nm [Fig. 57(b)]. These wavelengths correspond to prominent gain peaks for Ho:YAG and, due to the quasi-three level system found in Ho^{3+}-doped gain media, feature some degree of absorption meaning that these dips are most likely caused by absorption of the seed by the amplifier gain element. When the pump power was increased to 44 W these dips were seen to be replaced with small peaks, as seen in Fig. 57(c). In addition to

these small peaks, the optical bandwidth of the pulse can be seen to have narrowed from a FWHM of 23 nm for the incident pulse to 15 nm for the amplified pulses (assuming a sech^2 fit). This narrowing of the optical spectrum continues as the pump is increased to 125 W [Fig. 57(d)]. At this pump power the bandwidth of the optical spectrum has decreased to 12 nm, whilst the peaks at 2090.7 nm and 2097 nm have grown; the 2090.7 nm peak quite considerably. This reduction in optical bandwidth is due to the phenomenon of gain narrowing, whereby the centre of the broad optical spectrum experiences more gain than the wings. In the case of a seed pulse with a much narrower optical spectrum, a few nanometres for example, one would not expect to see such narrowing as the pulse would be fully amplified. In this scenario, this narrower pulse would be able to fully utilise the gain that can be seen near 2091 nm.
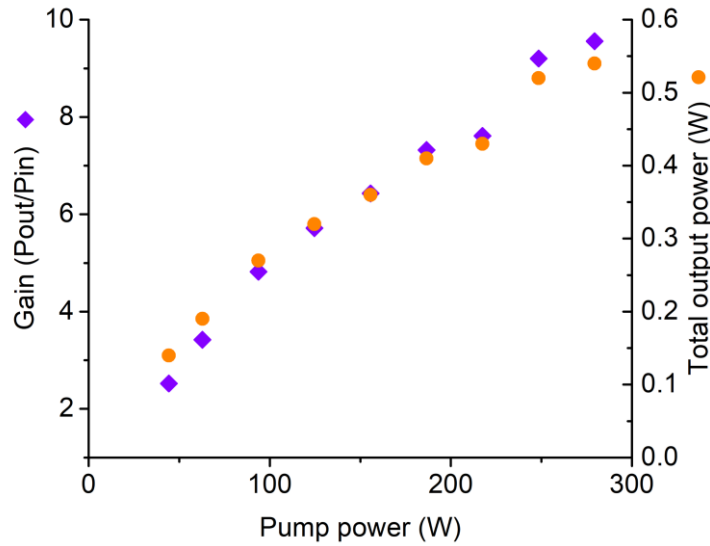
Fig. 56. Gain and total amplifier output power characteristics from the Ho:YAG slab amplifier as a function of incident pump power for 57 mW of seed power.

In the absence of an autocorrelator, bandwidths of the recorded optical spectra were used to infer a pulse duration assuming a TBP of 0.33. This TBP was found to be consistent for the Tm:LuScO$_3$ seed laser when it was operating in the labs at Fraunhofer. However, it is appreciated that some dispersion would be expected from the various lenses and the Ho:YAG slab meaning that the post-amplifier pulse durations are rough approximations only. Following this assumption, pulse durations were estimated to vary from 210 fs for the seed pulse to around 400 fs for the amplifier output pulse at 125 W pump power. It is expected that further narrowing of the optical spectrum and inferred increasing of the pulse duration would have been recorded for

higher pump powers. Due to the requirement of the dry air box at higher pump powers though, it was impossible to redirect the beam towards the spectrometer when operating beyond 125 W pump power.
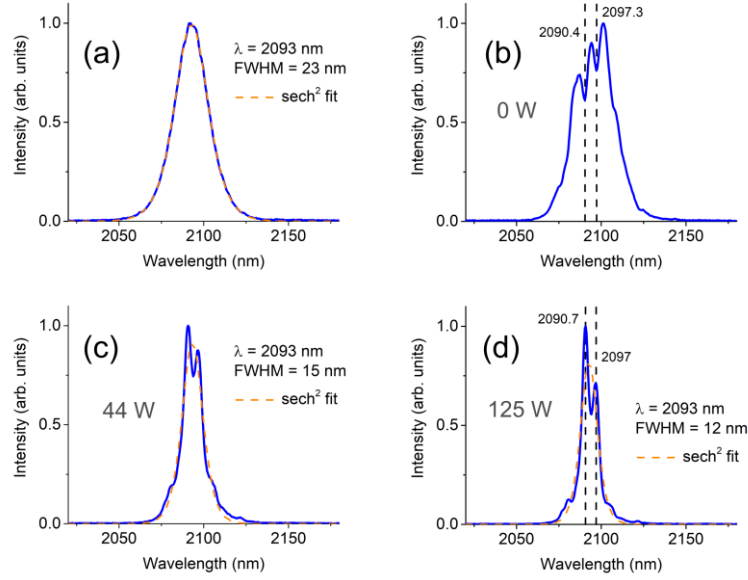
Fig. 57. Optical spectra of the pulse recorded before the amplifier (a) and after the amplifier at pump powers of 0 W (b), 44 W (c), and 125 W (d).

5.1.4   Conclusions

While a gain of 10 is reasonable it is believed that considerably more gain could be achieved through optimisation of the amplifier setup. Considering the substantial mismatch in pump/seed overlap in the horizontal direction within the amplifier gain element when using the spherical doublet pair focusing lens, there is only a small fraction of the applied pump power that is deemed "useful" to amplification. To utilise this unused pump volume a multi-pass zig-zag setup would need to be employed. Alternatively, pre-amplification of the low power seed source in combination with a cylindrical focusing lens would provide a better overlap with the pump beam in the horizontal direction whilst increasing the fluence so as to match that achieved when using the spherical doublet pair. Indeed, a pre-amplifier based on a Tm:fiber pumped Ho:YAG rod had initially been planned for the system but time constraints prevented this from being realised. This Ho:YAG rod has since been developed into a *Q*-switched seed source by the group at Heriot-Watt and amplification experiments using the Ho:YAG slab amplifier have continued. Such nanosecond pulses are clearly better

suited to the narrow gain peaks of Ho:YAG, though the gain around 2091 nm is still enough to support the complete amplification of picosecond pulses.

As a proof-of-concept investigation and given the time constraints, this collaboration should be classed as a success and will undoubtedly lead to further high energy joint experiments between Heriot-Watt University and Fraunhofer CAP in the future.

5.2   Tm:Lu$_2$O$_3$ femtosecond pulse amplifier

Following the collaboration with Heriot-Watt University, work to develop a system capable of fully amplifying femtosecond pulses in the 2–2.1 μm region within Fraunhofer began. This system would not seek to reach such high gain available from the likes of the Ho:YAG slab amplifier, instead it would be more of a pre-amplifier "power booster" based on a MOPA configuration. The arbitrary goal set for this amplifier system would be 1 W of average power and a pulse energy of 10 nJ.

Whilst the Tm:LuScO$_3$ seed source, having now been returned to Fraunhofer and successfully demonstrating tunable femtosecond pulses once again, had proved itself more than capable of generating the desired femtosecond pulses, the gain material is not well suited to fulfil the role of the amplifier gain material. To reiterate what has been said earlier in this chapter; in order to fully amplify the broad spectrum of ultrashort pulses, the amplifier gain medium should have equally broad gain in the wavelength region of interest. This would mean that Tm:LuScO$_3$ would also need to be used in the amplifier. The use of Tm^{3+}-doped LuScO$_3$ in the amplifier is primarily limited by two factors; the gain materials availability and its low thermal conductivity restricting the use of high power pump sources. To the best of the authors knowledge, no commercial route currently exists to acquire Tm:LuScO$_3$ gain elements. Furthermore, having already damaged a laser crystal with only 4 W of pump radiation, there were concerns that pump powers on the order of the tens of watts required to produce significant gain would result in considerable damage to the gain element. The Tm^{3+}-doped sesquioxide laser gain medium Tm:Lu$_2$O$_3$ counters both of these limitations.

As was shown in Section 4.2, the high thermal conductivity of Tm:Lu$_2$O$_3$ meant that high power pump sources could be used without increased risk of damaging the laser gain element. In addition, the commercial availability of ceramic gain media means that Tm:Lu$_2$O$_3$ gain elements for the amplifier could be sourced. Considering these points in combination with the previously discussed demonstration of the high average power mode-locked Tm:Lu$_2$O$_3$ laser, one makes a compelling case for a MOPA system based

on Tm:Lu$_2$O$_3$. An alternative option would be to use Tm:Lu$_2$O$_3$ as the amplifier gain media but use the Tm:LuScO$_3$ femtosecond laser tuned to ~2060–2080 nm as the seed source. However, in this wavelength range the tunable femtosecond Tm:LuScO$_3$ source was only able to generate output powers in the range of 71–106 mW. This is significantly less than that recorded from the mode-locked Tm:Lu$_2$O$_3$ laser source when tuned over the same range. As such, it was decided that a seed oscillator and amplifier both based on Tm:Lu$_2$O$_3$ would provide the best route to success.

5.2.1   Spectroscopic evaluation of the amplifier

Investigations into the use of Tm:Lu$_2$O$_3$ as an amplifier gain medium began by examining the luminescence spectrum under different pump intensities. In order to give the best chance of success, a high beam quality pump source in the form of a commercial Raman shifted Er:fibre laser was chosen. With a maximum output power of 30 W, an M^2 beam quality factor of 1.2, and emitting at 1620 nm, this source would in-band pump the $^3F_4 - {}^3H_6$ lasing transition and provide the best possible overlap with the seed in the gain element. The output from the Raman laser was collimated at the end fibre facet by a factory installed lens assembly, resulting in a ~4.4 mm diameter beam. The beam was then focused into the 10 mm long, 6 mm × 3 mm aperture AR coated 1.5 at.% Tm^{3+}-doped Lu$_2$O$_3$ ceramic amplifier gain element (AGE) using a 250 mm focal length lens. Waste heat was extracted from the gain element by mounting it between two water-cooled copper blocks maintained at 20°C, using indium foil to ensure good thermal contact. A 2 inch diameter lens with a focal length of 60 mm placed behind a 1.65 μm silicon substrate longpass filter was used to collect the luminescence and couple it into a multimode fibre that was connected to a high resolution optical spectrum analyser. The luminescence spectra for pump powers of 0.5 W, 2.2 W, 4 W, and 5.5 W can be seen in Fig. 58.

As one would expect, the general profile of the emission spectrum recorded is very similar to that reported in the past [245]. Peaks between 1760 nm and 1820 nm line up well with features recorded in previously published results, as do the main emission peaks at 1943 nm and 1965 nm. The effect of atmospheric water absorption can be see between approximately 1820 nm and 1930 nm where the comparatively smooth emission spectra becomes spikey. The inset of Fig. 58 details the region of interest in regards to mode-locking of Tm:Lu$_2$O$_3$ sources and the target wavelength used in these amplification experiments.
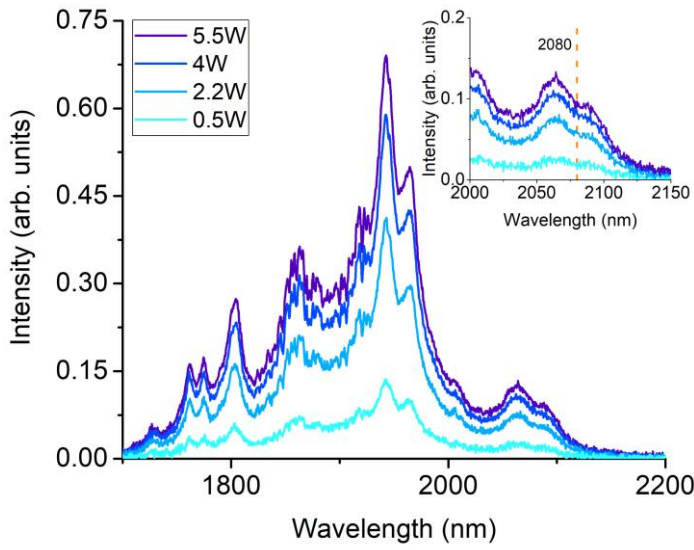
Fig. 58. Luminescence spectra collected from the ceramic Tm:Lu$_2$O$_3$ amplifier gain element when in-band pumped at incident pump powers of 0.5 W, 2.2 W, 4 W, and 5.5 W. Inset shows a zoomed in view of the spectral region of interest around 2080 nm.

The spectra did raise some concerns as to how much gain would be available around 2060–2100 nm for the amplification of the ultrashort seed pulses. When lasing, the available gain is dependent on the inversion level; only in low inversion scenarios is the gain beyond 2 μm greater than that found around 1943 nm and 1965 nm. It is clear looking at the recorded emission spectra that the intensity of the peaks at 1943 nm and 1965 nm are considerably higher than those beyond 2 μm. It was feared that at high pump powers a significant amount of gain would go onto these lines and therefore not be used in the amplification of the ultrashort pulses.

5.2.2 Tm:Lu$_2$O$_3$ seed source

Having decided to use Tm:Lu$_2$O$_3$ as the amplifier gain medium it made sense to also use a Tm:Lu$_2$O$_3$ laser source as the seed. As discussed, this does away with needing to tune over large spans to match the gain peaks of the amplifier and ensures the broad spectrum of the seed will be fully amplified. The six mirror diode-pumped mode-locked Tm:Lu$_2$O$_3$ source presented in 4.2 was used as a seed source going forward with these amplification experiments. This mode-locked laser source was able to achieve output powers up to 500 mW with similar temporal and spectral properties as those previously demonstrated. A beam divergence measurement also showed that the output beam from the laser was near-diffraction-limited with an M^2 of approximately 1. Before attempts to

amplify the seed source were made it was important to analyse its long term stability. Fig. 59 shows the long term power stability recorded over three hours. After an initial warm-up period of roughly 20 minutes, the output power was found to remain around 493 mW (rms = 0.1 %) over the remainder of the test with the run being manually terminated after a further 165 minutes (2 hr 45 min). It was fully expected that such performance could have been maintained for longer if allowed to. Given there were no fluctuations in the output power it can be assumed that pulse durations remained near constant over the run.
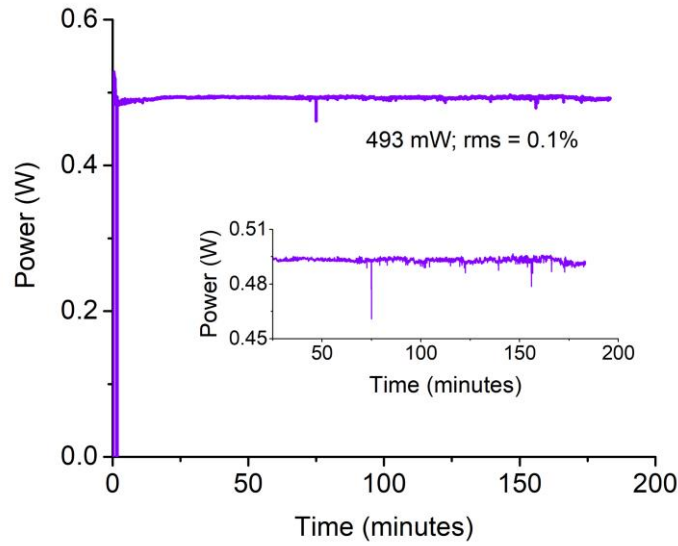
Fig. 59. Long term power stability of the ultrashort pulse Tm:Lu$_2$O$_3$ seed laser recorded over nearly three hours. Inset shows a zoomed in view of the power fluctuations. It is believed that the larger instantaneous drops recorded over this run are more likely to be due to contaminants, dust, *etc.*, passing through the beam rather than degradation of power caused by thermal or mechanical instabilities.

5.2.3   Amplified pulses near 2080 nm

With the seed source performing reliably, evaluation of Tm:Lu$_2$O$_3$ as a gain medium for the amplification of ultrashort pulses in the ~2–2.1 μm region could begin. Seed and pump reshaping optics were chosen so that the pump and seed closely matched a waist size in the amplifier gain element of approximately 50 μm radius when using a common focusing lens. The seed beamline, as shown in red in Fig. 60, consisted of a gold coated steering mirror orientated at a ~50° angle of incidence (M6), a plano-convex spherical lens telescope (f$_{L3}$ = 50 mm, f$_{L4}$ = 75 mm), and dielectric steering mirror (M7; HR 2050 nm, AR 1620 nm) orientated at an angle of incidence of ~4° . The telescope resized and

collimated the seed laser output beam from diameters of 1.6 mm and 1.8 mm, in the *x* and *y* directions respectively, to beam diameters of 2.3 mm and 2.8 mm. An AR coated optical isolator (OI) with a 4 mm diameter clear aperture was placed in the beam path after the telescope and introduced losses in the region of 9%. A gold coated flip mirror orientated at a 45° angle of incidence was used to allow for fast transition between seed oscillator diagnostic equipment (power meter, spectrometer, and autocorrelator) and steering the beam towards the amplifier. This flip mirror is not shown in the optical setup shown in Fig. 60. In addition, lenses L3, L4, L7, and L8 were broadband AR coated for wavelengths between 1.65 μm and 3 μm and made from CaF_2.

Fig. 60. Experimental setups used during the Tm:Lu$_2$O$_3$ MOPA investigations in the single-pass (a) and double-pass (b) configurations.

The pump beam was reshaped through a telescope consisting of two plano-convex spherical AR coated, NBK-7 lenses (f_{L5} = 75 mm, f_{L6} = 25.4 mm) and passed through the dichroic mirror M7 in a direction collinear to the seed beam. The telescope resized the pump beam from an average diameter of 4.4 mm to 1.4 mm. The combined seed and pump beams were then focused through a common plano-convex spherical lens of focal length 75 mm (L7). The measured waists at the position of the amplifier gain element (AGE) for the seed and pump beams were 46 μm x 43 μm and 53 μm x 52 μm, respectively. These measurements were carried out using a scanning slit pyroelectric detector beam profiler. A plot of the measured beam sizes, showing a slight astigmatism in the pump, can be seen in Fig. 61. A 100 mm focal length lens (L8) collimated the post-amplifier seed and pump beams before the beams went further down the beamline. The process and included optics beyond this point will be discussed in the following subsections detailing the single-pass and double-pass amplification results.

Fig. 61. Modal overlap of the seed and pump beams in the horizontal (a) and vertical (b) directions. The grey area, representing the gain element, gives some indication of how these waists would sit within the gain element.

Single-pass

In the single-pass configuration [Fig. 60(a)], the amplified output power was measured directly after the gain element following the collimation lens L8 and a 1.65 μm longpass pump filter (PF). Measurements of the pump filters transmission at the seed wavelength provided a transmission loss figure of approximately 11%. It was found that of the ~11% transmission loss, nearly 10% of the incident 2 μm seed light was reflected. It is presumed that the remaining percentage of lost seed light was absorbed by the filter. These losses were taken into account when examining the amplifiers performance. At the pump wavelength, the filter was found to reflect approximately 93% of the incident light when aligned at a small non-normal angle of incidence. The small percentage of light that was transmitted by the filter could be accounted for by recording the response of the power meter in the absence of any seed and then subtracting it from the total measured power in the presence of the amplified seed. Significant heating of the filter at higher pump powers suggested that the filter also absorbed some of the pump radiation.

The single-pass power amplifier was fully characterised at an average seed output power of 458 mW (392 mW incident power on the amplifier gain element). The corresponding pulse duration and optical bandwidth of the seed pulses at this output power were recorded as 327 fs and 14.6 nm, respectively. At a central wavelength of 2080 nm, this equated to a TBP of 0.33. After optimisation of the waist positioning and mode overlap within the gain element a maximum amplifier output power of 556 mW for an absorbed pump power of 10.3 W (incident pump power of 27 W) was recorded. This equated to a gain of 1.4 (Fig. 62). Recorded optical spectra and intensity autocorrelation traces for the amplified pulse train at various different pump powers showed little to no change in the pulse profile or duration with increasing pump power. The optical spectra and

autocorrelation traces for the input pulse and the output pulses recorded at absorbed pump powers of 0.7 W, 4.8 W, and 10.3 W are shown in Fig. 63.
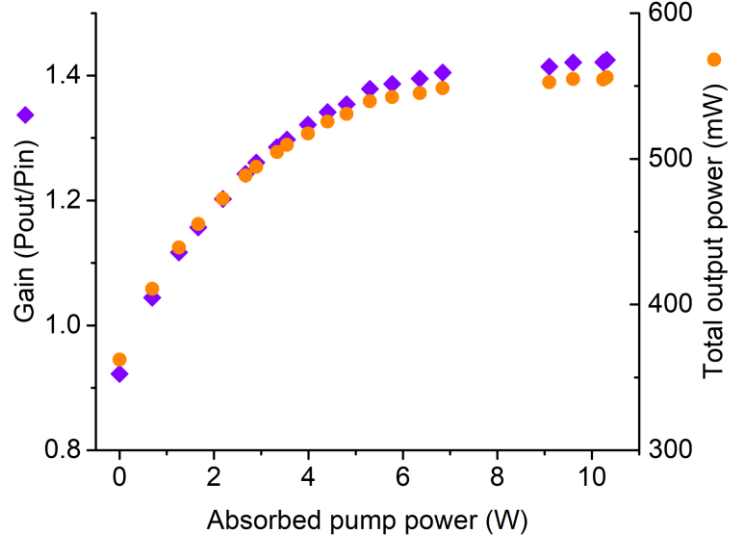
Whilst the traces in Fig. 63 show very little change in the optical bandwidth or pulse duration one would expect some kind of broadening and chirp to be imparted on the pulse due to material dispersion. Due to the "long" pulse durations used here and the combined GDD of the CaF$_2$ lenses and Tm:Lu$_2$O$_3$ gain element at 2080 nm being approximately -661 fs^2 (effective thickness of CaF$_2$ = 19.2 mm at -25.5 fs^2/mm plus 10 mm of Lu$_2$O$_3$ at -17.1 fs^2/mm) this broadening would be expected to be only very slight though. A Gaussian pulse with a similar pulse duration of 330 fs would only be theoretically broadened by 0.05 fs according to (2.11). Indeed, it would take a much shorter incident pulse for any detectable broadening to occur; for example, a 33 fs pulse would be broadened to 65 fs through the same dispersive elements. The apparent broadening of the recorded pulses at higher pump powers as seen in Fig. 63(g) and Fig. 63(h) is more likely to be the result of fluctuations in the pulse durations of the incoming seed pulse as similar broadening is not seen at the lower pump powers. Regarding any imparted chirp; with the negative GDD one would expect the chirp to be negative (blue travelling faster than red). In the intensity autocorrelation used, no qualitative information about the chirp can be gathered. An interferometric autocorrelation would provide some information, but for a much clearer and more accurate result a FROG approach, for example, would provide a full characterisation of

any imparted phase change. However, as the apparatus to perform such a characterisation was not available it was not undertaken.

It should also be highlighted that the optical isolator and mirrors have been excluded from this analysis purely on the grounds that their material composition could not be found, as in the case of the isolator, or it was assumed that the thin dielectric or metallic layers found on mirrors and AR coatings would introduce negligible dispersion in comparison to the dispersion introduced by other optics. Regardless of their inclusion, it is still felt that the most prevalent sources of material dispersion in the beamline are the amplifier gain element and the CaF_2 lenses. In the case of much shorter pulse durations when even a single lens would introduce a measureable increase in pulse duration, a greater effort to ascertain values of GDD for the likes of the optical isolator and mirror coatings would need to be made.

Fig. 63. Recorded optical spectra and autocorrelation traces for the pre-amplifier seed pulses [(a) and (b)] and for the single-pass amplified pulses under 0.7 W [(c) and (d)], 4.8 W [(e) and (f)], and 10.3 W [(g) and (h)] of absorbed pump power.

Double-pass

With the intention of extracting more energy from the amplifier, the single-pass amplifier was modified to achieve a second pass through the amplifier gain element. For this double-pass configuration the pump filter was removed and a further two mirrors along with a thin film polariser (TFP) and quarter-wave plate were added to the amplifier beamline [Fig. 60(b)]. The AR-coated zero-order quartz quarter-wave plate and dielectric mirror (M6; HR 2050 nm, AR 1620 nm) were orientated and aligned

together to rotate the polarisation of the incoming horizontally polarised beam (p-polarisation) by 90° and direct the beam back along the beam path. A pin hole placed between M7 and L7 was used to align the second pass, now vertically polarised (s-polarisation), and achieve reasonable overlap with the pump volume within the gain element. The TFP, coated for <1% reflectivity for p-polarised light at 2050 nm and >99.8% for s-polarised light when orientated at an incident angle of 56°, was then used to pick off the second pass beam, directing it towards a gold coated mirror aligned at an approximately 54° angle of incidence which then directed the amplified beam out of the amplifier setup towards diagnostic equipment. Despite the added complication of the quarter-wave plate and TFP, power measurement was made easier with the removal of the pump filter and the separation of the pump and amplified seed beams. In the double-pass configuration the unabsorbed pump power could be directly measured after M8 while the amplifier output power could be measured at the output of the amplifier setup taking into account ~3% loss on the final gold mirror M9. Whilst some pump radiation was still found to leak through to the 2 µm detector on the amplifier output its negligible value (<1% of the detected amplifier output power) meant it could be ignored.

Optimal alignment of the double-pass was attained through fine adjustment of M8 and translation of the collimation/focusing lens L8. Performance of the amplifier was found to be very sensitive on the pointing of M8, presumably due to any large changes in pointing angle causing the second pass to move completely out of the pump volume. The positioning of L8 provided more a gradual variation in performance as the waist within the gain element was changed to match the pump waist and achieve the best pump overlap. Additionally, losses on the TFP were found to be very sensitive on the angular alignment of the quarter-wave plate. This is to be expected, as if the fast axis of the wave plate is orientated at an angle near but not equal to 45° to the incident p-polarised seed light the linear polarisation will be converted to elliptical polarisation rather than circular. This has the knock on effect of not being converted into truly linear s-polarised light when encountering the wave plate again, leading to losses through reduced reflectivity on the TFP.
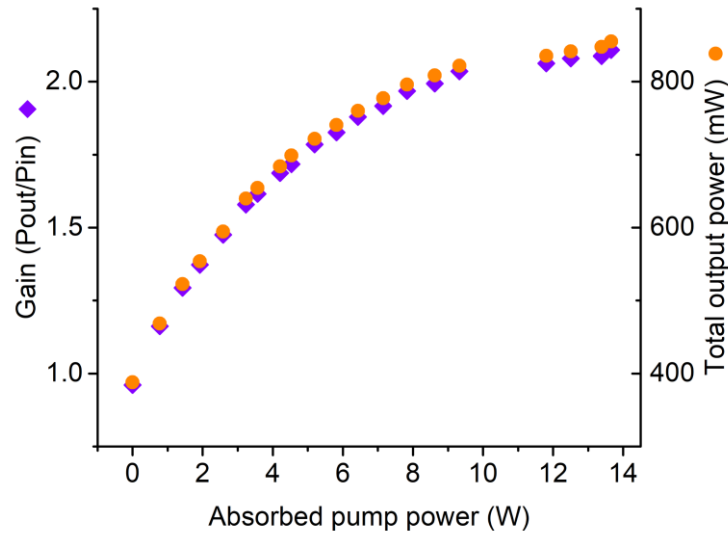
The highest output from the double-pass amplifier was recorded at an average incident
seed power of 405 mW (472 mW seed output power). At this output power, input
pulses were recorded to have a pulse duration of 305 fs at a central wavelength of 2081
nm and an optical bandwidth of 16 nm. This indicated a TBP of 0.34. For an absorbed
amplifier pump power of 13.7 W (incident pump power of 27 W), a total amplifier
output power of 855 mW was recorded corresponding to a gain of 2.1 (Fig. 64).
Examining the power curve it can be seen that the achieved output power does not
appear to saturate as rapidly as that seen in single-pass configuration. This would
suggest that the maximum output power recorded here was limited by the available
pump power. By projecting the recorded curve to higher pump powers, an asymptotic
saturation value for the total output power of approximately 875 mW is attained at an
absorbed pump power of 30 W. This would equate to a small increase in gain to a value
of 2.16.

As was found with the single-pass amplifier, very little change in the pulse profile or
duration was observed between the input pulse and the traces recorded at the output of
the double-pass amplifier when pumped at various different powers. The optical spectra
and autocorrelation traces for the input pulse and the output pulses at absorbed pump
powers of 0.8 W, 6.4 W, and 13.7 W are shown for reference in Fig. 65(a) and Fig.
65(b), Fig. 65(c) and Fig. 65(d), Fig. 65(e) and Fig. 65(f), and Fig. 65(g) and Fig. 65(h),
respectively. Material dispersion would of course be expected to have some effect on the
pulse duration, especially in the double-pass configuration where the effective length of

the dispersive medium is nearly doubled. However, for the ~305 fs long input pulses the increase in pulse duration is only approximately 0.15 fs according to (2.11), assuming a GDD equal to -1048 fs^2 for the 20 mm effective gain element length and 27.7 mm of CaF_2. The change in pulse durations recorded in Fig. 65 is more likely due to fluctuations in the seed laser changing the duration of the input pulse rather than any substantial dispersion in the beamline. For example, by (2.11) an increase in pulse duration from 305 fs to 310 fs would require -6100 fs^2 of dispersion. This would be roughly equivalent to a 24 cm long block of CaF_2 sitting in the beamline.
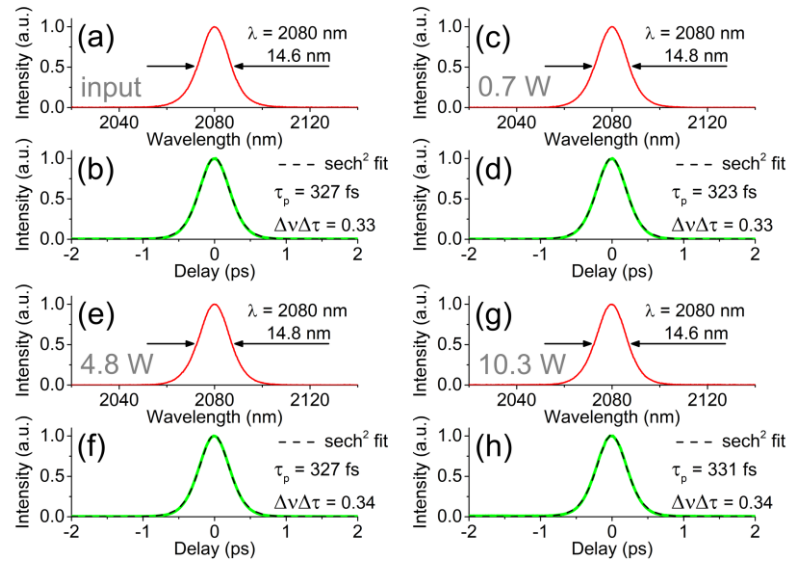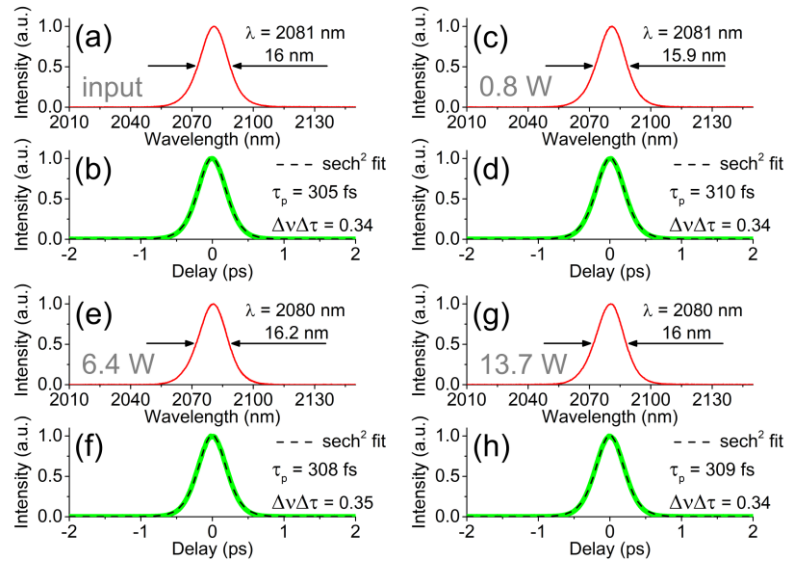

Fig. 65. Recorded optical spectra and autocorrelation traces for the pre-amplifier seed pulses [(a) and (b)] and for the double-pass amplified pulses under 0.8 W [(c) and (d)], 6.4 W [(e) and (f)], and 13.7 W [(g) and (h)] of absorbed pump power.

The small signal gain of the amplifier was also measured in this double-pass configuration. To achieve this, the seed input power (pulse energy) was attenuated using a step variable metallic neutral density filter with optical densities of 0.1, 0.2, 0.3, 0.4, 0.5, 0.8, 1.0. Placing the filter before M6 allowed the initially unattenuated incident seed power of 407 mW to be varied from 60 mW to 354 mW in discrete intervals. The amplifier gain as a function of the incident seed power for pump powers of 10 W, 15 W, and 27 W can be seed in Fig. 66. A maximum gain of 2.2 was recorded at the maximum pump power applied for an incident seed power of 60 mW. Increasing the seed power to its maximum by completely removing the filter provided a gain of 2.1 at the same pump power level. As the difference in values of gain between the small input signal and the large input signal is only slight, it would suggest that the seed powers used here are close to the saturation intensity/power of the laser amplifier. The fairly rapid onset of saturation seen from both the single- and double-pass amplifier is most

likely due to losses caused by amplified spontaneous emission around 1940 nm. This loss mechanism is common in laser amplifiers and dominates at increased pump powers [186]. Parasitic lasing, another common loss mechanism, was not observed.
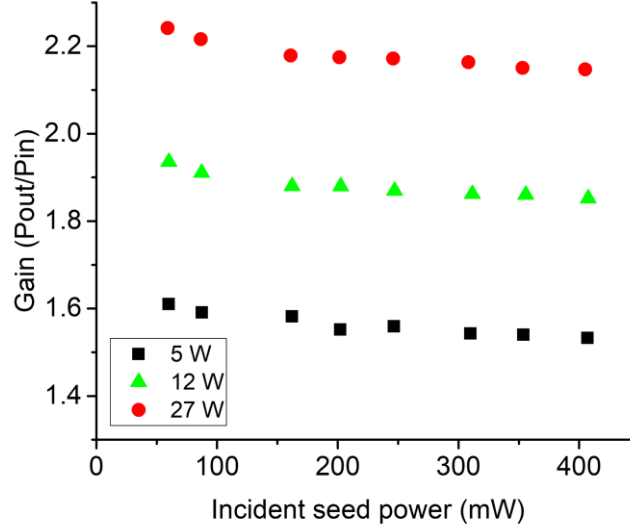
Fig. 66. Measured small and large signal gain values from the Tm:Lu$_2$O$_3$ amplifier for different levels of absorbed pump power.

5.2.4   Conclusions

To the best of the authors knowledge this was the first demonstration of an ultrashort pulse MOPA system based entirely on the Tm:Lu$_2$O$_3$ sesquioxide ceramic gain medium. Even though the gain achieved is considerably lower than that attained in the more conventional Ho:YAG amplifier discussed in the Section 5.1, the consistency in recorded pulse durations and optical profiles is in stark contrast to that found with Ho:YAG and demonstrates the benefit of using the broad gain bandwidth of Tm:Lu$_2$O$_3$ in the amplification of ultrashort pulses. While no saturation of gain was experienced with the single-pass Ho:YAG amplifier, a clear roll-off around 7 W can be seen in Fig. 62 for the single-pass Tm:Lu$_2$O$_3$ amplifier. Improved output powers were achieved from the double-pass configuration. At the maximum applied pump, an average output power of 855 mW, corresponding to a pulse energy of 10.4 nJ, was achieved. Though it is anticipated that the availability of more pump power would realise slightly higher output powers in the double-pass configuration, the simplest route to higher output powers would be to optimise the coatings of the mirror and lens used, reducing the losses of the seed though the beamline and increasing the incident seed power. For

example, the gold steering mirrors used had a manufacturer specified reflectivity of ~97% at a 45° angle of incidence. These could be replaced with off-the-shelf low GDD >99% reflectivity, 45° angle of incidence mirrors relatively easily and, had time allowed, would have been installed in the next iteration of the double-pass amplifier. This improved version would have also replaced L7 and L8 with equivalent focal length achromatic doublets with the aim of producing a tighter waist with reduced aberrations within the gain element thus enhancing the performance of the amplifier by providing a superior overlap over that achievable with plano-convex spherical singlet lenses. A more challenging route to improve the performance of the amplifier would be to redesign it more akin to that seen in Fig. 18(a). This form of multi-pass design would facilitate many more passes through the AGE and would allow for a more thorough investigation of gain as a function of the number of passes. Most importantly though, in regards to compactness and moving towards fully diode-pumped systems, would be the move from a Raman fibre amplifier pump source to a fibre-couple diode laser source.

Although the optical setup of the MOPA system was built in a relatively compact form factor that comfortably fitted on a 0.9 m × 0.6 m breadboard (Fig. 67), the Raman shifted Er:fibre laser used as a pump source for the amplifier is itself bulky, easily able to occupy half of the breadboard alone, and expensive as a commercial laser source. Fibre-coupled laser diode modules around 795 nm, as discussed, offer a much more compact and more powerful alternative pump source at the expense of beam quality. This reduction in beam quality would certainly bring challenges when considering mode overlap but these could be offset with the maximum available power.
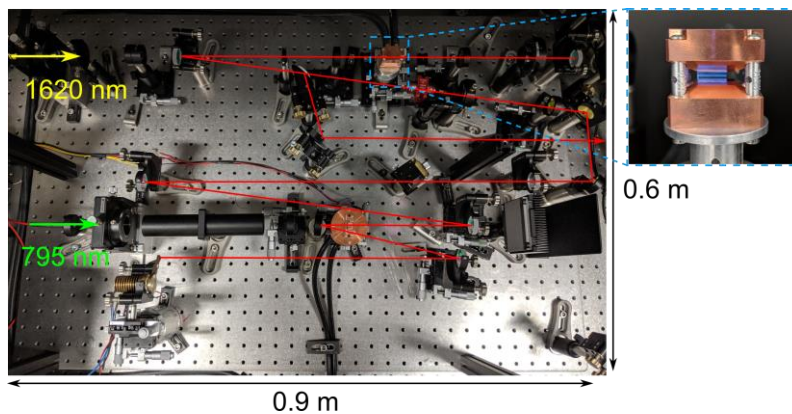
Fig. 67. Top down view of the Tm:Lu$_2$O$_3$ MOPA on a 0.9 m × 0.6 m breadboard. Inset shows the Tm:Lu$_2$O$_3$ amplifier gain element with visible upconversion emission.

The replacement of the Raman fibre pump source with a laser diode module would certainly have be undertaken if striving to create a compact and affordable ultrashort

pulse laser source in the 2–2.1 μm region. If the performance presented in this section can be matched or improved upon with the use of a laser diode based amplifier pump source at 795 nm, then that would represent a significant step towards the development of a fully diode pumped ultrashort pulse laser source capable of acting as a seed source for further high energy amplification in the 2 μm region or as a fundamental source for spectral broadening techniques such as SCG [97,105] or optical parametric conversion [52,96] to access the further mid-IR.

6 Tm-doped sesquioxide waveguide laser: towards the development of compact 2 μm sources

In the previous chapters of this thesis we have developed compact and robust 2 μm laser sources primarily by targeting the pump source. Another potential route would be instead to look at the main oscillator cavity. Fibre based sources do a good job of this; utilizing the flexibility and robustness that comes naturally with fibre drawn gain media combined with fibre-coupled pump modules allows for the entire system to be neatly spooled into a compact housing. Good modal confinement within the fibre core also leads to low laser thresholds and high efficiency. However, achieving direct lasing in the 2–2.1 μm region is not straight forward when using a doped fibre gain medium. As discussed in Chapter 1, fibre laser sources around 2 μm tend to either be spectrally shifted Er:fibre sources or Tm:fibre pumped Ho:fibre sources. The requirement of additional nonlinear stages and numerous pump sources leads to an increased overall system cost and reduced efficiency. Whilst it has been shown that the Tm^{3+}-doped sesquioxides are capable of accessing the 2–2.1 μm region, the difficulties faced when growing the gain media mean that drawing it into a fibre would be extremely difficult. Fortunately, other approaches to produce fibre like waveguide structures exist and provide a means to gain the associated benefits of fibre based media in what are conventionally solid-state gain media. Some examples of these techniques are introduced below.

A well proven route to fabricate both planar and channel waveguide devices is that of the ion-exchange technique [246]. Typically, heavily doped sodium-rich glasses are placed in a salt melt in which ions from the melt diffuse into the glass in exchange for the sodium ions. This results in a localised change in refractive index. By photolithographically patterning the substrate prior to submersion in the melt, one can define the regions of index change and produce waveguide structures. Despite being used to demonstrate waveguide lasers based on a wide variety of dopants, including Tm^{3+} [247], the technique is limited only to doped glasses. Unfortunately this rules out its use with Tm^{3+}-doped sesquioxides.

A waveguide fabrication technique open to all forms of solid-state gain media is found with the use of rib channel waveguides. These structures are produced by etching a

specially designed and constructed layered gain substrate [248] using standard photolithography methods, such as Ar^+-ion etching [249]. The end result is a small strip of gain medium capable of guiding both the pump and lasing modes. Whilst this method has been used to successfully demonstrate a Tm^{3+}-doped waveguide lasers in the past [250,251], the etching stages require the use of complicated technology and, as a result, are time consuming and expensive. Another method, similar in that the waveguide is fabricated by the removal of material, uses diamond saw dicing to precisely grind away unwanted areas of the gain layer leaving only the waveguide structure. This process benefits from the well-known and commercialised technology, more commonly used for silicon wafer cutting, and has recently used to demonstrate $Tm:LiYF_4$ [252,253] and Tm:KYW [254] waveguide lasers capable of low threshold and high efficiency operation.

An alternative approach to produce waveguide structures in bulk material, without the need to remove material or use costly etching equipment, is that of ultrafast laser inscription (ULI). This method utilizes multiphoton absorption to induce a change in the refractive index of the material. Light can then be guided along the inscribed line or in-between the lines depending on whether the refractive index of the modified region has increased or decreased. Much recent work has gone into writing waveguides into doped crystals, ceramics, and glasses [255], demonstrating this methods capability to quickly and cleanly produce waveguides in a wide array of substrates.

The application of these compact sources in the 2–2.1 μm regime would be very similar to any other source emitting in the same range, the main differences being the size of the final device and the low power required to reach threshold. Combining the quasi-monolithic cavity with diode pumping brings the possibility of an ultra-compact and transportable source that can be taken into the field. Such a laser source could be used in part for real-time environmental monitoring in areas of interest or as a precise breath analysis tool in regions lacking medical access. CW mid-IR solid-state lasers could also be well suited to provide a stop-gap solution as the driving source for 2 μm telecommunications. Numerous examples of low threshold Tm:waveguide lasers have been reported in recent years, fabricated in glass [256,257], crystalline [252,254], and ceramic [258,259] substrates using various fabrication techniques. Whilst these sources currently tend to use Ti:sapphire pump sources and butt-coupled conventional bulk mirrors when demonstrating laser action and characterising performance, the move to a more compact configuration is not beyond the realm of possibility. Dielectric coatings applied directly onto the substrate facets provides a relatively straight forward route to removing bulk mirrors but would be costly when trying to achieve the narrow linewidth

operation required for techniques such as wavelength division multiplexing. A truly robust and monolithic approach would be to integrate Bragg gratings into the waveguide to form distributed feedback or distributed Bragg reflector structures [260]. Numerous waveguides could then be fabricated in the same substrate material and modified to operate at specified wavelengths. Commercial single mode laser diodes around 808 nm and 1625 nm are now available with appreciable power to be considered as pump sources for these waveguide lasers, removing the need for large and expensive Ti:sapphire pump sources. Techniques such as dichroic beam combining could then be used to increase the available pump power such that one pump module could pump multiple waveguide lasers. With appropriate engineering, the entire multiple emitter waveguide laser could be packaged into a housing suitable for the demanding environment found in telecom racks.

If the demand for a new telecom band grows, such efficient diode-pumped solid-state Tm^{3+}-doped waveguide lasers could be developed into a solution until reliable semiconductor laser diode sources for 2 μm become available. Mode-locking of these miniature cavities would then realise gigahertz repetition frequency combs; commonly known as "astrocombs" due to their application in the calibration of spectrographs used in astronomy [261].

This chapter covers an early investigation in combining the unique optical and thermo-mechanical properties of $Tm:Lu_2O_3$ with ultrafast laser inscription to create a compact and robust microchip laser source capable of emitting in the mid-IR spectral region.

6.1 $Tm:Lu_2O_3$ waveguide laser

While waveguides have been successfully fabricated in many Tm^{3+}-doped glasses and crystal hosts in the past, there had previously been no reported demonstration of waveguides constructed in the $Tm:Lu_2O_3$ gain medium. The benefits this host brings in terms of thermal conductivity and shifting of the spectrum beyond 2 μm have been discussed in previous chapters. The increase in thermal conductivity is especially clear when comparing Lu_2O_3 to glass. As an initial proof of concept, waveguides were fabricated in a ceramic sample of $Tm:Lu_2O_3$.

Using the method of ULI, waveguides were written with a number of different parameters covering a range of pulse energies and inscription track separations. This was done in order to fully characterise the properties of the fabricated waveguides and to give a better chance of finding a waveguide suitable for sustaining laser action.

6.1.1 Fundamentals of ultrafast laser inscription

The underlying phenomena behind ultrafast laser inscription is that of multi-photon absorption. Conventional linear absorption will only occur if the photon energy is equal to or larger than the bandgap energy of the material. However, under high optical intensities the simultaneous absorption of two or more lower energy photons means it is possible to bridge the bandgap (Fig. 68). By this process a material that is transparent under normal radiation will absorb when the photon density reaches a critical point. For example, a material could be transparent at 1030 nm but given a high enough photon density absorption occurs and energy is deposited in the material. Clearly, to reach this critical point the photon density must be very high. As such, the densities required are only possible at the tightly focused waist of ultrashort pulsed lasers where extremely high irradiances on the order of 10^{13} W/cm^2 are achieved. Similar to that observed in multi-photon fluorescence microscopy, only the material within the volume of the waist is excited whilst the surrounding material remains unchanged. Within the waist volume, the nonlinear ionisation processes of tunnelling ionisation, photoionisation, and avalanche ionisation lead to high temperatures and pressures through an induced micro-plasma, imprinting a permanent change in the structure of the material [262,263]. It is this process that allows for the fabrication of highly detailed micro- and nano-scaled structures. Utilising the imprinted structural change for selective etching means that devices such as micro-fluidic channels and high quality factor micro-toroids can be produced, opening up the fabrication technique beyond that of purely waveguide optical devices. These optical devices are not limited to waveguide lasers, however. Examples of interferometers [264] and Bragg gratings [265] have also been reported.
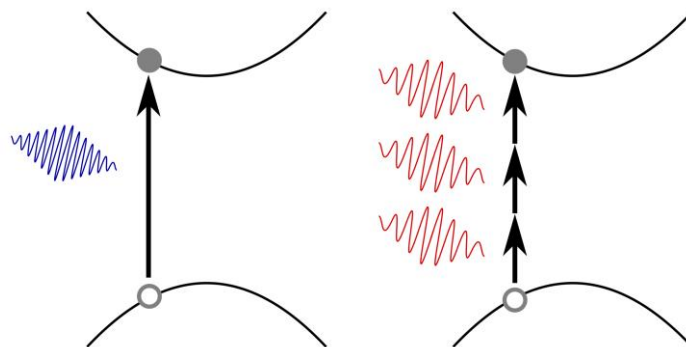
Fig. 68. Simplified schematic of multi-photon absorption. Traditional linear absorption is shown on the left, while multiphoton absorption is depicted on the right. In this case, three photons have been required to bridge the bandgap.

Examining the waveguide fabrication process in more detail means discussing the different waveguide structures that can be written. Depending on the material properties and the inscribing laser parameters one of two modifications can be made. These are generally referred to as Type I and Type II [266]. In Type I, the modification causes the refractive index of the localised material to increase relative to the surrounding unirradiated bulk substrate ($\Delta n > 0$). Therefore guiding, in this case, occurs within the modified region [Fig. 69(a)]. It is also possible to inscribe two damage lines either side of an unirradiated region which acts like the waveguide core. This is known as Type II ($\Delta n < 0$). In this case, guiding is made possible through the stress induced refractive index modification effect, reducing the refractive index around the damage line such that guided mode is supported between the lines [Fig. 69(b)]. A variation of Type II guiding is possible when the unirradiated guiding region is surrounded on all sides by lower index damage lines. This structure is known as depressed cladding [Fig. 69(c)].
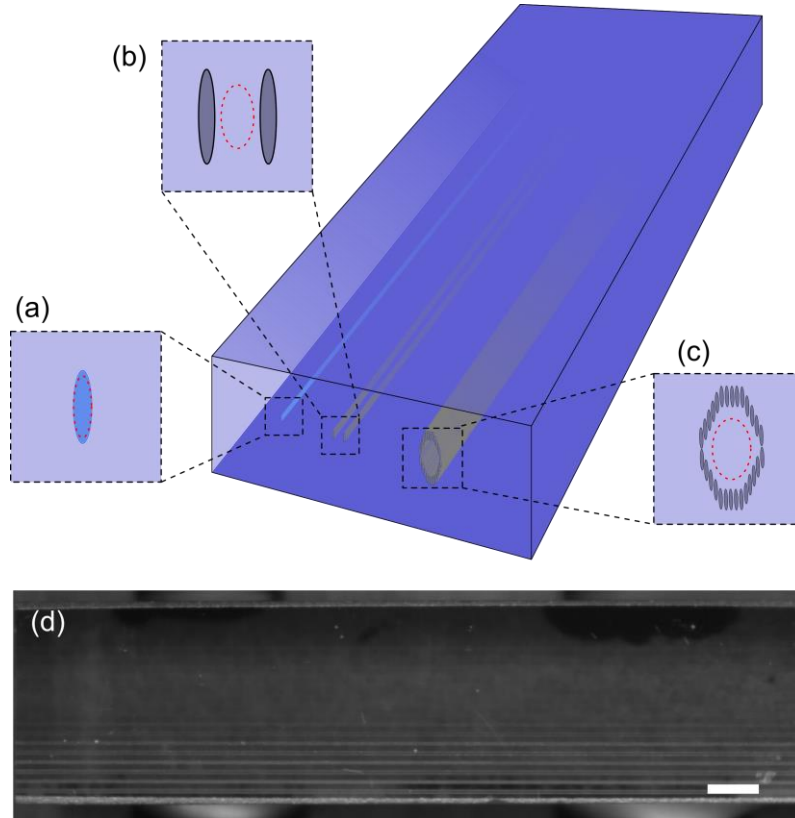
Fig. 69. Ultrafast laser inscribed waveguides in a substrate. Type I, Type II, and cladding waveguides can be seen in (a), (b), and (c), respectively. The red dotted ellipses show the guiding regions. A top down view of the inscribed tracks forming the waveguides in the Tm:Lu$_2$O$_3$ substrate can be seen in (d). A 0.5 mm scale bar has been included.

6.1.2 Tm:Lu$_2$O$_3$ waveguide fabrication and analysis

Arrays of 10 mm long tracks were written in the 2.3 × 5 × 10 mm sample of 1 at.% Tm^{3+}-doped Lu$_2$O$_3$ ceramic using different pulse energies and track separations. The inscriptions were performed at Heriot-Watt University using an ultrashort pulse laser emitting 200 fs pulses at a pulse repetition frequency of 500 kHz and a central wavelength of 1040 nm. Using a 0.4 NA aspheric lens the inscription beam was focused to a spot diameter of approximately 1.8 μm, 300 μm beneath the surface of the sample. The inscription depth was chosen to avoid any surface ablation during the writing process. The Tm:Lu$_2$O$_3$ substrate was translated through the focus of the laser at a constant speed of 5 mm/s. This translation speed was selected after taking into account the capabilities of the translation stages, writing time, and ensuring good overlap of the pulses within the substrate. Pulse energy over the waveguide arrays was varied from 0.4–5 μJ, while track separations of 20 μm and 30 μm were used. A full list of the inscription parameters for each guide can be found in Table 6 in the appendix. Once the fabrication process had been complete, the sample end facets were ground back and re-polished to optical quality. This grinding was performed to remove any defects caused by clipping of the inscription beam near the edges of the sample and resulted in a final waveguide length of 9 mm.

Guiding characteristics of the fabricated waveguides were initially studied in a passive manner using a 980 nm fibre-coupled diode laser. Using the setup shown in Fig. 70(a), the output from the laser source was collimated using a 2.75 mm focal length aspheric lens (L1) before being coupled into the waveguide under investigation (WG) with a 11 mm focal length aspheric lens (L2). The resulting spot from the second aspheric lens had a diameter of 24 μm. The rear end of the waveguide was imaged using a 20x microscope objective (L3), through a variable attenuator (VA) onto a CMOS camera. With the Tm:Lu$_2$O$_3$ substrate and coupling lens mounted on their own x, y, z translation stages, the guiding properties of the inscribed waveguides could then be viewed.

For the track waveguides written with pulse energies from 0.4–0.8 μJ, Type I guiding was observed. The guiding mode was found to overlap with the modified region as seen in Fig. 70(b). Type II guiding was observed in the structures written with pulse energies of 0.9–3 μJ [Fig. 70(c)]. In this range, tracks written with a 20 μm separation were found to support single mode operation while tracks separated by 30 μm were found to be multi-mode. The guiding properties of tracks written with pulse energies of >3 μJ were found to be limited. This can be associated to large material damage features that were viewed surrounding the inscribed tracks. Additionally, Type II guiding was found to be

strongly polarisation dependant. Only light polarised parallel to the *y*-axis would guide. The likely cause of this strong dependence is a combination of the asymmetrical structure of the waveguide and the stress induced in the irradiated tracks during the inscription process.
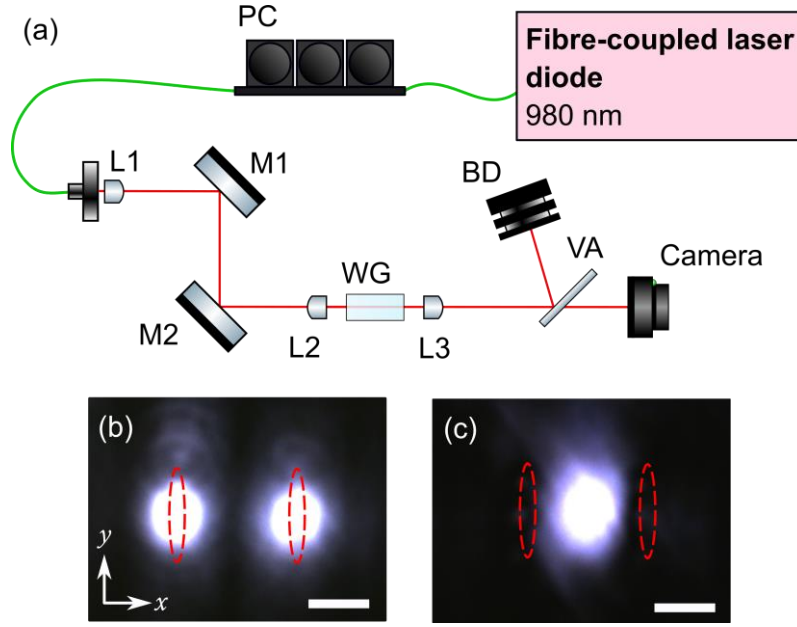
Fig. 70. (a) Optical setup used to investigate the guiding characteristics of the fabricated tracks in the Tm:Lu$_2$O$_3$ substrate. PC, polarisation controller; M1 and M2, silver mirrors; BD, beam dump. Mode images of Type I and Type II guiding in waveguides written with a 20 μm track separation are shown in (b) and (c), respectively. Red dashed ellipses indicate the location of the inscribed tracks. A 10 μm scale bar is included.

6.1.3 Waveguide laser results

To test the potential for laser action with the inscribed waveguides, a cavity was formed around the sample using two plane dielectric mirrors mounted up against the uncoated 2.3 mm × 5 mm end facets. The input pump mirror (PM) was coated for high reflectively in the 1.9–2.1 μm region and high transmission at the pump wavelength of 796 nm, while the output couplers (OC) used were coated for transmissions of 2%, 9%, 20%, 30%, 40%, and 75% between 1.9–2.1 μm. A linearly polarised Ti:sapphire laser tuned to 796 nm with a maximum output power of 2 W was used as the pump source. The pump beam was coupled into the waveguides using a 20 mm focal length aspheric lens (L1), resulting in an average diameter spot size of 28 μm. Incident pump power could be varied using a half-wave plate (HWP) and polarising beam splitter (PBS). As in the guiding characterisation setup, the Tm:Lu$_2$O$_3$ sample with its inscribed waveguides (WG), and the pump lens L1 and the imaging aspheric lens (L2) were all

mounted on their own *x*, *y*, *z* translation stages. However, in this case the sample was mounted on a water-cooled cooper block and kept at a constant temperature of 20 °C. The layout of the entire set up can be seen in Fig. 71. Using this configuration, pump light was coupled into each waveguide in the array in turn with the alignment checked at low power using L2 to image the waveguide end facet onto a camera sensor using a variable attenuator (VA) to avoid saturating the sensor. This systematic approach allowed for the fluorescence of each of the Tm:Lu$_2$O$_3$ waveguides to be monitored on an individual basis using an unbiased photodetector (D) positioned after a pump filter (PF) providing >40 dB of attenuation at the pump wavelength. The fluorescence signal was maximized by tuning the cavity alignment and input coupling of the pump beam. Checking for a lasing threshold was then undertaken by increasing the pump power. Of all the waveguides tested, laser action was only achieved in the structures written with 2 µJ and 3 µJ energy pulses and 30 µm track separation. Of these two waveguides, the best performance was observed from the 2 µJ structure.
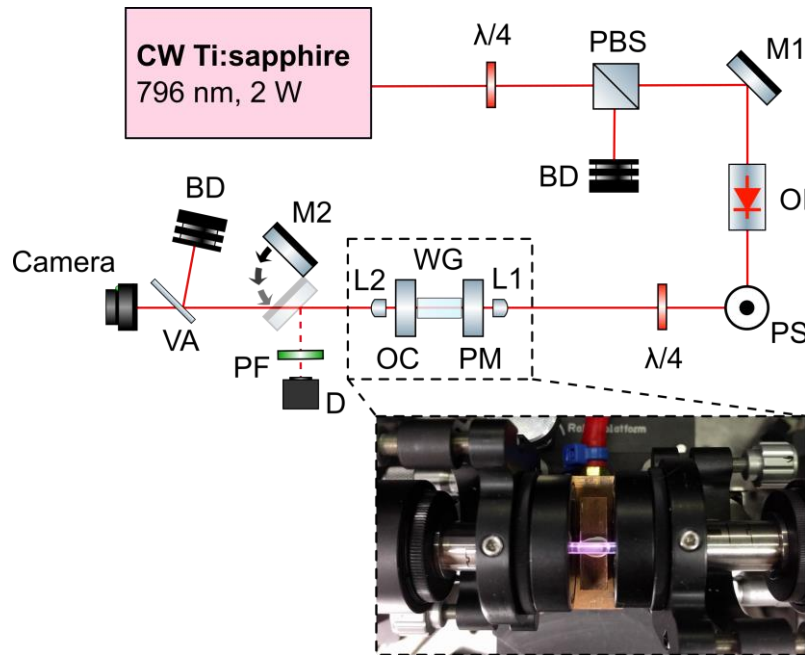
Fig. 71. Optical setup used when investigating the potential for laser action in the Tm:Lu$_2$O$_3$ waveguides. M1 and M2, gold mirrors with M2 mounted on a flip mount; OI, optical isolator; PS, periscope; BD, beam dump. The inset image of the sample clearly shows the illuminated waveguide. The pinkish colour is due to the combination of the pump wavelength, as seen by the infrared sensitive camera sensor, and the blue upconversion light.

Having found the waveguide with the best performance, it was characterised with the range of OC. A power characteristic plot showing the output power with respect to the absorbed pump power for the 9%, 20%, and 40% output coupler can be seen in Fig. 72.

The output power emitted from the waveguides could be calculated by incorporating the manufacturers quoted losses at the signal wavelength for the optics downstream from the output coupler. Absorbed pump power was determined by measuring the residual transmitted pump with the pump filter removed and subtracting the signal power. In order to complete such a conversion, a perfect coupling of the pump signal into the waveguide was assumed except for a single Fresnel reflection from the uncoated end facets. That is to say that, it was assumed that there was no coupling loss due to mode field mismatch between the guided pump mode and the pump spot profile. This assumption gives conservative (higher) values for absorbed pump power due to the uncertainties in calculating the coupling loss into the waveguide.
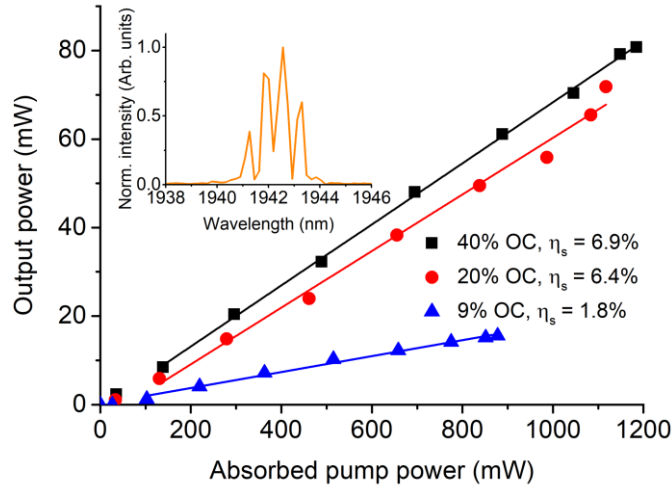
Fig. 72. Power characteristics of the Tm:Lu$_2$O$_3$ waveguide laser with different output couplers. The inset shows the laser emission spectrum.

Using the 40% OC, a maximum output power of 81 mW was achieved for 1.18 W of absorbed pump power, corresponding to a slope efficiency of 6.9%. A higher slope efficiency of 9.5% was attained under further refined alignment conditions, but a slight degradation in available pump power meant a lower output power of only 52 mW was generated. Across the series of output coupler tested, the laser threshold was recorded to be in the range of 50–200 mW and the laser emission spectrum remained centred at 1942 nm.

Analysis of the pump and lasing mode profiles were completed using commercially available visible and mid-infrared cameras, respectively. The pump mode was imaged directly onto the camera sensor, while the lasing signal mode was imaged onto a screen through the pump filter and subsequently viewed with the infrared camera. Under

optimal performance conditions it was found that the waveguide structure supported multimode propagation at the pump wavelength of 796 nm but single mode characteristics at the laser wavelength, as seen in Fig. 73 (b) and Fig. 73(c). A Gaussian fit of the lasing mode was performed using a scaled image containing a calibrated target. The results of this fit gave a mode field diameter of the signal of 22.5 μm and 25.2 μm in the *x* and *y* directions, respectively [Fig. 73(d) and Fig. 73(e)].
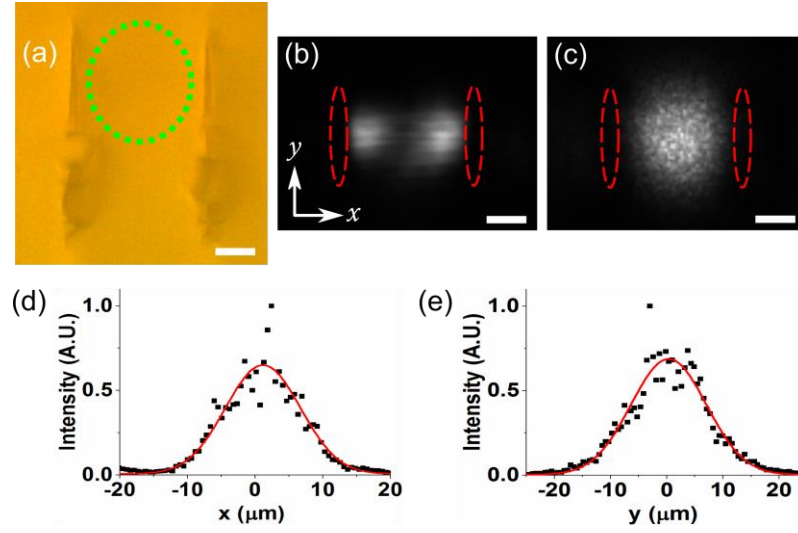
Fig. 73. (a) False coloured microscope image of the waveguide used in the laser experiments. The unmodified guiding region is shown by the green dotted circle. (b) and (c) show the pump and laser mode images, respectively. Red dashed ellipses indicate the area of the inscribed tracks. (d) and (e) are the Gaussian fits to slices through the laser mode image in *x* and *y* directions, respectively. 10 μm scale bars are included in (a), (b), and (c).

Propagation loss of the waveguide at the laser wavelength was determined using a modified Caird analysis. A standard Caird analysis determines the cavity losses (*L*) by using a relationship between the measured slope efficiencies (η_s) and the known losses from the associated output couplers (T_{OC}) assuming the conditions of a low loss cavity, such that

$$\frac{1}{\eta_s} = \frac{1}{\eta_0}\left(1 + \frac{2\gamma_i}{\gamma_{OC}}\right). \tag{6.1}$$

where $\gamma_i \approx L$, $\gamma_{OC} \approx T_{OC}$, and η_0 is the limiting slope efficiency that be achieved in the absence of passive loss. However, in the case of large losses logarithmic arguments must be added to *L* and T_{OC} [259]. The parameters γ_i and γ_{OC} are modified such that $\gamma_i = -\ln(1-L)$ and $\gamma_{OC} = -\ln(1-T_{OC})$. By fitting (6.1) to the measured slope efficiencies

(Fig. 74) the propagation loss of the waveguide at the lasing wavelength was estimated to be 0.7 ± 0.3 dB/cm.
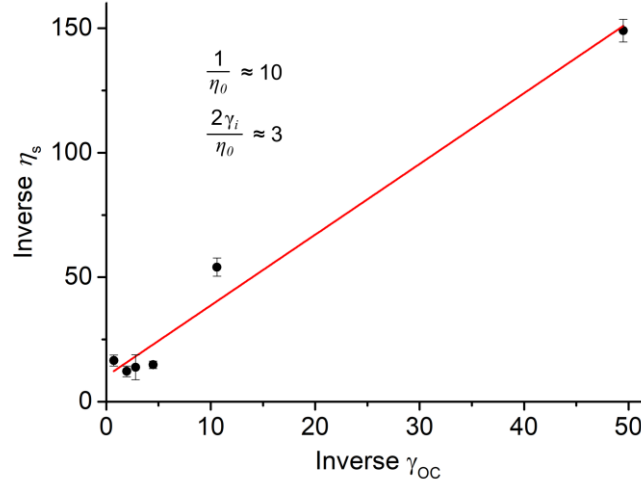
Fig. 74. Linear fit of the inverse slope efficiencies against inverse output coupling used for the modified Caird analysis of the Tm:Lu$_2$O$_3$ waveguide laser.

Investigations into the waveguide losses at the pump wavelength were undertaken using a modified version of the setup shown in Fig. 71. The removal of the cavity mirrors and pump filter, combined with the detuning of the Ti:sapphire to a wavelength of 860 nm where there is negligible absorption by the Tm:Lu$_2$O$_3$ substrate, allowed for the measurement of the total insertion loss for the laser waveguide at near the pump wavelength. Incident and transmitted power measurements were taken with the optimal coupling into the waveguide used in the laser experiments. In addition, a background loss value was taken by measuring the incident and transmitted power for just the lenses used by translating the sample out of the beamline. These results gave an estimated insertion loss for the laser waveguide at the pump wavelength of 1.6 dB.

6.1.4   Conclusions

This work represented, to the best of the authors knowledge, the first demonstration of a waveguide laser fabricated in Tm:Lu$_2$O$_3$ ceramic using ULI. Improvements in the performance of the device could still be sought, however. A laser emission at 1942 nm is indicative of high loss operation suggesting that the waveguide structure could be improved. The occurrence of Type I guiding means that ULI waveguide writing using a method optimised for this regime could be investigated further. An example method would be that of multiscan inscribing, which has been shown to be a route towards low

threshold and high slope efficiency waveguide lasers in other materials [267]. In addition, the writing of depressed cladding waveguide structures is also a feasible route to providing better optical confinement and improving laser performance [256,268]. Mode mismatch between the pump and lasing wavelengths could also be addressed by adopting this waveguide structure. However, the large difference between the pump wavelength at 795 nm and the lasing wavelength of ~2 μm would still make this a non-trivial task. Reducing the difference in pump/laser wavelength by utilising in-band pumping at 1620 nm would greatly increases the likelihood of being able to design a structure that could support both the pump and lasing wavelengths in single mode operation. Indeed, this pumping scheme has been reported to demonstrate highly efficient and low threshold operation in a Tm^{3+}-doped waveguide laser the past [253].

Methods to ascertain a more accurate value of absorbed pump power by determining the coupling efficiency were undertaken but proved unsuccessful. Having established the total insertion loss at the pump wavelength, measurements of the propagation loss of the waveguide would have allowed for the extraction of the coupling efficiency and refinement of the conservative values used for absorbed pump power. The standard cut back method, whereby the transmitted power is measured through decreasing lengths of the sample waveguide, could have been used here to determine the propagation loss. However, this ultimately destroys the sample and was therefore not chosen. An alternate technique of imaging the decaying light intensity as it propagated through the waveguide was also undertaken by analysing images similar to that shown in Fig. 69(d). The values calculated from this approach proved to be unreliable though, generating propagation loss figures in excess of that measured for the total insertion loss. This inability to accurately ascertain a value of the propagation loss ultimately meant that a more accurate value of the absorbed pump power could not be determined.

Steps to improve the CW performance, such as those discussed, would need to be undertaken before any useful mode-locked operation could be realised. Once improvement in the power has been achieved though, mode-locking techniques similar to those reported in previous works could be applied [269,270]. Additionally, the increased availability of commercial 808 nm and 1625 nm single mode laser diodes, with sufficient power to be considered as pump sources, opens new avenues of investigation aimed towards efficient, stable, compact, and direct diode-pumped ultrashort pulse sources in the 2 μm spectral region.

7 Final remarks

This final chapter is included to summarise the key results of the thesis and provide a prospective outlook on related work that could be achieved in the short and long term following this thesis.

7.1 Summary

The experimental results presented in this thesis represent, at the time of writing and to the best of the authors knowledge, some of the shortest pulse durations and highest average powers achieved from diode-pumped mode-locked femtosecond laser sources in the ~2–2.1 μm spectral region. CW characterisation of the Tm^{3+}-doped sesquioxide sources showed high slope efficiencies and broad tunability from the diode pumped laser sources. A maximum output power of 660 mW for 2.3 W of absorbed pump power, corresponding to a slope efficiency of 33%, at a central emission wavelength of 2103 nm was realised from the single crystal $Tm:LuScO_3$ laser, while the ceramic $Tm:Lu_2O_3$ laser achieved a maximum output power of 901 mW from approximately 2.7 W of absorbed pump power at an emission wavelength of 2065 nm. This CW performance corresponded to a slope efficiency of 40%. In both cases, broad and continuous CW tuning ranges were recorded, with the $Tm:LuScO_3$ laser demonstrating a smooth tuning range between 1973 nm and 2141 nm, and the $Tm:Lu_2O_3$ demonstrating similarly broad, albeit not as smooth, tuning range of 1941–2126 nm.

When operating in the mode-locked regime, the broad gain demonstrated by the recorded tuning ranges aided in realising true femtosecond pulse operation. Indeed, at the time of writing, the shortest reported pulse durations from a diode-pumped mode-locked Tm^{3+}-doped laser source were realised from the developed $Tm:LuScO_3$ laser. Pulse durations as short as 170 fs were recorded at an average output power of 113 mW around a central emission wavelength of 2093 nm. Whilst difficulties were initially faced when trying to mode-lock the previously characterised $Tm:Lu_2O_3$ laser, greater success was found with the high power $Tm:Lu_2O_3$ laser pumped with a fibre-coupled laser diode module. With the addition of the SD-BRF, near-transform-limited pulses with a minimum pulse duration of 278 fs, were generated at a central wavelength of 2081 nm with an average output power of 555 mW.

The use of a SD-BRF to spectrally tune the mode-locked Tm^{3+}-doped sesquioxide laser sources is believed to be the first demonstration of such an approach in the 2 μm spectral region and has shown significant advantages in size and robustness compared with the more traditionally used slit and prism pair. With the SD-BRF operating in its 1st order, the mode-locked $Tm:LuScO_3$ laser demonstrated a continuous tuning range of 2019–2110 nm. Stable femtosecond mode-locked operation was maintained throughout this tuning range, with a minimum pulse duration of 240 fs recorded at a central emission wavelength of 2090 nm and an output power of 93 mW. Operating in the 2nd order of the filter realised a similar tuning range but pulse durations and average powers were comparably lower, with a minimum pulse duration of 349 fs recorded at a central wavelength of 2085 nm and an output power of 62 mW.

Tuning of the mode-locked $Tm:Lu_2O_3$ laser using the SD-BRF was met with some added complications believed to be due to the inversion level dependant gain profile of $Tm:Lu_2O_3$. The mode-locked tuning range was found to depend on the applied pump power, with widest recorded tuning range of 2069–2093 nm being measured at a pump power of 8 W. At this pump power, average powers and pulse durations were found to remain around ~260 mW and between 489 fs and 598 fs, respectively, over the majority of the range. This is in comparison with the tuning range of 2073–2091 nm that was recorded for a pump power of 11.6 W. Under this operating condition, average powers were found to remain around ~440 mW while pulse durations were measured to vary between 315 fs and 383 fs following the change in output power.

Amplification of the developed Tm^{3+}-doped sesquioxide seed sources was met with success across the two separate demonstrations. Though it is acknowledged that further refinement could have led to improved performance in both cases. Whilst appreciable gain (~10) was achieved from the single-pass Ho:YAG slab amplifier when seeded by the ultrashort pulse $Tm:LuScO_3$ laser source, it is believed that further amplification could have been achieved had the seed source been optimised to better suit the narrower gain bands of Ho:YAG. This mismatch is well seen when examining the recorded optical spectra following the amplifier. It is believed that implementation of the SD-BRF and optimisation of the pump/seed mode overlap within the amplifier gain crystal would have realised further amplification and less reshaping of the pulse profile due to gain mismatch and narrowing.

In regards to the femtosecond pulse $Tm:Lu_2O_3$ MOPA system, a gain of >2 demonstrates the potential for the system to be developed into a relatively compact source for further mainstage amplification or spectral broadening through the likes of DFG or SCG. The benefit of using $Tm:Lu_2O_3$, with its broad gain bandwidth, as the

amplifier gain medium was well demonstrated by the consistency of the spectral pulse profile and pulse duration between the incident seed and the amplified output. It is believed that refinement of the optics used in the amplifier beamline and seed delivery path would result in higher output powers from the amplifier. However, the main hurdle to overcome in realising a compact high energy pulse source would be the replacement of the Raman fibre amplifier pump source with that of a laser diode based source.

Finally, the first reported demonstration of an ULI waveguide laser in $Tm:Lu_2O_3$ realised early steps towards the potential development of a compact and efficient 2 μm laser source. Guiding was demonstrated in both Type I and Type II inscriptions, while low threshold lasing was achieved in a Type II waveguide. A maximum output power of 81 mW at an emission wavelength of 1942 nm was achieved for 1.18 W of absorbed pump power. Further investigations into the refinement of the waveguide inscription parameters or the use of a depressed cladding structure are believed to be a route to enhanced laser performance by providing better optical confinement and reducing the pump/laser mode mismatch. An alternate route to improve the guiding characteristics of the pump and laser modes would be to utilise in-band pumping. Indeed, either of these approaches could be realised with high power single mode laser diodes (≥0.5 W) operating near 808 nm and 1625 nm.

7.2   Outlook

The diode-pumped mode-locked Tm^{3+}-doped sesquioxide laser sources developed during the course of this thesis can be said to have achieved their goal of demonstrating high power ultrashort laser pulses in the 2 μm spectral region. In respect to their individual performance, it is felt that only marginal improvements could be made to the $Tm:LuScO_3$ laser while the fibre-coupled laser diode pumped $Tm:Lu_2O_3$ laser could realise improvements in both average power and pulse duration if further refinement of cavity parameters was undertaken. For the $Tm:LuScO_3$ laser, the implementation of lower output coupling, in the hope of realising even shorter pulse durations, or higher pump powers to realise higher output powers at the risk of damaging the laser crystal are both potential avenues of investigation. It is believed that the $Tm:Lu_2O_3$ laser could realise stable mode-locked emission around 2060 nm and broadband mode-locked tuning if more time was spent optimising important mode-locking parameters, such as the SESAM and gain element waist sizes. However, in this case, the waist size within the gain element, and consequently the strength of the SPM, would ultimately be

determined by the minimum achievable pump waist that retains good mode overlap within the gain element.

The refinements and changes that could be applied to the Tm:Lu$_2$O$_3$ MOPA system to realise a fully diode-pumped high pulse energy source have already been discussed. An alternate avenue of investigation that could realise much higher pulse energies, however, would be that of a regenerative amplifier. The existing femtosecond pulse Tm:Lu$_2$O$_3$ seed source would still prove useful in this regard and only the amplifier stage need face substantial rebuilding. The commercial availability of pulse pickers able to operate over a suitable spectral and repetition frequency range aid in this regard. Variation of the number of passes would allow for a complete analysis into the limit of gain one can attain from Tm:Lu$_2$O$_3$ in the amplification of femtosecond pulses. Care would of course have to be taken to manage dispersion within the amplifier, however.

Either of the above tasks could be accomplished in a relatively short time frame following this thesis, should the interest arise. More long term goals can be found with the continued improvement in the performance of single mode laser diodes that can be used to pump Tm^{3+}-doped gain media. Whereas even longer goals, not so within the scope of this thesis, relate to the availability of Tm^{3+}-doped gain elements.

Whilst the high power, low beam quality laser diode sources used in the majority of this thesis clearly provided a suitable pump source, poor pump/laser mode overlap can lead to high thermal loads within the laser gain element. Moreover, efficiently coupling these multimode pump sources into waveguide lasers can prove very challenging. Single mode laser diodes offer the same compact and cost effective pump solution as their multimode brethren but with much lower output powers. The current state-of-the-art commercial single mode laser diodes around 808 nm and 1625 nm are still unable to achieve watt level power levels. However, methods of beam combining, *e.g.*, polarisation combining or dichroic mirror combination, could realise watt level pump sources with comparable characteristics, in terms of output power and beam quality, to Ti:sapphire lasers using off-the-shelf optics. The use of these compact high beam quality laser diodes would be well suited to pump Tm^{3+}-doped waveguide lasers similar to that demonstrated in this thesis. With further improvement in the waveguide performance, compact and low threshold 2 μm laser devices could then be realised. Likewise, these laser diodes could be used to further advance the diode-pumped ultrashort pulse laser sources developed during this thesis. Either of these proposals would of course require a financial and time investment to construct and characterise the laser diode pump modules.

A significant drawback of the Tm^{3+}-doped sesquioxides that needs to be overcome is the limited number of suppliers of laser gain elements; be this in single crystal or ceramic form. In comparison to the wide commercial availability of more well-known Tm^{3+}-doped gain media, such as Tm:YAG, Tm:YLF, or Tm:KYW, the Tm^{3+}-doped sesquioxides appear to have virtually no easily accessible means of acquiring gain elements. This is presumably due to the difficulties faced when growing sesquioxide crystals using established crystal growth techniques. Whilst ceramic laser gain media offer an alternate route to produce the gain elements, only ceramic forms of $Tm:Lu_2O_3$ are currently commercially available. With multiple demonstrations of ceramic $Tm:LuScO_3$ having now been reported this may change in the coming years, however.

The restricted availability of gain elements will undoubtedly hamper efforts to further the development of the diode-pumped mode-locked laser sources reported on in this thesis. It is hoped that this situation improves, as the research carried out during the course of this thesis clearly demonstrates that Tm^{3+}-doped sesquioxide laser sources hold a prominent role in the generation of ultrashort pulses in the 2–2.1 μm spectral region. Furthermore, it has been shown that expensive and bulky high beam quality pump sources, such as Ti:sapphire lasers, need not be the only choice when looking to further develop these mode-locked ultrashort pulse laser sources. Indeed, the high power laser diode pump sources used during this thesis provided a means to demonstrate average powers and pulse durations comparable to, and in some cases superior to, previously reported Ti:sapphire pumped solid-state Tm^{3+}-doped mode-locked lasers via a much more economic route. Going forward, the development of such diode-pumped mode-locked lasers should be held in high regard when considering the commercialisation of ultrashort pulse laser sources for scientific research and industrial applications in the mid-IR photonics sector.

Reference list

1.   T. H. Maiman, "Stimulated Optical Radiation in Ruby," Nature **187**, 493–494 (1960).

2.   "Physics History. May 16, 1960: Maiman Builds First Working Laser," APS News **19**, (2010).

3.   H. Pires, M. Baudisch, D. Sanchez, M. Hemmer, and J. Biegert, "Ultrashort pulse generation in the mid-IR," Prog. Quantum Electron. **43**, 1–30 (2015).

4.   F. Pristera, M. Halik, A. Castelli, and W. Fredericks, "Analysis of Explosives Using Infrared Spectroscopy," Anal. Chem. **32**, 495–508 (1960).

5.   S. Wartewig and R. H. H. Neubert, "Pharmaceutical applications of Mid-IR and Raman spectroscopy," Adv. Drug Deliv. Rev. **57**, 1144–1170 (2005).

6.   B. Stuart, "Industrial and Environmental Applications," in *Infrared Spectroscopy: Fundamentals and Applications* (Wiley, 2004), pp. 167–185.

7.   M. Mürtz and P. Hering, "Online Monitoring of Exhaled Breath Using Mid-Infrared Laser Spectroscopy," in *Mid-Infrared Coherent Sources and Applications* (2008), pp. 535–555.

8.   F. Adler, M. J. Thorpe, K. C. Cossel, and J. Ye, "Cavity-Enhanced Direct Frequency Comb Spectroscopy : Technology and Applications," Annu. Rev. Anal. Chem. **3**, 175–205 (2010).

9.   The included molecule model images exist in the public domain and were sourced from their respective articles, www.wikipedia.org.

10.   S. D. Lord, "A New Software Tool for Computing Earth's Atmospheric Transmission of Near- and Far-Infrared Radiation," NASA Tech. Memo. 103957 (1992).

11.   G. Lask, M. Elman, M. Slatkine, A. Waldman, and Z. Rozenberg, "Laser-assisted Hair Removal by Selective Photothermolysis Preliminary Results," Dermatologic Surg. **23**, 737–739 (1997).

12.   S. L. Kilmer and R. R. Anderson, "Clinical Use of the Q-Switched Ruby and the Q-Switched Nd:YAG (1064 nm and 532 nm) Lasers for Treatment of Tattoos," J. Dermatol. Surg. Oncol. **19**, 330–338 (1993).

13.   V. A. Serebryakov, É. V. Boĭ ko, N. N. Petrishchev, and A. V. Yan, "Medical applications of mid-IR lasers. Problems and prospects," J. Opt. Technol. **77**, 6–17 (2010).

14.   D. Theisen-Kunde, V. Ott, R. Brinkmann, and R. Keller, "Potential of a new cw 2μ m laser scalpel for laparoscopic surgery," Med. Laser Appl. **22**, 139–145 (2007).

15.   J. Lawrence and L. Li, "The Challenges Ahead for Laser Macro, Micro and Nano Manufacturing," in *Advances in Laser Materials Processing* (Woodhead Publishing, 2018), pp. 23–42.

16.   S. Nisar, M. A. Sheikh, L. Li, and S. Safdar, "Effect of thermal stresses on chip-free diode laser cutting of glass," Opt. Laser Technol. **41**, 318–327 (2009).

17.	I. Mingareev, F. Weirauch, A. Olowinsky, L. Shah, P. Kadwani, and M. Richardson, "Welding of polymers using a 2μ m thulium fiber laser," Opt. Laser Technol. **44**, 2095–2099 (2012).

18.	J. Bonse, S. Hohm, S. V. Kirner, A. Rosenfeld, and J. Kruger, "Laser-Induced Periodic Surface Structures— A Scientific Evergreen," IEEE J. Sel. Top. Quantum Electron. **23**, (2017).

19.	M. Sparkes and W. M. Steen, ""Light" industry: an overview of the impact of lasers on manufacturing," in *Advances in Laser Materials Processing*, II (Woodhead Publishing, 2018).

20.	J. Bonse, S. Hohm, S. V. Kirner, A. Rosenfeld, and J. Kruger, "Laser-Induced Periodic Surface Structures-A Scientific Evergreen," IEEE J. Sel. Top. Quantum Electron. **23**, 9000615 (2017).

21.	I. Mingareev, L. Shah, M. Richardson, and M. Ramme, *Direct Infrared Laser Machining of Semiconductors for Electronics Applications*, Second Edi (Elsevier Ltd., 2018).

22.	J. Miao, T. Ishikawa, B. Johnson, E. H. Anderson, B. Lai, and K. O. Hodgson, "High Resolution 3D X-Ray Diffraction Microscopy," Phys. Rev. Lett. **89**, 88303 (2002).

23.	W. Chao, B. D. Harteneck, J. A. Liddle, E. H. Anderson, and D. T. Attwood, "Soft X-ray microscopy at a spatial resolution better than 15 nm," Nature **435**, 1210–1213 (2005).

24.	B. J. Hillier, K. S. Christopherson, K. E. Prehoda, D. S. Bredt, and W. A. Lim, "Unexpected modes of PDZ domain scaffolding revealed by structure of nNOS-syntrophin complex," Science (80-.). **284**, 812–815 (1999).

25.	H. Luecke, B. Schobert, H. T. Richter, J. P. Cartailler, and J. K. Lanyi, "Structural changes in bacteriorhodopsin during ion transport at 2 angstrom resolution," Science (80-.). **286**, 255–260 (1999).

26.	R. Neutzo, R. Wouts, D. Van Der Spoel, E. Weckert, and J. Hajdu, "Potential for biomolecular imaging with femtosecond X-ray pulses," Nature **406**, 752–757 (2000).

27.	A. Föhlisch, P. Feulner, F. Hennies, A. Fink, D. Menzel, D. Sanchez-Portal, P. M. Echenique, and W. Wurth, "Direct observation of electron dynamics in the attosecond domain," Nature **436**, 373–376 (2005).

28.	M. Drescher, M. Hentschel, R. Kienberger, M. Uiberacker, V. Yakovlev, A. Scrinzi, T. Westerwalbesloh, U. Kleineberg, U. Heinzmann, and F. Krausz, "Time-resolved atomic inner-shell spectroscopy," Nature **419**, 803–807 (2002).

29.	M. Hentschel, R. Kienberger, C. Spielmann, G. A. Reider, N. Milosevic, T. Brabec, P. Corkum, U. Heinzmann, M. Drescher, and F. Krausz, "Attosecond metrology," Nature **414**, 509–513 (2001).

30.	A. McPherson, G. Gibson, H. Jara, U. Johann, T. S. Luk, I. A. McIntyre, K. Boyer, and C. K. Rhodes, "Studies of multiphoton production of vacuum-ultraviolet radiation in the rare gases," J. Opt. Soc. Am. B **4**, 595–601 (1987).

31.	L. Young, K. Ueda, M. Gühr, P. H. Bucksbaum, M. Simon, S. Mukamel, N. Rohringer, K. C. Prince, C. Masciovecchio, M. Meyer, A. Rudenko, D. Rolles, C. Bostedt, M. Fuchs, D. A. Reis, R. Santra, H. Kapteyn, M. Murnane, H. Ibrahim, F. Légaré, M. Vrakking, M. Isinger, D. Kroon, M. Gisselbrecht, A. L'Huillier, H. J. Wörner, and S. R. Leone, "Roadmap of ultrafast x-ray atomic

and molecular physics," J. Phys. B At. Mol. Opt. Phys. **51**, 32003 (2018).

32.   F. Labaye, M. Gaponenko, N. Modsching, P. Brochard, C. Paradis, S. Schilt, V. J. Wittwer, and T. Sudmeyer, "XUV Sources Based on Intra-Oscillator High Harmonic Generation With Thin-Disk Lasers: Current Status and Prospects," IEEE J. Sel. Top. Quantum Electron. **25**, 1–19 (2019).

33.   D. Strickland and G. Mourou, "Compression of amplified chirped optical pulses," Opt. Commun. **56**, 219–221 (1985).

34.   M.-C. Chen, C. Mancuso, C. Hernandez-Garcia, F. Dollar, B. Galloway, D. Popmintchev, P.-C. Huang, B. Walker, L. Plaja, A. A. Jaro -Becker, A. Becker, M. M. Murnane, H. C. Kapteyn, and T. Popmintchev, "Generation of bright isolated attosecond soft X-ray pulses driven by multicycle midinfrared lasers," Proc. Natl. Acad. Sci. **111**, E2361–E2367 (2014).

35.   T. Popmintchev, M.-C. Chen, D. Popmintchev, P. Arpin, S. Brown, S. Ališauskas, G. Andriukaitis, T. Balč iunas, O. D. Mücke, A. Pugzlys, A. Baltuška, B. Shim, S. E. Schrauth, A. Gaeta, C. Hernández-García, L. Plaja, A. Becker, A. Jaron-Becker, M. M. Murnane, and H. C. Kapteyn, "Bright coherent ultrahigh harmonics in the keV x-ray regime from mid-infrared femtosecond lasers," Science (80-.). **336**, 1287–1291 (2012).

36.   F. Gunning and B. Corbett, "Time to Open the 2-µ m Window?," Opt. Photonics News (2019).

37.   A. D. Ellis, J. Zhao, and D. Cotter, "Approaching the Non-Linear Shannon Limit," J. Light. Technol. **28**, 423–433 (2010).

38.   D. J. Richardson, "Filling the Light Pipe," Science (80-.). **330**, 327–328 (2010).

39.   M. N. Petrovich, F. Poletti, J. P. Wooler, A. M. Heidt, N. K. Baddela, Z. Li, D. R. Gray, R. Slavík, F. Parmigiani, N. V. Wheeler, J. R. Hayes, E. Numkam, L. Grű ner-Nielsen, B. Pálsdóttir, R. Phelan, B. Kelly, J. O'Carroll, M. Becker, N. MacSuibhne, J. Zhao, F. C. G. Gunning, A. D. Ellis, P. Petropoulos, S. U. Alam, and D. J. Richardson, "Demonstration of amplified data transmission at 2 µm in a low-loss wide bandwidth hollow core photonic bandgap fiber," Opt. Express **21**, 28559–28569 (2013).

40.   H. Zhang, N. Kavanagh, Z. Li, J. Zhao, N. Ye, Y. Chen, N. V. Wheeler, J. P. Wooler, J. R. Hayes, S. R. Sandoghchi, F. Poletti, M. N. Petrovich, S. U. Alam, R. Phelan, J. O'Carroll, B. Kelly, L. Grüner-Nielsen, D. J. Richardson, B. Corbett, and F. C. Garcia Gunning, "100 Gbit/s WDM transmission at 2 µm: transmission studies in both low-loss hollow core photonic bandgap fiber and solid core fiber," Opt. Express **23**, 4946–4951 (2015).

41.   Z. Li, A. M. Heidt, J. M. O. Daniel, Y. Jung, S. U. Alam, and D. J. Richardson, "Thulium-doped fiber amplifier for optical communications at 2 µm," Opt. Express **21**, 9289–9297 (2013).

42.   Z. Li, A. M. Heidt, N. Simakov, Y. Jung, J. M. O. Daniel, S. U. Alam, and D. J. Richardson, "Diode-pumped wideband thulium-doped fiber amplifiers for optical communications in the 1800 – 2050 nm window," Opt. Express **21**, 26450–26455 (2013).

43.   W. Cao, D. Hagan, D. J. Thomson, M. Nedeljkovic, C. G. Littlejohns, A. Knights, S.-U. Alam, J. Wang, F. Gardes, W. Zhang, S. Liu, K. Li, M. S. Rouifed, G. Xin, W. Wang, H. Wang, G. T. Reed, and G. Z. Mashanovich, "High-speed silicon modulators for the 2 µ m wavelength band," Optica **5**, 1055–1062 (2018).

44.   A. Schliesser, N. Picqué, and T. W. Hänsch, "Mid-infrared frequency combs," Nat. Photonics **6**, 440–449 (2012).

45.   O. Kara, F. Sweeney, M. Rutkauskas, C. Farrell, C. G. Leburn, and D. T. Reid, "Open-path multi-species remote sensing with a broadband optical parametric oscillator," Opt. Express **27**, 21358–21366 (2019).

46.   J. Thomas, A. Polak, and D. J. M. Stothard, "Quantum cascade laser-based trace detection of gases in the deep-infrared region using phase fluctuation optical heterodyne spectroscopy," in *Chemical, Biological, Radiological, Nuclear, and Explosives (CBRNE) Sensing XX*, J. A. Guicheteau and C. R. Howle, eds. (SPIE, 2019), p. 40.

47.   L. Maidment, Z. Zhang, C. R. Howle, and D. T. Reid, "Stand-off identification of aerosols using mid-infrared backscattering Fourier-transform spectroscopy," Opt. Lett. **41**, 2266–2269 (2016).

48.   Z. Zhang, R. J. Clewes, C. R. Howle, and D. T. Reid, "Active FTIR-based stand-off spectroscopy using a femtosecond optical parametric oscillator," Opt. Lett. **39**, 6005–6008 (2014).

49.   P. G. Schunemann, K. T. Zawilski, L. A. Pomeranz, D. J. Creeden, and P. A. Budni, "Advances in nonlinear optical crystals for mid-infrared coherent sources," J. Opt. Soc. Am. B **33**, D36–D43 (2016).

50.   S. Chaitanya Kumar, J. Krauth, A. Steinmann, K. T. Zawilski, P. G. Schunemann, H. Giessen, and M. Ebrahim-Zadeh, "High-power femtosecond mid-infrared optical parametric oscillator at 7 μm based on CdSiP2," Opt. Lett. **40**, 1398–1401 (2015).

51.   L. Maidment, O. Kara, P. G. Schunemann, J. Piper, K. McEwan, and D. T. Reid, "Long-wave infrared generation from femtosecond and picosecond optical parametric oscillators based on orientation-patterned gallium phosphide," Appl. Phys. B **124**, 143 (2018).

52.   N. Leindecker, A. Marandi, R. L. Byer, K. L. Vodopyanov, J. Jiang, I. Hartl, M. Fermann, and P. G. Schunemann, "Octave-spanning ultrafast OPO with 2.6-6.1μm instantaneous bandwidth pumped by femtosecond Tm-fiber laser," Opt. Express **20**, 7046–7053 (2012).

53.   C. Gmachl, F. Capasso, D. L. Sivco, and A. Y. Cho, "Recent progress in quantum cascade lasers and applications," Reports Prog. Phys. **64**, 1533–1601 (2001).

54.   P. Rauter and F. Capasso, "Multi-wavelength quantum cascade laser arrays," Laser Photon. Rev. **9**, 452–477 (2015).

55.   K. Ohtani, M. Beck, M. J. Süess, J. Faist, A. M. Andrews, T. Zederbauer, H. Detz, W. Schrenk, and G. Strasser, "Far-Infrared Quantum Cascade Lasers Operating in the AlAs Phonon Reststrahlen Band," ACS Photonics **3**, 2280–2284 (2016).

56.   J. Hodgkinson and R. P. Tatam, "Optical gas sensing: a review," Meas. Sci. Technol. **24**, 12004 (2013).

57.   S. B. Mirov, V. V. Fedorov, D. Martyshkin, I. S. Moskalev, M. Mirov, and S. Vasilyev, "Progress in Mid-IR Lasers Based on Cr and Fe-Doped II–VI Chalcogenides," IEEE J. Sel. Top. Quantum Electron. **21**, 292–310 (2015).

58.   S. Vasilyev, I. Moskalev, M. Mirov, S. Mirov, and V. Gapontsev, "Multi-Watt mid-IR femtosecond polycrystalline Cr^2+:ZnS and Cr^2+:ZnSe laser amplifiers

with the spectrum spanning 2.0–2.6 μm," Opt. Express **24**, 1616–1623 (2016).

59. P. Koopmann, S. Lamrini, K. Scholle, M. Schäfer, P. Fuhrberg, and G. Huber, "Holmium-doped Lu2O3, Y2O3, and Sc2O3 for lasers above 2.1 μm," Opt. Express **21**, 3926–3931 (2013).

60. P. Koopmann, S. Lamrini, K. Scholle, P. Fuhrberg, K. Petermann, and G. Huber, "Efficient diode-pumped laser operation of Tm:Lu2O3 around 2 μm," Opt. Lett. **36**, 948–950 (2011).

61. J. J. Pigeon, S. Y. Tochitsky, C. Gong, and C. Joshi, "Supercontinuum generation from 2 to 20 μm in GaAs pumped by picosecond CO2 laser pulses," Opt. Lett. **39**, 3246–3249 (2014).

62. C. R. Petersen, U. Møller, I. Kubat, B. Zhou, S. Dupont, J. Ramsay, T. Benson, S. Sujecki, N. Abdel-Moneim, Z. Tang, D. Furniss, A. Seddon, and O. Bang, "Mid-infrared supercontinuum covering the 1.4–13.3 μm molecular fingerprint region using ultra-high NA chalcogenide step-index fibre," Nat. Photonics **8**, 830–834 (2014).

63. U. Møller, Y. Yu, I. Kubat, C. R. Petersen, X. Gai, L. Brilland, D. Méchin, C. Caillaud, J. Troles, B. Luther-Davies, and O. Bang, "Multi-milliwatt mid-infrared supercontinuum generation in a suspended core chalcogenide fiber," Opt. Express **23**, 3282–3291 (2015).

64. I. Kubat, C. Rosenberg Petersen, U. V. Møller, A. Seddon, T. Benson, L. Brilland, D. Méchin, P. M. Moselund, and O. Bang, "Thulium pumped mid-infrared 0.9–9μm supercontinuum generation in concatenated fluoride and chalcogenide glass fibers," Opt. Express **22**, 3959–3967 (2014).

65. Y. Yu, X. Gai, P. Ma, D.-Y. Choi, Z. Yang, R. Wang, S. Debbarma, S. J. Madden, and B. Luther-Davies, "A broadband, quasi-continuous, mid-infrared supercontinuum generated in a chalcogenide glass waveguide," Laser Photon. Rev. **8**, 792–798 (2014).

66. D. D. Hudson, S. Antipov, L. Li, I. Alamgir, T. Hu, M. El Amraoui, Y. Messaddeq, M. Rochette, S. D. Jackson, and A. Fuerbach, "Toward all-fiber supercontinuum spanning the mid-infrared," Optica **4**, 1163 (2017).

67. C. R. Petersen, R. D. Engelsholm, C. Markos, L. Brilland, C. Caillaud, J. Trolès, and O. Bang, "Increased mid-infrared supercontinuum bandwidth and average power by tapering large-mode-area chalcogenide photonic crystal fibers," Opt. Express **25**, 15336–15347 (2017).

68. F. Adler, K. C. Cossel, M. J. Thorpe, I. Hartl, M. E. Fermann, and J. Ye, "Phase-stabilized, 1.5 W frequency comb at 2.8–4.8 μm," Opt. Lett. **34**, 1330–1332 (2009).

69. C. Gaida, M. Gebhardt, T. Heuermann, F. Stutzki, C. Jauregui, J. Antonio-Lopez, A. Schülzgen, R. Amezcua-Correa, A. Tünnermann, I. Pupeza, and J. Limpert, "Watt-scale super-octave mid-infrared intrapulse difference frequency generation," Light Sci. Appl. **7**, 94 (2018).

70. R. Holzwarth, M. Zimmermann, T. Udem, and T. W. Hansch, "Optical clockworks and the measurement of laser frequencies with a mode-locked frequency comb," IEEE J. Quantum Electron. **37**, 1493–1501 (2001).

71. M. Takamoto, F.-L. Hong, R. Higashi, and H. Katori, "An optical lattice clock," Nature **435**, 321–324 (2005).

72. S. A. Diddams, "The evolving optical frequency comb [Invited]," J. Opt. Soc.

Am. B **27**, B51 (2010).

73.   G. B. Rieker, F. R. Giorgetta, W. C. Swann, J. Kofler, A. M. Zolot, L. C. Sinclair, E. Baumann, C. Cromer, G. Petron, C. Sweeney, P. P. Tans, I. Coddington, and N. R. Newbury, "Frequency-comb-based remote sensing of greenhouse gases over kilometer air paths," Optica **1**, 290–298 (2014).

74.   O. Meyer-Streng, "Frequency combs in the molecular fingerprint region," Max Plank Ist. Quantum Opt. 1–2 (2015).

75.   A. Schliesser, O. Arcizet, T. Wilken, R. Holzwarth, T. J. Kippenberg, P. Del'Haye, and P. Del Haye, "Optical frequency comb generation from a monolithic microresonator.," Nature **450**, 1214–1217 (2007).

76.   T. J. Kippenberg, R. Holzwarth, and S. a Diddams, "Microresonator-based optical frequency combs.," Science **332**, 555–559 (2011).

77.   I. Pupeza, D. Sánchez, J. Zhang, N. Lilienfein, M. Seidel, N. Karpowicz, T. Paasch-Colberg, I. Znakovskaya, M. Pescher, W. Schweinberger, V. Pervak, E. Fill, O. Pronin, Z. Wei, F. Krausz, A. Apolonski, and J. Biegert, "High-power sub-two-cycle mid-infrared pulses at 100 MHz repetition rate," Nat. Photonics **9**, 721–724 (2015).

78.   S. Vasilyev, I. S. Moskalev, V. O. Smolski, J. M. Peppers, M. Mirov, A. V. Muraviev, K. Zawilski, P. G. Schunemann, S. B. Mirov, K. L. Vodopyanov, and V. P. Gapontsev, "Octave-Spanning Mid-Infrared Intrapulse Difference Frequency Generation With A Few-Cycle Cr:ZnS Laser," in *Conference on Lasers and Electro-Optics* (OSA, 2019), p. STh4E.6.

79.   C. Lecaplain, C. Javerzac-Galy, E. Lucas, J. D. Jost, and T. J. Kippenberg, "Quantum cascade laser-based Kerr frequency comb generation," in *CLEO: 2015* (OSA, 2015), Vol. 2014–Janua, p. SW4F.2.

80.   A. A. Savchenkov, V. S. Ilchenko, F. Di Teodoro, P. M. Belden, W. T. Lotshaw, A. B. Matsko, and L. Maleki, "Generation of Kerr combs centered at 4.5 µm in crystalline microresonators pumped with quantum-cascade lasers.," Opt. Lett. **40**, 3468–71 (2015).

81.   C. Y. Wang, L. Kuznetsova, V. M. Gkortsas, L. Diehl, F. X. Kärtner, M. A. Belkin, A. Belyanin, X. Li, D. Ham, H. Schneider, P. Grant, C. Y. Song, S. Haffouz, Z. R. Wasilewski, H. C. Liu, and F. Capasso, "Mode-locked pulses from mid-infrared Quantum Cascade Lasers," Opt. Express **17**, 12929 (2009).

82.   S. Barbieri, M. Ravaro, P. Gellie, G. Santarelli, C. Manquest, C. Sirtori, S. P. Khanna, E. H. Linfield, and A. G. Davies, "Coherent sampling of active mode-locked terahertz quantum cascade lasers and frequency synthesis," Nat. Photonics **5**, 306–313 (2011).

83.   M. Bagheri, C. Frez, L. A. Sterczewski, I. Gruidin, M. Fradet, I. Vurgaftman, C. L. Canedy, W. W. Bewley, C. D. Merritt, C. S. Kim, M. Kim, and J. R. Meyer, "Passively mode-locked interband cascade optical frequency combs," Sci. Rep. **8**, 1–7 (2018).

84.   A. Hugi, G. Villares, S. Blaser, H. C. Liu, and J. Faist, "Mid-infrared frequency comb based on a quantum cascade laser.," Nature **492**, 229–33 (2012).

85.   D. Burghoff, T.-Y. Kao, N. Han, C. W. I. Chan, X. Cai, Y. Yang, D. J. Hayton, J.-R. Gao, J. L. Reno, and Q. Hu, "Terahertz laser frequency combs," Nat. Photonics **8**, 462–467 (2014).

86.   L. Consolino, M. Nafa, F. Cappelli, K. Garrasi, F. P. Mezzapesa, L. Li, A. G. Davies, E. H. Linfield, M. S. Vitiello, P. De Natale, and S. Bartalini, "Fully

phase-stabilized quantum cascade laser frequency comb," Nat. Commun. **10**, 2938 (2019).

87.   G. Villares, A. Hugi, S. Blaser, and J. Faist, "Dual-comb spectroscopy based on quantum-cascade-laser frequency combs.," Nat. Commun. **5**, 5192 (2014).

88.   G. Villares, J. Wolf, D. Kazakov, M. J. Süess, A. Hugi, M. Beck, and J. Faist, "On-chip dual-comb based on quantum cascade laser frequency combs," Appl. Phys. Lett. **107**, 251104 (2015).

89.   K. Kieu and F. W. Wise, "Soliton Thulium-Doped Fiber Laser With Carbon Nanotube Saturable Absorber," IEEE Photonics Technol. Lett. **21**, 128–130 (2009).

90.   M. Engelbrecht, F. Haxsen, A. Ruehl, D. Wandt, and D. Kracht, "Ultrafast thulium-doped fiber-oscillator with pulse energy of 4.3 nJ," Opt. Lett. **33**, 690–692 (2008).

91.   M. Jung, J. Koo, J. Park, Y.-W. Song, Y. M. Jhon, K. Lee, S. Lee, and J. H. Lee, "Mode-locked pulse generation from an all-fiberized, Tm-Ho-codoped fiber laser incorporating a graphene oxide-deposited side-polished fiber," Opt. Express **21**, 20062–20072 (2013).

92.   R. C. Sharp, D. E. Spock, N. Pan, and J. Elliot, "190-fs Passively Mode-Locked Thulium Fiber Laser With a Low Threshold," Opt. Lett. **21**, 881–883 (1996).

93.   Q. Wang, J. Geng, T. Luo, and S. Jiang, "Mode-locked 2 µ m laser with highly thulium-doped silicate fiber," Opt. Lett. **34**, 3616–3618 (2009).

94.   R. Kadel and B. R. Washburn, "All-fiber passively mode-locked thulium/holmium laser with two center wavelengths," Appl. Opt. **51**, 6465 (2012).

95.   S. A. Filatova, V. A. Kamynin, N. R. Arutyunyan, A. S. Pozharov, A. I. Trikshev, I. V. Zhluktova, I. O. Zolotovskii, E. D. Obraztsova, and V. B. Tsvetkov, "Hybrid mode locking of an all-fiber holmium laser," J. Opt. Soc. Am. B **35**, 3122–3125 (2018).

96.   P. A. Budni, L. A. Pomeranz, M. L. Lemons, C. A. Miller, J. R. Mosto, and E. P. Chicklis, "Efficient mid-infrared laser using 1.9-µm-pumped Ho:YAG and ZnGeP2 optical parametric oscillators," J. Opt. Soc. Am. B **17**, 723–728 (2000).

97.   J. Swiderski, "High-power mid-infrared supercontinuum sources: current status and future perspectives," Prog. Quantum Electron. **38**, 189–235 (2014).

98.   L. D. DeLoach, R. H. Page, G. D. Wilke, S. A. Payne, and W. F. Krupke, "Transition metal-doped zinc chalcogenides: Spectroscopy and laser demonstration of a new class of gain media," IEEE J. Quantum Electron. **32**, 885–895 (1996).

99.   R. H. Page, K. I. Schaffers, L. D. DeLoach, G. D. Wilke, F. D. Patel, J. B. Tassano, S. A. Payne, W. F. Krupke, K.-T. Chen, and A. Burger, "Cr2+ -doped zinc chalcogenides as efficient, widely tunable mid-infrared lasers," IEEE J. Quantum Electron. **33**, 609–619 (1997).

100.   I. T. Sorokina and E. Sorokin, "Femtosecond Cr 2 + -Based Lasers," IEEE J. Sel. Top. Quantum Electron. **21**, 2–4 (2015).

101.   Y. Wang, T. T. Fernandez, N. Coluccelli, A. Gambetta, P. Laporta, and G. Galzerano, "47-fs Kerr-lens mode-locked Cr:ZnSe laser with high spectral purity," Opt. Express **25**, 25193–25200 (2017).

102. S. Vasilyev, I. Moskalev, M. Mirov, S. Mirov, and V. Gapontsev, "Three optical cycle mid-IR Kerr-lens mode-locked polycrystalline Cr^2+:ZnS laser," Opt. Lett. **40**, 5054–5057 (2015).

103. E. Sorokin, N. Tolstik, K. I. Schaffers, and I. T. Sorokina, "Femtosecond SESAM-modelocked Cr:ZnS laser," Opt. Express **20**, 28947–28952 (2012).

104. S. Xie, F. Tani, J. C. Travers, P. Uebel, C. Caillaud, J. Troles, M. A. Schmidt, and P. S. J. Russell, "As2S3-silica double-nanospike waveguide for mid-infrared supercontinuum generation.," Opt. Lett. **39**, 5216–5219 (2014).

105. S. Xie, N. Tolstik, J. C. Travers, E. Sorokin, C. Caillaud, J. Troles, P. S. J. Russell, and I. T. Sorokina, "Coherent octave-spanning mid-infrared supercontinuum generated in As_2S_3-silica double-nanospike waveguide pumped by femtosecond Cr:ZnS laser," Opt. Express **24**, 12406–12413 (2016).

106. S. Mirov, V. Fedorov, I. Moskalev, D. Martyshkin, and C. Kim, "Progress in Cr2+ and Fe2+ doped mid-IR laser materials," Laser Photonics Rev. **4**, 21–41 (2010).

107. S. Mirov, V. Fedorov, I. Moskalev, M. Mirov, and D. Martyshkin, "Frontiers of mid-infrared lasers based on transition metal doped II-VI semiconductors," J. Lumin. **133**, 268–275 (2013).

108. A. Lancaster, G. Cook, S. A. McDaniel, J. Evans, P. A. Berry, J. D. Shephard, and A. K. Kar, "Mid-infrared laser emission from Fe:ZnSe cladding waveguides," Appl. Phys. Lett. **107**, (2015).

109. M. P. Frolov, Y. V Korostelin, V. I. Kozlovsky, Y. P. Podmar'kov, S. a Savinova, and Y. K. Skasyrsky, "3 J pulsed Fe:ZnS laser tunable from 3.44 to 4.19 μ m," Laser Phys. Lett. **12**, 55001 (2015).

110. T. Dai, C. Guo, Y. Li, Y. Ju, B. Yao, and X. Duan, "A room temperature operation mid-IR Fe:ZnSe laser pumped by Ho,Pr:LiLuF4 laser at 2.9-μ m," Opt. Laser Technol. **118**, 179–182 (2019).

111. F. V Potemkin, E. A. Migal, A. V Pushkin, A. A. Sirotkin, V. I. Kozlovsky, Y. V Korostelin, Y. P. Podmar'kov, V. V Firsov, M. P. Frolov, and V. M. Gordienko, "Mid-IR (4–5 μ m) femtosecond multipass amplification of optical parametric seed pulse up to gigawatt level in Fe 2+ :ZnSe with optical pumping by a solid-state 3 μ m laser," Laser Phys. Lett. **13**, 125403 (2016).

112. E. Migal, A. Pushkin, B. Bravy, V. Gordienko, N. Minaev, A. Sirotkin, and F. Potemkin, "35-mJ 150-fs Fe:ZnSe hybrid mid-IR femtosecond laser at 44 μ m for driving extreme nonlinear optics," Opt. Lett. **44**, 2550–2553 (2019).

113. J. Ma, Z. Qin, G. Xie, L. Qian, and D. Tang, "Review of mid-infrared mode-locked laser sources in the 2.0 μ m–3.5 μ m spectral region," Appl. Phys. Rev. **6**, 21317 (2019).

114. N. Nagl, S. Gröbmeyer, V. Pervak, F. Krausz, O. Pronin, and K. F. Mak, "Directly diode-pumped, Kerr-lens mode-locked, few-cycle Cr:ZnSe oscillator," Opt. Express **27**, 24445 (2019).

115. S. Amini-Nik, D. Kraemer, M. L. Cowan, K. Gunaratne, P. Nadesan, B. A. Alman, and R. J. D. Miller, "Ultrafast mid-IR laser scalpel: protein signals of the fundamental limits to minimally invasive surgery," PLoS One **5**, e13053 (2010).

116. V. Petrov, F. Rotermund, and F. Noack, "Generation of high-power femtosecond light pulses at 1 kHz in the mid-infrared spectral range between 3 and 12 μm by second-order nonlinear processes in optical crystals," J. Opt. A

Pure Appl. Opt. **3**, R1–R19 (2001).

117.   D. M. Bubb, M. R. Papantonakis, J. S. Horwitz, R. F. Haglund Jr., B. Toftmann, R. A. McGill, and D. B. Chrisey, "Vapor deposition of polystyrene thin films by intense laser vibrational excitation," Chem. Phys. Lett. **352**, 135–139 (2002).

118.   B. Wolter, M. G. Pullen, M. Baudisch, M. Sclafani, M. Hemmer, A. Senftleben, C. D. Schröter, J. Ullrich, R. Moshammer, and J. Biegert, "Strong-Field Physics with Mid-IR Fields," Phys. Rev. X **5**, 21034 (2015).

119.   A. E. Siegman, *Lasers* (University Science Books, 1986).

120.   O. Svelto, *Principles of Lasers*, V (Springer, 2010).

121.   J.-C. Diels and W. Rudolph, *Ultrashort Laser Pulse Phenomena*, II (Elsevier, 2006).

122.   S. G. Grubb, K. W. Bennett, R. S. Cannon, and W. F. Humer, "CW room-temperature blue upconversion fibre laser," Electron. Lett. **28**, 1243 (1992).

123.   R. Paschotta, N. Moore, W. A. Clarkson, A. C. Tropper, D. C. Hanna, and G. Maze, "230 mW of blue light from a thulium-doped upconversion fiber laser," IEEE J. Sel. Top. Quantum Electron. **3**, 1100–1102 (1997).

124.   D. N. Messias, M. V. D. Vermelho, M. T. de Araujo, A. S. Gouveia-Neto, and J. S. Aitchison, "Blue energy upconversion emission in thulium-doped-SiO2-P2O5 channel waveguides excited at 1.064 µ m," IEEE J. Quantum Electron. **38**, 1647–1650 (2002).

125.   L. F. Johnson, "Optical Maser Characteristics of Rare-Earth Ions in Crystals," J. Appl. Phys. **34**, 897 (1963).

126.   J. A. Caird, L. G. DeShazer, and J. Nella, "Characteristics of room-temperature 2.3-µ m laser emission from Tm3+ in YAG and YAlO3," IEEE J. Quantum Electron. **11**, 874–881 (1975).

127.   P. F. Moulton, "Spectroscopic and laser characteristics of Ti:Al2O3," J. Opt. Soc. Am. B **3**, 125 (1986).

128.   P. F. Moulton, G. A. Rines, E. V. Slobodtchikov, K. F. Wall, G. Frith, B. Samson, and A. L. G. Carter, "Tm-doped fiber lasers: Fundamentals and power scaling," IEEE J. Sel. Top. Quantum Electron. **15**, 85–92 (2009).

129.   P. Koopmann, "Thulium- and Holmium-Doped Sesquioxides for 2µm Lasers," University of Hamburg (2012).

130.   C. T. Wu, Y. L. Ju, F. Chen, and G. Y. Jin, "Research on 2-µ m solid-state lasers," Laser Phys. **22**, 635–647 (2012).

131.   Y. Wang, W. Chen, M. Mero, L. Zhang, H. Lin, Z. Lin, G. Zhang, F. Rotermund, Y. J. Cho, P. Loiko, X. Mateos, U. Griebner, and V. Petrov, "Sub-100 fs Tm:MgWO_4 laser at 2017 nm mode locked by a graphene saturable absorber," Opt. Lett. **42**, 3076–3079 (2017).

132.   Y. Wang, Y. Zhao, Z. Pan, J. E. Bae, S. Y. Choi, F. Rotermund, P. Loiko, J. M. Serres, X. Mateos, H. Yu, H. Zhang, M. Mero, U. Griebner, and V. Petrov, "78 fs SWCNT-SA mode-locked Tm:CLNGG disordered garnet crystal laser at 2017 nm," Opt. Lett. **43**, 4268–4271 (2018).

133.   Y. Wang, W. Jing, P. Loiko, Y. Zhao, H. Huang, X. Mateos, S. Suomalainen, A. Härkönen, M. Guina, U. Griebner, and V. Petrov, "Sub-10 optical-cycle passively mode-locked Tm:(Lu2/3Sc1/3)2O3 ceramic laser at 2 µm," Opt. Express **26**, 10299–10304 (2018).

134. E. P. Chicklis, C. S. Naiman, R. C. Folweiler, D. R. Gabbe, H. P. Jenssen, and A. Linz, "High-efficiency room-temperature 2.06-µ m laser using sensitized Ho 3+:YLF," Appl. Phys. Lett. **19**, 119–121 (1971).

135. K. Scholle and P. Fuhrberg, "In-band pumping of high-power Ho:YAG lasers by laser diodes at 1.9µ m," in *2008 Conference on Quantum Electronics and Laser Science Conference on Lasers and Electro-Optics, CLEO/QELS* (IEEE, 2008), pp. 90–91.

136. S. Lamrini, P. Koopmann, M. Schäfer, K. Scholle, and P. Fuhrberg, "Efficient high-power Ho:YAG laser directly in-band pumped by a GaSb-based laser diode stack at 1.9 µ m," Appl. Phys. B Lasers Opt. **106**, 315–319 (2012).

137. A. Berrou, T. Ibach, M. Schellhorn, W. Hu, R. Lammert, L. Vaissié, J. Ungar, and M. Eichhorn, "Crystalline fiber Ho 3+ :YAG laser resonantly pumped by high-spectral-brightness laser diodes," in *Solid State Lasers XXI - Technology and Devices* (SPIE, 2012), p. 823518.

138. I. F. Elder and M. J. P. Payne, "Lasing in diode-pumped Tm : YAP, Tm,Ho : YAP and Tm,Ho : YLF," Opt. Commun. **145**, 329–339 (1998).

139. V. Sudesh and K. Asai, "Spectroscopic and diode-pumped-laser properties of Tm, Ho:YLF; Tm, Ho:LuLF; and Tm, Ho:LuAG crystals: a comparative study," J. Opt. Soc. Am. B **20**, 1829 (2003).

140. Y. Zhao, Y. Wang, W. Chen, Z. Pan, L. Wang, X. Dai, H. Yuan, Y. Zhang, H. Cai, J. E. Bae, S. Y. Choi, F. Rotermund, P. Loiko, J. M. Serres, X. Mateos, W. Zhou, D. Shen, U. Griebner, and V. Petrov, "67-fs pulse generation from a mode-locked Tm,Ho:CLNGG laser at 2083 nm," Opt. Express **27**, 1922–1928 (2019).

141. Z. Pan, Y. Wang, Y. Zhao, M. Kowalczyk, J. Sotor, H. Yuan, Y. Zhang, X. Dai, H. Cai, J. E. Bae, S. Y. Choi, F. Rotermund, P. Loiko, J. M. Serres, X. Mateos, U. Griebner, and V. Petrov, "Sub-80 fs mode-locked Tm,Ho-codoped disordered garnet crystal oscillator operating at 2081 nm," Opt. Lett. **43**, 5154–5157 (2018).

142. Y. Zhao, Y. Wang, X. Zhang, X. Mateos, Z. Pan, P. Loiko, W. Zhou, X. Xu, J. Xu, D. Shen, S. Suomalainen, A. Härkönen, M. Guina, U. Griebner, and V. Petrov, "87 fs mode-locked Tm,Ho:CaYAlO 4 laser at ~2043 nm," Opt. Lett. **43**, 915–918 (2018).

143. A. A. Lagatsky, X. Han, M. D. Serrano, C. Cascales, C. Zaldo, S. Calvez, M. D. Dawson, J. A. Gupta, C. T. A. Brown, and W. Sibbett, "Femtosecond (191 fs) NaY(WO4)2 Tm,Ho-codoped laser at 2060 nm," Opt. Lett. **35**, 3027–3029 (2010).

144. A. A. Lagatsky, F. Fusari, S. Calvez, S. V Kurilchik, V. E. Kisel, N. V Kuleshov, M. D. Dawson, C. T. A. Brown, and W. Sibbett, "Femtosecond pulse operation of a Tm,Ho-codoped crystalline laser near 2 µ m," Opt. Lett. **35**, 172–174 (2010).

145. V. Aleksandrov, A. Gluth, V. Petrov, I. Buchvarov, S. Y. Choi, M. H. Kim, F. Rotermund, X. Mateos, F. Díaz, and U. Griebner, "Tm,Ho:KLu(WO4)2 laser mode-locked near 2 µ m by single-walled carbon nanotubes," Opt. Express **22**, 26872–26877 (2014).

146. A. A. Lagatsky, F. Fusari, S. Calvez, J. A. Gupta, V. E. Kisel, N. V Kuleshov, C. T. A. Brown, M. D. Dawson, and W. Sibbett, "Passive mode locking of a Tm,Ho:KY(WO4)2 laser around 2 µ m," Opt. Lett. **34**, 2587–2589 (2009).

147. V. Aleksandrov, A. Gluth, V. Petrov, I. Buchvarov, G. Steinmeyer, J. Paajaste, S. Suomalainen, A. Hürkünen, M. Guina, X. Mateos, F. Díaz, and U. Griebner, "Mode-locked Tm,Ho:KLu(WO4)2 laser at 2060 nm using InGaSb-based SESAMs," Opt. Express **23**, 4614–4619 (2015).

148. O. Svelto, "Solid-State, Dye, and Semiconductor Lasers," in *Principles of Lasers*, V (Springer, 2010), pp. 375–430.

149. D. A. Neamen, "Optical Devices," in *Semiconductor Physics and Devices* (McGraw-Hill Education, 2012), pp. 618–669.

150. U. Keller, "2.1 Ultrafast solid-state lasers," in *Laser Physics and Applications* (Springer-Verlag, 2007).

151. O. Svelto, "Transient Laser Behavior," in *Principles of Lasers* (Springer US, 2010), pp. 313–373.

152. D. E. Spence, P. N. Kean, and W. Sibbett, "60-fsec pulse generation from a self-mode-locked Ti:sapphire laser.," Opt. Lett. **16**, 42–44 (1991).

153. U. Keller, "Recent developments in compact ultrafast lasers.," Nature **424**, 831–838 (2003).

154. F. Salin, M. Piché, and J. Squier, "Mode locking of Ti:Al_2O_3 lasers and self-focusing: a Gaussian approximation," Opt. Lett. **16**, 1674–1676 (1991).

155. G. Cerullo, S. De Silvestri, and V. Magni, "Self-starting Kerr-lens mode locking of a Ti:sapphire laser," Opt. Lett. **19**, 1040–1042 (1994).

156. I. D. Jung, F. X. Kärtner, N. Matuschek, D. H. Sutter, F. Morier-Genoud, Z. Shi, V. Scheuer, M. Tilsch, T. Tschudi, and U. Keller, "Semiconductor saturable absorber mirrors supporting sub-10-fs pulses," Appl. Phys. B Lasers Opt. **65**, 137–150 (1997).

157. D. H. Sutter, G. Steinmeyer, L. Gallmann, N. Matuschek, F. Morier-Genoud, U. Keller, V. Scheuer, G. Angelow, and T. Tschudi, "Semiconductor saturable-absorber mirror–assisted Kerr-lens mode-locked Ti:sapphire laser producing pulses in the two-cycle regime," Opt. Lett. **24**, 631 (1999).

158. U. Keller, D. A. B. Miller, G. D. Boyd, T. H. Chiu, J. F. Ferguson, and M. T. Asom, "Solid-state low-loss intracavity saturable absorber for Nd:YLF lasers: an antiresonant semiconductor Fabry–Perot saturable absorber," Opt. Lett. **17**, 505 (1992).

159. U. Keller, K. J. Weingarten, F. X. Kärtner, D. Kopf, B. Braun, I. D. Jung, R. Fluck, C. Hönninger, N. Matuschek, and J. Aus Der Au, "Semiconductor saturable absorber mirrors (SESAM's) for femtosecond to nanosecond pulse generation in solid-state lasers," IEEE J. Sel. Top. Quantum Electron. **2**, 435–451 (1996).

160. E. Lugagne Delpon, J. L. Oudar, N. Bouché, R. Raj, A. Shen, N. Stelmakh, and J. M. Lourtioz, "Ultrafast excitonic saturable absorption in ion-implanted InGaAs/InAlAs multiple quantum wells," Appl. Phys. Lett. **72**, 759–761 (1998).

161. M. J. Lederer, V. Kolev, B. Luther-Davies, H. H. Tan, and C. Jagadish, "Ion-implanted InGaAs single quantum well semiconductor saturable absorber mirrors for passive mode-locking," J. Phys. D. Appl. Phys. **34**, 2455–2464 (2001).

162. C. G. Leburn and D. T. Reid, "Advances in Solid-State Ultrafast Laser Oscillators," in *Ultrafast Nonlinear Optics*, R. Thomson, C. Leburn, and D. Reid, eds. (Springer International Publishing, 2013).

163.   E. U. Rafailov, S. J. White, A. A. Lagatsky, A. Miller, W. Sibbett, D. A. Livshits, A. E. Zhukov, and V. M. Ustinov, "Fast Quantum-Dot Saturable Absorber for Passive Mode-Locking of Solid-State Lasers," IEEE Photonics Technol. Lett. **16**, 2439–2441 (2004).

164.   A. A. Lagatsky, C. G. Leburn, C. T. A. Brown, W. Sibbett, S. A. Zolotovskaya, and E. U. Rafailov, "Ultrashort-pulse lasers passively mode locked by quantum-dot-based saturable absorbers," Prog. Quantum Electron. **34**, 1–45 (2010).

165.   F. X. Kärtner and U. Keller, "Stabilization of solitonlike pulses with a slow saturable absorber," Opt. Lett. **20**, 16–18 (1995).

166.   H. A. Haus, "Mode-locking of lasers," IEEE J. Sel. Top. Quantum Electron. **6**, 1173–1185 (2000).

167.   F. X. Kärtner, J. Aus-der-Au, and U. Keller, "Mode-locking with slow and fast saturable absorbers-what's the difference?," IEEE J. Sel. Top. Quantum Electron. **4**, 159–168 (1998).

168.   M. J. Lederer, B. Luther-Davies, H. H. Tan, C. Jagadish, N. N. Akhmediev, and J. M. Soto-Crespo, "Multipulse operation of a Ti:sapphire laser mode locked by an ion-implanted semiconductor saturable-absorber mirror," J. Opt. Soc. Am. B **16**, 895 (1999).

169.   F. X. Kaertner, L. R. Brovelli, D. Kopf, M. Kamp, I. G. Calasso, and U. Keller, "Control of solid state laser dynamics by semiconductor devices," Opt. Eng. **34**, 2024–2036 (1995).

170.   C. Hönninger, R. Paschotta, F. Morier-Genoud, M. Moser, and U. Keller, "Q-switching stability limits of continuous-wave passive mode locking," J. Opt. Soc. Am. B **16**, 46 (1999).

171.   V. G. Savitski, A. J. Kemp, S. Calvez, and D. Burns, "Optically Pumped Saturable Bragg Reflectors: Nonlinear Spectroscopy and Application in Ultrafast Lasers," IEEE J. Quantum Electron. **46**, 1650–1655 (2010).

172.   C. Crombie, D. A. Walsh, W. Lu, S. Zhang, Z. Zhang, K. Kennedy, S. Calvez, W. Sibbett, and C. T. A. Brown, "Electrically-controlled rapid femtosecond pulse duration switching and continuous picosecond pulse duration tuning in an ultrafast Cr^4+:forsterite laser," Opt. Express **20**, 18138 (2012).

173.   A. E. Siegman, "Linear Pulse Propagation," in *Lasers* (University Science Books, 1986).

174.   F. Gires and P. Tournois, "Interféromètre utilisable pour la compression d'impulsions lumineuses modulées en fréquence," C. R. Acad. Sci. Paris **258**, 6112–6115 (1964).

175.   B. Golubovic, R. R. Austin, M. K. Steiner-Shepard, M. K. Reed, S. a Diddams, D. J. Jones, and A. G. Van Engen, "Double Gires–Tournois interferometer negative-dispersion mirrors for use in tunable mode-locked lasers," Opt. Lett. **25**, 275 (2000).

176.   K. Sala, G. Kenney-Wallace, and G. Hall, "CW autocorrelation measurements of picosecond laser pulses," IEEE J. Quantum Electron. **16**, 990–996 (1980).

177.   D. J. Kane and R. Trebino, "Characterization of arbitrary femtosecond pulses using frequency-resolved optical gating," IEEE J. Quantum Electron. **29**, 571–579 (1993).

178.   R. Trebino, K. W. DeLong, D. N. Fittinghoff, J. N. Sweetser, M. A. Krumbügel, B. A. Richman, and D. J. Kane, "Measuring ultrashort laser pulses

in the time-frequency domain using frequency-resolved optical gating," Rev. Sci. Instrum. **68**, 3277–3295 (1997).

179. C. Iaconis and I. A. Walmsley, "Spectral phase interferometry for direct electric-field reconstruction of ultrashort optical pulses," Opt. Lett. **23**, 792 (1998).

180. L. Gallmann, D. H. Sutter, N. Matuschek, G. Steinmeyer, and U. Keller, "Techniques for the characterization of sub-10-fs optical pulses: a comparison," Appl. Phys. B **70**, S67–S75 (2000).

181. S. M. J. Kelly, "Characteristic sideband instability of periodically amplified average soliton," Electron. Lett. **28**, 806 (1992).

182. O. Svelto, "Laser Beam Transformation: Propagation, Amplification, Frequency Conversion, Pulse Compression and Pulse Expansion," in *Principles of Lasers*, V (Springer, 2010), pp. 505–545.

183. N. Coluccelli, A. Gambetta, D. Gatti, M. Marangoni, A. Di Lieto, M. Tonelli, G. Galzerano, and P. Laporta, "16-W self-referenced frequency comb at 2.06 μ m using a Ho:YLF multipass amplifier," Opt. Lett. **36**, 2299 (2011).

184. M. Hinkelmann, D. Wandt, U. Morgner, J. Neumann, and D. Kracht, "High repetition rate, μJ-level, CPA-free ultrashort pulse multipass amplifier based on Ho:YLF," Opt. Express **26**, 18125–18130 (2018).

185. X. Ren, L. H. Mach, Y. Yin, Y. Wang, and Z. Chang, "Generation of 1 kHz, 23 mJ, 88 fs, 2.5 μ m pulses from a Cr 2+ :ZnSe chirped pulse amplifier," Opt. Lett. **43**, 3381 (2018).

186. W. Koechner, "Laser Amplifier," in *Solid-State Laser Engineering*, VI (Springer New York, 2006), pp. 156–209.

187. L. von Grafenstein, M. Bock, U. Griebner, and T. Elsaesser, "High-energy multi-kilohertz Ho-doped regenerative amplifiers around 2 μm," Opt. Express **23**, 14744–14752 (2015).

188. M. Hemmer, D. Sánchez, M. Jelínek, V. Smirnov, H. Jelinkova, V. Kubeč ek, and J. Biegert, "2-μ m wavelength, high-energy Ho:YLF chirped-pulse amplifier for mid-infrared OPCPA," Opt. Lett. **40**, 451–454 (2015).

189. L. von Grafenstein, M. Bock, D. Ueberschaer, U. Griebner, and T. Elsaesser, "Ho:YLF chirped pulse amplification at kilohertz repetition rates – 4.3 ps pulses at 2 μ m with GW peak power," Opt. Lett. **41**, 4668–4671 (2016).

190. A. Wienke, D. Wandt, U. Morgner, J. Neumann, and D. Kracht, "Comparison between Tm:YAP and Ho:YAG ultrashort pulse regenerative amplification," Opt. Express **24**, 8632–8640 (2016).

191. A. Wienke, D. Wandt, U. Morgner, J. Neumann, and D. Kracht, "700 MW peak power of a 380 fs regenerative amplifier with Tm:YAP," Opt. Express **23**, 16884–16889 (2015).

192. J. Czochralski, "Ein neues Verfahren zur Messung der Kristallisationsgeschwindigkeit der Metalle," Zeitschrift für Phys. Chemie **92U**, 219–221 (1918).

193. K. Lehovec, J. Soled, R. Koch, A. MacDonald, and C. Stearns, "Apparatus for Crystal Pulling in Vacuum Using a Graphite Resistance Furnace," Rev. Sci. Instrum. **24**, 652–655 (1953).

194. G. Müller, "The Czochralski Method - where we are 90 years after Jan Czochralski's invention," Cryst. Res. Technol. **42**, 1150–1161 (2007).

195. R. Nacken, "Über das Wachsen von Kristallpolyedern in ihrem Schmelzfluß," Neues Jahrb. für Geol. und Paläontologie **2**, 133 (1915).

196. S. Kyropoulos, "Ein Verfahren zur Herstellung großer Kristalle," Zeitschrift für Anorg. und Allg. Chemie **154**, 308–313 (1926).

197. F. Schmid and D. Viechnicki, "Growth of Sapphire Disks from the Melt by a Gradient Furnace Technique," J. Am. Ceram. Soc. **53**, 528–529 (1970).

198. V. Peters, A. Bolz, K. Petermann, and G. Huber, "Growth of high-melting sesquioxides by the heat exchanger method," J. Cryst. Growth **237**–**239**, 879–883 (2002).

199. A. Ikesue, Y. L. Aung, T. Taira, T. Kamimura, K. Yoshida, and G. L. Messing, "Progress in Ceramic Lasers," Annu. Rev. Mater. Res. **36**, 397–429 (2006).

200. A. Ikesue and Y. L. Aung, "Synthesis and Performance of Advanced Ceramic Lasers," J. Am. Ceram. Soc. **89**, 1936–1944 (2006).

201. D. Kracht, M. Frede, R. Wilhelm, and C. Fallnich, "Comparison of crystalline and ceramic composite Nd:YAG for high power diode end-pumping," Opt. Express **13**, 6212–6216 (2005).

202. S. Zhang, M. Wang, L. Xu, Y. Wang, Y. Tang, X. Cheng, W. Chen, J. Xu, B. Jiang, and Y. Pan, "Efficient Q-switched Tm:YAG ceramic slab laser," Opt. Express **19**, 727–732 (2011).

203. A. Pirri, D. Alderighi, G. Toci, and M. Vannini, "High-efficiency, high-power and low threshold Yb^3+:YAG ceramic laser," Opt. Express **17**, 23344–23349 (2009).

204. O. L. Antipov, A. A. Novikov, N. G. Zakharov, and A. P. Zinoviev, "Optical properties and efficient laser oscillation at 2066 nm of novel Tm:Lu2O3 ceramics," Opt. Mater. Express **2**, 183 (2012).

205. W. Jing, P. Loiko, J. M. Serres, Y. Wang, E. Vilejshikova, M. Aguiló, F. Díaz, U. Griebner, H. Huang, V. Petrov, and X. Mateos, "Synthesis, spectroscopy, and efficient laser operation of "mixed" sesquioxide Tm:(Lu,Sc)_2O_3 transparent ceramics," Opt. Mater. Express **7**, 4192 (2017).

206. H. Furuse, N. Horiuchi, and B.-N. Kim, "Transparent non-cubic laser ceramics with fine microstructure," Sci. Rep. **9**, 10300 (2019).

207. P. G. Klemens, "Thermal Resistance due to Point Defects at High Temperatures," Phys. Rev. **119**, 507–509 (1960).

208. R. Peters, C. Kränkel, S. T. Fredrich-Thornton, K. Beil, K. Petermann, G. Huber, O. H. Heckl, C. R. E. Baer, C. J. Saraceno, T. Südmeyer, and U. Keller, "Thermal analysis and efficient high power continuous-wave and mode-locked thin disk laser operation of Yb-doped sesquioxides," Appl. Phys. B Lasers Opt. **102**, 509–514 (2011).

209. C. Kränkel, "Rare-earth-doped sesquioxides for diode-pumped high-power lasers in the 1-, 2-, and 3-µm spectral range," IEEE J. Sel. Top. Quantum Electron. **21**, 1602013 (2015).

210. L. Fornasiero, "Nd3+- und Tm3+-dotierte Sesquioxide," University of Hamburg (1999).

211. D. E. Zelmon, J. M. Northridge, N. D. Haynes, D. Perlov, and K. Petermann, "Temperature-dependent Sellmeier equations for rare-earth sesquioxides," Appl. Opt. **52**, 3824 (2013).

212.   P. Koopmann, S. Lamrini, K. Scholle, P. Fuhrberg, K. Petermann, and G. Huber, "Laser Operation and Spectroscopic Investigations of Tm : LuScO3," in *CLEO/Europe and EQEC 2011 Conference Digest* (OSA, 2011), Vol. CA1, p. CA1_4.

213.   X. Xu, Z. Hu, D. Li, P. Liu, J. Zhang, B. Xu, and J. Xu, "First laser oscillation of diode-pumped Tm^3+-doped LuScO3 mixed sesquioxide ceramic," Opt. Express **25**, 15322–15329 (2017).

214.   A. A. Lagatsky, F. Fusari, S. V. Kurilchik, V. E. Kisel, A. S. Yasukevich, N. V. Kuleshov, A. A. Pavlyuk, C. T. A. Brown, and W. Sibbett, "Optical spectroscopy and efficient continuous-wave operation near 2 µm for a Tm, Ho:KYW laser crystal," Appl. Phys. B **97**, 321–326 (2009).

215.   D. Findlay and R. A. Clay, "The measurement of internal losses in 4-level lasers," Phys. Lett. **20**, 277–278 (1966).

216.   W. Koechner, "Laser Oscillator," in *Solid-State Laser Engineering*, VI (Springer New York, 2006), pp. 102–155.

217.   J. A. Caird, S. A. Payne, P. R. Staver, A. J. Ramponi, L. L. Chase, and W. F. Krupke, "Quantum electronic properties of the Na3Ga2Li3F12:Cr3+ laser," IEEE J. Quantum Electron. **24**, 1077–1099 (1988).

218.   S. M. Kobtsev and N. A. Sventsitskaya, "Application of birefringent filters in continuous-wave tunable lasers : a review," Opt. Spectrosc. (English Transl. Opt. i Spektrosk. **73**, 114–123 (1992).

219.   O. Svelto, "Continuous wave laser behavior," in *Principles of Lasers*, V (Springer, 2010).

220.   S. A. Payne and W. F. Krupke, "A Glimpse into the Laser-Crystal Ball," Opt. Photonics News **7**, 31 (1996).

221.   A. A. Lagatsky and J.-M. Hopkins, "Diode-pumped femtosecond Tm-doped Lu2O3 ceramic laser," in *Laser Congress 2016 (ASSL, LSC, LAC)* (Optical Society of America, 2016), p. JTu2A.5.

222.   H. Cheng, X. D. Jiang, X. P. Hu, M. L. Zhong, X. J. Lv, and S. N. Zhu, "Diode-pumped 1988-nm Tm:YAP laser mode-locked by intracavity second-harmonic generation in periodically poled LiNbO_3," Opt. Lett. **39**, 2187 (2014).

223.   J. Ma, G. Q. Xie, P. Lv, W. L. Gao, P. Yuan, L. J. Qian, H. H. Yu, H. J. Zhang, J. Y. Wang, and D. Y. Tang, "Graphene mode-locked femtosecond laser at 2 µm wavelength," Opt. Lett. **37**, 2085–2087 (2012).

224.   J. Ma, G. Q. Xie, W. L. Gao, P. Yuan, L. J. Qian, H. H. Yu, H. J. Zhang, and J. Y. Wang, "Diode-pumped mode-locked femtosecond Tm:CLNGG disordered crystal laser," Opt. Lett. **37**, 1376–1378 (2012).

225.   C. Luan, K. Yang, J. Zhao, S. Zhao, T. Li, H. Zhang, J. He, L. Song, T. Dekorsy, M. Guina, and L. Zheng, "Diode-pumped mode-locked Tm:LuAG laser at 2 µm based on GaSb-SESAM," Opt. Lett. **42**, 839 (2017).

226.   Z. Qin, G. Xie, L. Kong, P. Yuan, L. Qian, X. Xu, and J. Xu, "Diode-Pumped Passively Mode-Locked Tm:CaGdAlO4 Laser at 2-µm Wavelength," IEEE Photonics J. **7**, 1–5 (2015).

227.   M. Gaponenko, V. J. Wittwer, A. Härkönen, S. Suomalainen, N. Kuleshov, M. Guina, and T. Südmeyer, "Diode-pumped Tm:KY(WO4)2 laser passively modelocked with a GaSb-SESAM," Opt. Express **25**, 25760–25766 (2017).

228.   J. Ma, G. Xie, J. Zhang, P. Yuan, D. Tang, and L. Qian, "Passively Mode-

Locked Tm:YAG Ceramic Laser Based on Graphene," IEEE J. Sel. Top. Quantum Electron. **21**, 1100806 (2015).

229. T. Feng, K. Yang, J. Zhao, S. Zhao, W. Qiao, T. Li, T. Dekorsy, J. He, L. Zheng, Q. Wang, X. Xu, L. Su, and J. Xu, "1.21 W passively mode-locked Tm:LuAG laser," Opt. Express **23**, 11819–11825 (2015).

230. C. Y. Cho, Y. F. Chen, G. Zhang, W. D. Chen, and H. C. Liang, "Exploring the self-mode locking of the 2 μm Tm:YAG laser with suppression of the self-pulsing dynamic," Opt. Lett. **42**, 5226 (2017).

231. N. K. Stevenson, C. T. A. Brown, J.-M. Hopkins, M. D. Dawson, C. Kränkel, and A. A. Lagatsky, "Diode-pumped femtosecond Tm3+-doped LuScO3 laser near 2.1 μm," Opt. Lett. **43**, 1287–1290 (2018).

232. A. A. Lagatsky, P. Koopmann, O. L. Antipov, C. T. A. Brown, G. Huber, and W. Sibbett, "Femtosecond pulse generation with Tm-doped sesquioxides," in *2013 Conference on Lasers & Electro-Optics Europe & International Quantum Electronics Conference CLEO EUROPE/IQEC* (IEEE, 2013), p. CA_6_3.

233. A. A. Lagatsky, P. Koopmann, P. Fuhrberg, G. Huber, C. T. a Brown, and W. Sibbett, "Passively mode locked femtosecond Tm:Sc2O3 laser at 2.1 μm," Opt. Lett. **37**, 437–9 (2012).

234. A. A. Lagatsky, O. L. Antipov, and W. Sibbett, "Broadly tunable femtosecond Tm:Lu2O3 ceramic laser operating around 2070 nm," Opt. Express **20**, 19349–19354 (2012).

235. A. A. Lagatsky, P. Koopmann, P. Fuhrberg, G. Huber, C. T. A. Brown, and W. Sibbett, "148-fs passively mode-locked Tm : LuScO3 laser at 2100 nm," in *Proceedings of EPS-QEOD Europhoton Conference 2012* (2012), p. WeD.7.

236. A. Schmidt, P. Koopmann, G. Huber, P. Fuhrberg, S. Y. Choi, D.-I. Yeom, F. Rotermund, V. Petrov, and U. Griebner, "175 fs Tm:Lu2O3 laser at 2.07 μm mode-locked using single-walled carbon nanotubes," Opt. Express **20**, 5313–5318 (2012).

237. G. Ghosh, "Dispersion-equation coefficients for the refractive index and birefringence of calcite and quartz crystals," Opt. Commun. **163**, 95–102 (1999).

238. K. Naganuma, G. Lenz, and E. P. Ippen, "Variable bandwidth birefringent filter for stable femtosecond lasers," IEEE J. Quantum Electron. **28**, 2142–2150 (1992).

239. B. Stormont, A. J. Kemp, I. G. Cormack, B. Agate, C. T. A. Brown, W. Sibbett, and R. Szipöcs, "Broad tunability from a compact, low-threshold Cr:LiSAF laser incorporating an improved birefringent filter and multiple-cavity Gires-Tournois interferometer mirrors," J. Opt. Soc. Am. B **22**, 1236–1243 (2005).

240. U. Demirbas, "Off-surface optic axis birefringent filters for smooth tuning of broadband lasers," Appl. Opt. **56**, 7815–7825 (2017).

241. T. Radhakrishnan, "The dispersion, briefringence and optical activity of quartz," Proc. Indian Acad. Sci. - Sect. A **25**, 260 (1947).

242. T. Radhakrishnan, "Further studies on the temperature variation of the refractive index of crystals," Proc. Indian Acad. Sci. - Sect. A **33**, 22 (1951).

243. U. Demirbas, J. Wang, G. S. Petrich, S. Nabanja, J. R. Birge, L. A. Kolodziejski, F. X. Kärtner, and J. G. Fujimoto, "100-nm tunable femtosecond Cr:LiSAF laser mode locked with a broadband saturable Bragg reflector," Appl. Opt. **56**, 3812–3816 (2017).

244. A. Berrou, O. J. P. Collett, D. Morris, and M. J. D. Esser, "Comparative study of high power Tm:YLF and Tm:LLF slab lasers in continuous wave regime," Opt. Express **26**, 10559–10572 (2018).

245. P. Koopmann, R. Peters, K. Petermann, and G. Huber, "Crystal growth, spectroscopy, and highly efficient laser operation of thulium-doped Lu2O3 around 2 μm," Appl. Phys. B **102**, 19–24 (2011).

246. D. P. Shepherd, A. Choudhary, A. A. Lagatsky, P. Kannan, S. J. Beecher, R. W. Eason, J. I. Mackenzie, X. Feng, W. Sibbett, and C. T. A. Brown, "Ultrafast High-Repetition-Rate Waveguide Lasers," IEEE J. Sel. Top. Quantum Electron. **22**, (2016).

247. A. Choudhary, P. Kannan, J. I. Mackenzie, X. Feng, and D. P. Shepherd, "Ion-exchanged Tm^3+:glass channel waveguide laser," Opt. Lett. **38**, 1146–1148 (2013).

248. B. Ferrand, B. Chambaz, and M. Couchaud, "Liquid phase epitaxy: A versatile technique for the development of miniature optical components in single crystal dielectric media," Opt. Mater. (Amst). **11**, 101–114 (1999).

249. C. Grivas, D. P. Shepherd, T. C. May-Smith, R. W. Eason, M. Pollnau, A. Crunteanu, and M. Jelinek, "Performance of Ar+-milled Ti:sapphire rib waveguides as single transverse-mode broadband fluorescence sources," IEEE J. Quantum Electron. **39**, 501–507 (2003).

250. K. van Dalfsen, S. Aravazhi, C. Grivas, S. M. García-Blanco, and M. Pollnau, "Thulium channel waveguide laser in a monoclinic double tungstate with 70% slope efficiency," Opt. Lett. **37**, 887–889 (2012).

251. K. van Dalfsen, S. Aravazhi, C. Grivas, S. M. García-Blanco, and M. Pollnau, "Thulium channel waveguide laser with 1.6 W of output power and ~80% slope efficiency," Opt. Lett. **39**, 4380–4383 (2014).

252. P. Loiko, R. Soulard, G. Brasse, J.-L. Doualan, B. Guichardaz, A. Braud, A. Tyazhev, A. Hideur, and P. Camy, "Watt-level Tm:LiYF 4 channel waveguide laser produced by diamond saw dicing," Opt. Express **26**, 24653–24662 (2018).

253. P. Loiko, R. Thouroude, R. Soulard, L. Guillemot, G. Brasse, B. Guichardaz, A. Braud, A. Hideur, M. Laroche, H. Gilles, and P. Camy, "In-band pumping of Tm:LiYF 4 channel waveguide: a power scaling strategy for ~2 μm waveguide lasers," Opt. Lett. **44**, 3010–3013 (2019).

254. E. Kifle, P. Loiko, U. Griebner, V. Petrov, P. Camy, A. Braud, M. Aguiló, F. Díaz, and X. Mateos, "Diamond saw dicing of thulium channel waveguide lasers in monoclinic crystalline films," Opt. Lett. **44**, 1596–1599 (2019).

255. F. Chen and J. R. V. de Aldana, "Optical waveguides in crystalline dielectric materials produced by femtosecond-laser micromachining," Laser Photonics Rev. **8**, 251–275 (2014).

256. D. G. Lancaster, S. Gross, H. Ebendorff-Heidepriem, K. Kuan, T. M. Monro, M. Ams, A. Fuerbach, and M. J. Withford, "Fifty percent internal slope efficiency femtosecond direct-written Tm3+:ZBLAN waveguide laser," Opt. Lett. **36**, 1587 (2011).

257. D. G. Lancaster, S. Gross, A. Fuerbach, H. E. Heidepriem, T. M. Monro, and M. J. Withford, "Versatile large-mode-area femtosecond laser-written Tm:ZBLAN glass chip lasers," Opt. Express **20**, 27503–27509 (2012).

258. Y. Ren, G. Brown, A. Ródenas, S. Beecher, F. Chen, and A. K. Kar, "Mid-

infrared waveguide lasers in rare-earth-doped YAG," Opt. Lett. **37**, 3339 (2012).

259. J. Morris, N. K. Stevenson, H. T. Bookey, A. K. Kar, C. T. A. Brown, J.-M. Hopkins, M. D. Dawson, and A. A. Lagatsky, "1.9 μm waveguide laser fabricated by ultrafast laser inscription in Tm:Lu_2O_3 ceramic," Opt. Express **25**, 14910–14917 (2017).

260. S. Gross, M. Ams, D. G. Lancaster, T. M. Monro, A. Fuerbach, and M. J. Withford, "Femtosecond direct-write überstructure waveguide Bragg gratings in ZBLAN," Opt. Lett. **37**, 3999–4001 (2012).

261. R. A. McCracken, J. M. Charsley, and D. T. Reid, "A decade of astrocombs: recent advances in frequency combs for astronomy [Invited]," Opt. Express **25**, 15058 (2017).

262. R. R. Gattass and E. Mazur, "Femtosecond laser micromachining in transparent materials," Nat. Photonics **2**, 219–225 (2008).

263. D. Tan, K. N. Sharafudeen, Y. Yue, and J. Qiu, "Femtosecond laser induced phenomena in transparent solid materials: Fundamentals and applications," Prog. Mater. Sci. **76**, 154–228 (2016).

264. A. Crespi, Y. Gu, B. Ngamsom, H. J. W. M. Hoekstra, C. Dongre, M. Pollnau, R. Ramponi, H. H. van den Vlekkert, P. Watts, G. Cerullo, and R. Osellame, "Three-dimensional Mach-Zehnder interferometer in a microfluidic chip for spatially-resolved label-free detection," Lab Chip **10**, 1167 (2010).

265. V. Maselli, J. R. Grenier, S. Ho, and P. R. Herman, "Femtosecond laser written optofluidic sensor: Bragg grating waveguide evanescent probing of microfluidic channel," Opt. Express **17**, 11719 (2009).

266. D. Choudhury, J. R. Macdonald, and A. K. Kar, "Ultrafast laser inscription: perspectives on future integrated applications," Laser Photon. Rev. **8**, 827–846 (2014).

267. R. Mary, S. J. Beecher, G. Brown, R. R. Thomson, D. Jaque, S. Ohara, and A. K. Kar, "Compact, highly efficient ytterbium doped bismuthate glass waveguide laser," Opt. Lett. **37**, 1691–1693 (2012).

268. D. G. Lancaster, S. Gross, A. Fuerbach, M. J. Withford, and T. M. Monro, "2.1 μm waveguide laser fabricatedby femtosecond laser direct-writing in Ho3+, Tm3+ : ZBLAN glass," Opt. Lett. **37**, 996–998 (2012).

269. A. Choudhary, A. A. Lagatsky, P. Kannan, W. Sibbett, C. T. a Brown, and D. P. Shepherd, "Diode-pumped femtosecond solid-state waveguide laser with a 4.9 GHz pulse repetition rate," Opt. Lett. **37**, 4416–4418 (2012).

270. A. A. Lagatsky, A. Choudhary, P. Kannan, D. P. Shepherd, W. Sibbett, and C. T. A. Brown, "Fundamentally mode-locked, femtosecond waveguide oscillators with multi-gigahertz repetition frequencies up to 15 GHz.," Opt. Express **21**, 19608–19614 (2013).

Appendix

Table 6. Summary of waveguide inscription parameters and detected fluorescent signals.

Pulse energy (μJ)	Guide diameter (μm)	Guiding type	Detected fluorescent signal (mV)	Comments
0.4	20	I	-	
0.4	30	I	-	
0.5	20	I	-	
0.5	30	I	-	
0.6	20	I	-	
0.6	30	I	-	
0.7	20	I	-	
0.7	30	I	-	
0.8	20	I	-	
0.8	30	I	-	
0.9	20	II	-	
0.9	30	II	-	
1.0	20	II	-	
1.0	30	II	-	
1.1	20	II	-	
1.1	30	II	-	
1.2	20	II	6.38	Visible guiding and evidence of upconversion.
1.2	30	II	6.51	Better confinement in vertical direction compared with 20 μm guide.
1.3	20	II	6.42	
1.3	30	II	6.21	
1.4	20	II	6.73	
1.4	30	II	5.8	
1.5	20	II	6.64	
1.5	30	II	5.74	
2.0	20	II	4.61	
2.0	30	II	34	Laser action achieved. Guide used for further laser performance investigations.
3.0	20	II	4.82	
3.0	30	II	21.7	Laser action achieved.
4.0	20	-		Very low fluorescent signal.
4.0	30	-		Very low fluorescent signal.
5.0	20	-		Very low fluorescent signal.
5.0	30	-		Very low fluorescent signal.